UNIVERSITÀ POLITECNICA DELLE MARCHE

DOCTORAL THESIS

Self-assembling properties of mono and di-rhamnolipids and their interactions with model membranes

Phd Student:
Alessandra Marega Motta

Supervisor:
Prof. Francesco Spinozzi

Coordinators:
Prof. Paolo Mariani
Prof. Rosangela Itri

Department of Life and Environmental Sciences (DiSVA)
XXXIV cycle
Ancona, 2018-2022

Declaration of Authorship

I, Alessandra Marega Motta, declare that this thesis titled "Self-assembling properties of mono and di-rhamnolipids and their interactions with model membranes" and the work presented in it are my own and has been generated by me as the result of my own original research.

I confirm that:

- This work was done wholly or mainly while in candidature for a research degree at this University;
- Where any part of this thesis has previously been submitted for a degree or any other qualification at this University or any other institution, this has been clearly stated;
- Where I have consulted the published work of others, this is always clearly attributed;
- Where I have quoted from the work of others, the source is always given. With exception of such quotations, this thesis is entirely my own work;
- Where the thesis is based on work done by others and what I have contributed myself.

Abstract

This doctoral thesis reports an extensive biophysical study concerning the two major categories of molecules that compose a biological surfactant called rhamnolipid, which are mono- and di-rhamnolipids. Understanding the differences in chemical and physical properties of mono-rhamnolipids and di-rhamnolipids is important in view of their potential applications as emulsifying and dispersing agents in bioremediation processes and in other biotechnological sectors, such as in the cosmetics industry. Also, although there are a few studies concerning the molecular properties of mono- and di-rhamnolipids, information is scarce regarding the mechanisms by which each of the two components interacts with cell membranes.

In order to be able to study the chemical and physical properties of the two components, my thesis work started from the chemical separation of the mono and the di-rhamnolipids from the commercial mixture (RLs), performed by using a silica gel column chromatography. After separation and purification, electrospray mass spectroscopy was used to confirm the quality of the process. Then, I performed surface tension measurements to determinate the CMC (Critical Micelle Concentration) of each of them.

The physical chemical characterization started using X-ray diffraction (XRD) techniques, conducted in our biophysics laboratory on samples of mono and di-RLs dissolved in concentrated water solutions ranging from 10 to 45 w/w %. This technique allows to determine the characteristic lyotropic polymorphism, as well as the molecular packing and properties at a few Angstrom resolutions. To derive the structural properties in dilute solutions, mono or di-RL samples dissolved at concentration from 10 to 100 mM in water were then analysed by performing Synchrotron Small Angle X-ray Scattering (SAXS) experiments at the Diamond Light Source synchrotron (Didcot, UK). Results allowed to characterize the different micellar structures formed by mono-RL and di-RL in water.

Finally, I extensively studied the interactions between model membranes with mono- and di-RLs, showing how it is possible, by assuming a kinetic model, to derive relevant physical parameters from optical microscopy images. I performed phase contrast and fluorescence microscopy experiments on plasma membrane models represented by Giant Unilamellar Vesicles (GUVs), composed of single lipid POPC and ternary GUVs containing DOPC:SM:CHOL in three molar ratios, 1:1:1, 3:5:2 and 5:3:2. The experiments were performed with GUVs in the presence of either mono-RL or di-RL in 0.06, 0.12 and 0.25 mM concentrations. Novel methods have been developed and applied to microscopy images allowing the determination the area and the volume of GUVs with asymmetrical shape and the description of the GUV-RL interaction in terms of two kinetic mechanisms, RL-insertion and pore formation.

Summary

Figures

Tables

List of Abbreviations

CMC: Critical Micellar Concentration

ESI: Electrospray Ionisation

GUV: Giant Unilamellar Vesicle

ITO: Indium Tin Oxide

LUV: Large Unilamellar Vesicle

POM: Polarized Optical Microscopy

RL: Rhamnolipids

SAS: Small Angle Scattering

SAXS: Small Angle X-ray Scattering

SUV: Small Unilamellar Vesicle

XRD: X-ray Diffraction

HLB: Hydrophilic-Lipophilic Balance

Lo: Liquid Ordinate Phase

Ld: Liquid Disordinate Phase

TLC: Thin-Layer Chromatography

UV: Under Ultraviolet

 API: Atmospheric Pressure Ionisation

ES-MS: Electrospray Mass Spectrometry

1.Introduction

1.1 Hydrocarbon contamination in the marine environment

The worldwide rapid growth of industrial activities leads to the environmental risks and contamination, such as petroleum pollution. The offshore exploitation of petroleum may cause incidents that have deep impact on marine ecosystems [Etkin1997]. As well as leaks and oil spills, due to a large variety of human activities related to crude oil refining, handling, storage and different forms of transportation of petroleum and its distilled products. Oil spills are environmental disasters that often lead to negative long-term ecological and social impacts. An oil spill is usually described as a release of a liquid petroleum hydrocarbon into the environment due to human activities or natural disasters [Li2016] and usually happens worldwide in different types of environment such as land, ocean and watershed, but especially in marine areas [McCoy2010].

On a global basis, the size and number of oil spills are declining, fortunately representing less than 5% of the oil contamination in the oceans, but even that small percentage of pollution significantly affects marine ecosystems [Ornitz2002]. It is worth to emphasize that all the progresses regarding prevention strategies, regulations and treaties are responsible for minimizing pollution problems and accidents. According to Ref. [Ornitiz2002], by comparing the data for the number of major oil spills (those with 700 tons or more) and the number of accidents from 10 to 25 years ago, it results that the volume of oil spilled and the number of large spills are decreasing worldwide.

Despite the good news, the contamination of the oceans with hydrocarbons derived from petroleum is still a big environmental issue: from 1907 to 2014 more than 7 million tons of oil has been released to the environment from more than 140 large spills [Li2016]. Among different disasters involving management of petroleum, the main spills include the Exxon Valdez incident, which happened in Alaska on march 1989, the Hebei Spirit spill, which occurred in South Korea in December 2007, and the Prestige spill, which occurred in Spain in November 2002. The Deepwater Horizon oil spill, which is considered the largest marine oil spill in the history of the petroleum industry, was a disaster caused by an explosion that began in April 2010 and released over 700.000 tons of crude oil in the Gulf of Mexico during a period of three months [Vilcaez2013].
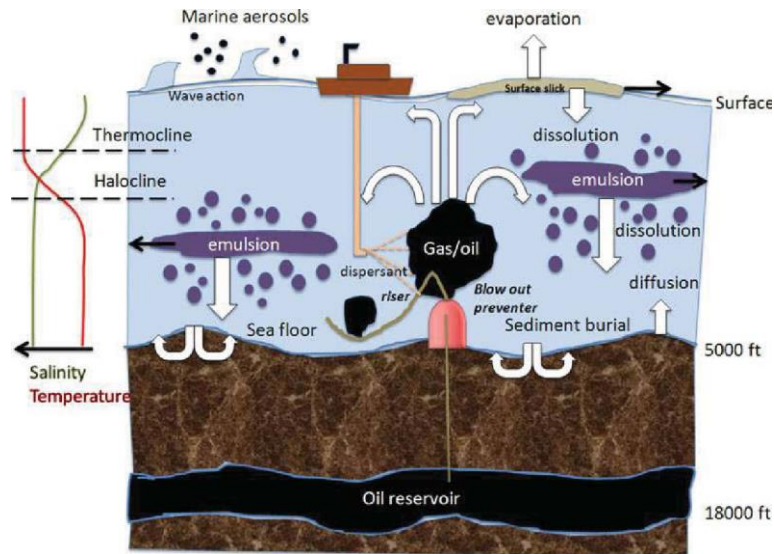
Figure 1.1 Illustration of sea floor leak and oil fate processes [Thibodeaux2010]

1.1.1 Bioremediation

Environmental biotechnologies, such as composting and wastewater treatments, have long been exploited for remediation of contaminated sites [Mueller1996]. However, recent studies in molecular biology and ecology have been giving opportunities for more efficient biological processes to clean up polluted air, water and land sites [Vidali2001]. Bioremediation is one of these more efficient processes, based on the metabolic potential of microorganisms to clean up contaminated environments. Bioremediation includes two categories of processes: *in situ* or *ex situ*. *In situ* bioremediation treats the contaminated water, soil or groundwater in the site where the contamination has happened. *Ex situ* bioremediation processes require excavation of contaminated soil or pumping of groundwater before treatment.

The more relevant characteristic of bioremediation is that it can be carried out in open environments that contain a variety of different organisms. Bacteria, especially those capable of degrading pollutants, usually have a central role in bioremediation, while other organisms (plants, fungi and protozoa) also affect the process. For this reason, a deeper understanding of the microbial ecology of the contaminated site is necessary to improve bioremediation processes [Watanabe2001]. In this context, the control and the optimization of bioremediation processes is a complex system of many factors. These factors include the existence of a microbial population capable of degrading the pollutants, the availability of contaminants to the microbial population, the environment factors such as type of soil, temperature, and pH, the presence of oxygen or other electron acceptors and nutrients [Vidali2001].

1.1.2 Bioremediation of groundwater

Groundwater ecosystems have many advantages and can be a water storage for human use. In the world, 33% of drinking water, 20% of irrigation and 40% of the water used in industry is provided from groundwater [Griebler2015]. At the same time it is a fragile environment: for example a significant amount of gasoline can enter into the groundwater due to leakage from underground storage tanks, accidental spills, inappropriate waste disposal operations or transfer of polluted rainwater [Mitra2011]. Dispersion, retardation and solubility are some of the chemical-physical processes that affect natural attenuation of contaminants concentration and therefore make their removal from groundwater one of the most expensive environmental issues [Raei2017].

For the past decades, the most used method for groundwater cleanup regards the pump-and-treat system, consisting of a series of recovery wells, located in the heart of the plume, where groundwater is pumped to and cleaned by a treatment facility [Okoh2006]. This *ex situ* method is used to control contaminant migration and to remove the contaminant mass. However, many contaminants, such as hydrocarbon byproducts, become trapped in the subsurface. For this reason, a complete decontamination may require the pumping of large volumes of water over a long period of time [Okoh2006]. Because it treats contaminants in place instead of requiring their extraction, *in situ* bioremediation takes care of these shortcomings in a completed cleanup process and, consequently leads to faster decontamination results when used together with pump-and-treat technology [Testa1991].

Several studies have shown that *in situ* biodegradation can effectively decrease the contaminant concentration up to the standard level. *In situ* bioremediation systems include injection wells, infiltration galleries and extraction wells [Raei2017]. The injection wells promote the growth of microorganisms by providing electron acceptors, such as oxygen, and nutrients, such as nitrogen or phosphorus. The extraction wells increase the hydraulic gradients and improve the movement of the injected substances [Yoon1999].

Potential advantages of *in situ* bioremediation of groundwater compared to other methods include destruction rather than transfer of the contaminant to another place, minimal exposure of the on site workers to the contaminant, long time protection of public health and possible reduction of the duration of the remedial process [Okoh2006].

1.1.3 Bioremediation in oil spill cases

As discussed before, unfortunately crude oil spill accidents have happened throughout the history of the petroleum industry. The traditional physical treatment processes used to clean up the polluted areas are efficient to quickly remove contamination by crude oil but, in most cases, the pollutants may not be completely removed or may transform into toxic byproducts. The accidental spills of hydrocarbons damage marine ecosystems and, due to the difficulty of cleaning up oil at the sea, may cause contamination of shorelines. The fuel that reaches the coast is formed by a water-in-oil emulsion that is different from the original transported fuel, due to spreading, evaporation, dispersion and emulsification processes. A secondary and more precise cleanup of the shoreline is necessary after the removal of the oil accumulation of the coast by mechanical procedures [Mateo2005].

Physical collection methods such as booms, skimmers and adsorbents typically recover no more than 10-15% of the spilled oil [Thavasi2010] and the generated byproducts of petroleum have toxic effects on the local ecosystem, such as fishes, corals, planktons, microorganisms, sediments and marine fauna. For this reason, some biological alternatives need to be used together with physicochemical technologies [Malik2012]. In this context, biosurfactants play an important role in remediation processes due to their efficacy as dispersion and remediation agents as well as their environmentally friendly characteristics, such as low toxicity and high biodegradability [Silva2014].

Petroleum pollution has a particular effect on microbial population. The first step of this effect is hydrocarbon transportation to the surface of the microbial cell through the contact and then transportation across the cell membrane [Ampelli2016]. Some bacterial populations exhibit resistance to oil transportation and a few bacterial populations efficiently degrade oils and hydrocarbons [Karlapudi2017].

The interest in using microorganisms to clean up oil spills in marine, estuarine and shoreline environments has existed for many decades. However it was during the accident involving the tanker Exxon Valdez, which was stuck on a reef in Alaska in 1989, that an important bioremediation process in surface waters was undertaken [Okoh2006]. Microbial degradation of oil hydrocarbons is often limited by several factors, such as availability of nutrients and oxygen, reduced bioavailability of the contaminants, site-specific physical conditions and contaminant specific conditions [Margesin1999].

1.2 Surfactants and Biosurfactants

1.2.1 Surfactants

Surfactants, also called surface-active agents, are compounds that, when added to a liquid, reduce its surface tension, thereby increasing its spreading and wetting properties. Surface-active molecules should be partly hydrophilic (water-soluble) and partly lipophilic (soluble in lipids or oils). They concentrate at the interfaces between bodies or droplets of water and those of oil or lipids to act as emulsifying or foaming agents. Surfactants that are more lipophilic and less hydrophilic may be used as defoaming agents or demulsifiers [Encyclopedia Britannica, Inc.]. Surfactants can be either chemically synthesized (synthetic surfactants) or microbially produced (biosurfactant).

The term interface indicates a boundary between any two immiscible phases and the term surface denotes an interface where one phase is a gas, usually air, and the other is a liquid, typically water. A surfactant has the property of adsorbing onto the surface and changing its free energy, which is the amount of work required to create that interface. The hydrophobic portion concentrates at the surface while the hydrophilic portion is oriented towards the solution. Surfactants have the ability of lower the surface tension, which is a measure of the surface free energy per unit area required to bring a molecule from the bulk phase to the surface [Rosen2012]. Due to the presence of a surfactant, less work is required to bring a molecule to the surface and the surface tension is reduced, consequently increasing solubility, wetting ability and foaming capacity [Mulligan2004].

Surfactants dispersed in solution are also able to form self-assembled molecular clusters called micelles. Usually the molecules of surfactants are formed by an alkyl chain with 8-22 carbons, called hydrophobic group (or tail), which does not show affinity to water, and a functional group, called the hydrophilic group (or head), that shows water affinity. This kind of structure with two opposing functions is called an amphiphilic structure [Nakama, Chapter15].

Critical micelle concentration (CMC)

Surfactant activities can be determined by measuring the changes in surface and interfacial tensions, stabilization or destabilization of emulsions, and hydrophilic-lipophilic balance (HLB). Surface tension in the air/water and oil/water interfaces can easily be measured with a tensiometer. When a surfactant is added to air/water or oil/water systems at increasing concentrations, a reduction of surface tension is observed up to a critical level, above which amphiphilic molecules associate readily to form supramolecular structures like micelles, bilayers and vesicles. This value is known as the critical micelle concentration (CMC) [Nakama, Chapter15].

The CMC is then commonly used to measure the efficiency of a surfactant [Desai1997]. To sum up, the surface tension is correlated with the concentration of the surface-active compound until the CMC is reached. This means that efficient surfactants have a low CMC because less surfactant is necessary to decrease the surface tension [Mulligan2004]. More in detail, the CMC is defined as the minimum concentration of surfactant necessary to initiate micelle formation [Becher1965].

The micellization process in water results from a delicate balance of intermolecular forces, including hydrophobic, steric, electrostatic, hydrogen bonding and van der Walls interactions. The main attractive force results from the hydrophobic effect associated with the nonpolar surfactant tails and the main opposing repulsive force results from steric interactions and electrostatic interactions (in the case of ionic and zwitterionic surfactants) between the surfactant polar heads. Micellization occurs when the attractive and the repulsive forces balance each other [Rangel-Yagui2004].

As already stated, above their CMC surfactants show self-assembling properties. Once the water/air surface is saturated, surfactants start to self-assemble in water into supramolecular aggregates, whose structure is determined by geometric as well as energetic factors. These structures, generally called micelles, are supramolecular aggregates obtained by the packing of hydrophobic tails, forming the core of the micelle, and the outward exposition of hydrophilic heads, which result to be in contact with the aqueous environment [Perinelli2020].
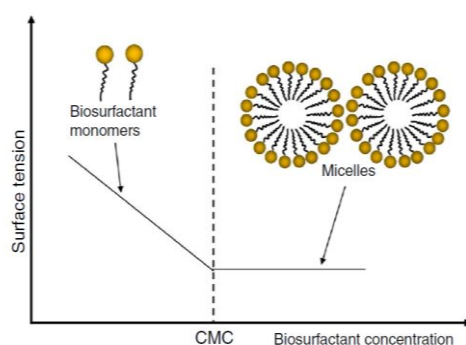
Figure 1.2 CMC and micelle (conical shape) formation of biosurfactant monomers.

Further self-assembled structures that surfactants can form are double layers (also referred to as bilayers). The surfactant molecules that form bilayers have a tail and a head with similar dimensions and this implies that each molecule is, on average, arranged in the form of a cylinder. In the double layer, the surfactants dispose of the hydrocarbon tails inwards and the heads in contact with the aqueous solvent. In order to avoid the solvent contact with the hydrophobic tails of the surfactant placed at the end of the double layer, this structure tends to close on itself by joining the ends together and then to maintain the tails within a unique hydrophobic environment. The resulting structure is a thin, large and almost planar surface that, in most cases, can wrap around itself leading to the

formation of large and mostly spherical shells called vesicles or liposomes. The strong tension that is created between the lipids in the inner layer prevents pore formation in the vesicle unless they are destabilized by the presence of conical proteins or surfactants. Notice that the structure is maintained by non-covalent interactions [Schindler1980].

Micelle shape and size can be controlled by changing the surfactant chemical structure as well as by varying solution conditions including temperature, overall surfactant concentration, surfactant composition (in the case of mixed surfactant systems), ionic strength and pH. Depending on the surfactant type and on the solution conditions, spherical micelles can grow dimensionally into cylindrical micelles or dimensionally into bilayers or discoid micelles. Micelle growth is controlled primarily by the surfactant heads, since both one dimensional and two dimensional growth require bringing the surfactant heads closer to each other in order to reduce the available area per surfactant molecule at the micelle surface and also the curvature of the micelle surface [Rangel-Yagui2004].

The properties of surfactants and their applications are strongly influenced by their physical state as single molecules or micellar self-assemblies. To note, the solubilizing effect of surfactants appears only at concentrations above CMC, since in most cases it is proportional to the number of micelles in water. Hence, the CMC of surfactants mostly depends on the hydrophobicity of the amphiphiles, due to the length of the hydrophobic tail, and on the nature and the size of the polar head and is also strongly influenced by the characteristics of solutions, for example by pH or by the presence of salts. The number of amphiphilic molecules that form the micellar structure is called aggregation number and it is a useful parameter to describe the size of the micelles [Perinelli2020].

1.2.2 Surfactant applications

The petroleum industry has traditionally been the major user of surfactants to enhance oil removal processes [Falatko1991]. Traced back from the ancestral Babylonian oil soap formula to the currently available soaps, cleansers and detergents, surfactants appear in various forms. Apart from serving as cleansing agents, surfactants find many industrial applications as additives in paints, as textile softeners, as antistatic agents, in metal processing and in oil drilling operations. Some surfactants have antimicrobial properties, which provide the basis for their utility as biocides [Rebello2014].

Surfactants are among the most versatile products of the chemical industry, appearing in such diverse products as the motor oils we use in our automobiles, the pharmaceuticals we take when we are ill, the detergents we use in cleaning our laundry and our homes, the drilling muds used in prospecting for petroleum and the floatation agents use in beneficiation of ores. The last decades have seen the

extension of surfactant applications to such high-technology areas as electronic printing, magnetic recording, biotechnology, microelectronics and viral research [Rosen2012].

The global surfactant market has been estimated as $ 43655 million in 2017 and is expected to reach $ 66408 million by 2025, with a compound annual growth rate of 5.4%, according to Laxman et al. [Laxman2018]. The growth and high demand for surfactants is due to their wide use, from household detergents and personal care products to industrial applications as cleaners, food, textiles, plastics processing, or oilfield and agricultural chemicals. As regards pharmaceutical and cosmetic formulations, surfactants are excipients required for stabilization of all dispersed systems [Perinelli2020]. They act as emulsifiers in the formulation of emulsions and creams and as stabilizers, flocculating or wetting agents in the formulations of suspensions [Tcholakova2008].

These molecules are also able to interact with biological membranes, thanks to their amphiphilic structure, increasing drug permeability across skin or mucosa. For this reason, several studies have been conducted to evaluate the potential use of different classes of surfactants as drug permeability enhancers. Almost all these interesting and exploitable applications arise from the amphiphilic nature of surfactant molecules, which, as already discussed, determines their chemical-physical properties [Perinelli2020].

1.2.3 Classification of surfactants

Surfactants are classified into ionic and nonionic surfactants. **Ionic surfactants** are subclassified into anionic surfactants (when the hydrophilic groups are anions in aqueous solutions), cationic surfactants (with positively charged hydrophobic groups), and amphoteric surfactants (that could be anions or cations, depending on pH). **Nonionic surfactants** are surfactants that do not dissociate into ions in aqueous solutions and they are subclassified depending on the type of their hydrophilic group (Figure 1.3). Common hydrophilic groups of ionic surfactants are carboxylate ($-COO^-$), sulfate ($-OSO_3^-$), sulfonate (SO_3^-), carboxybetaine ($-NR_2CH_2COO^-$), sulfobetaine ($-N(CH_3)_2C_3H_6SO_3^-$), and quaternary ammonium ($-R_4N^+$). As an example, a soap molecule has a hydrocarbon chain as its lipophilic functional group that has affinity to lipids (the lipophilic group) and a carboxylate anion as its functional group that has affinity to water (the hydrophilic group). In an aqueous solution, the carboxylate anion forms a structure with counterions such as Na^+, K^+ or Mg^{2+} (Figure 1.3) [Nakama, Chapter15].
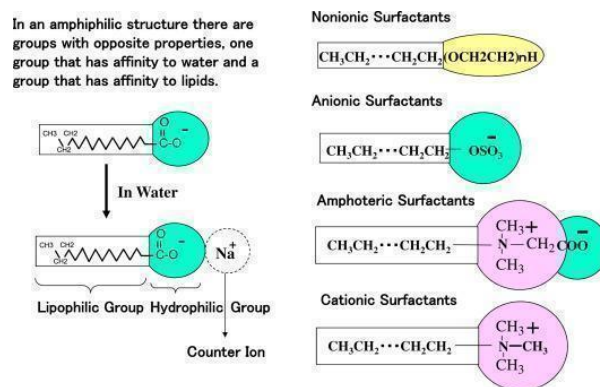
Figure 1.3 Structure and classification of surfactants [Nakama, Chapter15]

The hydrophilic group of nonionic surfactants is usually a polyoxyethylene (-(CH$_2$-CH$_2$-O)$_n$-), but there are also nonionic surfactants with glyceryl groups or sorbitol groups, and nonionic surfactants with these different hydrophilic groups are also used depending on the application. Surfactants are also classified depending on their solubility, such as hydrophilic surfactants that are soluble in water or hydrophobic (lipophilic) surfactants that are soluble in lipids. Ionic surfactants are generally hydrophilic surfactants, but nonionic surfactants can be either hydrophilic or lipophilic, depending on the balance of the hydrophilic group and lipophilic group. In other words, the solubility of nonionic surfactants depends on the balance between the hydrophilic group's capacity of attracting water and the lipophilic group's capacity of attracting oil [Nakama, Chapter15].

1.2.4 Biosurfactants

Although almost all surfactants currently in use are chemically derived from petroleum, an interest in microbial surfactants has been steadily increasing in recent years, due to their diversity and environmentally friendly nature. Biosurfactants, as already introduced, are surface active molecules synthesized by microorganisms, as it shows Table 1.1 extract from Desai et. al. [Desai1997].

There are a number of reports on the synthesis of biosurfactants by hydrocarbon degrading microorganisms, some biosurfactants have been reported to be produced on water-soluble compounds such as glucose, sucrose, glycerol or ethanol. The microorganisms that produce biosurfactants are distributed among a wide variety of genera, as it is shown on Table 1.1 [Desai1997].

Biosurfactants can be produced by bacteria, yeast or fungi and may be located inside the cells (intracellular) or secreted outside the cells (extracellular). In most cases, these compounds are produced by microorganisms to give them the ability of making substrates available to be uptaken by the cells [Abbasi2013].

Biosurfactant	Organisms	Surface tension (mN/m)	CMC (μM)	Interfacial tension (mN/m)
Glycolipids				
Rhamnolipids	*P. aeruginosa*	29		0.25
	Pseudomonas sp.	25-30	0.1-10	1
Trehalolipids	*R. erythropolis*	32-36	4	14-17
	N. erythropolis	30	20	3.5
	Mycobacterium sp.	38	0.3	15
Sophorolipids	*T. bombicola*	33		1.8
	T. apicola	30		0.9
	T. petrophilum			
Cellobiolipids	*U. zeae, U. maydis*			
Lipopeptides and lipoproteins				
Peptide-lipid	*B. licheniformis*	27	12-20	0.1-0.3
Serrawettin	*S. maarcescens*	28-33		
Viscosin	*P. fluorescens*	26.5	150	
Surfactin	*R. subtilis*	27-32	23-160	1
Subtilisin	*R. subtilis*			
Gramicidins	*R. brevis*			
Polymyxins	*R. polymyxa*			
Fatty acids, neutral lipids, and phospholipids				
Fatty acids	*C. lepus*	30	150	2
Neutral lipids	*N. erytropolis*	32		3
Phospholipids	*T. tiooxidans*			
Polymeric surfactants				
Emulsan	*A. calcoaceticus*			
Bioodispersan	*A. calcoaceticus*			
Mannan-lipid-protein	*C. tropicalis*			
Liposan	*C. lipolytica*			
Carbohydrate-protein-lipid	*P. fluorescens*	27	10	
	D. polymorphis			
Protein PA	*P. aeruginosa*			
Particulate biosurfactants				
Vesicles and fimbriae	*A. calcoaceticus*			
Whole cells	Variety of bacteria			

Table 1.1 Microbial source and properties of important types of microbial surfactants [Desai1997].

Biosurfactants are classified on the basis of their chemical composition and their microbial origin, which means the species of microorganisms that produced them. In general, their structure includes a hydrophilic moiety consisting of amino acids or peptide anions or cations, mono, di or polysaccharide (Table 1.1). The hydrophobic moiety is usually constituted by saturated, unsaturated, linear, branched or hydroxylated fatty acid. The major classes of biosurfactants are: glycolipids (for example rhamnolipids and sophorolipids), phospholipids (for example phosphatidylethanolamine), lipopeptide/lipoproteins (for example surfactin and fengycins), polymeric surfactants and particulate surfactants [Edwards2003].
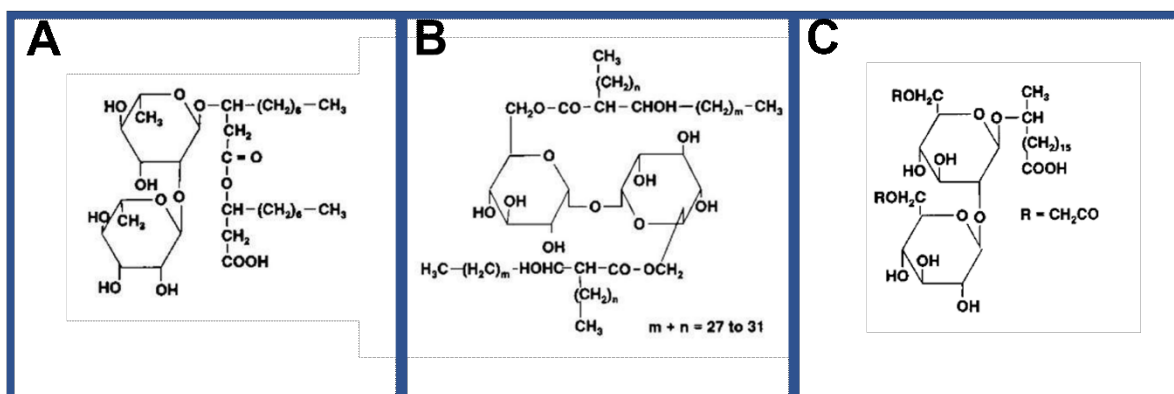
Figure 1.4 Structure of some common glycolipid biosurfactants. A: Rhamnolipid type 1 from P. aeruginosa. B: Trehalose dimycolate from Rhodococcus erythropolis,. C: Sophorolipid from Torulopsis bombicola.

Most bacteria degrading hydrophobic substrates release biosurfactants that facilitate the uptake and assimilation of hydrocarbons [Hommel1994]. Hydrocarbons are very good nutrient sources for *P. aeruginosa* but alkanes are insoluble in water, their solubility decreases as the molecular weight increases. This characteristic limits their sufficient uptake by bacteria and it is not obvious how these hydrophobic molecules enter the cells to sustain their growth. For medium and long chain *n*-alkanes, it is likely that bacteria gain access to them either by a surfactant-facilitated process (emulsification and solubilization) or by directly adhering to hydrocarbon droplets (surfactant-mediated increase of cell surface hydrophobicity) [Abdel-Mawgoud2010].

Glycolipids are the most known biosurfactants. They are carbohydrates in combination with long-chain aliphatic acids or hydroxy aliphatic acids. Among the glycolipids, the best known are rhamnolipids, trehalopids and sophorolipids [Desai1997].

1.3 Rhamnolipds

Rhamnolipids are the most widely studied compounds among biosurfactants. As biosurfactants, rhamnolipids can effectively reduce the surface tension of air-liquid or liquid-liquid interfaces even at low concentrations, a characteristic that allows them to be applied in the environmental remediation, washing or cleaning industry and cosmetic industry. In addition, the anti-microbial, anti-adhesive and anti-biofilm activity properties are other important and exploitable characteristics of rhamnolipids [Shao2017]. Characteristics such as the drastically tensioactive, emulsifying properties have led more and more attention to rhamnolipids through the years.

They are mainly produced by the *Pseudomonas aeruginosa* bacterium, isolated from different habitats (water, soil or plants), and by the genus *Burkholderia* [Shao2017]. *P. auruginosa*, a gram negative bacterium known for its environmental versatility, can utilize a wide range of organic compounds as food sources, giving these microorganisms an exceptional ability to colonize ecological niches where nutrients are limited. Rhamnolipids are the main biosurfactants produced by *P. aeruginosa* when grown under appropriate conditions [Jarvis1949].

Finding new bacteria that produce rhamnolipids is favorable from a biotechnological point of view as it might result in the discovery of producers that are nonpathogenic compared to the pathogenic *P. aeruginosa* strains. Hence, these bacteria alternatives to *P. aeruginosa* may become more appropriate candidates for the industrially safe production of rhamnolipids [Abdel-Mawgoud2010].

From an industrial point of view, the production of rhamnolipids is difficult due to the costly raw materials used in bacterial fermentation and the complex purification process that limits the application of this biosurfactant at large scale. Therefore, many efforts have been carried out in order to reduce the costs and increase yield in the former studies, such as cheap substrates, optimized production conditions using different processes, screening new natural producing strains and researching more efficient methods for separation and purification of rhamnolipids homologues [Shao2017].

There are many studies for the use of rhamnolipids as alternatives for bioremediation of pollutants, especially hydrophobic organic pollutants. It is well known that the elimination of pollutants by microorganisms is a systemic bioprocess and can be separated in two phases: a rapid removal process by adsorption and a following degradation process. The adsorption process is not only influenced by the types and physicochemical properties of pollutants, but is closely related to the surface properties and the cell membrane structure of microorganisms. The degradation process is related to internal activities of microbes, and is catalyzed by degrading enzymes which are controlled by related genes.

The bio removal process including adsorption and degradation steps may experience alteration in the presence of rhamnolipids, which exert impacts on the cell surface properties, membrane structure and the internal activities of microorganisms [Shao2017].

The cell surface properties are important characteristics of microorganisms, which directly affect the interactions among microorganisms, between microorganisms and the external environment, and also affect material transport, growth and metabolism of microorganisms. These properties, together with cell surface hydrophobicity, cell surface charge, are influenced by each other and by the environmental conditions. As a matter of fact, the compounds on the cell surface are composed by both hydrophilic and hydrophobic groups [Shao2017].

According to previous studies, biosurfactants have effects on the cell surface properties when used for bioremediation. For example, Liu et. al. observed that rhamnolipids, when adsorb on cell surface of *Penicillium simplicissimum*, can modify its hydrophobicity and charge due to the change of the cell surface functional groups concentrations [Liu2012].

The effects of rhamnolipids on cell surface properties depend on the concentration and types of rhamnolipids, the species of microorganism and environmental conditions. Figure 1.4 shows the main mechanisms by which rhamnolipids can affect microorganism's membrane [Shao2017].
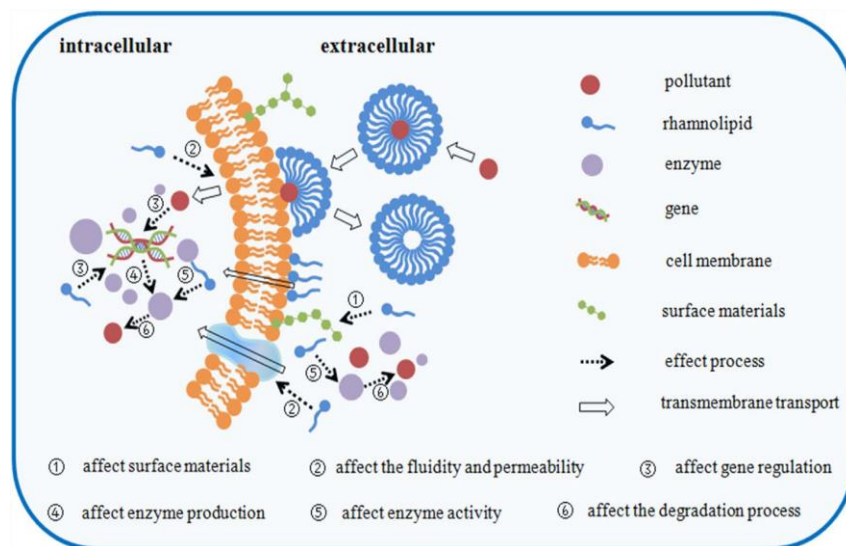
Figure 1.5 The process of rhamnolipids effects on microorganisms characteristics and the degradation of pollutants [Shao2017].

Rhamnolipids promote the uptake and biodegradation of poorly soluble substrates and have been mostly studied for their ability to mediate the assimilation of hydrophobic substrates in liquid cultures, especially hydrocarbons such as *n*-alkanes [Abdel-Mawgoud2010]. Rhamnolipids also enhance the

biodegradation of poorly soluble molecules by causing the cell surface to become more hydrophobic [Zhang1994].

Although many studies have been performed in the field of rhamnolipids, the exact physiological functions of these molecules regarding the bacteria that produce them have not yet been clarified. Many of these functions are derived from the well-known physicochemical properties of rhamnolipids, such as surface activity, wetting ability, detergency, and others. Taken together, these studies suggest that rhamnolipids might play multifunctional roles for the producing organisms [Abdel-Mawgoud2010].

1.3.1 Characterization of rhamnolipids

Natural rhamnolipids always appear as mixtures of different congeners. The hydrophilic heads of rhamnolipids produced by *P. aeruginosa* are composed of one or two rhamnose sugar moieties, which classify these molecules as mono-rhamnolipids (mono-RL) or di-rhamnolipids (di-RL). The head is linked to the hydrophobic tail formed by one or two β-hydroxy fatty acid chains. The development of sensitive and high analytical techniques has led to the further discovery of a wide diversity of rhamnolipids congeners and homologues (about 60) produced in different concentrations by various *Pseudomonas* species and other bacteria. Table 1.2 shows the chemical structure of different identified rhamnolipid congeners and homologues [Abdel-Mawgoud2010].

The complexity of rhamnolipids mixtures depends on various factors, including origin of bacteria strain, type of carbon substrate, culture conditions, age of the culture, *P. aeruginosa* strain itself, as well as the method of rhamnolipids isolation and purification [Rikalovic2014].

Among all the structures of rhamnolipids, some are classified as the major structures, because they are predominant in all rhamnolipids mixture produced by *P. aerugionosa*. The other structures, referred to as minor rhamnolipids structures, are rarely found or are found in low abundance [Rikalovic2014].

The studies performed with rhamnolipids produced by *P. aeruginosa* strains have shown that these mixtures contain, in the lipid part, chains with length from C8 to C12, being the Rha-C10-C10 and Rha-Rha-C10-C10 the predominant congeners [Rikalovic2014].

As previous studies have shown, there are four major structures of rhamnolipids produced by *P. aeruginosa*: 3-[3-(α-L-Rhamnopyranosyloxy)decanoyloxy]decanoic acid (Rha-C10-C10), 3-[3-(2-O-α-L-Rhamnopyranosyl-α-L-rhamnopyranosyloxy)decanoyloxy]decanoic acid (Rha2-C10-C10), 3-[(2-O-α-L-Rhamnopyranosyl-α-L-rhamnopyranosyl) oxy] decanoic acid (Rha2-C10) and 3-[(6-Deoxy-α-L-mannopyranosyl) oxy]decanoic acid (Rha-C10) [Hoskova2015].

For example, Arino et. al. [Arino1996] have described a mixture of rhamnolipids produced by a strain of *Pseudomonas* composed, in units of percentage mole fraction, by 67% of di-rhamno-di-lipid, 22% of mono-rhamno-di-lipid, 9% of di-rhamno-mono-lipid and less than 3% of mono-rhamno-mono-lipid. Also Perinelli et. al. [Perinelli2017] have determined commercial rhamnolipids from *P. aeruginosa* composed by 33-37% of mono-rhamnolipids and 63-67% of di-rhamnolipids.

The Tables 1.2 and 1.3, extracted from the article of Abdel-Mawgoud et al. [Abdel-Mawgoud2010], shows the chemical structure of diverse rhamnolipids congeners and homologues investigated during the last years.

By referring to all the structures reported in Table 1.2 and 1.3, it can be inferred that rhamnolipids are glycosides composed of rhamnose moieties (glycon part) and lipid moieties (aglycon part) linked to each other via an O-glycosidic linkage. The glycon part is composed of one (mono-RLs) or two (di-RLs) rhamnose moieties linked to each other through a α-1,2-glycosidic linkage. Differently, the aglycon part is mainly one or two (in few cases three) β-hydroxyl fatty acid chains (saturated, mono- or poly-unsaturated and of chain length varying from C_8 to C_{16}) linked to each other through an ester bond formed between the β-hydroxyl group of the distal (relative to the glycosidic bond) chain with the carboxyl group of the proximal chain. In most cases the carboxyl group of the distal β-hydroxy fatty acid chain remains free, whereas few congeners have this group esterified with a short alkyl group. Similarly, the 2-hydroxyl group of the distal (relative to the glycosidic bond) rhamnose group remains mostly free, although in some rare homologues it can be acylated with chain alkenoic acid [Abdel-Mawgoud2010].

No.	Symbol	M. Form.	MW	R1	n1	n2	R2	Structure
Mono-rhamno-mono-lipidic congeners								

No.	Symbol	M. Form.	MW	R1	n1	n2	R2	Structure
				Mono-rhamno-mono-lipidic congeners				
1	Rha-C$_{8-2}$	C$_{14}$H$_{22}$O$_{7}$	302.35	H	1(-4H)	-	H	
2	Rha-C$_{8}$	C$_{14}$H$_{26}$O$_{7}$	306.35	H	1	-	H	
3	Rha-C$_{10}$	C$_{16}$H$_{30}$O$_{7}$	334.41	H	3	-	H	
4	Rha-C$_{12-2}$	C$_{18}$H$_{30}$O$_{7}$	358.43	H	5(-4H)	-	H	
5	Rha-C$_{12}$	C$_{18}$H$_{34}$O$_{7}$	362.46	H	5	-	H	
6	Rha-C$_{14-2}$	C$_{20}$H$_{34}$O$_{7}$	386.48	H	7(-4H)	-	H	
				Mono-rhamno-di-lipidic congeners				
7	Rha-C$_{8}$-C$_{8}$	C$_{22}$H$_{42}$O$_{9}$	448.55	H	1	1	H	
8	Rha-C$_{8}$-C$_{10:1}$	C$_{24}$H$_{42}$O$_{9}$	474.58	H	1	3(-2H)	H	
9	Rha-C$_{10:1}$-C$_{8}$	C$_{24}$H$_{42}$O$_{9}$	474.58	H	3(-2H)	1	H	
10	Rha-C$_{8}$-C$_{10}$	C$_{24}$H$_{44}$O$_{9}$	476.60	H	1	3	H	
11	Rha-C$_{10}$-C$_{8}$	C$_{24}$H$_{44}$O$_{9}$	476.60	H	3	1	H	
12	Rha-C$_{10}$-C$_{10:1}$	C$_{26}$H$_{46}$O$_{9}$	502.64	H	3	3(-2H)	H	
13	Rha-C$_{10}$-C$_{10}$	C$_{26}$H$_{48}$O$_{9}$	504.65	H	3	3	H	
14	Rha-C$_{8}$-C$_{12}$	C$_{26}$H$_{48}$O$_{9}$	504.65	H	1	5	H	
15	Rha-C$_{12}$-C$_{8}$	C$_{26}$H$_{48}$O$_{9}$	504.65	H	5	1	H	
16	Rha-C$_{10}$-C$_{12:1}$	C$_{26}$H$_{50}$O$_{9}$	530.69	H	3	5(-2H)	H	
17	Rha-C$_{12:1}$-C$_{10}$	C$_{28}$H$_{50}$O$_{9}$	530.69	H	5(-2H)	3	H	
18	Rha-C$_{10}$-C$_{12}$	C$_{28}$H$_{52}$O$_{9}$	532.71	H	3	5	H	
19	Rha-C$_{12}$-C$_{10}$	C$_{28}$H$_{52}$O$_{9}$	532.71	H	5	3	H	
20	Rha-C$_{10}$-C$_{14:1a}$	C$_{30}$H$_{54}$O$_{9}$	558.74	H	3	7(-2H)	H	
21	Rha-C$_{12}$-C$_{12:1a}$	C$_{30}$H$_{54}$O$_{9}$	558.74	H	5	5(-2H)	H	
22	Rha-C$_{10}$-C$_{14}$	C$_{30}$H$_{56}$O$_{9}$	560.76	H	3	7	H	
23	Rha-C$_{12}$-C$_{12}$	C$_{30}$H$_{56}$O$_{9}$	560.76	H	5	5	H	
24	Rha-C$_{12}$-C$_{14}$	C$_{32}$H$_{60}$O$_{9}$	588.81	H	5	7	H	
25	Rha-C$_{14}$-C$_{14}$	C$_{34}$H$_{64}$O$_{9}$	616.87	H	7	7	H	
26	Rha-C$_{14}$-C$_{16}$	C$_{36}$H$_{68}$O$_{9}$	644.92	H	7	9	H	
27	Rha-C$_{16}$-C$_{16}$	C$_{38}$H$_{72}$O$_{9}$	672.97	H	9	9	H	
28	Rha-C$_{10}$-C$_{10}$-CH$_{3}$	C$_{27}$H$_{50}$O$_{9}$	518.68	H	3	3	CH$_{3}$	
29	Decenoyl-Rha-C$_{10}$-C$_{10}$	C$_{36}$H$_{64}$O$_{10}$	656.89	b	3	3	H	

b: α-decenoyl group

Table 1.2 Chemical structure of different identified mono-rhamnolipids congeners and homologues [Abdel-Mawgoud2010]

No	Symbol	M. Form.	MW	R1	n1	n2	R2	Structure
Di-rhamno-mono-lipidic congeners								
30	Rha-Rha-CH$_8$	C$_{20}$H$_{36}$O$_{11}$	452.49	H	1	-	H	
31	Rha-Rha-CH$_{10}$	C$_{22}$H$_{40}$O$_{11}$	480.55	H	3	-	H	
32	Rha-Rha-CH$_{12:1}$	C$_{24}$H$_{42}$O$_{11}$	506.58	H	5(-2H)	-	H	
33	Rha-Rha-CH$_{12}$	C$_{24}$H$_{44}$O$_{11}$	508.60	H	5	-	H	
34	Rha-Rha-CH$_{14}$	C$_{26}$H$_{38}$O$_{11}$	536.68	H	7	-	H	
Di-rhamno-di-lipidic congeners								
35	Rha-Rha-C$_8$-C$_8$	C$_{28}$H$_{50}$O$_{13}$	594.69	H	1	1	H	
36	Rha-Rha-C$_8$-C$_{10}$	C$_{30}$H$_{54}$O$_{13}$	622.74	H	1	3	H	
37	Rha-Rha-C$_{10}$-C$_8$	C$_{30}$H$_{54}$O$_{13}$	622.74	H	3	1	H	
38	Rha-Rha-C$_{10}$-C$_{10:1}$	C$_{32}$H$_{56}$O$_{13}$	648.78	H	3	3(-2H)	H	
39	Rha-Rha-C$_{10}$-C$_{10}$	C$_{32}$H$_{56}$O$_{13}$	650.79	H	3	3	H	
40	Rha-Rha-C$_8$-C$_{12:1}$	C$_{32}$H$_{56}$O$_{13}$	648.78	H	1	5(-2H)	H	
41	Rha-Rha-C$_{12:1}$-C$_8$	C$_{34}$H$_{60}$O$_{13}$	648.78	H	5(-2H)	1	H	
42	Rha-Rha-C$_{10}$-C$_{12:1}$	C$_{34}$H$_{60}$O$_{13}$	676.83	H	3	5(-2H)	H	
43	Rha-Rha-C$_{12:1}$-C$_{10}$	C$_{34}$H$_{62}$O$_{13}$	676.83	H	5(-2H)	3	H	
44	Rha-Rha-C$_{10}$-C$_{12}$	C$_{34}$H$_{62}$O$_{13}$	678.84	H	3	5	H	
45	Rha-Rha-C$_{12}$-C$_{10}$	C$_{34}$H$_{62}$O$_{13}$	678.84	H	5	3	H	
46	Rha-Rha-C$_{10}$-C$_{14:1}$	C$_{36}$H$_{64}$O$_{13}$	704.89	H	3	7(-2H)	H	
47	Rha-Rha-C$_{12}$-C$_{12:1}$	C$_{36}$H$_{64}$O$_{13}$	704.89	H	5	5(-2H)	H	
48	Rha-Rha-C$_{12:1}$-C$_{12}$	C$_{36}$H$_{64}$O$_{13}$	704.89	H	5(-2H)	5	H	
49	Rha-Rha-C$_{12}$-C$_{12}$	C$_{36}$H$_{66}$O$_{13}$	706.90	H	5	5	H	
50	Rha-Rha-C$_{12}$-C$_{14}$	C$_{38}$H$_{70}$O$_{13}$	734.95	H	5	7	H	
51	Rha-Rha-C$_{14}$-C$_{12}$	C$_{38}$H$_{70}$O$_{13}$	734.95	H	7	5	H	
52	Rha-Rha-C$_{14}$-C$_{14}$	C$_{40}$H$_{74}$O$_{13}$	763.00	H	7	7	H	
53	Rha-Rha-C$_{14}$-C$_{16}$	C$_{42}$H$_{78}$O$_{13}$	791.06	H	7	9	H	
54	Rha-Rha-C$_{16}$-C$_{14}$	C$_{42}$H$_{78}$O$_{13}$	791.06	H	9	7	H	
55	Rha-Rha-C$_{16}$-C$_{16}$	C$_{44}$H$_{82}$O$_{13}$	819.11	H	9	9	H	
56	Rha-Rha-C$_{14}$-C$_{14}$-C$_{14}$	C$_{54}$H$_{100}$O$_{15}$	989.36	H				
57	Rha-Rha-C$_{10}$-C$_{10}$-CH$_3$	C$_{33}$H$_{60}$O$_{13}$	664.82	H	3	3	CH$_3$	
58	Decenoyl-Rha-Rha-C$_{10}$-C$_{10}$	C$_{42}$H$_{74}$O$_{14}$	803.03	H	3	3	H	

Table 1.3 Chemical structure of different identified di-rhamnolipids congeners and homologues [Abdel-Mawgoud2010]

Several physicochemical properties are the key factors to evaluate the applicability of biosurfactants, such as surface tension, interfacial tension, CMC, particle size and emulsification capacity. Rhamnolipids reduce the surface tension of water from 72 mN/m to values between 28 and 30 mN/m and have high emulsifying activity, with rates up to 60-70% [Gudina2015]. The CMC values for these biosurfactants, which depend on the chemical composition of the various species and the solution properties, range from 0.01 to 0.12 mM [Hung2001]. Mortensen et. al. described micelles of the

mixture rhamnolipids from *P. aeruginosa* with size between 20-30 nm [Mortensen2017], and molecular mass ranging from 500 to 1500 Da [Lang1987].

1.3.2 Mono-rhamnolipids and di-rhamnolipids

As we discussed before, rhamnolipids are composed of mono-RL and di-RL molecules. The main four types of rhamnolipids produced as a mixture by *P. aeruginosa* are shown in Figure 1.5 [Rikalovic2014].
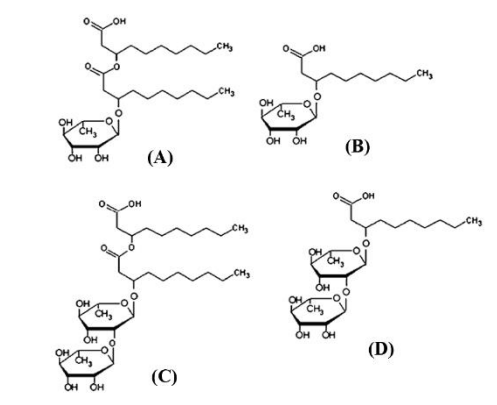
Figure 1.5. The four main structures of rhamnolipid biosurfactants produced by *P. Aeruginosa*: A) mono-rhamno-di-lipidic; B) mono-rhamno-mono-lipidic; C) di-rhamno-di-lipidic; and D) di-rhamno-mono-lipidic

It is worth noting that the composition of rhamnolipids mixtures determines their physicochemical properties, which are key factors of their potential application [Rikalovic2014]. According to previous studies, di-rhamnolipids (di-RL) have greater polarity compared to mono-rhamnolipids (mono-RL), due to the presence of two Rha groups, whereas mono-RL shows a higher ionization efficiency. Additionally, mono-RL, at room temperature, is oily, while di-RL is solid [Liu2014].

Previous studies have determined the CMC for the rhamnolipids mixtures and also for mono-RL and di-RL under different conditions. Abbasi et al. [Abbasi2013] reported a CMC for pure mono-RL of 0.070 mM at pH 7.4 and 0.050 mM at pH 4.0. Peker et al. found a CMC value of 0.150 mM also for mono-RL at pH 6.5 [Peker2003]. Chen et al. reported a higher value of CMC for mono-RL at pH 7.0, which is 0.180 mM [Chen2010]. These results show that even for the same mono-RL compound, different studies have reported different values. According to Abbasi et al. [Abbasi2013], these differences could be probably due to the different fatty acid composition of the samples, as well as the effect of the different ionic strength and pH of the solutions. Other authors have measured the CMC of di-RL. Zhong et al. found a CMC of 0.106 mM for di-RL in a pH 6.5 solution [Zhong2008]. This result was validated by Sanchez et al., who showed that CMC of di-RL decreases from 0.110 mM at pH 7.4 to 0.010 mM at pH 4.0 [Sanchez2007].

According to Chen et. al., 2004 [Chen2004], above the CMC, mono-RL forms predominantly planar structures (lamellar or unilamellar/bilamellar vesicles), whereas di-RL remains as globular micelles. In rhamnolipids mixtures, solutions rich in di-RL are predominantly micellar and those rich in mono-RL have predominantly planar structures. At intermediate mono-RL/di-RL compositions, lamellar/micellar coexistence exists, but the higher curvature associated with di-RL dominates the mono-RL/di-RL mixing behavior. Clearly, the CMC of the mixture of rhamnolipids strongly depends on the chemical composition and has been found to range from 0.080 to 0.400 mM [Benicasa2004].

In this context, the capacity of rhamnolipids to form micellar or lamellar structures has been evaluated for crude extracts containing undefined mixtures of mono and di rhamnolipids components. However, since the compounds secreted by *P. aeruginosa* constitute a heterogeneous mixture of mono-RL and di-RL, it is important to analyze the individual contribution of each species to the physicochemical properties of the mixture, in order to obtain a rhamnolipid with the desired properties for specific uses [Abbasi2013].

2 Lipid phase and membrane models

2.1 Lipid polymorphism

Lipids are amphiphilic molecules, constituted by a hydrophilic and a hydrophobic parts, that when dispersed in an aqueous solvent, are affected by the hydrophobic effect, which represents their propensity to organize themselves in order to avoid the contact between their hydrophobic domains with the solvent. Based on the geometrical characteristics of the lipid molecules, they have a tendency to aggregate in different shapes, influenced by some parameters.

The parameters are: the area a_0 occupied by the head group (due to the electrostatic repulsion between neighbor molecules); the length of the aliphatic chains l_c, which also establishes the size of the micelle; and the volume of the aliphatic chains v [Frolov2011].

It is possible to calculate the shape factor of the lipid using these parameters:

Equation 2.1

$$\eta = \frac{v}{a_0 l_c}$$

Phospholipids or surfactants tend to be disposed along the air-water interface when they are in an aqueous environment. In this situation, they form a monolayer in which the polar heads are completely immersed in the polar solvent and the hydrophobic tails are directed towards the gas phase. In solution, small amounts of molecules, in the form of monomers, tend to fold the hydrophobic tail in order to minimize the interactions with the solvent.

As previously discussed, by increasing the concentration of phospholipids or surfactants, the CMC is achieved and lipids self-aggregate forming complexes in which the tails form a hydrophobic core shield by the hydrophilic heads (micelles).

The micelles are the simplest lipid structure. Lipids that form micelles should possess short and voluminous hydrophobic tails and large polar heads. The shape factor must be <1/3 for micelles and lipids with these geometrical characteristics are called tapered. Figure 2.1 shows a conical shape lipid and its micellar phase in solution.
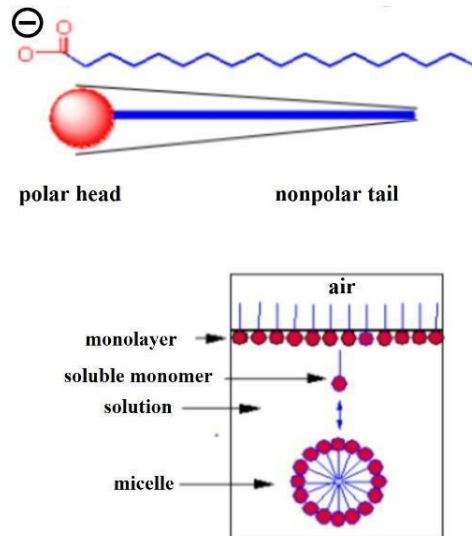
Figure 2.1 Conical shape and micellar phase of lipids.

The shape and size of these aggregates depend on numerous factors, such as: the length of the non-polar tail, the nature and the size of the polar or ionic head, the acidity of the solution, the temperature and the presence of added salts. The number of amphiphilic molecules that form the micellar structure is called aggregation number and it is useful to describe the size of micelles.

The amphiphilic molecules tend to form the inverse micelles when dispersed in a non-polar organic solvent. These aggregates indeed show an upside down arrangement, that is, the hydrocarbon tails are exposed to the non-polar solvent, while the polar heads are directed inside the aggregate to avoid contact with the solvent. In this situation, an ideal pocket is created to melt and transport polar solutes through a non-polar solvent [Baeurle2004].

The second structure that lipids can form are double layers or lipid bilayers. The lipids that tend to form this structure should have a tail and a head of similar dimensions so that they are attributable to the shape of a cylinder, called cylindrical lipids ($1/2 < \eta < 1$). Figure 2.2 shows a lipid in cylindrical form and the formation of liposomes in solution.
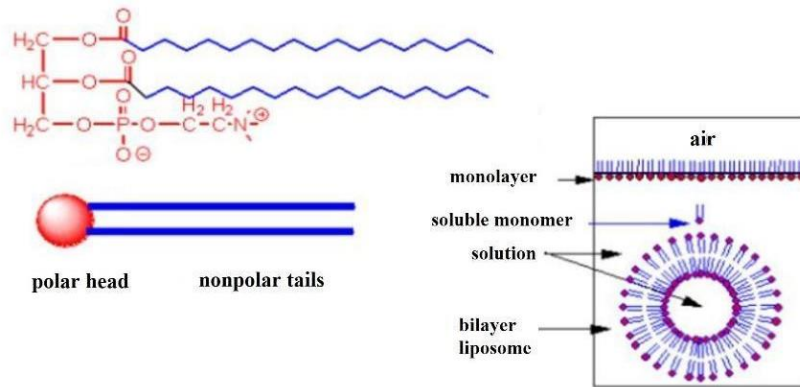
Figure 2.2 Cylindrical shape lipid and formation of liposomes.

In the double layer lipids arranged, the two hydrocarbon tails are positioned inward and the heads are in contact with the aqueous solvent. This structure tends to close on itself by joining the ends, to avoid the solvent exposure of the hydrophobic part of the lipids located at the ends of the double bilayer maintaining the tails with a single hydrophobic environment.

The structure formed is a spherical shell called vesicle or liposome. The strong tension that is created between the lipids in the inner layer prevents pore formation in the vesicle, unless they are destabilized by the presence of conical proteins or surfactants. The structure is maintained by non-covalent interactions [Schindler1980]. Figure 2.3 shows different structures that can be formed by different lipids in solution.
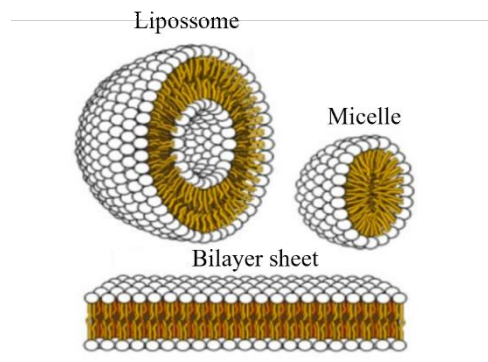
Figure 2.2.3 Different structures formed by lipids

2.1.1 Lipid phases

Lipid phases are all the possible spatial organizations that lipids are able to form and the various morphologies are: spheres of lipid molecules (micelles); lamellar phases (the two double phospholipid layers are arranged in parallel); tubular arrangement of the lipid molecules (hexagonal) and cubic

phases. The structural phase of the aggregation is also influenced by the ratio of the lipids present, the temperature, hydration, pressure and ionic strength.

The structural characteristics of the lipids allow them to show liquid-crystalline phases. The main structural characteristics of the lipids are: elongated shape, marked asymmetry, polar character present in a narrow portion of the molecule, with a clear division of the polar portion from the apolar, possibility of forming two orders of bounds, strong interactions between the polar heads and weak interactions between the aliphatic tails. The liquid-crystalline (or liquid crystal) phase is an intermediate phase, comprised between the solid phase and the liquid phase, which shows some characteristic properties of the former state (ordered arrangement of the molecules) and some of the latter (fluidity).

The property of phospholipids forming liquid-crystalline phases are the basis for the structure of cell membranes. The possibility of a single lipid species to present different liquid-crystalline phases is called polymorphism. Besides temperature and concentration, the specific liquid-crystalline phase of the phospholipids depends on the shape of the molecule, which is given by the shape of the head, tail and steric bulk. The size of the head depends on its charge, the degree of hydrophilicity and repulsions or electrostatic attractions with the heads of the adjacent molecules. In the case of tails, the length and degree of unsaturation of the aliphatic chains determine the volume occupied by the phospholipid tail. The temperature has a very important influence, since it determines the degree of thermal agitation of the aliphatic chains and, therefore, leads to a strong change of the volume occupied by the tails.

The conical molecules have the area occupied by the fatty acid chains greater than that occupied by the polar head, such as phosphatidylethanolamine, plasmenyl ethanolamine. These kinds of lipids tend to form inverted Hexagonal Phase (H_{II}) in solution.

The inverted cone-shaped molecules have the area occupied by the apolar part smaller than that occupied by the polar head. These types of lipids form micelles (micellar phase) and hexagonal phases (H_I) and only gangliosides (glyco sphingophospholipids) and lysophospholipids belong to this group. These lipids are produced by the hydrolysis of phospholipids by phospholipases and therefore possess only fatty acid.

The cylindrical molecules have similar areas of polar head and fatty acids, for example phosphatidylcholine. These lipids form bimolecular laminae (lamellar phase).

The structural typology cubic phase occurs when the aggregates are arranged within a cubic lattice. The aggregates can be curved lamellae or micelle. The lipid cubic phase consists of a single lipid bilayer that follows an infinite periodic minimal surface, dividing the space into two networks of

aqueous channels that do not intersect. There are different types of cubic phases that have different spatial symmetries.

The lipid polymorphism mentioned above can be seen in Figure 2.4, which shows the different lipid forms and their corresponding lipid phase.
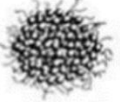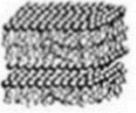
Configuration		Form	
Reversed convertion cone			Reverse micella
			Hecagonal phase HII
			Cubic phase
Cylinder			Lamellar phase
Truncated cone			Hexagonal phase H
Cone			Micellar phase

Figure 2.4 Lipid polymorphism, lipid form and corresponding lipid phase.

The lamellar liquid-crystalline phases are of extreme importance for the phospholipids, since they form the structural units of the lipid bilayer of biological membranes. The phospholipid bilayers undergo phase transitions, generally defined as the passage from one aggregation layer to another, that derives from an alteration in the packaging and the mobility of the lipids obtained by varying the temperature.

The acyl chains of the phospholipids are tightly packed and placed perpendicular to the plane of the bilayer at low temperatures. The individual molecules are limited in their movements and cannot spread laterally. This highly compact state is the L_β gel phase (crystalline phase). Increasing the temperature leads to the transition to the liquid-crystalline phase L_α. The double layer undergoes a

phase transition and becomes fluid, consequently, the molecules of the phospholipid start to rotate around its axis and there is a flexion of the acyl chains and the diffusion of the molecules from one position to the other of the double layer Lo. The three phases are shown in Figure 2.5.
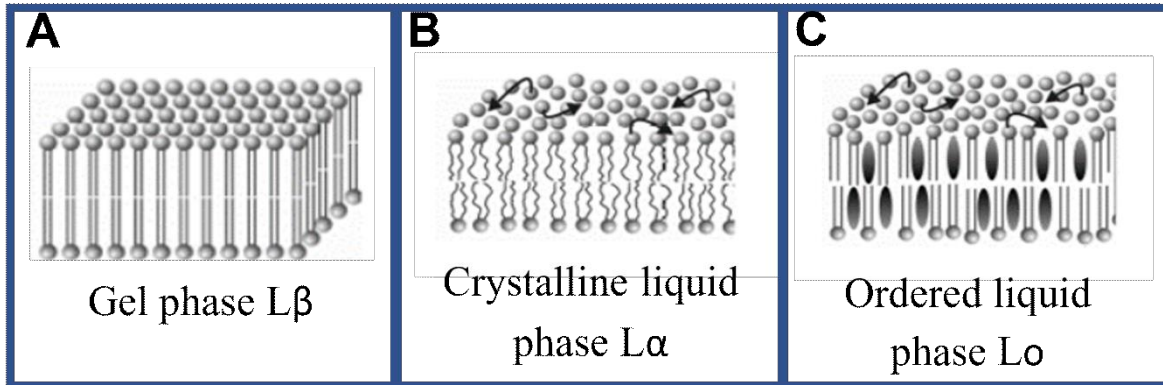
Figure 2.5 Different physical states of lipid bilayers.

The transition from one phase to another takes place at a specific temperature, called critical temperature T_C (or transition temperature or melting temperature T_m), characteristic for each phospholipid species. Several factors affect the transition temperature: length of fatty acids; degree of unsaturation of fatty acids, and hydrophilicity of the polar head.

Cholesterol can intermingle in the phospholipid double layer and establish hydrophobic interactions with lipid chains. A new phase is obtained, the liquid ordered phase (Lo in Figure 2.5), where the lipid chains are packed in an orderly manner thanks to the interaction with the cholesterol, allowing however the diffusion of the lipid molecules inside the bilayer. The introduction of cholesterol in the bilayer has a double effect: at low temperatures there is a decrease in the order of the aliphatic chains of fatty acids, an effect that prevents crystallization; on the other hand, at temperatures above T_m, the order of the proximal tract of the fatty acid chains increases, an effect that limits the movement of the acyl chains, leading overall to a reduction in the fluidity of the membrane.

2.2 Membrane models: Giant Unilamellar Vesicles (GUV)

The lipid bilayer is the basic building block of the cell membranes, which serve to structure and compartmentalize living matter in the form of cells and subcellular structures [Feigenson2007]. The complexity of cellular membranes in composition and dynamic organization has motivated the development of a variety of simpler model systems that serve as strong bends for understanding more complex biological membranes [Lingwood2010]. These include bilayers in the form of vesicles of

sizes ranging from 50 nm (Small Unilamellar Vesicles, SUVs) to 100 μm (Giant Unilamellar Vesicles, GUVs). The vesicle membrane involves a self-assembly of lipid molecules in water, owing its stability to mainly weak physical forces of electrostatic and colloidal nature [Bhatia2015].

In this PhD project, my interests are in GUVs, which are giant unilamellar vesicle liposomes that have diameters in the range of about 1-100 μm, considered remarkably large and also have the size range of most biological cells [Becker2009]. GUVs are definitely a fascinating model system. The size of GUVs and their curvature enable us to visualize them individually, using an optical microscope. GUVs have application in numerous biophysical contexts, in which membrane composition, tension and geometry are controlled and manipulated using microscopy techniques, such as membrane flickering analyses or fluorescence imaging of lateral membrane organization [Bhatia2015].

When we discuss GUVs, the term vesicle is used to designate a particular type of compartment formed in vitro in an aqueous medium. The interior of a vesicle is a small aqueous volume and the boundary of each vesicle is constituted by one or a few thin layers, also called membranes, composed of amphiphilic molecules. The amphiphiles are often bilayer-forming low-molar-mass compounds (phospholipids or synthetic surfactants) or amphiphilic block copolymers. The amphiphiles in a vesicle membrane are arranged in such a way that the hydrophilic parts are in contact with the aqueous medium, while the hydrophobic parts associate to form the interior in each layer [Walde2010].

For the unilamellar vesicles, composed of conventional biomembrane phospholipid that have one hydrophilic head group and two lipophilic chains, the membrane is built from one single bilayer with the head groups of the lipids of the inner layer facing towards the interior of the vesicles and the head groups of the outer layer being in contact with the external aqueous medium [Walde2010], as we can see in Figure 2.6.
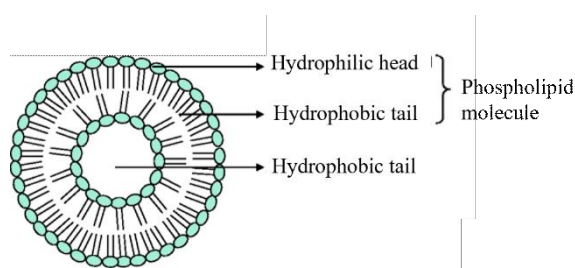
Figure 2.6 Structure of unilamellar liposome.

The lipid composition of vesicles can be varied from a single lipid component to mixtures of lipids (synthetic or natural lipid extracts) containing proteins or fragments from natural cell membrane [Bhatia2015].

Depending on the experimental conditions, such as the osmotic pressure difference between the interior and exterior of the vesicles, they can be spherical or nonspherical. As GUVs can be observed by optical microscopy, it is possible to do experiments that allow a real time monitoring of morphological changes of individual vesicles and of the chemical and enzymatic reactions occurring on the surface of within a single vesicle [Walde2010]. To illustrate the geometric properties, a spherical unilamellar giant vesicle formed of lipid POPC may have a diameter of 50 μm and a membrane thickness of 4 nm, which is the thickness of hydrated POPC bilayer [Tahara2005].

Membrane biology fields have focused on the role that lipids play in membrane organization over the last few years. In cell membranes, lipid rafts are currently thought to be localized regions that are on the order of 100 nm in diameter in which certain proteins and lipids are concentrated. The raft domains and the surrounding lipid matrix are both liquid [Veatch2003].

Liquid domains in model lipid bilayers are frequently studied as models of raft domain in cell plasma membranes. Micron-scale liquid domains are easily produced in vesicles composed of ternary mixtures of a high melting temperature lipid, a low melting temperature lipid and cholesterol. Lipid domains are often circular, but can become non-circular when membranes are near critical points. Fluorescence microscopy is used to directly observe coexisting liquid phases in GUVs containing ternary mixtures of saturated lipids, unsaturated lipids and cholesterol [Veatch2005]. This model system has the advantage that micron-scale domains can be directly observed by fluorescence microscopy, that miscibility transition temperatures can be measured and that liquid phases can be studied from a more controlled physical perspective than cells [Veatch2005].

In this context, recently some of us studied the interactions of a commercial mixture of rhamnolipids with plasma membrane models represented by ternary DOPC:sphingomyelin:cholesterol GUVs and also POPC GUVs. Results indicated that rhamnolipids, at concentrations from 0.1 to 0.5 mM, are able to promote membrane remodeling, with no lytic effect [Come2021].

2.2.1 GUVs formed by the lipid film hydration method

The classical technique for the formation of giant vesicles is first to dissolve lipids (or mixture of lipids) in an organic solvent and then a film of this lipid solution is spread on a support, such as glass. In order to prepare giant liposomes, the organic solvent is evaporated and the lipids are hydrated, at a temperature above the main chain melting transition [Bhatia2015]. This method was originally developed by Reeves and Dowben [Reeves1969] and it is known as spontaneous swelling, natural swelling or gentle hydration method [Tsumoto2009].

Figure 2.6 describes the formation of GUVs by controlled lipid film hydration of a film of bilayer-forming lipids deposited onto a solid surface. Application of an external electric field leads to a better control of the hydration process, if an electric field is absent, the method is called gentle hydration, natural swelling or spontaneous swelling [Walde2010].
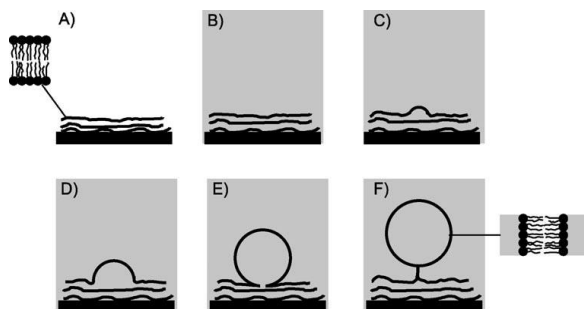
Figure 2.7 Representation of the formation of giant vesicles by controlled hydration of a film of bilayer-forming lipids deposited onto a solid surface (A). Application of an external electric field (B) leads to a better control of the hydration process [Walde2010].

This method is particularly successful for the preparation of GUVs from samples containing charged lipids. It is important to consider that the hydration has to be carried out in the liquid-disordered state of the bilayers, which is on temperature above T_m that corresponds to the solid-ordered (s_o)/liquid-disordered (Ld) or gel/liquid-crystalline main phase transition temperature [Walde2010].

A study of Hishida et al. showed that hydration of smooth, flat layers in the Ld phase resulted in the successful formation of GUVs, while hydration in the (s_o) phase did not generate giant vesicles, showing a correlation between physical state of the lipid layers and ability to generate GUVs [Hishida2005].

Choosing a lipid composition is the first step in planning your experiments with GUVs. For testing your ability to make GUVs, a single, unsaturated lipid such as dioleylphosphatidylcholine (DOPC) may be useful for problems resolution and learning. For model raft mixtures, a 1:1:1 molar composition of DOPC:sphingomyelin:cholesterol is typical and is commonly referred to as the regular mixture. However, this mixture produces GUVs that may not be phase-separated at room temperature and the electro formation must be done in temperatures over 50° C[Manley2008].

3 Aim of the present study

It is clear that contamination of water and soil environments by oil-derived hydrocarbons is a critical problem nowadays. Many alternatives for remediation have been studied and rhamnolipids are already used as an important option for bioremediation of oil spill accidents [Shao2017]. Even if rhamnolipids are natural biosurfactants produced by fungi and bacteria, it is important to understand how toxic this substance can be to the microbiota of environments such as oceans, soils and underground water.

During this PhD work, we carried on a study concerning the two major types of molecules that compose rhamnolipids, which are mono-rhamnolipids, that contains one rhamnose group in the molecular polar head, and di-rhamnolipids, with two rhamnose groups. Since the compounds secreted by *P. aeruginosa* constitute a heterogeneous mixture of mono-RL and di-RL, in order to obtain biosurfactants with tailored properties for specific uses, it is necessary to investigate not only the physicochemical properties of the mixture, but also the ones of each component.

In this context, the aim of my PhD work is to perform a physicochemical characterization of either mono-RL and di-RL. The activities carried out during this study are summarized below.

First, silica gel column chromatography techniques have been used to separate mono-RL and di-RL from a commercial rhamnolipids mixture.

Secondly, concentrated water solutions (from 10 to 45 water w/w %) of either mono-RL or di-RL have been studied with laboratory X-ray diffraction (XRD), with the aim of determining the molecular packing properties at a few Angstrom resolutions.

Thirdly, Small-Angle X-ray Scattering (SAXS) experiments, performed at the Diamond Light Source synchrotron (Didcot, United Kingdom) on diluted water and artificial sea water solutions of either mono-RL or di-RL well above their CMC (from 10 to 100 mM), have shown their different micellar structures.

Fourthly, phase-contrast and fluorescence-mode optical microscopy experiments have been carried out on GUVs exposed to mono-RL and di-RL, with the aim to investigate the interaction of these biosurfactants with plasma membrane at molecular level and, consequently, to understand their impact in local microbiota. Indeed, GUVs are simple model membrane systems of cell-size, that mimic biological membranes so they are instrumental to study the function of more complex biological membranes [Bhatia, 2015].

4 Mono and di-rhamnolipids separation from the rhamnolipids mixture

4.1 Silica gel column chromatography

Column chromatography is a simple and the most popular separation and purification technique. Both solid and liquid samples can be separated and purified by column chromatography. The mobile phase is introduced into the solid phase and the components move depending on their relative affinities [Mukherjee2019]. The process of column chromatography is the oldest and most common technique for the separation of complex mixtures packed in a column [Srivastava2021].

Column chromatography consists of a stationary solid phase that adsorbs and separates the compounds passing through it with the help of a liquid mobile phase. On the basis of their chemical nature, compounds get adsorbed and elution is based on differential adsorption of a substance by the adsorbent. Various stationary phases are used in column chromatography, such as silica, alumina, calcium phosphate, calcium carbonate, starch, and magnesia, and different solvent compositions based on the nature of compounds to be separated and isolated [Srivastava2021].

The choice of the solvent constituting the mobile phase depends on the solubility characteristics of the mixture. The solvents should also have sufficiently low boiling temperature to permit the recovery of the eluted material by the end of the purification. In column chromatography, it is possible to use different mobile phases, in increasing order of polarity. For example, ether, hexane, methanol, chloroform or ethyl acetate. However, the polarity of both the stationary and mobile phases is the most important factor in adsorption chromatography. It is very useful in the separation of mixtures of compounds, purification processes, and the isolation of active constituents [Mukherjee2019].

The optimization of the method is an important task in the separation of different groups of compounds. In the column chromatography, a cylindrical glass tube, which is plugged at the bottom by a piece of glass wool or porous disc, is filled with slurry (adsorbent) and a suitable solvent. Samples to be separated are introduced at the top of the column and allowed to move with the solvent. With polarity differences, compounds are adsorbed at different regions and desorbed with suitable solvent polarity. The compound of higher adsorption ability will be adsorbed at the top and the one with the lower adsorption ability will be at the bottom. By adding the solvent at the top, compounds get desorbed and pass through the column and this process is called elution. A schematic diagram of column chromatography is shown in Figure 4.1 [Srivastava2021].
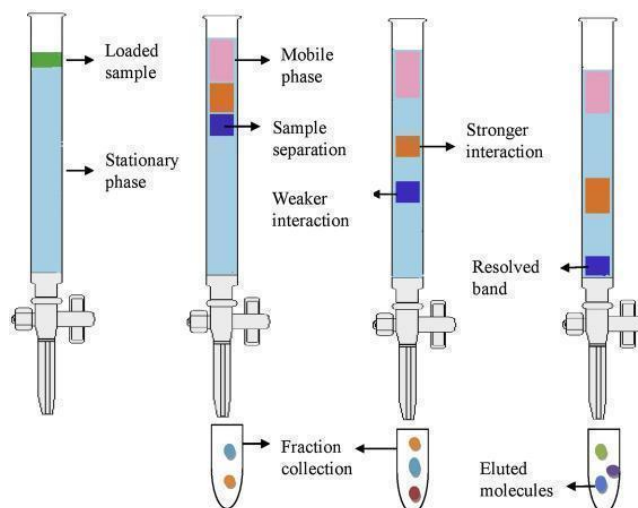
Figure 4.1 Schematic diagram of column chromatography [Srivastava2021].

The principle of active compound separation depends on the activity of adsorbents and polarity of the solvent. If the polarity of the solvent is very low and the activity of the adsorbent is strong and high, then the result of separation of compound is good. On the other hand, if the polarity of the solvent is very high and the activity of adsorbents is high then poor results of compound separation are reached [Srivastava2021].

4.2 Thin-layer chromatography

Thin-layer chromatography (TLC) and paper chromatography comprise "planar chromatography". TLC consists in a suitable closed vessel containing solvent and a coated plate to carry out separations or qualitative and semiquantitative analysis. With the optimization of techniques and materials, an accurate and precise qualification or quantification can be achieved [Sherma2003].

TLC can be used: to simply check the purity of a substance, to attempt to separate and identify the components in a mixture, or to obtain a quantitative analysis of one or more of the components present [Touchstone1992].

Basic TLC is carried as follows. A small aliquot of sample is placed near one end of the stationary phase, a thin layer of sorbent, to form the initial zone. The sample is then dried. The end of the stationary phase with the initial zone is placed into the mobile phase, usually a mixture of two to four pure solvents, inside a closed chamber. If the layer and mobile phase were chosen correctly, the components of the mixture migrate at different rates during movement of the mobile phase through the stationary phase. This is termed development of the chromatogram. When the mobile phase has moved to an appropriate distance, the stationary phase is removed, the mobile phase is rapidly dried, and the

zones are detected in daylight or under ultraviolet (UV) light with or without the application of a suitable visualization reagent [Sherma2003].

Differential migration is the result of varying degrees of affinity of the mixture components for the stationary and mobile phases. Various separation mechanisms are involved, the predominant forces depending upon the exact properties of the two phases and the solutes. The interactions involved in determining chromatographic retention and selectivity include hydrogen bonding, electron-pair donor/electron-pair acceptor (charge transfer), ion-ion, ion-dipole and van der Waals interactions. Among the latter there are dipole-dipole, dipole-induced dipole, and instantaneous dipole-induced dipole interactions [Sherma2003].

4.3 Electrospray mass spectroscopy

The Navigator Mass Detector system, used to confirm mono-RL and di-RL separation, has been specifically designed and engineered for liquid chromatographic detection, using Atmospheric Pressure Ionisation (API) and Mass Spectrometry technology, to provide the most sensitive and selective detection of organic molecules.

During the measurements, the sample is introduced into the source via inlet, then in an API mass spectrometer the source is held at atmospheric pressure. The sample is then ionized and turned into a gas and the ions, now in the gas phase, pass through the mass analyzer where they are detected. The detected signal is sent to the data system and stored for processing.

The basic function of a mass detector is to measure the masses of individual compounds that have been converted to ions, i.e. given an electrical charge. As the molecules that make up these compounds are so small, the unit of mass that is used is the dalton (Da). Mass spectroscopy is a very powerful analytical technique used mostly for: identification of unknown compounds, quantitation of known compounds and determination of chemical and structural properties.

Electrospray ionization (ESI) is a technique used in mass spectrometry to produce ions using an electrospray in which a high voltage is applied to a liquid to create an aerosol. It is especially useful in producing ions from macromolecules because it overcomes the propensity of these molecules to fragment when ionized. ESI may produce multiple-charged ions, effectively extending the mass range of the analyzer to accommodate the mDa-kDa orders of magnitude [Ho2003].

The mass spectrometry using ESI is called electrospray ionization mass spectrometry (ESI-MS) or electrospray mass spectrometry (ES-MS). ESI is a soft ionization technique, since there is very little fragmentation. This can be advantageous since the molecular ion is almost always observed. However

very little structural information can be gained from the simple mass spectrum obtained. Another important advantage of ESI is that solution-phase information can be retained into the gas-phase [Pitt2009].

4.4 Mono and di-rhamnolipids purification using silica gel column chromatography

The separation of mono-RL and di-RL from a commercial rhamnolipids mixture was conducted using a silica gel column chromatography as described by Aranda et al [Aranda2007]. Rhamnolipids from *Pseudomonas aeruginosa* (in powder and purity of 90%) was purchased from Sigma-Aldrich (Poole, UK). This commercial product was described by Perinelli et al [Perinelli2017] and is composed of a mixture of mono-rhamnolipds (33-37 mol%) and di-rhamnolipids (63-67 mol%).

Silica gel 60 (SiO$_2$) was also purchased from Sigma-Aldrich (Poole, UK) in powder form. Silica gel 60 is a highly porous non crystalline form of silica with particle size of 0.040-0.063 mm and pore size of 60 Å. The solvents used during the execution of chromatography were chloroform (C$_{12}$H$_{22}$O$_{11}$) and methanol (CH$_3$OH), also purchased from Sigma-Aldrich (Poole, UK).

Briefly, a slurry of silica gel 60 in chloroform was poured onto a glass chromatography column (2×40 cm). Then 2.0 g of the crude rhamnolipids mixture was dissolved in 4 mL of chloroform and loaded into the column. Using the force of gravity, the column was washed with chloroform, followed by chloroform/methanol 50:3 and 50:5, which eluted mono-RL components. Then chloroform/methanol 50:50 was loaded into the column, followed by pure methanol, to elute di-RL components (Figure 4.2).

During the separation of mono-RL and di-RL the composition of the fractions were checked by thin-layer chromatography on silica gel plates using chloroform/methanol (9:1) as mobile phase (panel B on Figure 4.2).

Figure 4.2 Silica gel column chromatography at the beginning of experiment (A). The fractions of mono-RL and di-RL being checked by TLC during separation (B).

The purified mono-RL and di-RL components were quantified by weighing after desiccation under high vacuum, as we can see on Figure 4.3.

Figure 4.3 Desiccation of the fractions of mono-RL and di-RL under high vacuum

The purification of the fractions containing mono-RL or di-RL was verified through a chemical characterization of the compounds by electrospray mass spectroscopy [Aranda2007]. The mass was compared as previously described [Abdel-Mawgoud2010].

For each fraction, a small amount of maximum 0.100 mg was dissolved in water and analyzed by direct injection in an electrospray ionization (ESI) mass apparatus in a Navigator Mass Detector. The negative ESI mass spectrum results, obtained after direct injection of the samples, confirms the separation and purification of mono-RL and di-RL from the commercial rhamnolipids.

Figure 4.4 shows the electrospray mass spectroscopy results from the sample containing purified mono-RL. The highest peak represents the major part of the molecules that composed the sample, which had a molecular weight of 502 Da. The results for the mass spectroscopy in the sample containing purified di-RL are shown in Figure 4.5, where a peak corresponding to 648 Da can be seen.

According to the literature [Abdel-Mawgoud2010], these molecular weights can be attributed to mono-RL Rha-C_{10}-$C_{10:1}$ and di-RL Rha-Rha-C_{10}-$C_{10:1}$, respectively (Table 1.2 from Chapter 1).

The results of the electrospray mass spectroscopy showed that the chromatography successfully separated both mono-RL and di-RL from the commercial rhamnolipids mixture, allowing me to start the studies for the characterization of these biosurfactants.
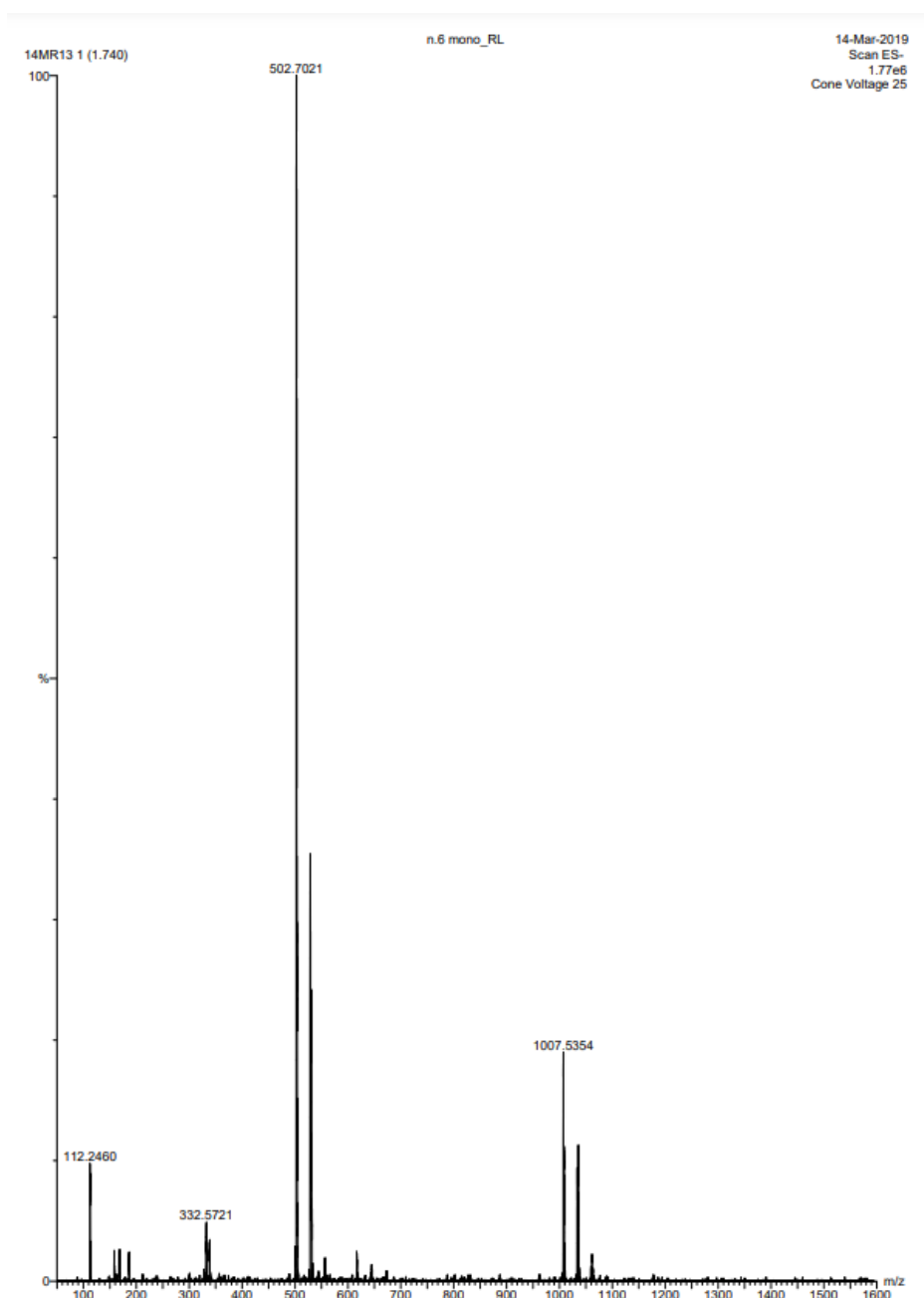
Figure 4.4 Result of electrospray mass spectroscopy for a sample of mono-rhamnolipids
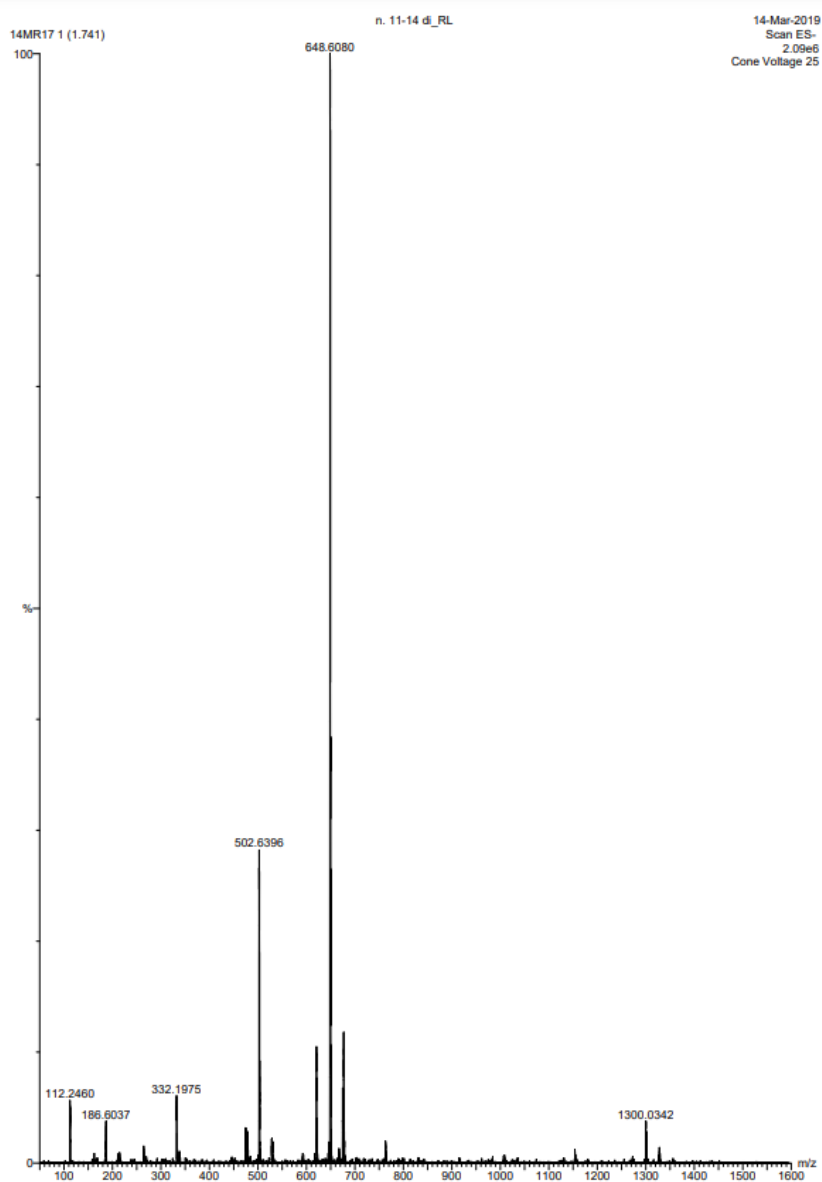
Figure 4.5 Result of electrospray mass spectroscopy for a sample of di-rhamnolipids

5 CMC determination of mono and di-rhamnolipids

5.1 Surface tension measurements

As it was explained in Chapter 2, rhamnolipids in water behave as self-assembling molecules, able to aggregate and form micelles when they reach a concentration above the CMC. The ability of rhamnolipids to form micelles gives them the capability of increasing solubilization of organic compounds, for example hydrocarbons from petroleum, by dissolving the compounds and keeping them inside the hydrophobic core of the micelles.

The surfactants exist as monomer molecules at low concentration in aqueous solutions. Above the CMC, surfactant molecules assemble, forming aggregates. The CMC depends on surfactant structure, composition, temperature, ionic strength and the presence and types of organic additives in the solutions [Fuget2005]. At the CMC, a drastic change in many physicochemical properties occurs in surfactant solutions, such as surface tension, conductivity or turbidity [Xu2005]. Micelles are capable of dissolving hydrophobic contaminants in their hydrophobic core, which results in an increased apparent aqueous solubility of the pollutants [Karsa1991].

The determination of the CMC for mono-RL and di-RL has been performed via surface tension measurements using a Langmuir equipment. A home-built round Teflon trough (diameter 20 mm, thickness 2 mm) filled with 1200 µL of either mono-RL or di-RL solutions has been used for the experiments (Figure 4.1). A stock solution of mono-RL and di-RL was prepared and then diluted to obtain different concentrations. The samples were diluted in both milliQ water and 0.2 M glucose.

The calculation of the CMC in 0.2 M glucose was necessary since this is the solution where GUVs are dispersed to be observed, under the best optical contrast conditions, in the microscope, during the experiments that regard the interaction of GUVs with mono-RL and di-RL (see Chapter 6).

Then measurements of surface tension for mono-RL and di-RL were performed at temperature of 23±1ºC for the different concentrations in stock, from 0.005 to 0.800 mM (Figure 5.1). All measurements were performed in triplicate.
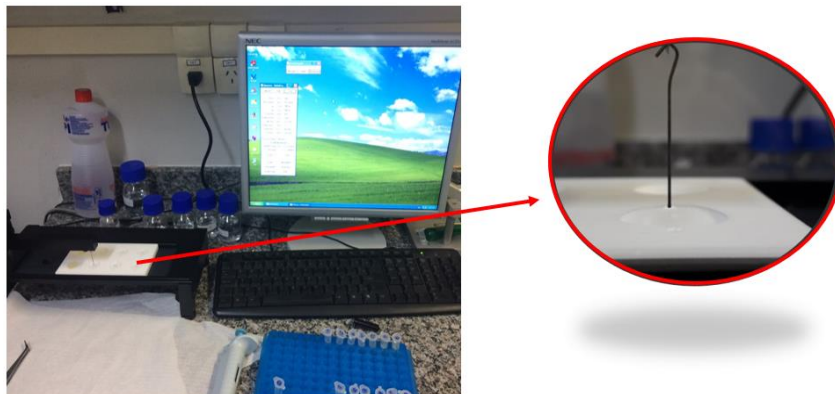
Figure 5.1 Surface tension measurements using Langmuir equipment.

The CMC has been determined from the break point observed in the plot of the surface tension *vs.* log surfactant concentration. Plots of the surface tension as a function of mono-RL and di-RL concentration are shown in Figure 5.2, in water, and in Figure 5.3, in 0.2 M glucose solution, where the best fit with piecewise straight lines are also reported. The plots were performed with OriginPro program [citation].
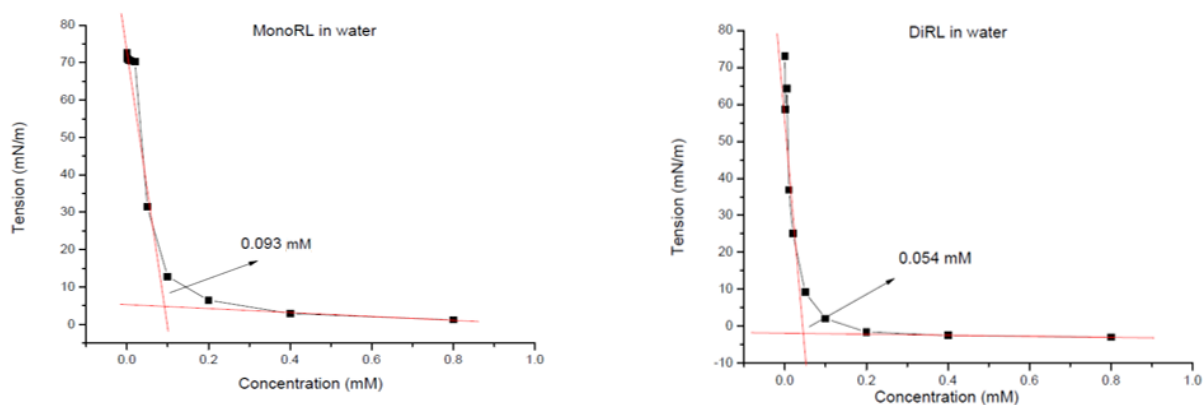
Figure 5.2 Surface tension measurements and related CMC determination for mono-RL and di-RL in water.
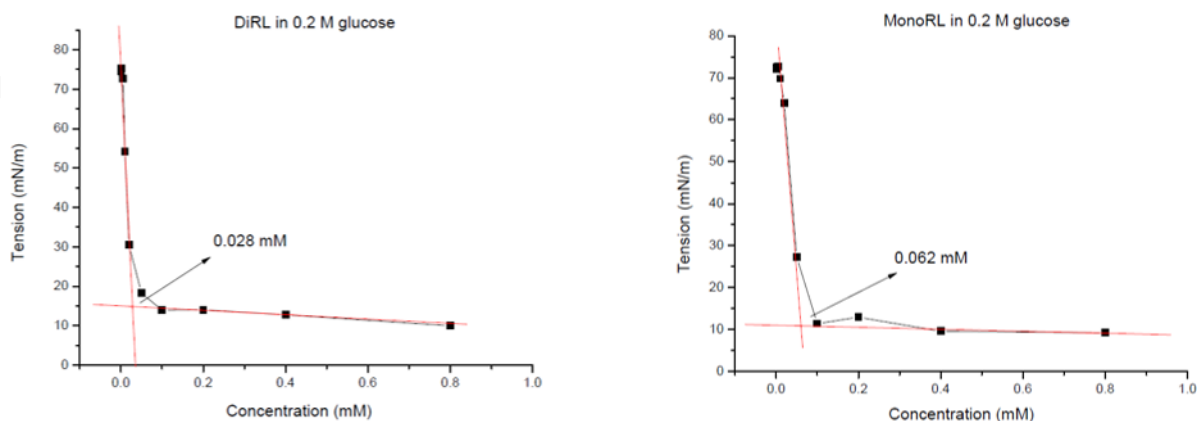
Figure 5.3 Surface tension measurements and related CMC determination for mono-RL and di-RL in 0.2M glucose solution.

Results indicate that the CMC for mono-RL is 0.093±0.005 mM in water and 0.062±0.005 mM in 0.2 M glucose solution and, for di-RL, the CMC is 0.054±0.005 mM in water and 0.028±0.005 mM in 0.2 M glucose solution (Table 5.1).

	mono-RL (mM)	di-RL (mM)
water	0.093±0.005	0.054±0.005
0.2 M glucose	0.062±0.005	0.028±0.005

Table 5.1 Critical micelle concentration (CMC) calculated for mono-RL and di-RL in water and in 0.2 M glucose solution.

6 Characterizing the self-assembling properties of mono and di-rhamnolipids

6.1 X-ray diffraction (XRD)

After successful separation, mono-RL and di-RL were studied with X-ray diffraction (XRD) experiments, with the aim to describe their structural molecular organization at few Angstrom resolutions.

The determination of the structure and typology of a lipid system is possible thanks to several methods, being the X-ray diffraction one of the most informative technique. The X-ray beam hits the sample allowing it to be scattered on the basis of its structure. As a result, a diffraction pattern can be obtained, which is typically constituted by a series of peaks centered on particular scattering angles. It is possible to determine the lipid phase of the sample by analyzing the relative ratio of the positions of the diffraction peaks.

XRD is a technique mainly used for structural investigations of ordered or partially ordered systems, allowing reaching resolutions of about 1.5 Å, comparable with the interatomic distances of condensed matter. Indeed, ordered structures are able to scatter X-rays according to specific angles that depend on the nature and arrangement of the molecules [Bugaev2010]. The nondestructive nature of the XRD technique makes it particularly valuable because one frequently needs to obtain a large amount of information about a relatively small sample of material [Ryland1958].

XRD is used for analyzing a wide range of materials including fluids, metals, minerals, polymers, catalysts, plastics, pharmaceuticals, thin-film, coatings, ceramics, solar cells and semiconductors. The technique finds innumerable practical applications in various industries, including microelectronics, power generation, aerospace among many others. For example, XRD can easily detect the existence of defects in a particular crystal and virtually any other variable relating to the sample's basic structure [Bunaciu2015].

XRD technique is based on the constructive interference of monochromatic X-rays impinging on a sample. In the laboratory XRD instruments, X-rays are generated by a cathodic ray tube, filtered to produce monochromatic radiation, collimated to concentrate and directed toward the sample [Bunaciu2015].

Max von Laue suggested that a crystalline solid, consisting of ordered arrays of atoms, could serve as a diffraction lattice for electromagnetic waves displaying wavelengths comparable with the

interatomic distances. The experiments proved soon that the X-rays scattered by a crystal really showed the peaks of a diffraction pattern. XRD technique has been revealed to be very efficient for exploring the world of atoms and molecules. Today this technique plays a key role in the study of crystals and any other system with repeating order in one, two or three dimensions.

6.1.1 The XRD principles and Bragg's law

X-rays are electromagnetic waves with wavelength ranging from 0.1 to 100 Å (1 Å=10^{-10} m), corresponding to frequencies in the range 3×10^{16} Hz to 3×10^{19} Hz and energies in the range 120 eV to 120 keV. The wavelength λ frequently used for diffraction experiments can vary from 0.5 to 2.5 Å. Moreover, according to λ, X-rays can be divided into (λ ≥ 1 Å) and hard (λ ≤ 1 Å). Hard X-rays are very close to γ-rays but different from them since X-ray photons are produced by atomic electrons (electronic sources), while γ-rays are generated by sub-atomic (nuclear) transitions.

When an X-ray beam passes through the matter, it can follow two different ways: it can be deflected from its path without loss of energy and this is the elastic scattering radiation (Thomson scattering), which has the same wavelength of the incident radiation, or it can be deviated with a small loss of energy and a consequent slight variation of the wavelength. This latter is the Compton or incoherent scattering [Lytvynenko2005]. The Thomson scattering is due to the vibration of each electron of the system, which, being affected by the oscillating electric field of the X-ray radiation, becomes a source of a spherical wave with the same wavelength of the impinging X-ray. The XRD pattern originates from the constructive interference of these spherical waves and depends on the distribution of the electrons on the systems, referred to as electron density [Lytvynenko2005].

The energy carried by the radiation is given by:

<div align="right">Equation 6.1</div>

$$E = h\nu$$

where ν is Planck's constant and ν is the X-ray frequency.

The interaction of waves with periodic structures produces diffraction effects if the wavelength and the periodicity of the ordered structures are of the same order of magnitude. X-rays can be easily produced with wavelengths matching the unit cell dimensions of crystals, but electrons or neutrons of appropriate energy can also be used for diffraction experiments on crystals.

Considering that atoms in molecules are at distances in the order of Angstroms, the unit cells in the crystals have dimensions of several Å. This implies that crystals with sizes of microns or larger consist

of billions of unit cells, which repeat periodically in all three dimensions, i.e. they possess long-range order. This kind of order distinguishes crystalline materials from amorphous ones, which have only short-range order. Since the quality of diffraction effects in XRD strongly depends on the strict and undisturbed periodicity of atoms, any kind of deviation from the ideal order is shown in the X-ray diffraction diagram. Even small crystallite size is a deviation from the theoretically infinite perfect crystal.

Without any diffraction effects, the incidence of a primary X-ray beam onto a sample volume would produce scattering in all directions. Diffraction redistributes intensity from the completely scattering sphere into distinct directions. Therefore, intensity peaks arise in certain directions, whereas in directions between peaks the intensity decreases drastically [Eby2004].

To explain this property, consider a crystal with lattice planar distances *d*. Where the travel path length difference between the ray paths ABC and A'B'C' is an integer multiple of the wavelength, constructive interference will occur for a combination of that specific wavelength, crystal lattice planar spacing and angle of incidence (θ). Each plane of atoms in a crystal will undergo refraction at a single, unique angle (for X-rays of a fixed wavelength). The intensity integrated over the sphere, however, remains constant due to energy conservation. One way of describing these directions is the notion of scattering lattice planes and interference between the wavelengths scattered by neighboring lattice planes [Eby2004]. Figure 6.1 illustrates this situation.
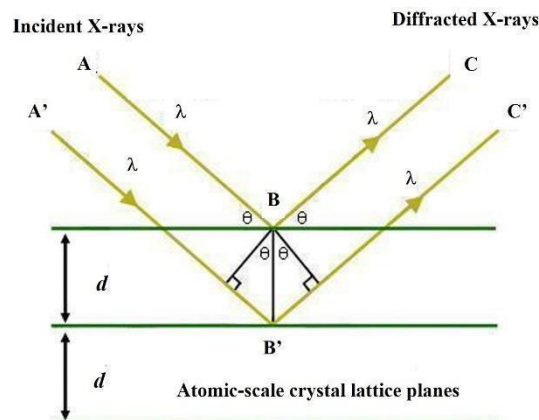
Figure 6.1 Bragg's Law reflection. The diffracted X-rays exhibit constructive interference when the distance between paths ABC and A'B'C' differs by an integer number of wavelengths (λ).

Hence, the interaction of the incident rays with the sample produces constructive interference and a diffracted ray, when conditions satisfy Bragg's law:

.

Equation 6.2

$$n\lambda = 2d\sin\theta$$

where *n* is an integer number, λ is the wavelength of the X-rays, *d* is the interplanar spacing generating the diffraction, and θ is the diffraction angle. This law relates the wavelength of electromagnetic radiation to the diffraction angle and the lattice spacing in a crystalline sample.

These diffracted X-rays are then detected, processed and counted. By scanning the sample through a range of 2θ angles, all possible diffraction directions of the lattice should be attained due to the random orientation of the material. Conversion of the diffraction peaks to *d-spacings* allows identification on the compound because each compound has a set of unique *d-spacings*. Typically, this is achieved by comparison of *d-spacings* with standard reference patterns [Bunaciu2015].

6.1.2 X-Ray diffractometer

The instrumentation that is used for powder diffraction measurements has not changed much from that developed in the late 1940s. The major difference found in modern instrumentation is the use of the minicomputer for control, data acquisition and data processing [Bunaciu2015].

X-ray diffractometers consist of three basic elements: an X-ray tube, a sample holder and an X-ray detector. The X-ray are generated in a cathode ray tube by heating a tungsten filament to release thermal electrons, accelerating the electrons toward a target by applying a voltage, and bombarding the target material with electrons. Following this interaction, X-rays are emitted at different wavelengths characteristic of each substance. When electrons have sufficient energy to dislodge inner shell electrons of the target material, characteristic X-ray spectra are produced [Connolly2007].

The monochromatizating system consists of quartz monochromator crystals that have the function of selecting the chosen radiation (typically 1.5 Å). The collimation system makes it possible to define the shape and size of the beam, for this purpose a sequence of slits that control the angular divergence of the beam is used. The beam thus obtained hits the sample inserted in a sample holder.

The incident X-ray beam is diffracted from the sample and collected on a detector that measures the intensity of the radiation (*I*) as a function of the diffraction angle 2θ. Between the detector and the sample, a small lead plate is positioned to block the transmitted beam (beam stop).

The detection system used is a photographic plate with active phosphors (Image Plate) in which the blackening of the emulsion is proportional to the intensity of the diffracted beam. The image is

impressed on the plate, displayed using a scanner and processed by a computer. Figure 6.2 shows how X-ray diffraction works.
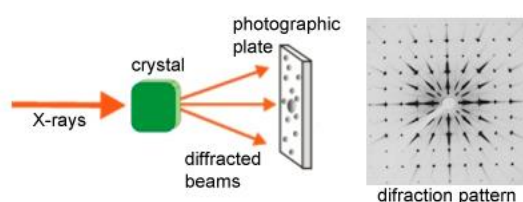
Figure 6.2 Schematic diagram of a X-ray diffractometer.

The specific wavelengths are characteristic of the target material (Cu, Fe, Mo, Cr). These X-rays are collimated and directed onto the sample. As the sample and detector are rotated, the intensity of the incident X-rays impinging the sample satisfies Bragg's law, constructive interference occurs and a peak in intensity appears. A detector records and processes this X-ray signal and converts the signal to a count rate, which is then output to a device such as a computer monitor [Bunaciu2015].

The geometry of an X-ray diffractometer is such that the sample rotates in the path of the collimated X-ray beam at an angle θ while the X-ray detector is mounted on an arm to collect the diffracted X-rays and rotates at an angle of 2θ. The instrument used to maintain the angle and rotate the sample is termed a goniometer. For typical powder patterns, data are collected at 2θ from 5º to 70º, angles that are present in the X-ray scan [Bunaciu2015].

The tricosane is used to obtain a calibration line necessary to convert the values of the screen pixels into the modulus of the scattering vector defined as $q=4\pi \sin \theta/\lambda$. This molecule, extensively described in the literature, forms a precise lamellar phase characterized by a sequence of interference peaks whose positions are known. Therefore, from the calibration line it is possible to convert the value of the pixels on the abscissa axis into q values for any sample.

6.2 X-ray diffraction measurements for mono and di-rhamnolipids

6.2.1 Preparation of samples for diffraction measurements (XRD)

XRD experiments were performed with concentrated mono-RL and di-RL separated by chromatography from the commercial rhamnolipids (see Chapter 4).

Measurements were carried out with di-RL in different concentrations of water (w/w): 10%, 15%, 20%, 40% and 45%. However, it was not possible to to perform XRD measurements with mono-RL in

different concentrations of water because after purification, the mono-RL showed an oily consistency, what made difficult to obtain samples of mono-RL diluted in high concentrations, i. e. with small amounts of water.

The weight of di-RL and amount of milliQ water used for each concentration are reported in Table 6.1.

water content h (w/w %)	di-RL weighed mass (g)	added water volume (μL)
10	0.0968	10.8
15	0.0267	4.7
20	0.0280	7.0
40	0.0416	27.7
45	0.0189	15.5

Table 6.1 Experimental conditions of the di-RL hydrated samples.

The samples were inserted inside the 1 mm thick teflon disk sample holder, sealed by two thin mylar sheets and two perforated aluminum disks, which constitute the windows where the X-ray passes through. This sample holder was sealed together by a brass shirt formed by two cylindrical parts closed and sealed by four screws, which prevented the sample from drying out (Figure 5.3). The formation of air bubbles must be avoided during this operation, because it may produce interferences in the X-ray diffraction patterns.

Figure 6.3 Sample holder, brass ring

The samples were measured as a function of temperature, from 20 to 60°C, increasing the temperature by 10°C. At the end of each measurement, the image printed on the photographic plate was scanned

and displayed on the computer with the ImageJ Launcher software. Subsequently, the diffraction analysis was performed with a software running under Igor Pro (Wavemetrics, Lake Oswego, OR, USA).

6.3 Analysis of mono-RL and di-RL diffraction

X-ray diffraction experiments were carried out using a 3.5 kW Philips PW 1830 X-ray generator (Amsterdam, Netherlands) equipped with a bent quartz crystal monochromator with λ=1.54 Å and a Guinier-type focusing camera (homemade design and construction, Polytechnic University of Marche, Ancona, Italy). Diffraction patterns were recorded on GNR Analytical Instruments Imaging Plate system (Novara, Italy). Samples were prepared by placing them in a vacuum cylindrical cell provided with thin mylar windows. Samples (mono-RL and di-RL) were measured at the temperatures of 20, 30, 40, 50, 60°C and at different hydration content h, defined as weight percentage of water (10, 15, 20, 40, 45 w/w %). In each experiment, the positions of Bragg peaks were detected by using a homemade macro developed under Igor Pro (Wavemetrics, Lake Oswego, OR, USA).

Dry mono-RL and dry di-RL two-dimensional diffraction images are shown in Figure 5.4, where it is possible to observe that the diffraction pattern obtained from di-RL, panel B, is sharper than the diffraction from mono-RL.
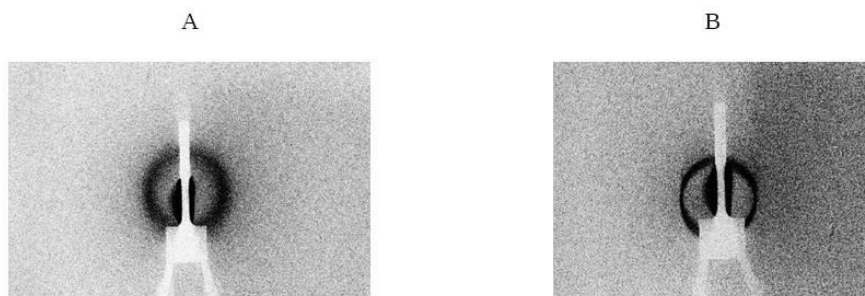
Figure 6.4 Diffraction images of dry mono-RL (A) and dry di-RL (B).

A radial portion of the image was selected and then the pixels from this selected portion were converted into scattered intensity and reported as a function of the distance from the beam position. The obtained two-dimensional graphs were saved as text files and loaded into the Igor Pro program (Wavemetrics, Lake Oswego, OR, USA).

Before performing the sample data analysis, it is necessary to calibrate the instrument through the diffraction pattern of the calibrant, tricosane in our case. From the tricosane diffractometric analysis

we can obtain the calibration line that allows the conversion of the distance measured in pixels from the center of the beam into the values of the q expressed in Å^{-1}.

The derived diffraction patterns of dry mono-RL and dry di-RL samples are shown in Figure 5.5, panels A and B respectively.
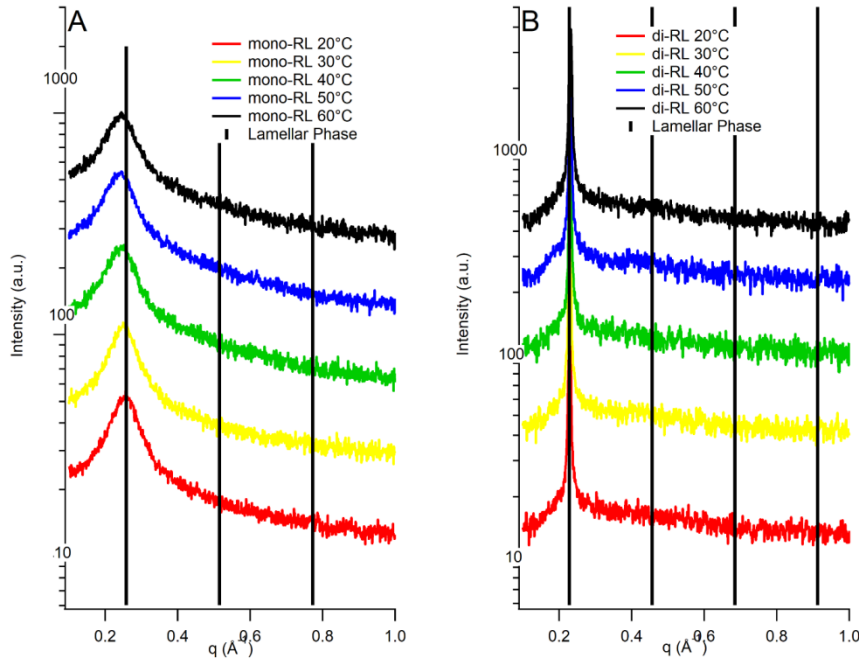
Figure 6.5 Dry mono-RL (A) and dry di-RL (B).

Despite the lack of the second and higher orders peaks, it is possible to attribute the presence of a lamellar phase as show in [Howe 2006]. This peak is more marked in the di-RL sample. In fact, as it can be seen from Figure 5.5, panel A, the mono-RL sample shows a broad peak while, in the case of the di-RL sample, the Bragg peak is much better defined. This result may indicate that the lamellar structure of the di-RLs is more ordered and organized than the one of mono-RLs.

By assuming that the diffraction arises from a lamellar order, it is possible to determine from the diffraction patterns the staking distance d, which represents the thickness of the bilayers plus the thickness of the water layer located between two bilayers (Figure 5.6). By combining the Bragg law (Equation 5.1) and the definition of q, it is possible to calculate the staking distance d from the position q_1 of the first Bragg peak (n=1):

Equation 6.3

$$d = \frac{2\pi}{q_1}$$

The distance d of the lamellar phase is the thickness of the double layers (d_{HH}) plus the thickness of the water (d_w),

$$d = d_{HH} + d_w$$
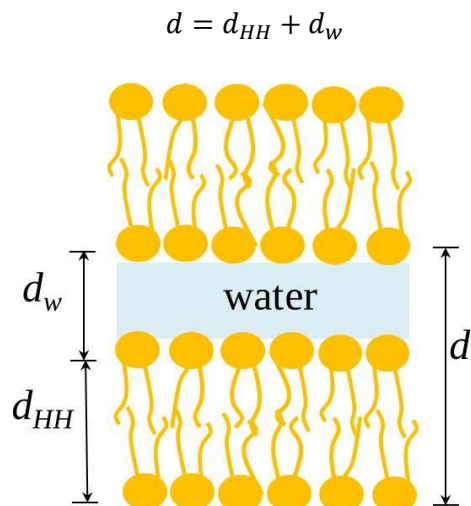
Figure 6.6 The cell parameter d of the lamellar phase is given by the sum of the thickness of the bilayers d_HH and the thickness of the water d_w.

From the position of the peaks of the dry samples shown in Figure 6.5, we have found $d_{HH} = 25.8 \pm 0.1$ Å for mono-RL and $d_{HH} = 27.5 \pm 0.1$ Å for di-RL. The larger value for the di-RL can be easily explained considering the presence of two rhamnose groups the polar head.

The diffraction patterns measured for the di-RL samples with different water content and temperature are shown in Figure 6.7, panels A-E. Each panel reports the XRD profiles recorded at the same temperature and with different water contents, as reported in the color box beside each panel. The vertical black line indicates the optimized positions of the peaks according to a lamellar order. It is evident that the peak position decreases toward lower q by increasing the water content, suggesting a concomitant increase of the stacking distance.
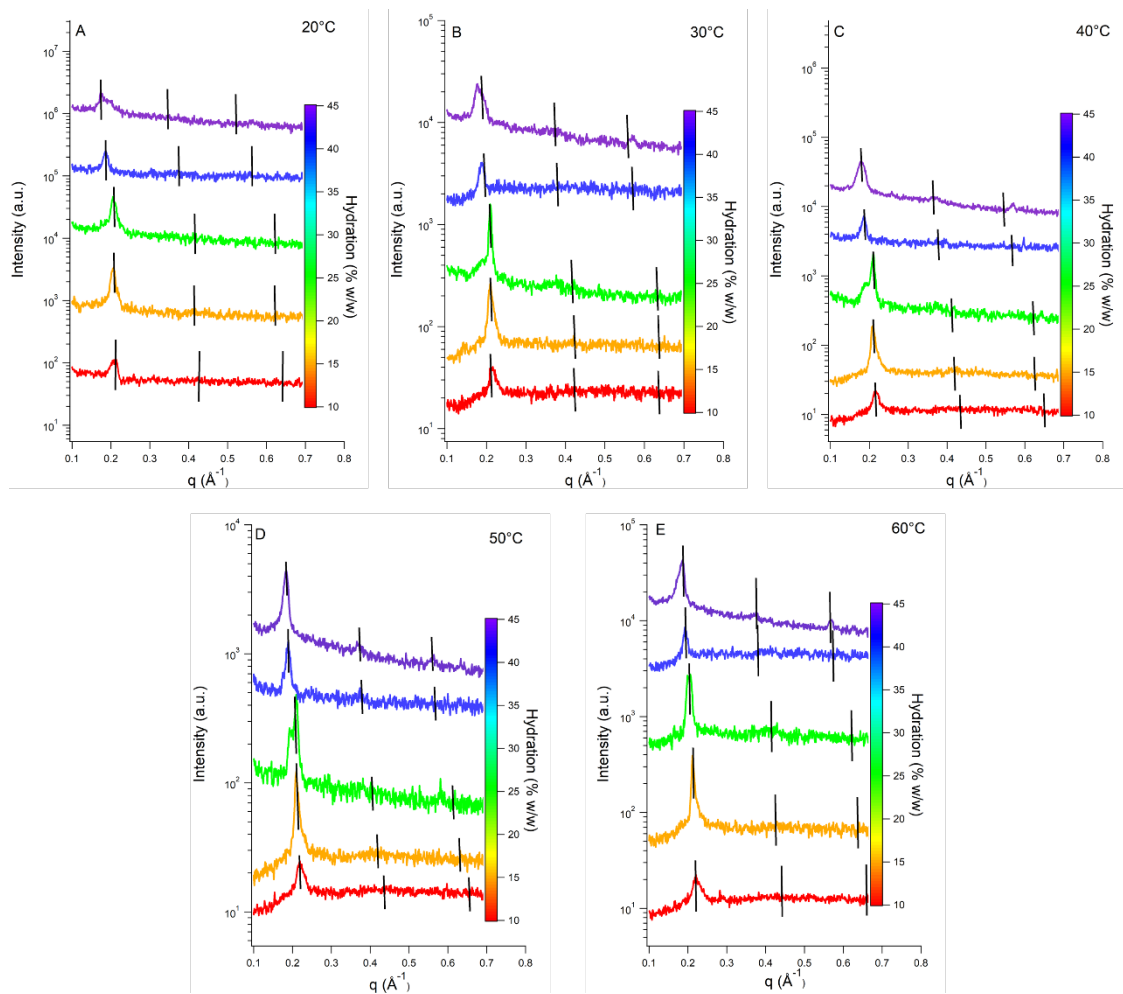
Figure 6.7 Diffraction patterns of di-RL at different temperatures and water concentrations. In each panel, from bottom to top, red, orange, green, blue, and violet curves refer to samples with water content of 10, 15, 20, 40 and 45% w/w, respectively.
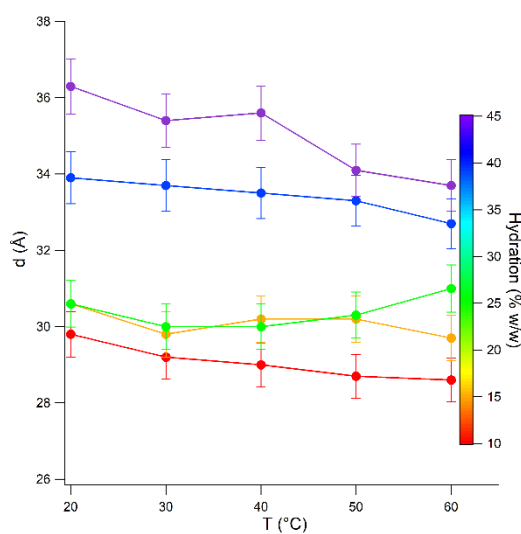
Figure 6.8 Cell parameter d of di-RL samples at different water content reported as a function of temperature.

We have subsequently calculated the thickness of the water layer between two bilayer, according to Equation 6.4 and by fixing, in a first approximation, for all the temperatures the bilayer thickness to the value previously derived, $d_{HH} = 27.5 \pm 0.1$ Å. Results are reported in Table 6.2 and in Figure 6.9.

	T (°C)				
	20	30	40	50	60
h (w/w %)	d_w (Å)				
10	2.3 ± 0.2	1.7 ± 0.2	1.5 ± 0.2	1.2 ± 0.2	1.1 ± 0.2
15	3.1 ± 0.2	2.3 ± 0.2	2.7 ± 0.2	2.7 ± 0.2	2.2 ± 0.2
20	3.1 ± 0.2	2.5 ± 0.2	2.5 ± 0.2	2.8 ± 0.2	3.5 ± 0.2
40	6.4 ± 0.2	6.2 ± 0.2	6.0 ± 0.2	5.8 ± 0.2	5.2 ± 0.2
45	8.8 ± 0.2	7.9 ± 0.2	8.1 ± 0.2	6.6 ± 0.2	6.2 ± 0.2

Table 6.2 Thickness of the water layer, expressed in A

Results show that d_W increase with h. Indeed, for ideal lamellar phases, d_W should be proportional to d according to $d_w = \phi(h)d$, where $\phi(h)$ is the volume fraction of water in the mixture, a parameter related to h percentage according to

Equation 6.5

$$\phi(h) = \frac{1}{1 + \dfrac{100 - h}{h}\dfrac{v_{\mathrm{W}}}{v_{\mathrm{RL}}}}$$

In this equation, v_{W} and v_{RL} are the specific volumes of water and RL, which have been calculated on the basis of the van der Waals volumes of the different groups. We have obtained $v_{\text{mono-RL}}$=0.62 mL/g and $v_{\text{di-RL}}$=0.60 mL/g.
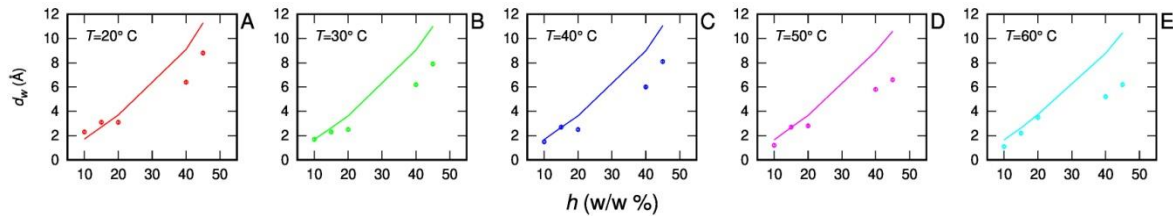
Figure 6.9 Thickness of the water layer between di-RL bilayers determined by XRD and reported as a function of the hydration content h. Panels A-E refer to different temperatures, as shown on to top left. Solid lines represent the values calculated according to $d_w = \phi(h)d$.

In Figure 6.9 values of d_w are reported as a function of d together with the values calculated according to $d_w = \phi(h)d$. It can be observed that only up to h=20 there is an agreement between the two values, indicating that at higher hydration content the di-RL are no more organized in a lamellar phase.

6.4 Small angle X-ray scattering (SAXS)

The interaction of X-ray radiation with electron density inhomogeneity in matter can cause a small deviation from its incident direction, called small angle scattering (Figure 6.9). Such small angle scattering (SAS) occurs in all kinds of materials, be they partially crystalline or amorphous solids, liquids or even gases, and can take place for a wide variety of radiation, such as electrons (SAES), gamma rays (SAGS), light (LS), x-rays (SAXS) and neutrons (SANS) [Pauw2013].
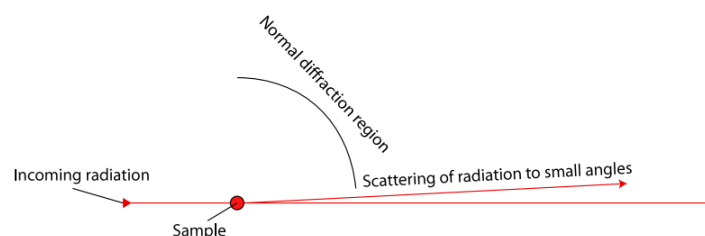
Figure 6.10 The scattering of a radiation to small angles by a sample (small angle scattering) [Pauw2013].

In solution small-angle scattering of X-rays or neutrons (SAXS and SANS) is a powerful tool for determining the structural features of biologically relevant macromolecules in solution. SAS can provide not only precise information concerning the size and shape of single molecules (also in terms of molecular weight, volume, compactness degree and aggregation state) but also detailed information from large, multicomponent macromolecular complexes such as protein complexes. Moreover size and shape of the protein in solution can be obtained in very different experimental conditions, for example as function of pH [Barbosa2010], salt concentration [Zhang2007], temperature or pressure [Otore2009], presence of cosolvents, ligands or denaturing agents. In a SAXS experiment, the elastic scattering of X-rays (typical wavelength $\lambda \approx 1$ Å) by a sample with nanometric inhomogeneities is recorded at very low angles (scattering angles 2θ typically from 0.1º to 10º).

The whole system is enclosed in vacuum chambers in order to avoid the non-negligible SAS of air. If the sample consists of particles or aggregates dispersed in a homogeneous solution, the intensity scattered in this angular region contains information about the shape, size, and interactions of the dispersed particles. The analysis of the SAS curve can be limited to the determination of few parameters, but other information can be also derived. The first is the particle form factor, which is

directly related to the in-solution structure of the scattering particles. When the particle-particle interactions cannot be neglected, an additional scattering signal related to the spatial distribution of the particles is detected and the presence of a structure factor should be considered. In this context, an analysis of the structure factor leads to the correlation function, which describes the spatial arrangement of the particles and the direct pair potential that describes particle-particle interaction force [Ottore2009, Barbosa2010].

Although SAXS has a wider field of applicability in systems with only one or two phases, one additional limitation of SAXS, besides its preference for two-phase systems, is the ambiguity of the resulting data [Pauw2013]. During SAXS measurements, only the scattering intensity is collected, so critical information is lost, which prevents the full retrieval of the original structure. Such loss of information is present in all the techniques based on X-ray scattering and is in general referred to as the phase problem. Shull and Roess explained: "Basically it is the distribution of electron density which produces the scattering, and therefore nothing more than this distribution, if that much, can be obtained without ambiguity from the X-ray data." [Shull1947]. This means that a multitude of solutions may be equally valid for a particular set of collected intensities, which may only be resolved by obtaining structural information from other techniques, such as transmission electron microscopy or atom probe [Pauw2013].

From the three most demanded morphological aspects, shape, polydispersity and packing, two must be known to obtain information on the third [Pedersen1997]. Despite these disadvantages, many practical applications have confirmed the validity of the small angle scattering derived information. SAXS needs to be combined with supporting techniques and when these conditions are achieved; it will provide information on morphological features ranging from the sub-nanometer region to several micrometers. Furthermore, it can quantify the structural details of samples that are more challenging to quantify using electron microscopy, such as structures of glasses, fractal structures and numerous in situ studies, as well as volume fraction and size distribution studies [Pauw2013].

6.4.1 General equation of SAXS

The most general equation of Small Angle Scattering [Guinier1955] is

Equation 6.6

$$\frac{d\Sigma}{d\Omega}(\mathbf{q}) = \frac{1}{V}\langle\int_V \rho(\mathbf{r})e^{i\mathbf{q}\cdot\mathbf{r}}\,d\mathbf{r}\rangle$$

where $\frac{d\Sigma}{d\Omega}(\mathbf{q})$ is the scattering intensity, more precisely called macroscopic differential excess scattering cross section, as a function of the exchanged wave vector $\mathbf{q}$. The modulus q depends on the scattering angle 2θ as:

$$q = \frac{4\pi \sin\theta}{\lambda}$$

In Equation 6.6 the integral is extended over the irradiated sample volume V and $\mathbf{r}$ is the position vector. The angular brackets indicate an average over all positions, orientations and microstates of the particles in the systems. Finally, $\rho(\mathbf{r})$ is the electron density of the sample multiplied for the classical electron radius, $r_e = 2.8 \cdot 10^{-13}$ cm.

In absence of long range order, the scattering density can be thought as having an uniform value ρ_0 on which fluctuations $\delta\rho(\mathbf{r})$ are superimposed. The amplitude of the X-ray wave scattered by one particle is, by definition, the normalized Fourier Transform of $\delta\rho(\mathbf{r})$ calculated only within the particle volume,

$$A(\mathbf{q}) = \frac{1}{f}\int_{V_p} \delta\rho(\mathbf{r})e^{i\mathbf{q}\cdot\mathbf{r}}\,d\mathbf{r}$$

where f is the scattering amplitude at $\mathbf{q} = \mathbf{0}$ and V_p is the volume of the scattering particle,

$$f = \int_{V_p} \delta\rho(\mathbf{r})\,d\mathbf{r}$$

The form factor of the particle is the orientational average of the square of its scattered amplitude and is defined by the integral over the two polar angle α_q and β_q of the scattering vector,

$$P(q) = \frac{1}{4\pi}\int_0^{2\pi}\int_0^{\pi} A(\mathbf{q})A^*(\mathbf{q})\sin\beta_q\,d\beta_q\,d\alpha_q$$

To note, $P(q)$ is a function that only depends on the modulus of the scattering vector. If there are particle with different structure or polydispersed over a physical parameters (for example the radius or

the length of a cylinder), it can be defined the effective form factor of the particles as an average, weighted on the system composition, of the form factor of any type of particle. The scattering intensity for randomly oriented particle can be written in a different form, which include the effective form factor,

$$\frac{d\Sigma}{d\Omega}(q) = n_p P(q) S_M(q)$$

where n_p is the particle number density and $S_M(q)$ is the effective structure factor, which takes into account the correlations among the centers of the scattering particles. It worth to notice that if particle are diluted, $S_M(q) \approx 1$: in this case the scattering intensity is simply proportional to the effective form factor.

6.5 SAXS analysis for mono and di-rhamnolipids

6.5.1 SAXS samples

We have investigated by SAXS dilute solutions of either mono-RL or di-RL obtained by means of the chromatographic separation discussed in Chapter 4. Samples were dissolved in milliQ water at different concentrations well above the CMC, from 10 to 100 mM and, for di-RL, in the presence of NaCl. In detail, di-RL samples in pure water have been prepared at concentrations of 30, 70, 90 and 110 mM and di-RL samples in the presence of 100 mM NaCl have been prepared at the concentrations 75, 80, 85, 90 and 110 mM. Regarding mono-RL, samples in pure water have been prepared at concentrations of 10, 18, 34 and 50 mM; no measurements were carried out in the presence of NaCl since this salt causes the total precipitation of mono-RL. The pH of all the investigated samples was 7.5 ± 0.1.

6.5.2 SAXS experiments

We have carried out a campaign of SAXS/WAXS (wide-angle X-ray scattering) measurements at the beam-line I22 of the synchrotron Diamond (Didcot, UK). Due to the covid-19 pandemics, samples have been sent to Diamond by exploiting the mail-in program. I22 was used in transmission mode and the dilute solutions of either mono-RL or di-RL were placed in polycarbonate capillaries. The camera length was 3.0 m and the related range of q was comprised between 0.008 and 3.23 Å^{-1}. All measurements were obtained at 20° C. SAXS patterns were recorded with a Pilatus P3-2M detector operating with 1475×1679 pixels, each with 172×172 µm² size. WAXS signals were collected by a

Pilatus P3-2M-DLS-L detector working with the same number and size of pixels. SAXS and WAXS raw data have been preliminary treated with the software Dawn operating at I22, in order to obtain the radial averages for both SAXS and WAXS curves. Subsequently, we have processed all the curves by a home-made software written under Gnuplot [Williams2011], aimed to perform a proper empty capillary subtraction, followed by a buffer subtraction. SAXS and WAXS profiles, these latter up to 0.8 Å^{-1} (before the broad diffraction band of water), have been merged in a unique SAXS curve by optimizing their overlap in a common q range. Absolute scale calibration has been calculated considering the scattering of pure water.

6.5.3 SAXS analysis

All the SAXS curves have been analyzed by using the Genfit software [Spinozzi2014, 10.1107/S1600576714005147], which has been developed in the Molecular Biophysics Laboratory of the DISVA department at the Polytechnic University of Marche. Genfit is a general-purpose software that performs a deep analysis of SAXS curves by adopting the more suitable structural model that the user can select from a very wide list of possible models. In our case, we have started to interpret with Genfit the SAXS data adopting the simplest models known from literature for surfactants, such as core-shell spheres or ellipsoids or infinite bilayers. Subsequently, we have identified two different models that are well-suited to fit the SAXS curves of mono-RL or di-RL. A complete description of these models, together with the best strategy to link the parameters that define them to the known chemical-physical characteristics of the two RL molecules, is shown in the next Sections.

6.5.3.1   SAXS of interacting two-density level spherocylinders

The SAXS curves of di-RL have been successfully analysed by modelling their shape in terms of spherocylinders and considering the effect of their interactions by assuming that they act as randomly oriented particles in solution. The macroscopic differential scattering cross sections is written according to the following equation

Equation 6.12

$$\frac{d\Sigma}{d\Omega_{SC}}(q) = C N_A\, r_e^2\, P(q) S_M(q),$$

where C is the molar concentration of spherocylinders, N_A is Avogadro's number, r_e is the classical radius of the electron (0.28 10^{-12} cm), $P(q)$ is the spherocylinder's form factor and $S_M(q)$ is the so-called measured or effective structure factor.

We have considered spherocylinders formed by two levels of electron densities, referred to as core and shell. A schematic representation of this particle is shown in Figure 6.11.
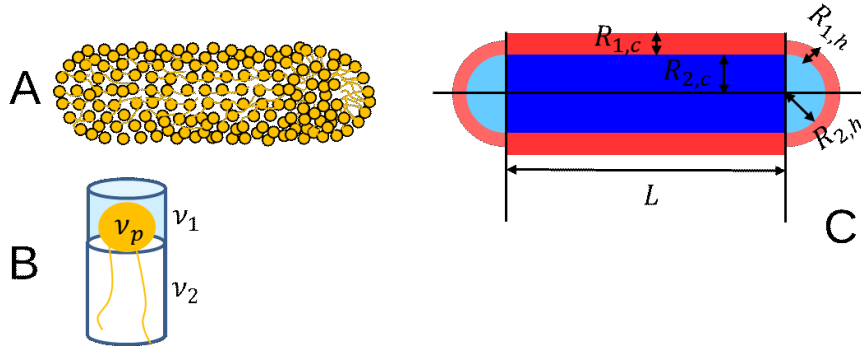
Figure 6.11 Scheme of the spherocylinder geometry. A) simplified molecular view. B) representation of one di-RL molecule with the indication of the dry polar head volume v_p, the hydrated polar head region v_1 and the paraffinic volume v_2. C) representation of the thicknesses of the polar head region (red) and the paraffinic region (blue) in the cylindrical domain and of the thicknesses of the polar head region (light red) and the paraffinic region (light blue) in the hemi-spherical domain.

The scattering amplitude of this kind of particle, which is defined as the Fourier transform of the excess electron density calculated inside the particle volume, results

Equation 6.13

$$A(q,\beta) = 2\pi L \frac{\sin\left(\frac{1}{2}qL\cos\beta\right)}{\frac{1}{2}qL\cos\beta} \sum_{k=1}^{2} (\rho_{k,c} - \rho_{k-1,c}) r_{k,c}^2 \frac{J_1(qr_k\sin\beta)}{qr_k\sin\beta} + 4\pi \sum_{k=1}^{2} (\rho_{k,h} - \rho_{k-1,h}) r_{k,h}^3$$

$$\times \int_0^1 x(1-x^2)^{\frac{1}{2}} J_0\left(qr_{k,h}x\sin\beta\right) \frac{\sin\left(\frac{1}{2}qr_{k,h}(1-x^2)^{\frac{1}{2}}\cos\beta\right)}{\frac{1}{2}qr_{k,h}(1-x^2)^{\frac{1}{2}}\cos\beta}$$

$$\times \cos\left(\frac{1}{2}q(L+r_{k,h}(1-x^2)^{\frac{1}{2}})\cos\beta\right) dx$$

In this equation, β represents the angle formed by the long axis of the spherocylinder (longest solid black line in Figure 6.11, panel C) and the scattering vector $\mathbf{q}$; for the cylindrical (c) domain and the hemi-spherical domain (h), $\rho_{k,c}$ and $\rho_{k,h}$ are the electron densities of solvent, shell and core with $k=0,1$ and 2, respectively; the two parameters $r_{k,c}$ (with $k=1,2$) are $r_{1,c} = R_{1,c} + R_{2,c}$ and $r_{2,c} = R_{2,c}$, where $R_{1,c}$ is the thickness of the cylindrical shell, which contains di-RL polar heads and hydration water, and $R_{2,c}$, is the inner radius of the cylindrical domain of the spherocylinder; regarding the two end hemispherical caps,, the parameters $r_{k,h}$ are defined in a similar way, with $r_{1,h} = R_{1,h} + R_{2,h}$ and $r_{2,h} = R_{2,h}$, $R_{1,h}$ being the thickness of the spherical shell and $R_{2,h}$ the radius of the inner sphere; L is the length of the cylindrical domain. Finally $J_0(x)$ and $J_1(x)$ are the Bessel functions of 0th and 1st order, respectively. The random orientation of the particles is reflected in a integration over the angle β, which leads to the calculation of the orientational average scattering amplitude

Equation 6.14

$$P_1(q) = \int_0^{\frac{\pi}{2}} \sin\beta \, A(q, \beta) d\beta.$$

On the other side, when we integrate the squared amplitude, we obtain the form factor of the spherocylinder, according to

$$P$$

Equation 6.15

$$(q) = \int_0^{\frac{\pi}{2}} \sin\beta A^2(q, \beta) d\beta.$$

The measured structure factor $S_M(q)$ is modelled on the basis of an assumption regarding the potential energy $u(r)$ (also simply referred to as the potential) between two particles at distance r. One of the simplest assumption is to consider the interaction between two rigid spheres (also called hard spheres, HS) combined with a repulsive and an attractive potential, both described by the Yukawian function. Hence this potential, referred to as HSDY (Hard-Spheres Double-Yukawian), is the sum of three terms, $u(r) = u_{HS}(r) + u_C(r) + u_A(r)$. The HS reads

Equation 6.16

$$u_{HS} = \begin{cases} +\infty & r < \sigma \\ 0 & r > \sigma \end{cases}$$

where σ is the HS diameter. The repulsive Yukawian term is the well-known screened Columbian potential

Equation 6.17

$$u_C(r) = \frac{Z^2 q_e^2}{\varepsilon \left(1 + \frac{\kappa_D \sigma}{2}\right)^2} \frac{\exp[-\kappa_D(r-\sigma)]}{r},$$

where Z is the number of elementary electric charges brought by the particle, q_e is the charge of the proton, κ_D is the inverse Debye length and ε is the relative dielectric constant of the solvent (water in our case). To note, $\kappa_D = (2N_A \, q_e^2 I / (\varepsilon_0 \, \varepsilon k_B T))^{1/2}$ depends on the total ionic strength of the solution, $I = I_S + I_c$, which is due, from one hand, to the contribution of the added salts, $I_S = \frac{1}{2} \sum z_k^2 C_k$, C_k being the molarity of the kth ionic species and z_k its charge, and, from the other hand, on the contribution I_c due to the RL counterions, here considered monovalent cations (Na$^+$). ε_0 is the dielectric permittivity of vacuum and k_B is Boltzmann's constant. The last term is the attractive Yukawian potential,

Equation 6.18

$$u_A(r) = -J\sigma \frac{\exp[-(r-\sigma)/d]}{r}.$$

The two parameters of this potential are the energy J when the two particles are in contact ($r = \sigma$) and the decay range d. A representation of the HSDY potential is reported in Figure 6.12.
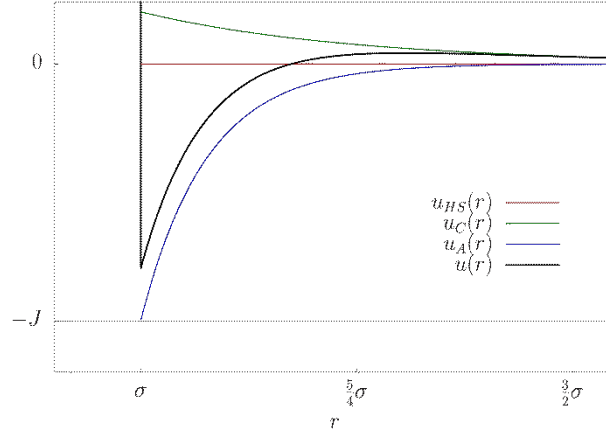
Figure 6.12 Example of a HSDY potential (black line) obtained by the sum of a HS term (red lines), a repulsive Yukawian term (green line) and the attractive Yukawian term (blue curve), whose value is -J when the two HS spheres are at the contact distance σ.

The determination of the particle-particle structure factor $S(q)$ from the pair potential could be performed only within a proper approximation. Here we use the Random Phase Approximation (RPA), one of the simplest approximation, which holds for diluted systems, i.e. systems with a total particle volume fraction η lower than ≈ 0.01,

Equation 6.19

$$S(q) = \frac{S_0(q)}{1+\beta C N_A S_0(q)[U_C(q)+U_A(q)]}.$$

In this equation, $S_0(q)$ is the structure factor related to the HS potential and obtained in the framework of the Mean Spherical Approximation (MSA),

Equation 6.20

$$[S_0(q)]^{-1} = 1 - \frac{12\eta[\eta(3-\eta^2)-2]}{(1-\eta)^4} \frac{j_1(\sigma q)}{\sigma q},$$

where $j_1(x)$ is the spherical Bessel function of 1st order, and $\beta = 1/k_B T$, T being the absolute temperature. To note, the volume fraction of the hard spheres is simply written as $\eta = C N_A \frac{\pi}{6}\sigma^3$. In

Equation 6.21, $U_j(q)$ (with j stands for C or A) is the isotropic Fourier Transform of the Yukawian function $u_j(r) = A_j \exp[-B_j(r - \sigma)]/r$, according to

$$U_j(q) = 4\pi A_j \frac{B_j \sin(q\sigma) + q\cos(q\sigma)}{q(q^2 + B_j^2)}$$

The last steps concerns the calculation of the measured structure factor from the particle-particle structure factor, according to the equation

$$S_M(q) = 1 + \frac{[P_1(q)]^2}{P(q)}[S(q) - 1]$$

It is important to introduce relevant constraints among the model parameters, which arise from known information regarding the system investigated with SAXS. Such information regards the sample composition, the molecular properties of di-RL and the packing of di-RL molecules within the spherocylinder.

First, we can relate the number of di-RL into the spherocylinder, a parameter known as aggregation number N_{agg}, with the area and volume of both the cylindrical domain of the spherocylinder and the hemi-spherical domains. Accordingly, we have

$$\begin{cases} 2\pi(R_{1,c} + R_{2,c})L = N_{agg,c}a_c \\ \pi R_{2,c}^2 L = N_{agg,c} v_2 \end{cases}$$

$$\begin{cases} 4\pi(R_{1,h} + R_{2,h})^2 = N_{agg,h}a_h \\ \frac{4\pi}{3} R_{2,h}^3 = N_{agg,h} v_2 \end{cases}$$

Here $N_{agg,c}$ and $N_{agg,h}$ are the aggregation numbers of di-RL in the cylindrical and in the hemi-spherical domain, respectively, with $N_{agg} = N_{agg,c} + N_{agg,h}$, and the corresponding areas *per* di-RL molecules are a_c and a_h. The parameter v_2 is the volume of the two hydrophobic chains of one di-RL molecule, which reads $v_2 = n_{CH_2} v_{CH_2} + n_{CH_3} v_{CH_3}$, where $n_{CH_2} = 12$ and $n_{CH_3} = 2$ (see Figure 6.13). Moreover, according to Ref. [Spinozzi2010], we write $v_{CH_3} = r_{13} v_{CH_2}$, where $r_{13} \approx 2$ is considered a parameter to be optimized. By considering $R_{1,c}$, $R_{2,c}$ and L as independent variables

(hence parameters to be optimized), the systems in Equations 6.23 can be solved in terms of $N_{agg,c}$, a_c, $N_{agg,h}$ and a_h leading to

$$N_{agg,c} = \frac{\pi R_{2,c}^2 L}{v_2}, a_c = \frac{2v_2(R_{2,c} + R_{1,c})}{R_{2,c}^2}, N_{agg,h} = \frac{4\pi R_{2,c}^3}{3v_2}, a_h = \frac{3v_2(R_{1,c} + R_{2,c})^2}{R_{2,c}^3}$$

These parameters allow to calculate the average number of water as well as the fraction of sodium counterions associated to the polar head of each di-RL molecule in both the cylindrical domain ($n_{w,c}$ and $\alpha_{Na,c}$, respectively) and the hemi-spherical domain ($n_{w,h}$ and $\alpha_{Na,h}$, respectively). Notice that, since the di-RL molecule contains two carboxylic groups, both having an effective acidic constant $pK_a = 5.5$, as reported by Ref. [Lebrón-Paler], the nominal number of sodium counterions *per* di-RL molecule depends on the pH at which di-RL has been purified (lyophilized) according to the following equation

$$\varphi_{Na} = \frac{10^{-pH} \boxtimes K_w + K_a K_w + 2 \boxtimes C_d \boxtimes 10^{-pH} \boxtimes K_a - 10^{-3pH} - 10^{-2pH} \boxtimes K_a}{C_d \boxtimes 10^{-pH} \boxtimes (K_a + 10^{-pH})} \approx \frac{2 \boxtimes K_a}{K_a + 10^{-pH}},$$

where $K_w = 10^{-14}$ is the water ion-product constant and C_d is the molar concentration of di-RL before the lyophilisation. In our case, since the lyophilisation occurred at pH=7.5, we derive $\varphi_{Na} = 1.98$.

For the cylindrical domain we have

$$\pi L \left[(R_{1,c} + R_{2,c})^2 - R_{2,c}^2 \right] = N_{agg,c} v_1$$

$$v_1 = v_p + \frac{n_{w,c} v_w}{d_c} + \varphi_{Na} \alpha_{Na,c} v_{Na},$$

where v_1 is the volume of one hydrated polar head in the presence of a fraction of sodium counterion, v_p is the molecular volume of a dry polar head of one di-RL molecule, $v_w = 30$ Å^3 and $v_{Na} = 4.17$ Å^3 are the known molecular volume of water and Na$^+$, respectively, [Spinozzi2016] and d_c represents the relative mass density of the water among the polar heads. For di-RL, we have estimated $v_p = 613.79$ Å^3. Hence, by considering $\alpha_{Na,c}$ and d_c independent parameters (fitting parameters), we can derive $n_{w,c}$. Considering the hemi-spherical domain, we obtain

Equation 6.27

$$\frac{4}{3}\pi\left[\left(R_{1,h} + R_{2,h}\right)^3 - R_{2,h}^3\right] = N_{agg,h}\left(v_p + \frac{n_{w,h}v_w}{d_h} + \varphi_{Na}\alpha_{Na,h}v_{Na}\right),$$

hence $n_{w,h}$ becomes a function of $\alpha_{Na,h}$ and d_h. All these parameters allow to calculate the electron densities, as follows

Equation 6.28

$$\rho_{2,c} = \rho_{2,h} = \frac{n_{CH_2}e_{CH_2} + n_{CH_3}e_{CH_3}}{v_2}$$

$$\rho_{1,c} = \frac{e_p + n_{w,c}e_w + \varphi_{Na}\alpha_{Na,c}e_{Na}}{v_p + \frac{n_{w,c}v_w}{d_c} + \varphi_{Na}\alpha_{Na,c}v_{Na}}$$

$$\rho_{1,h} = \frac{e_p + n_{w,h}e_w + \varphi_{Na}\alpha_{Na,h}e_{Na}}{v_p + \frac{n_{w,h}v_w}{d_h} + \varphi_{Na}\alpha_{Na,h}v_{Na}}$$

where $e_{CH_2} = 8$, $e_{CH_3} = 9$, $e_w = 10$, $e_{Na} = 10$ are the number of electrons in the methylene group, in the methyl group, in water and in the sodium cation, respectively; e_p is the number of electrons in the polar region of a di-RL molecule, which reads 240. The diameter σ of the HS sphere that describes the HSDY potential between two spherocylinders is a further model parameter. However, it can neither be greater than the total length of the spherocylinder nor be less than the diameter of its circular section. We have then calculated σ according to this equation

Equation 6.29

$$\sigma = 2\left(R_{1,c} + R_{2,c}\right)\gamma + \left(L + 2\left(R_{1,h} + R_{2,h}\right)\right)(1 - \gamma)$$

where γ is a fit parameter that can vary between 0 and 1. We finally note that the molar concentration C of spherocylinders is related to the molar concentration C_d of di-RL by the simple relation $C = C_d/N_{agg}$.

6.5.4 SAXS of interacting three-density level bicelles

Concerning the interpretation of the SAXS experiments of mono-RLs samples, we have found that the micellar shape that best fits all SAXS data is the three-density-level bicelle, in which both core and shell are formed by a cylinders with rounded rims having a half-toroidal profile. As for spherocylinders, we have also described the interactions among three-density-level bicelles assuming that they are randomly oriented particles. Equation 6.12 holds also form such bicelles, the only

difference is the form factor $P(q)$. In detail, according to Ref. [Spinozzi2010], the scattering amplitude of a three-density-level bicelle is

$$A(q,\beta) = 4\pi R^2 \frac{J_1(qR\sin\beta)}{qR\sin\beta} \sum_{k=1}^{3} (\rho_{k,c} - \rho_{k-1,c}) r_{k,c} \frac{\sin(qr_{k,c}\cos\beta)}{qr_{k,c}\cos\beta}$$

$$+ 4\pi \sum_{k=1}^{3} (\rho_{k,h} - \rho_{k-1,h}) r_{k,h}^2$$

$$\times \int_0^1 \frac{x^2}{(1-x^2)^{\frac{1}{2}}} \left(R + r_{k,h}(1-x^2)^{\frac{1}{2}}\right) \frac{\sin(qxr_{k,h}\cos\beta)}{qxr_{k,h}\cos\beta}$$

$$\times J_0\left(q(R + r_{k,h}(1-x^2)^{\frac{1}{2}})\sin\beta\right)dx$$

In this equation R is the major radius of the bicelle, corresponding to the radius of the inner cylindrical core region (see Figure 6.13); the parameters $r_{k,c}$ define the distances from the middle flat bilayer planes of the three canonical regions of electron density, according to $r_{k,c} = \sum_{j=4-k}^{3} R_{j,c}$, where $R_{1,c}$, $R_{2,c}$ and $R_{3,c}$ are the thicknesses of the outer layer (where hydrated polar heads are found), the intermediate layer (mostly occupied by methylene groups) and the inner core (where mostly the terminal methyl groups resides) layer of the cylinder domain, respectively; the electron densities of these cylindrical shells are $\rho_{k,c}$; likewise, for the toroidal rims, we have $r_{k,h} = \sum_{j=4-k}^{3} R_{j,h}$, where $R_{1,h}$, $R_{2,h}$ and $R_{3,h}$ are the thicknesses of the outer toroidal shell, the intermediate toroidal shell and the inner toroidal core, respectively. Note that the electron densities of these toroidal shells and their electron densities are $\rho_{k,h}$. The angle β is the one formed between the cylinder axis and the scattering vector **q**. By using Equations 6.14 and 6.15, we can calculated both $P_1(q)$ and $P(q)$, the bicelle form factor.
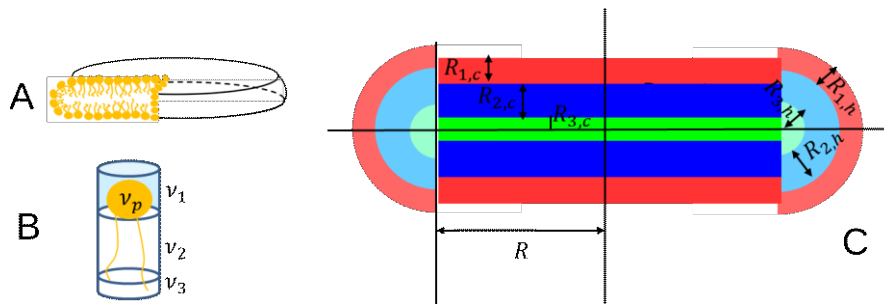
Figure 6.13 Scheme of the bicelle geometry. A) simplified molecular view. B) representation of one mono-RL molecule with the indication of the dry polar head volume v_p, the hydrated polar head region v_1 and the

intermediate paraffinic volume v_2 and the terminal paraffinic volume v_3. C) representation of the thicknesses of the polar head region (red), the intermediate paraffinic region (blue) and the terminal paraffinic region (green) in the flat domain and of the thicknesses of the polar head region (light red), the intermediate paraffinic region (light blue) and the terminal paraffinic region (light green) in the toroidal domain.

The interaction among bicelles is described by the same model exploited for spherocylinders and described by Equations from 6.16 to 6.22.

Also for bicelles we can set up important constraints that allow to properly describe the relationships among the model parameters and hence avoiding an over fitting of the SAXS data.

First, we write equations defining the mono-RL aggregation numbers $N_{agg,c}$ and $N_{agg,h}$ of flat and toroidal domains. For the flat domain, we have

Equation 6.31

$$\begin{cases} 2\pi\left(R_{2,c} + R_{3,c}\right)R^2 = N_{agg,c}(v_2 + v_3) \\ 2\pi R_{2,c} R^2 = N_{agg,c}(v_2 x_{2,c} + v_3 x_{3,c}) \end{cases}$$

where $v_2 = n_{CH_2}v_{CH_2}$ and $v_3 = n_{CH_3}v_{CH_3}$ are the volumes of all the methylene and all the methyl groups of one mono-RL molecule, respectively. As for di-RL, also for mono RL we have $n_{CH_2} = 12$ and $n_{CH_3} = 2$. In order to take into account the conformational disorder of the two hydrophobic chains, that could differ on going from flat to toroidal domains, we have introduced two fractions, $x_{2,c}$ and $x_{3,c}$, which represent the volume fractions of v_2 and v_3 that are associated to the intermediate layer. Conversely, $1 - x_{2,c}$ and $1 - x_{3,c}$, represent the volume fractions of v_2 and v_3 associated to the terminal layer. For ordered chains, we expect $x_{2,c} \approx 1$ and $x_{3,c} \approx 0$. On the other hand, for completely disordered chains, both intermediate and terminal layers should have the same composition, hence we expect $x_{2,c} \approx x_{3,c} \approx \frac{1}{2}$. The system in Equation 6.32 can be solved, assuming as independent variables R, the sum $R_{23,c} = R_{2,c} + R_{3,c}$, $x_{2,c}$ and $x_{3,c}$, in terms of $N_{agg,c}$, $R_{3,c}$ and $R_{2,c}$,

Equation 6.32

$$N_{agg,c} = \frac{2\pi R^2 R_{23,c}}{v_2 + v_3}$$

$$R_{2,c} = R_{23,c}\frac{v_2 x_{2,c} + v_3 x_{3,c}}{v_2 + v_3}$$

$$R_{3,c} = R_{23,c}\frac{v_2(1 - x_{2,c}) + v_3(1 - x_{3,c})}{v_2 + v_3}$$

We can also derive the area per polar head of mono-RL in the flat domain of the bicelle, $a_c = \frac{v_2 + v_3}{R_{23,c}}$.

Second, regarding the toroidal domain, we can define similar volumetric constraints that involve the sum of intermediate and terminal shells and the intermediate shell,

$$\begin{cases} \dfrac{4\pi\left(R_{2,h} + R_{3,h}\right)^3 + 3\pi^2\left(R_{2,h} + R_{3,h}\right)^2 R}{3} = N_{agg,h}(v_2 + v_3) \\[3mm] \dfrac{4\pi\left(R_{2,h} + R_{3,h}\right)^3 + 3\pi^2\left(R_{2,h} + R_{3,h}\right)^2 R}{3} - \dfrac{4\pi R_{3,h}^3 + 3\pi^2 R_{3,h}^2 R}{3} = N_{agg,h}(v_2 x_{2,h} + v_3 x_{3,h}) \end{cases}$$

Also in this case, assuming to independently select R, $R_{23,h} = R_{2,h} + R_{3,h}$, $x_{2,h}$ and $x_{3,h}$, by solving a third degree polynomial resulting from the system of Equation 6.33, we derive

$$N_{agg,h} = \frac{4\pi R_{23,h}^3 + 3\pi^2 R_{23,h}^2 R}{3(v_2 + v_3)}$$

$$R_{3,h} = D^{\frac{1}{3}} + \frac{B^2}{9 \times A^2 \times D^{\frac{1}{3}}} - \frac{B}{3 \times A}$$

$$R_{2,h} = R_{23,h} - R_{3,h}$$

where, for the sake of simplicity, we have introduced the following working parameters

$$A = \frac{4}{3}\pi,$$

$$B = \pi^2 R,$$

$$C = A R_{23,h}^3 + B R_{23,h}^2 - N_{agg,h}\left(v_2 x_{2,h} + v_3 x_{3,h}\right)$$

$$D = \frac{\sqrt{C} \times \sqrt{27 \times A^2 \times C - 4 \times B^3}}{2 \times 3^{\frac{3}{2}} \times A^2} + \frac{27 \times A^2 \times C - 2 \times B^3}{54 \times A^3}$$

To note, also in this case the two parameters $x_{2,h}$ and $x_{3,h}$ represent the volume fractions of v_2 and v_3 that are associated to the intermediate shell in the toroidal domain.

Regarding the hydrated polar region of the flat domain, we can immediately write an equation that relates the geometrical parameters of the flat part of the bicelle with volumetric parameters of one hydrated molecule of mono-RL

Equation 6.35

$$2\pi R_{1,c}R^2 = N_{agg,c}\left(v_p + \frac{n_{w,c}v_w}{d_c} + \varphi_{Na}\alpha_{Na,c}v_{Na}\right),$$

where $v_p = 374.79$ Å^3 is the calculated molecular volume of the polar head of mono-RL. To note, for the mono-RL molecule containing one carboxylic group with p$K_a = 5.5$, at pH=7.5, the nominal number of sodium counterions is

Equation 6.36

$$\varphi_{Na} = \frac{10^{-pH}⊠K_w + K_aK_w + C_m⊠10^{-pH}⊠K_a - 10^{-3pH} - 10^{-2pH}⊠K_a}{C_m⊠10^{-pH}⊠(K_a + 10^{-pH})} \approx \frac{⊠K_a}{K_a + 10^{-pH}},$$

C_m being the molar concentration of mono-RL before the lyophilisation. Accordingly, we have found $\varphi_{Na} = 0.99$.

Equation 6.35 allows to express, for example, the number of water molecule per polar head, $n_{w,c}$, as a function of their mass density d_c, of the thickness of the polar region, $R_{1,c}$, and of the fraction of Na$^+$ counterions remaining among the heads, $\alpha_{Na,c}$.

Likewise, for the toroidal domain, we can derive an equation the relates the geometrical thickness with the molecular volume of the polar head of mono-RL, v_p, the number of water molecules *per* polar head, $n_{w,h}$, the relative mass density of such water molecules, d_h, and the fraction $\alpha_{Na,h}$ the sodium counterions that remains among the polar heads,

Equation 6.37

$$\frac{4\pi\left(R_{1,h} + R_{23,h}\right)^3 + 3\pi^2\left(R_{1,h} + R_{23,h}\right)^2 R}{3} - \frac{4\pi R_{23,h}^3 + 3\pi^2 R_{23,h}^2 R}{3} = N_{agg,h}v_1$$

$$v_1 = v_p + \frac{n_{w,h}v_w}{d_h} + \varphi_{Na}\alpha_{Na,h}v_{Na}.$$

This equation can be solved, for example, by deriving $n_{w,h}$ once $R_{1,h,}d_h$ and $\alpha_{Na,h}$ have been independently selected.

All these parameters, allow to calculate the electron densities, according to the same equations used of spherocylinders (Equation 6.28) by considering the number of electrons of the mono-RL polar head as large as e_p =162. The derived area per polar head of mono-RL in the toroidal domain is

$$a_h = 6\pi(v_2 + v_3)\left(R_{1,h} + R_{23,h}\right) \frac{\pi R + 2\left(R_{1,h} + R_{23,h}\right)}{4\pi R_{23,h}^3 + 3\pi^2 R_{23,h}^2 R}.$$

Based on the same point of view used for the spherocylinders, the diameter σ of the HS sphere that describes the HSDY potential between two bicelles is a parameter that can neither be greater than the total length of the bicelle nor be less than the height of its flat domain. We have then calculated σ according to this equation

$$\sigma = 2\left(R_{1,c} + R_{2,c} + R_{3,c}\right)\gamma + 2(R + R_{1,h} + R_{2,h} + R_{3,h})(1 - \gamma)$$

where γ is a fit parameter that can vary between 0 and 1.

We finally note that the molar concentration C of bicelles is related to the molar concentration C_m of mono-RL by the simple relation $C = C_m/N_{agg}$, where $N_{agg} = N_{agg,c} + N_{agg,h}$.

6.5.4.1 Global fit of SAXS data

In order to derive in an efficient fashion the model parameters, it is preferable to fit with a unique calculation a set of SAXS curves measured for the same kind of sample and for some chemical−physical conditions. In this way it is possible to define parameters that are common to all the curves (common fitting parameters) and other fitting parameters that own to a single-curve (single-curve parameters). In our models (spherocylinders or bicelles), we have selected as common parameter only the volume of the methylene group, v_{CH_2}, and the ratio between the volume of the methyl group and the one of the methylene group, r_{13}. All the other parameters have been considered single-curve parameters. However, in order to increase the robustness of SAXS data analysis and avoid unlikely oscillations of the structural as well as scattering parameters when the physical-chemical conditions of two samples are very close, we have exploited a regularization algorithm [38,40Nanostar]. On this framework, the ensemble of SAXS curves, recorded for either mono-RL or di-RL samples have been simultaneously analyzed performing the minimization of the following score function

Equation 6.40

$$H = \chi^2 + \alpha\Psi$$

where χ^2 is the classical reduced chi square of the set of N_m SAXS curves,

Equation 6.41

$$\chi^2 = \frac{1}{N_m}\sum_{q=1}^{N_m}\frac{1}{N_m}\sum_{i=1}^{N_{q,m}}\frac{1}{N_{q,m}}{}^2\left(\frac{\frac{d\Sigma}{d\Omega_{m,ex}}(q_i) - \frac{d\Sigma}{d\Omega_{m,th}}(q_i)}{\sigma_m(q_i)}\right)^2$$

$N_{q,m}$ being the number of points of the m-experimental scattering curve, $\frac{d\Sigma}{d\Omega_{m,ex}}(q_i)$, with experimental uncertainty $\sigma_m(q_i)$, that should be fitted by the theoretical SAXS curve $\frac{d\Sigma}{d\Omega_{m,th}}(q_i)$. The second term of Equation 6.40 represents the regularization factor,

Equation 6.42

$$\Psi = \sum_{i=1}^{N_s}\sum_{m=1}^{N_m}\left(1 - \frac{X_{i,m'}}{X_{i,m}}\right)^2$$

in this equation, $X_{i,m}$ represent the i-th, among N_s, single-curve fitting parameters used to fit the m-th curve and $X_{i,m'}$ the parameter of the same kind used to fit the m'-th curve. This m'-th curve is that of the sample which has the chemical-physical characteristics (RL concentration or NaCl concentration, see the next Section) most similar to those of the sample of the m-th curve. The constant α is selected in such a way that near the end of the minimization, when $\chi^2 \approx 1$, the product $\alpha\Psi$ is 10-20% of χ^2. By repeating several times (typically 50 times) the minimization of H, the standard deviations of all fitting parameters can be estimated.

6.5.5   SAXS results

6.5.5.1   SAXS of di-RL

SAXS curves of di-RL samples recorded at the I22 beamline are shown in Figure 6.14 in the form of log-log plots. To note, the WAXS branches are easily identifiable at high q, as they show a lower standard deviation. On the other side, at very low q, corresponding to the region of the 2D detector closer to the beam-stop (a region that will be described by a small number of pixels – some of them have indeed been masked in order to avoid to take into account spurious reflections) the points are affected by a higher error bar.
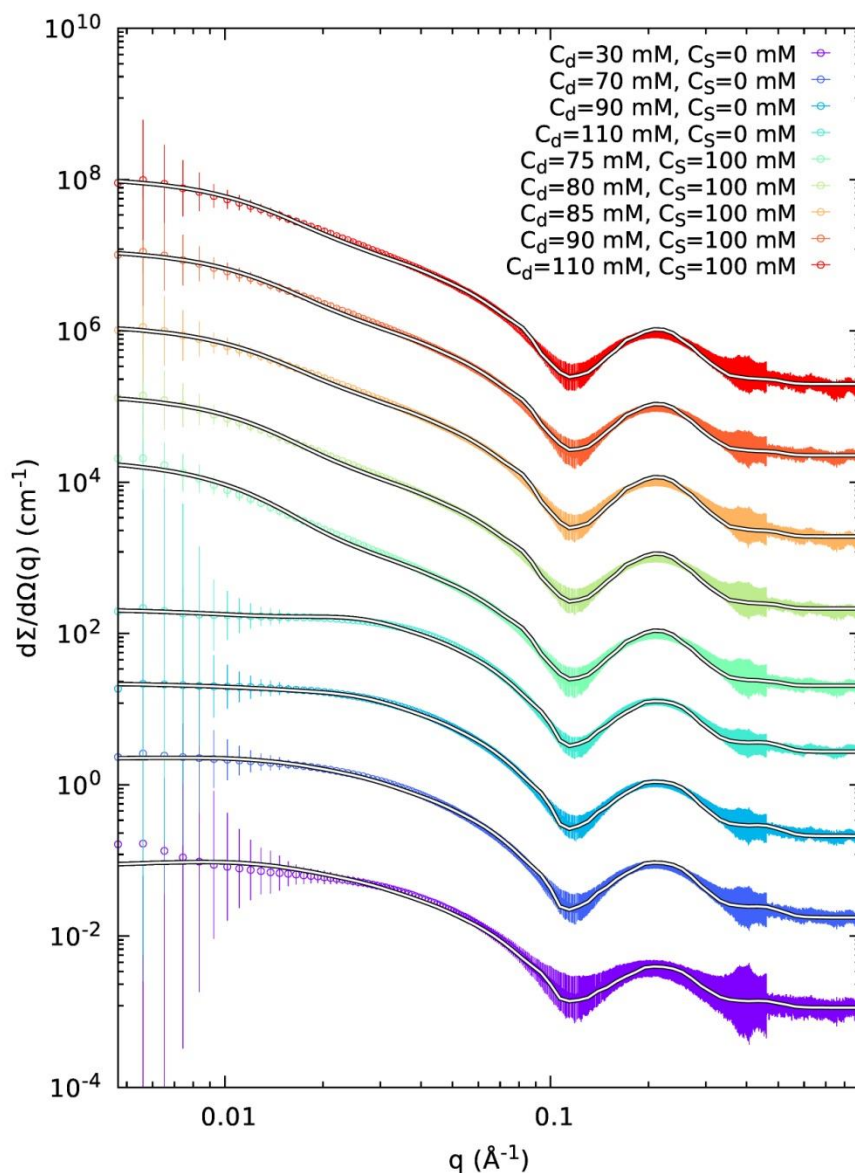
Figure 6.14 Log-log plot of SAXS curves of di-RL samples and their best fits (black and white solid lines) obtained with the spherocylinder model. Curves have been stacked by a factor 10k, where k is the index of the curves, starting from the one at the bottom with $k=0$.

Results clearly show that the presence of 100 mM NaCl (first five curves from the top) mainly modifies the low q region, which show a positive deviation with respect to the flat behaviour, as seen for the curves in the absence of NaCl (first four curves from the bottom), which is typical of non-interacting particles. This characteristic of the experimental data has led to exploit a fit model that includes the effect of the interaction between the particles, described by the structure factor.

The solid black and white lines in Figure 6.14 represent the best fits that we have obtained with the spherocylinder model, introduced in Section 6.5.3. All curves have been fitted by a unique calculation,

with the regularization method introduce above. Final values of the merit function H, the reduced chi squared χ^2 and the regularization term $\alpha\Psi$, obtained with $\alpha = 10^{-2}$, are 0.81, 0.75 and 0.06, respectively. The two common fitting parameters found by Genfit are $v_{CH_2} = 27.0 \pm 0.3$ Å^3 and $r_{13} = 1.97 \pm 0.02$, completely in line with literature values.
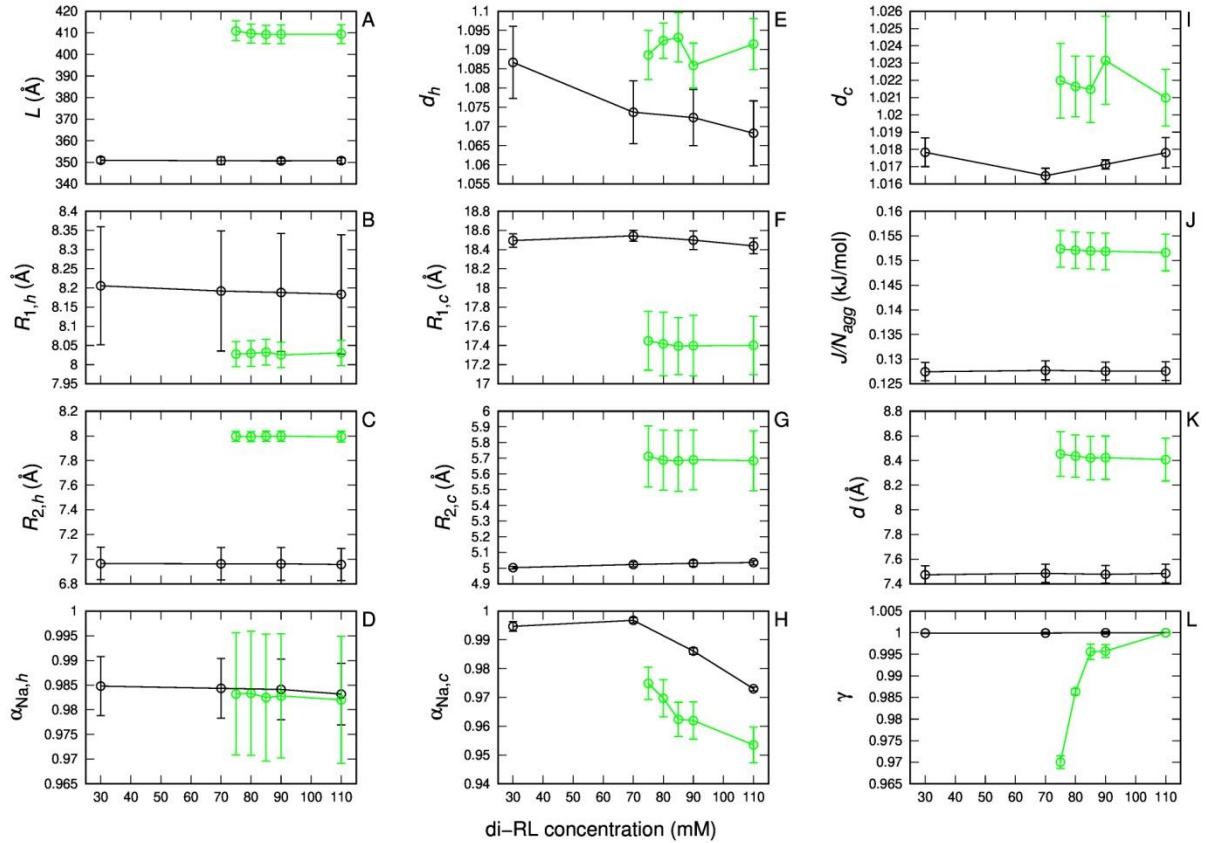
Figure 6.15 Single-curve fitting parameters of the SAXS analysis of di-RL samples in pure water (black points connected by lines) and in 100 mM NaCl (green points connected by lines) reported as a function of di-RL concentration.

All the single-curve fitting parameters are shown in Figure 6.15, panels A-L, where black points refer to samples without NaCl and green point to the ones with 100 mM NaCl. We first notice that the length of the cylinder (panel A) is quite large and changes from approximatively 350 Å for samples without sodium chloride to 410 Å in the presence of sodium chloride. The thickness of the polar heads in the hemi-cap domain, $R_{1,h}$ (panel B), is ≈ 8.1 Å and slightly decreases with in the presence of 100 mM NaCl. Otherwise, the thickness of the paraffinic region in the two hemispheres, $R_{2,h}$ (panel C) depends on the presence of NaCl, passing from ≈ 6.9 Å in its absence to ≈ 8.0 Å at 100 mM NaCl. More pronounced are the differences caused by the presence of NaCl regarding the cylindrical domain: the thickness of the polar heads, $R_{1,c}$ (panel F), is ≈ 18.5 Å when this salt is absent and $\approx$

17.4 Å in its presence. Regarding the thickness of the paraffin chains, $R_{2,c}$ (panel G), it changes from ≈ 5.0 Å to ≈ 5.7 Å when NaCl passes from 0 to 100 mM. To better clarify the results obtained, we have drawn in Figure 6.16 the profile of two spherocylinders with dimensions equal to those obtained for the first sample without NaCl and the last sample with NaCl.
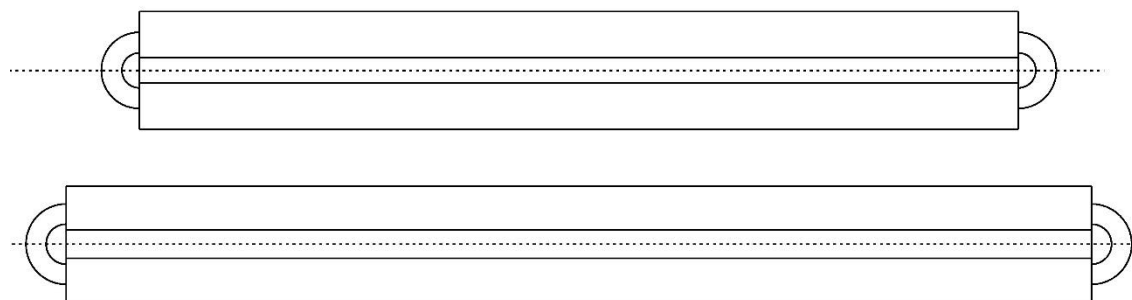
Figure 6.16 Representation of the spherocylinder geometries obtained by SAXS data analysis of 30 mM di-RL at 0 mM NaCl (top) and of 110 mM di-RL 100 mM NaCl (bottom).

We also note that the sodium counterion fractions per polar head in both the hemispherical caps and in the cylindrical domain ($\alpha_{\text{Na},h}$ and $\alpha_{\text{Na},c}$, respectively, panels D and H) are very close to 0.98. It should be considered that We should consider that the considerable change in the ionic strength of the solution influences the value of the Debye constant and therefore the contribution of the repulsive potential, which becomes less relevant at 100 mM NaCl. However, observing the behaviour of the parameter J per di-RL molecule (panel J), which measures the attractive energy at contact, we note that it is not constant but changes with the concentration of NaCl, passing from ≈ 0.128 kJ/mol in its absence to ≈ 0.152 kJ/mol when this salt is present. Even within the limits of the MSA approximation and the HSDW potential adopted, this result indicates that in the presence of NaCl not only a lower Coulomb repulsion occurs but to this is added a greater attraction energy, albeit at long range, between the spherocylinders, probably caused by the formation of ionic pairs or to the modification of the water structure provided by NaCl. Overall, the change in these physical parameters, which were quantitatively derived from the SAXS data analysis, justifies the marked positive deviation at low q of SAXS curves in the presence of NaCl, as discussed above.
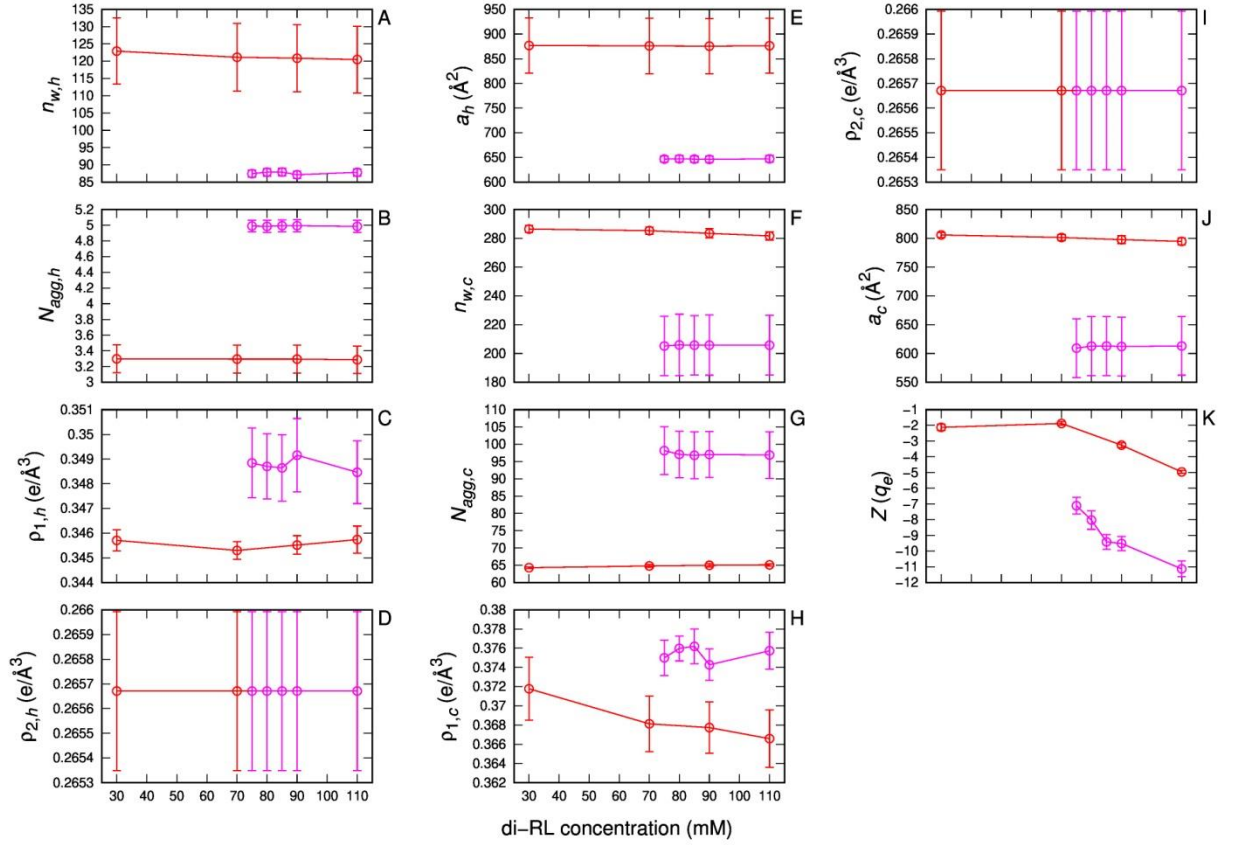
Figure 6.17 Derived parameters from the SAXS analysis of di-RL samples in pure water (red points connected by lines) and in 100 mM NaCl (magenta points connected by lines) reported as a function of di-RL concentration.

The other information that may be extracted from the global-fit is the set of the so-called derived parameters, which depend on the set of the fitting parameters optimized by Genfit. The whole set of such parameters is reported in a graphical form in Figure 6.17 (panels A-K), where, similarly to Figure Y, they are reported as a function of the di-RL concentration. Red points refer to the data without NaCl, magenta point to the ones with 100 mM NaCl. We can observe that a quite huge amount of water per polar head, in the absence of NaCl, is contained in the polar region of the hemispherical domain ($n_{w,h} \approx 122$, panel A) and an higher number in the cylindrical domain ($n_{w,c} \approx 290$, panel F). These number significantly decrease at 100 mM NaCl, becoming $n_{w,h} \approx 87$ (panel A) and $n_{w,h} \approx 210$ (panel F). These result are due to the high curvature of the spherocylinder combined with large values of the thicknesses $R_{1,h}$ and $R_{1,c}$. Coherently with these features, also the areas of the hydrated polar head attributed to each di-RL molecule are large, $a_h \approx 870$ Å^2 (panel E) and $a_c \approx 800$ Å^2 (panel E) at 0 mM NaCl whereas at 100 mM NaCl we found $a_h \approx 650$ Å^2 and $a_h \approx 610$ Å^2. We have also derived the areas per molecule, in both kind of domains, at the interface between polar and hydrophobic regions, according to the expressions $a_{h,\text{interface}} = 4\pi R_{2,h}^2/N_{agg,h}$ and $a_{c,\text{interface}} =$

$2\pi R_{1,c}L/N_{agg,c}$. We have calculated the average values over the values calculated at different di-RL concentrations. As a result, we have obtained, in the absence of NaCl, $a_{h,\text{interface}} = 184.9 \pm 0.1$ Å^2 and $a_{c,\text{interface}} = 170.8 \pm 0.5$ Å^2, whereas at 100 mM NaCl we have $a_{h,\text{interface}} = 161.0 \pm 0.1$ Å^2 and $a_{c,\text{interface}} = 150.8 \pm 0.3$ Å^2. The values of the electron densities (panels C-D and H-I) are totally in line for literature date of highly hydrated surfactants. Finally, in panel K we report the net charge Z of the whole spherocylinder, which is a function of both the overall aggregation number and the fractions $\alpha_{\text{Na},c}$ and $\alpha_{\text{Na},h}$: at 0 mM NaCl Z is small and slightly varies -2 to -4 as a function of di-RL concentration; at 100 mM NaCl, Z is higher (in absolute value) and changes with di-RL concentration from -7 to -11. As a matter of act, the long range pair potential between two spherocylinders at 0 mM NaCl is mostly repulsive and not negligible also at large distances, whereas it becomes attractive at 100 mM NaCl, as it can be seen in Figure 6.18.
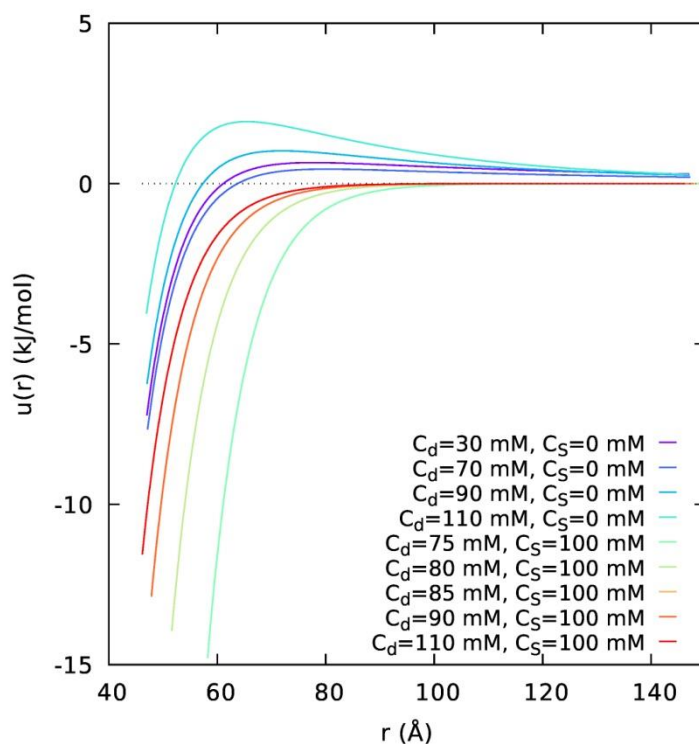
Figure 6.18 Pair potential between two spherocylinders derived by the analysis of di-RL SAXS data.

6.5.5.2   SAXS of mono-RL

Log-log plots of the SAXS curves recorded at Diamond (I22 beamline) for mono-RL samples are shown in Figure 6.19.
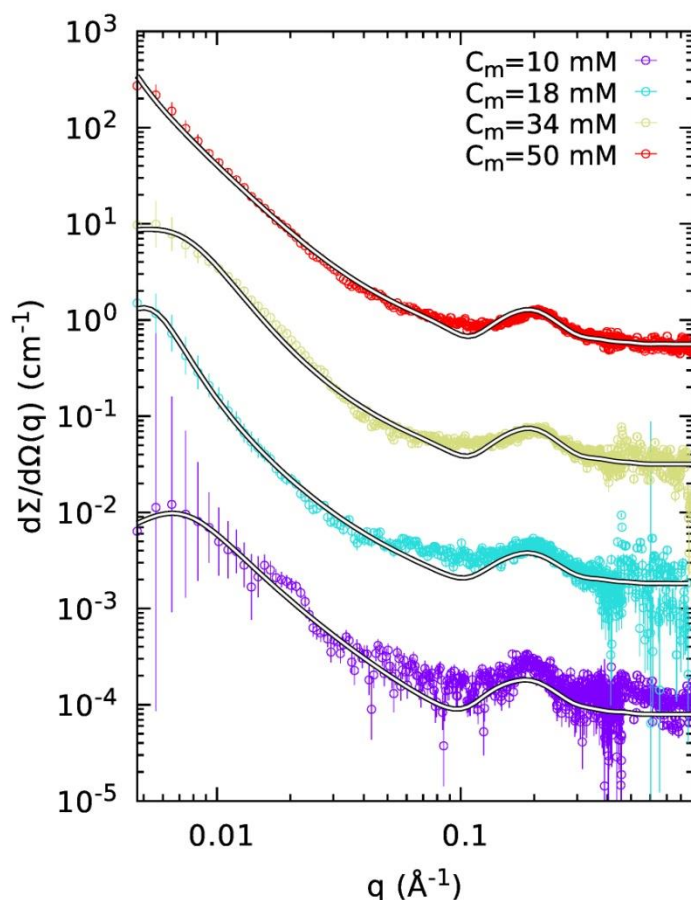
Figure 6.19 Log-log plot of SAXS curves of mono-RL samples and their best fits obtained with the bicelle model. Curves have been stacked by a factor 10k, where k is the index of the curves, starting from the one at the bottom with k=0.

We first observe that at low q the behaviour of the curves does not follow a q^{-2} trend, typical of infinite or large bilayer, that should have determine a linear trend in the log-log plot. On the contrary a broad peak is present, whose feature changes by increasing mono-RL concentration. On the other hand, at intermediate q, a typical flat bilayer band due to the electron density contrasts is clearly present. On the basis of these observations, and after having attempted to analyze the data with different types of micellar aggregates, we have been able to verify that the model that best fits the SAXS curves is that of bicelles, as extensively discussed in Section 6.5.4. Indeed, the interference peak at low q can be attributed to the interaction among particles with finite dimensions, bicelles in our case, that have been considered to be randomly oriented in the pure water solution. The global-fit analysis, which includes the regularization method, of all mono-RL SAXS data with this model has led to the best fitting curves shown as solid black and white lines in Figure 6.19. Final values of the merit function H, the reduced chi squared χ^2 and the regularization term $\alpha\Psi$, obtained with $\alpha = 10^{-1}$, are 0.78, 0.75 and 0.03, respectively. The two common fitting parameters found by Genfit are $\nu_{CH_2} =$

27.0 ± 0.3 Å^3 and $r_{13} = 1.97 \pm 0.02$, exactly the same found with the spherocylinder model applied to SAXS data of di-RL.
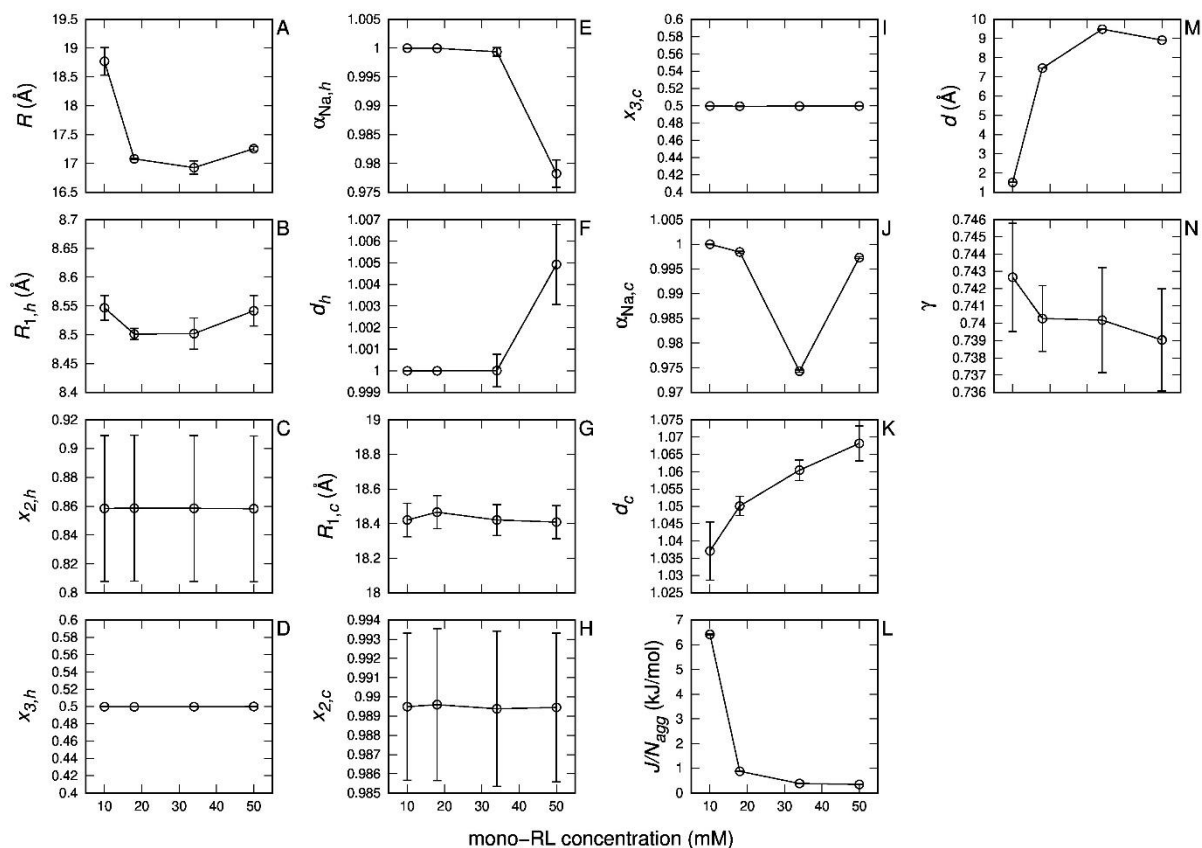
Figure 6.20 Single-curve fitting parameters of the SAXS analysis of mono-RL samples in pure water reported as a function of mono-RL concentration.

The single-curve parameters are shown in Figure 6.20, panels A-N. We first notice that the major radius of the bicelle (R, panel A), corresponding to the radius of the inner cylinder domain, is quite small and decreases as a function of mono-RL concentration from ≈ 19 Å to ≈ 17 Å. The thickness of mono-RL hydrated polar head is almost constant and as large as ≈ 8.5 Å for the rim domain ($R_{1,h}$, panel B) and much higher for the flat domain, $R_{1,c} \approx 18.4$ Å, panel G, suggesting a different arrangements of the polar heads in the two domains. The bicelle geometry with dimension corresponding to the one at 10 mM mono-RL is drawn in Figure 6.21.
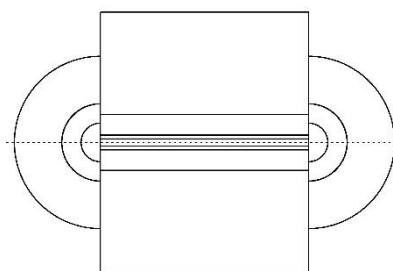
Figure 6.21 Representation of the bicelle geometry obtained by SAXS data analysis of 10 mM mono-RL.

The fractions of methylene and methyl groups in the intermediate and in the terminal regions are $x_{2,h} \approx 0.86$ (panel C) and $x_{2,h} \approx 0.50$ (panel D), indicating a moderate level of conformational disorder of the alkyl chains in the rim. Differently, in the flat domain, a less conformation disorder is found, being $x_{2,c} \approx 0.99$ (panel H) and $x_{2,c} \approx 0.50$ (panel I). A large variation as a function of mono-RL concentration has been found for the depth J per mono-RL molecule of the attractive Yukawian potential, which changes from ≈ 6.4 kJ/mol at 10 mM mono-RL to ≈ 0.3 kJ/mol at 50 mM mono-RL (panel L), this latter value quite similar to the ones recorded for di-RL. In the same manner, the range d of the attractive Yukawian potential greatly changes from ≈ 1.5 Å at 10 mM mono-RL to ≈ 9 Å at 50 mM mono-RL (panel M). It is known that a variation of both J and d with the particle concentration suggests that the interactions between anisometric shaped particles (such as bicelles) are predominantly anisotropic. In our case it could be inferred that there is a preferential stacking interaction between the bicelles and not a purely radial interaction.
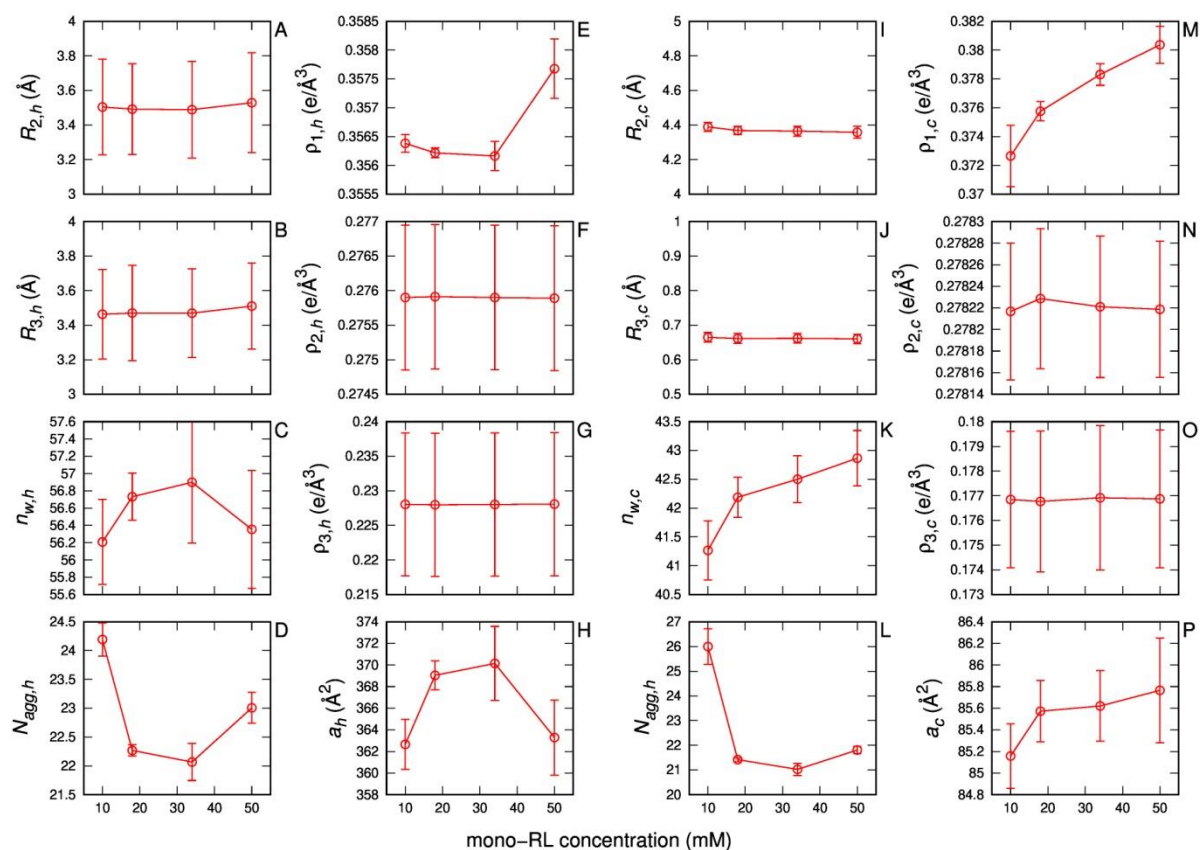
Figure 6.22 Derived parameters from the SAXS analysis of mono-RL samples in pure water reported as a function of mono-RL concentration.

The model parameters derived from the fitting parameters are reported, always as a function of mono-RL concentration, in Figure K (panels A-Q). We notice that the thicknesses of intermediate and terminal regions in the rim domain ($R_{2,h}$ and $R_{3,h}$, panels A and B, respectively) are quite similar and as large as ≈ 3.5 Å. Their sum, $R_{23,h} \approx 7.0$ Å, can be compared with the length $R_{2,h} \approx 7.0$ Å of the two alkyl chains of di-RL, which have the same chemical structure, and that are organized in the form of spherocylinders, according to our SAXS data (see panel C of Figure LL). On the contrary, the thicknesses of the intermediate and the terminal regions of the flat domain of the bicelle, $R_{2,c}$ and $R_{3,c}$ (panel I and J, respectively), are ≈ 4.4 Å and ≈ 0.7 Å, indicating a higher degree of conformational order of the paraffinic chains in the flat geometry in respect to the one in the rim geometry. These features are confirmed by the derived values of the number of water molecules per polar head of mono-RL, whose figure is ≈ 56 in the toroidal domain (panel C), whereas in the flat domain it increases from ≈ 41 at 10 mM mono-RL to ≈ 43 at 50 mM mono-RL. Finally, the obtained values of the areas per polar head in the two domains deserve a comment. In the rim domain, we have found

$a_h \approx 365$ Å² (panel H), whereas in the flat domain we have derived $a_c \approx 85$ Å² (panel P), a value that, in this geometry, should correspond to the area $a_{c,\text{interface}}$ at the interface between polar and hydrophobic regions. On the contrary, in the toroidal domain, the area at the polar/hydrophobic interface can be calculated by the equation

Equation 6.43

$$a_{h,\text{interface}} = 6\pi(v_2 + v_3)R_{23,h}\boxtimes\frac{\pi\boxtimes R + 2R_{23,h}}{4\pi R_{23,h}^3 + 3\pi^2 R_{23,h}^2 R}.$$

The average value calculated of the different mono-RL samples is e $a_{h,\text{interface}} = 132.2 \pm 0.8$ Å², to be compared with the ones of di-RL in the cylindrical and spherical geometry obtained by our SAXS data analysis (Section 6.5.5.1), which read $a_{c,\text{interface}} = 170.8 \pm 0.5$ Å² and $a_{h,\text{interface}} = 189.4 \pm 0.1$ Å², respectively. Finally, in panel Q the net charge Z of the whole bicelle is shown: it is small and varies from -0.5 to -1 as a function of mono-RL concentration. As a consequence, the long range pair potential is mostly attractive, as it can be seen in Figure 6.23.
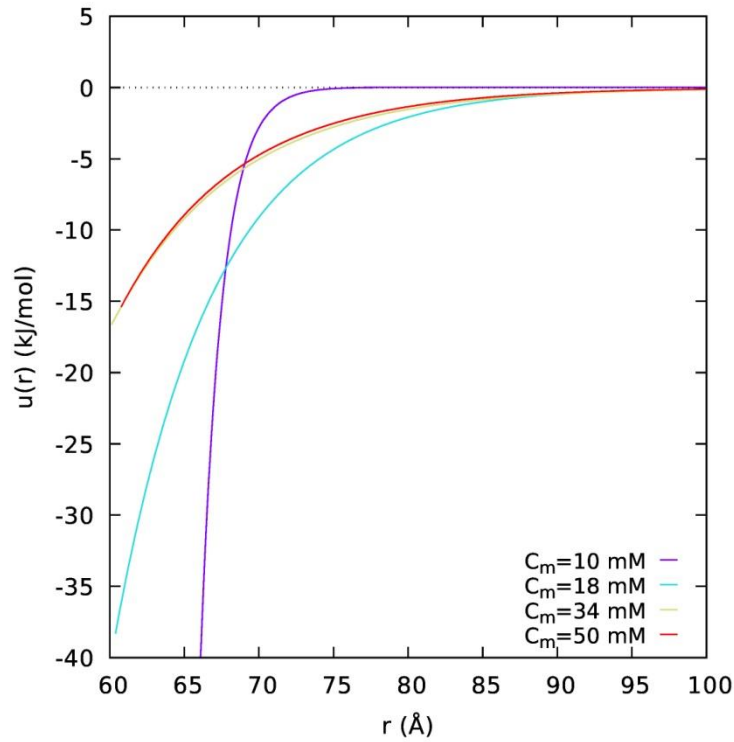
Figure 6.23 Pair potential between two bicelles derived by the analysis of mono-RL SAXS data.

6.5.5.3 Final note on SAXS results

Above their CMC, mono-RL and di-RL form micelles with different shape. For mono-RL, long spherocylinders have been found, with a length in the order of 300 Å, which increases as a function of

NaCl concentration. The micelles of di-RL have the shape of a bicelle, with a small radius in the order of 20 Å. In pure water, both shapes bear a small net negative charge a pH=7.5, since most of the carboxylic group are deprotonated but more the 95% of the sodium counterions remain in the large amount of water that hydrates the polar heads. The area at the polar / apolar regions of the two RLs are similar and their differences can be only attributed at the variations of the curvatures that the molecules show in the different domains of the spherocylinder and the bicelle geometries.

7 Interaction of mono and di-rhamnolipids with lipid bilayers

7.1 Electro formation for the synthesis of GUVs

Performing experiments with simple and ternary GUVs being exposed to mono-RL and di-RL allows investigating the interaction of these biosurfactants with lipid bilayers to understand their impact on plasma membrane.

As I will explain in this Chapter, during my PhD work, ternary GUVs were prepared by electro formation procedure [Come2021] using a combination of lipids DOPC and sphingomyelin with cholesterol (DOPC:SM:CHOL in molar ratio 1:1:1, 3:5:2 and 5:3:2), and also with a single lipid POPC. Totalizing four types of GUVs. After GUVs were prepared, they were mixed with a solution of mono-RL or di-RL at 0.06, 0.12 and 0.25 mM concentrations.

The observations were performed using the polarized optical microscopy technique, in both phase contrast and fluorescence modes, that requires the presence of the fluorescence probe Rho-PE in the membrane, which preferentially partitions into L_d phases [Veatch2005].

To perform observations of the interaction with mono-RL or di-RL, GUVs were prepared using the following lipid molecules and reagents:

- POPC (1-palmitoyl-2-oleoyl-sn-glycero-3-phosphocholine)

Purity degree < 99%

Conservation: -20ºC

MW: 760.100

- DOPC (1.2-di(cis-9-octadecenoyl)-*sn*-glycero-3-phosphocholine)

Purity degree < 99%

Conservation: -20ºC

MW: 786.113

- Sphingomyelin (SM, N-acyl-4-sphingenyl-1-O-phosphorylcholine, N-Acyl-D-sphingosine-1-phosphocholine)

Purity degree < 99%

Conservation: -20°C

MW: 815.241

- Cholesterol (CHOL, 3b-hydroxy-5-cholestene, 5-cholesten-3b-ol)

Purity degree < 99%

Conservation: -20°C

MW: 386.650

- DOPE (Rho-PE, 1,2-dioleoyl-*sn*-glycero-3-phosphoethanolamine)-rhodamine

A dye that emits fluorescence that binds vesicle lipids and allows visualization through the fluorescence microscope of any effects on the GUV that are not visible in the bright field.

MW: 1319.75

Conservation -20°C

- Chloroform

In liquid form.

Molecular formula: $CHCl_3$

MW:119.38

- Sucrose

In solid crystalline form.

Molecular formula: $C_{12}H_{22}O_{11}$

MW: 342.30

- Glucose

In solid crystalline form.

Molecular formula: $C_6H_{12}O_6$

MW:180.16

The solutions used for the electro formation of GUVs were:

- 0.2 M sucrose solution with milliQ water;

- 0.2 M glucose solution with milliQ water;

- POPC + Rho-PE solution 0.1%

- DOPC/SM/CHOL (1:1:1) + Rho-PE (0.1 mol%)

- DOPC/SM/CHOL (3:5:2) + Rho-PE (0.1 mol%)

- DOPC/SM/CHOL (5:3:2) + Rho-PE (0.1 mol%)

These are the instrumentation used for the electro formation of GUVs:

- ITO (coated with indium tin oxide) glass slides. They are glass slides able to conduct electricity on one of the two surfaces and present this darker compared to normal slides precisely following this characteristic

- Menzel-Glaser storage boxes 26 x 76 mm

- Thermo-scientific coverlips 20 x 40 mm, n° 1 thickness

- Hamilton syringes with 10 μl capacity

- Teflon separators

- GW INSTEK current generator – GFG-8015G

- TeKTromix DMM 249 TRUE RMS meter

- Fluorescence microscope

All the lipids, solvents and other chemicals were purchased from Sigma-Aldrich (Sant Louis, MO) and used without further purification.

Preparation of the electroforming chamber

Using a Hamilton syringe, 10 μL of 1.0 g/L total lipid in chloroform solution were taken and spread on the conductive surfaces of two ITO glass slides, forming a thin and uniform layer (Figure 7.1. A). This step is carried out at the environmental temperature to air-dry until complete evaporation of the organic solvent. The conductive glasses were placed with their conductive sides fronting each other, separated by a 2 mm thick Teflon frame made to adhere to the slides and blocked with clamps forming a chamber. Then, this chamber was filled with 1.0 mL of a 0.2 M sucrose solution, injected in the chamber through a small hole present on the side of the Teflon frame. The glass plates were connected to a voltage generator for 2 h with 10 Hz frequency and potential difference of 2 V (Figure 7.1. B).
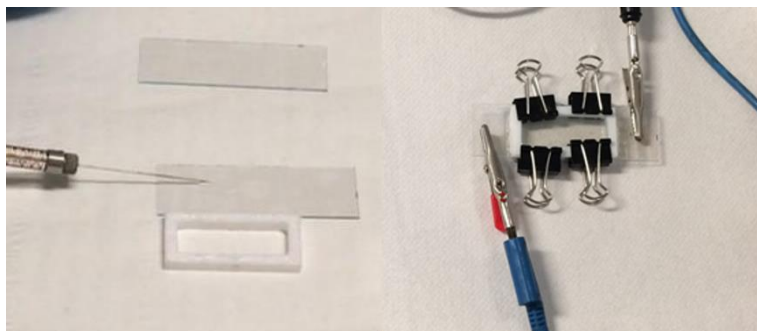
Figure 7.1 Preparation of the electro formation chamber. A: The lipid solution being spread on the surfaces of two ITO glass slides. B: Electro formation chamber connected to a voltage generator

It is important to say that the osmolarities of sucrose and glucose solutions were measured with a cryoscopic osmometer Osmomat 030 (Gonotec, Germany). The osmolarities of the solutions were carefully matched to 0.2 M to avoid osmotic pressure effects and guarantee the optimum visualization on the phase contrast microscope.

The electro formation of GUVs composed of POPC were conducted at room temperature. Although, for the GUVs composed of DOPC:SM:CHOL, the electro formation was conducted at 55°C. Subsequently, these GUVs were left at 4°C overnight and observed the following day.

7.2 Microscope observations of GUVs with mono or di-rhamnolipids

After the preparation, GUVs were observed in the phase contrast and fluorescence modes by means of an inverted microscope Axiovert 200 (Carl Zeiss, Jena Germany). The effect of lipid oxidation was controlled by a low intensity illumination in the fluorescence microscopy to avoid artifacts due to light-induced domain formation by the RHO-probe.

First an observation chamber was prepared using a Menzel-Glaser glass slide 26×76 mm, a 2 mm thick Teflon ring and a 22×22 mm coverslip. The Teflon ring was placed on the glove with the coverslip on it, all sealed with silicone placed on both sides of the Teflon ring forming an observation chamber (Figure 7.2). The chamber must be turned down and pressured to make sure that the three components adhere to each other.

To perform the observations, a solution of 100 mL of electroformed GUVs mixed to 600 mL of a 0.2 M glucose solution containing mono-RL or di-RL was prepared and 1.0 mL was immediately injected in the observation chamber, using an insulin syringe through a hole located on the side of the Teflon ring (Figure 7.2). The observation chamber allowed the GUVs to be in a more stable and an isosmotic medium (glucose 0.2 M), allowing them to be monitored over time.

Figure 7.2 Preparation of the observation chamber.

The observation chamber containing the GUVs was transferred as quickly as possible to the inverted microscope to perform continuous observations using the 60X objective, at temperature 23±2°C.

After mixing glucose 0.2 M with GUVs and specific concentrations of either mono-RL or di-RL, the observation of the vesicles were realized for nearly 20 min, taking one snapshot each second, totalizing 1200 images for each experiment, which were recorded in the computer attached to the microscope. The experiments were performed in triplicate.

Observations of GUVs dispersed only in glucose 0.2 M, without mono-RL or di-RL, were performed as control after each GUV preparation and before starting interaction with mono-RL or di-RL.

The final total lipid w/v concentration was 0.00286 g/L while the molar concentrations of either mono-RL or di-RL were 0.06 mM, 0.12 mM and 0.25 mM. Considering that the final volume to be introduced into the observation chamber is 700 µL and that the mother solution of the mono-RL and di-RL had a concentration of 50 mM, the samples were prepared as shown in Table 7.1.

mono-RL and di-RL (mM)	GUV (µL)	glucose (µL)	mother solution (µL)
0.06	100	0.84	599.16
0.12	100	1.68	598.30
0.25	100	3.50	596.50

Table 7.1 Volumes for the preparation of the GUV samples

7.2.1 Polarized light optical microscopy

Polarized optical microscopy is a technique that employs polarized light to study the microstructure of materials. This technique allows the observation of crystalline and amorphous areas of polymers. In the optical microscope, when the light from the microscope lamp passes through the condenser and

then through the specimen (assuming that the specimen is a light absorbing specimen), some of the light passes both around and through the specimen undisturbed in its path. Such light is called direct light or undeviated light. The background light (often called the surround) passing around the specimen is also undeviated light [Davidson2002].

During my PhD, GUVs were observed in phase contrast and fluorescence modes by means of an inverted microscope Axiovert 200 (Carl Zeiss, Jena Germany) equipped with a Plan Neo-Fluar 63x Ph2 objective (NA 0.75). The images were recorded with an AxioCam HSm digital camera (Carl Zeiss). A mercury lamp HBO 103 W, with excitation and emission filters at 540-552 nm and 575-640 nm in fluorescence mode was used.

The Zeiss Axiovert 200 Inverted Microscope is built for examination of tissue culture flasks, Petri dishes, microtiter plates, etc., in transmitted and reflected light. It can be used for bright field, phase contrast, differential interference contrast, and epi-fluorescence techniques. It is a relatively large microscope, the dimensions are 295×805×707 mm and the weight is approximately 26 kg. As for objectives, we have two of them on this instrument, one has the 10X (objective magnification) and 0.25 (numerical aperture), allowing overall visual magnification of 160X (10X objective magnification x 10X eyepiece magnification x 1.6X Optovar magnification). The second objective is the 40X/1.3 oil objective.
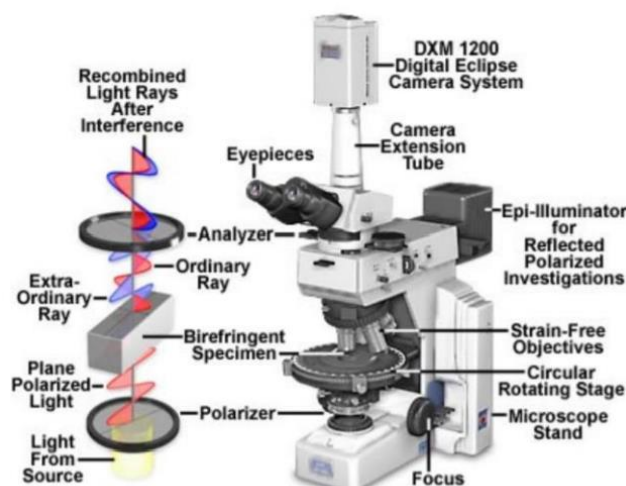
Figure 7.3 Classical configuration of Polarized Optical Microscope

A fluorescence microscope is an optical microscope used to study properties of organic or inorganic substances through fluorescence and phosphorescence instead of scattering, reflection, and attenuation or absorption. A component of interest in the specimen is labeled with a fluorescent molecule called a

fluorophore. The specimen is illuminated with light of a specific wavelength, which is absorbed by the fluorophores, causing them to emit longer wavelengths of light.

The illumination light is separated from the much weaker emitted fluorescence through the use of an emission filter. The typical components of a fluorescence microscope are the light source (xenon arc lamp or mercury-vapor lamp), the excitation filter, the dichroic mirror (or dichromatic beam splitter) and the emission filter. The filters and the dichroic are chosen to match the spectral excitation and emission characteristics of the fluorophore used to label the specimen. In this manner, a single fluorophore is imaged at a time. Multi-color images of several fluorophores must be composed by combining several single color images. These microscopes have become an important part in the field of biology.
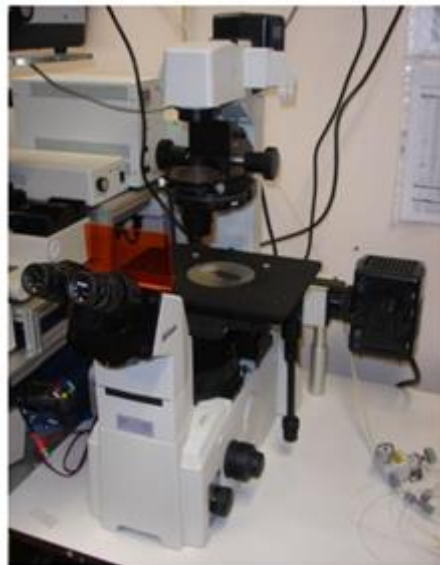
Figure 7.4 The inverted fluorescence microscope (Nikon TE2000) used during my experiments of GUV observations. The orange platform allows the operator to see the sample and, at the same time, protects it from the UV light used for excitation.

7.3 Microscope data analysis of asymmetrical GUVs image

This Section and Section 7.4 will explain the novel methods I used to analyze the images selected from the experiments of GUVs interacting with mono-RL or di-RL. Our study group developed this new method that allowed me to calculate the area (A) and volume (V) of the GUVs as a function of time.

As it was explained before, about 1200 snapshots were recorded for each experiment, as a function of time, after GUVs were mixed with a solution of either mono-RL or di-RL. To analyze the images

taken from the microscope observations, 120 snapshots were chosen from each experiment, selecting the images with a 10 seconds interval. The selected images can be seen in Figures 10.1 to 10.24 in the Appendix (Chapter 10).

The images collected for each sample of GUVs, prepared with a given lipid composition, as function of the time elapsed after the mixing with mono-RL or di-RL at given concentration, which is the $t=0$ time, were analyzed using a novel method that was implemented through a series of macros under the ImageJ software [Schneider2012].

We first developed a method for determining the surface area and volume of distorted or fluctuating circle-shaped GUV that does not show phase separation, that is **homogeneous GUV**.

A second method was developed for detecting the shape of a GUV that undergoes a phase separation process, clearly visible under fluorescence mode microscope observations, that is **two-phase-domain GUVs**. These GUVs, in general, are formed by two phases, whose edges, on average, follow the profile of two distinct arcs of circumference, which, in some cases, can show fluctuations.

First, let us assume that the users manually selected a series of $\{x_i, y_i\}$ points (pixel coordinates saved under ImageJ) around the border of a homogeneous GUV or around each of the two borders of a two-phase-domain GUV.

The purpose of the new method is to find the best smooth contour the passes among these points. To this aim, we assume that the border of the GUV around its center position x_c, y_c can be described by a positive function $r(\theta)$, in polar coordinates, giving the distance of the border from the center as a function of the angle θ formed by the radial direction with the x axis (Figure 7.5, panel A).
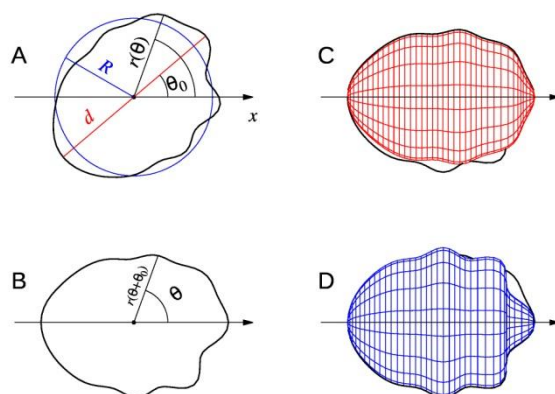
Figure 7.5 Representation of a homogeneous fluctuating GUV.

Clearly, this function must have a 2π periodicity; hence, it is well suited to be expanded in Fourier series,

$$r(\theta) = R\left[1 + \sum_{k=1}^{N_F} a_k \sin(k\theta) + b_k \cos(k\theta)\right]$$

where R is the average radius, N_F is the maximum order of the Fourier expansion and the dimensionless parameters a_k and b_k are the sine and cosine expansion coefficients, according to

$$R = \int_0^{2\pi} r(\theta)d\theta$$

$$a_k = \frac{1}{R}\int_0^{2\pi} r(\theta)\sin(k\theta)d\theta$$

$$b_k = \frac{1}{R}\int_0^{2\pi} r(\theta)\cos(k\theta)d\theta$$

Hence the position and the 2D shape of the GUV domain is mapped in a set of $m=3+2N_F$ parameters: $x_c, y_c, R, \{a_k\}, \{b_k\}$. The optimum values of these parameters are obtained by numerical minimization of the following merit function

$$H = \sum_i (x_i - x_{\text{fit},i})^2 + (y_i - y_{\text{fit},i})^2 + \alpha_F \sum_k a_k^2 + b_k^2$$

$$x_{\text{fit},i} = x_c + r_{\text{fit}}(\theta_i)\cos(\theta_i)$$

Equation 7.7

$$y_{\text{fit},i} \quad = \quad y_c + r_{\text{fit}}(\theta_i)\sin(\theta_i)$$

Equation 7.8

$$\theta_i \quad = \quad \text{atan2}(y_i - y_c, x_i - x_c)$$

where atan2(y,x) is the 2-argument arctangent function [Organick1966]. Notice that the merit function H is the sum between two terms: the squared distance between observed and fitted points and a "regularization" term that avoids large values of a_k and b_k, leading to oversized fluctuations. The relative weight between the two terms is ruled by the α_F parameter that was fixed in order that, at the end of the fit, the regularization term accounts for approximately 10% the first one. By repeating several times the H minimization, we can estimate the standard deviations of all fitting parameters. Some tests of the validity of this method are reported in Figure 7.6.

The red line represents the true contour of the GUV seen by the microscope. Green points $\{x_i , y_i\}$ are the ones selected by the users that could be affected by a 5% error with respect to the position in the red contour. The blue contour is the one obtained as best fit of the green point by the method, and within this blue contour, the magenta points $\{x_{\text{fit},i} , y_{\text{fit},i}\}$ are the best approximations of the green ones. Regarding the red contour, the parameters xc, yc, R, $\{a_k , b_k\}$ have been randomly chose, with $N \le 10$ and $-1000 \le x_c \le 1000$, $-1000 \le y_c \le 1000$, $1 \le R \le 300$, $-0.3 \le a_k \le 0.3$ and $-0.3 \le b_k \le 0.3$. The unit length is assumed to be in μm. The results of Figure 7.4 are very promising, because contours are very similar in all cases, blue and red.
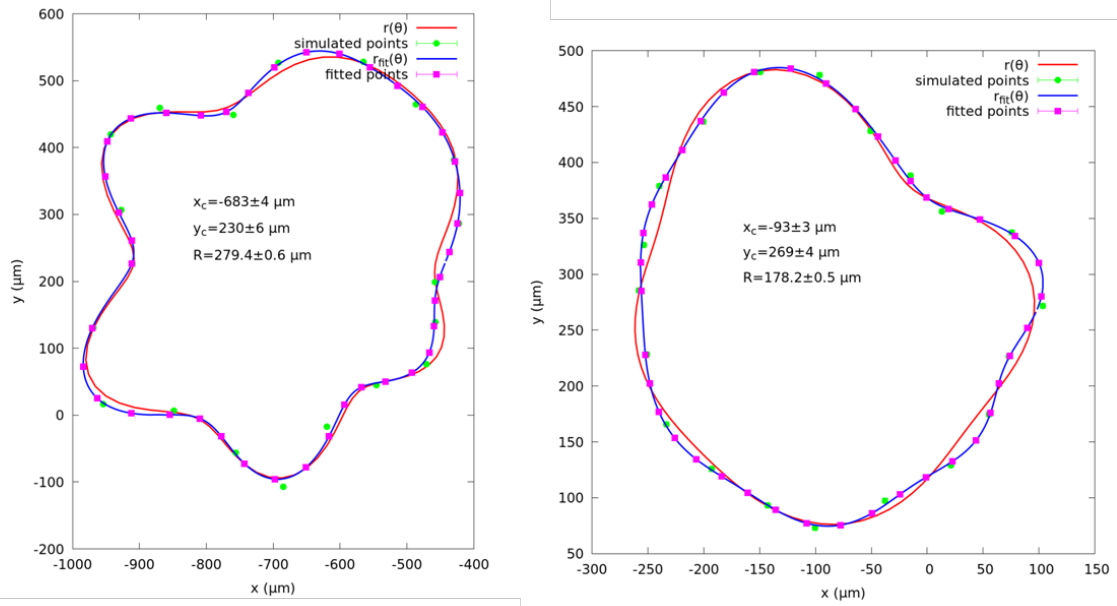
Figure 7.6 . Two selected examples of the determination of the contour of a GUV seen by inverted microscope.

Concerning homogeneous GUVs, the area and the volume are calculated on the basis of $r(\theta)$ by considering the revolution solid generated by a rotation of 2π around the x axis. Since in some circumstances the GUV border can be elongated, in order to avoid an over-estimation of both area and volume of the GUV, before to generate the solid of revolution, the function $r(\theta)$ is rotated around the z axis by the angle - θ_0, θ_0 being the angle formed by the direction of the maximum diameter with the axis x, according to $d=\{r(\theta_0)+r(\pi+\theta_0)\}_{max}$ (Figure 7.5, panels A and B).

On this basis, the homogeneous GUV area and volume are obtained by the well-known expressions of the differential calculus for polar functions,

Equation 7.9

$$A = \pi \int_0^{2\pi} r(\theta + \theta_0) |\sin\theta| \sqrt{r^2(\theta + \theta_0) + \left(\frac{dr(\theta)}{d\theta}\right)^2} \, d\theta$$

Equation 7.10

$$V = \frac{\pi}{3} \int_0^{2\pi} r^3(\theta + \theta_0) |\sin\theta| d\theta$$

Notice that, since, in general, $r(\theta)$ is asymmetric, when the border is rotated by 2π around x, two different solids of revolution are generated (Figure 7.5, panels C and D). Anyhow, it should be remarked that the upper integration bound 2π seen in both Equations 7.9 and 7.10 ensures a correct determination of the average area and the average volume of the two solids of revolution.

102

Now we turn to the case of GUVs that present phase coexistence (two-phase-domain GUVs). The selection by the user of two sets of points $\{x_i, y_i\}$ over the border of the two domains (L_d and L_o, shortly indexed by d and o), will allow to optimize the two corresponding functions $r_d(\theta)$ and $r_o(\theta)$ as well as the coordinates of their centers $x_{c,d}, y_{c,d}$ and $x_{c,o}, y_{c,o}$, which immediately allow to derive the centers' distance, $r_{do} = \sqrt{\{(x_{c,o} - x_{c,d})^2 + (y_{c,o} - y_{c,d})^2\}}$, and the angle θ_0 formed by the direction connecting the two centers with the x axis, $\theta_0 = \text{atan2}(y_{c,o} - y_{c,d}, x_{c,o} - x_{c,d})$ (Figure 7.7, panel A).
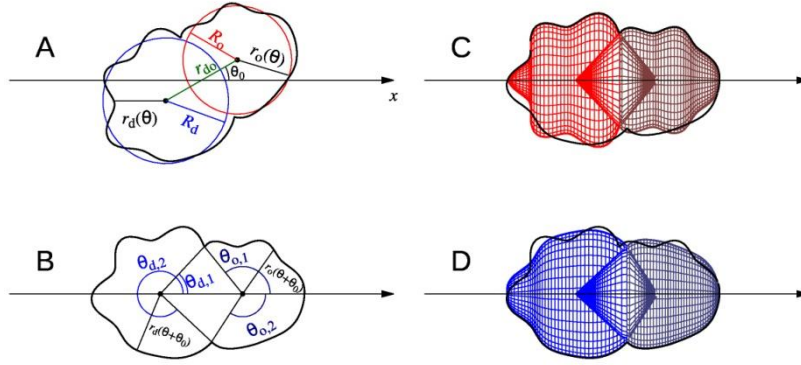
Figure 7.7 Representation of a two-phase-domain fluctuating GUV.

The two lipid domains are not totally separated when there are two points of intersection between the functions that define the two corresponding borders. It can be easily demonstrated that this condition is verified when there are two pairs of real solutions $\theta_{d,j}, \theta_{o,j}$ (with $j=1,2$) of the following equation (Figure 7.7, panel B)

<div align="right">Equation 7.11</div>

$$[r_{do} + r_o(\theta_{o,j} + \theta_0)\cos(\theta_{o,j}) - r_d(\theta_{d,j} + \theta_0)\cos(\theta_{d,j})]^2$$
$$+ [r_o(\theta_{o,j} + \theta_0)\sin(\theta_{o,j}) - r_d(\theta_{d,j} + \theta_0)\sin(\theta_{d,j})]^2 = 0$$

In the example of Figure 7.7, panel B, the four angles $\theta_{k,j}$ are indicated. If there are no real solutions of Equation 7.11, the two domains are totally separated and we take $\theta_{d,1} = \theta_{o,1} = 0$ and $\theta_{d,2} = \theta_{o,2} = 2\pi$. Under these conditions, the area of the α-phase ($\alpha = $ d,o) is

<div align="right">Equation 7.12</div>

$$A_\alpha = \pi \int_{\theta_{\alpha,1}}^{\theta_{\alpha,2}} r_\alpha(\theta + \theta_0) |\sin\theta| \sqrt{r_\alpha^2(\theta + \theta_0) + \left(\frac{dr_\alpha(\theta)}{d\theta}\right)^2} \, d\theta$$

To note, this area corresponds to the average to the areas of the two revolution solids shown in Figure 7.7, panels C and D, which are related to the rotation around the x axis of the function r_α $(\theta+\theta_0)$ (for α = d the two solids are shown in red (panel C) and blue (panel D), respectively; for α = o they are shown in dark-red (panel C) and dark-blue (panel D), respectively). The corresponding volumes are calculated by the integral with bounds $\theta_{\alpha,1}, \theta_{\alpha,2}$, to which the average of volumes of the two cones with radius r_α $(\theta_{\alpha,j}+\theta_0)$ $\sin\theta_{\alpha,j}$ and height $r_\alpha(\theta_{\alpha,j}+\theta_0)|\cos\theta_{\alpha,j}|$ (represented in Figure 7.6, panels C and D, in red and dark-red for α = d and in blue and dark-blue for α = o) should be added. Accordingly, we obtain

<div align="right">Equation 7.13</div>

$$
V_\alpha = \frac{\pi}{3}\left[\frac{1}{2}\sum_{j=1}^{2}r_\alpha^3(\theta_{\alpha,j}+\theta_0)\sin^2\theta_{\alpha,j}|\cos\theta_{\alpha,j}| + \int_{\theta_{\alpha,1}}^{\theta_{\alpha,2}}r_\alpha^3(\theta+\theta_0)|\sin\theta|d\theta\right]
$$

The total area and the total volume of the solid of revolution representing the two-phase-domain GUV will clearly be $A=A_d+A_o$ and $V=V_d+V_o$, respectively.

7.4 Kinetic model of GUV:RL interaction

Let us now consider the specific GUV that is observed under the microscope as a function of the time t after the mixing with a solution of either mono-RL or di-RL. The time evolution of both the GUV area and the GUV volume, derived by the analysis of microscopy images according to Section 7.3, cannot be approximated by simple linear functions, suggesting more complex kinetic processes triggered by the presence of the RLs.

We also notice that, in some cases, the increase of the area is followed by a concomitant increase of the GUV volume, clearly indicating that a not negligible amount of solution has entered into the GUV. In other circumstances, similar to the ones observed by Come et al. [Come2021] for commercial RL samples, the GUV volume remains almost constant, despite the increase of the area, showing that mono-RL and di-RL molecules mostly interact with the outer leaflet, with a small effect on the vesicle integrity.

These observations apply to both homogeneous and two-phase-domain GUVs, in this latter case with distinct effects on L_d and L_o phases. On these bases, we have worked out a basic kinetic model that includes two approaches, for either homogeneous or two-phase-domain GUVs, and that turned out to

be able to quantitatively catch the simple molecular mechanisms ruling the RL:GUV interactions.
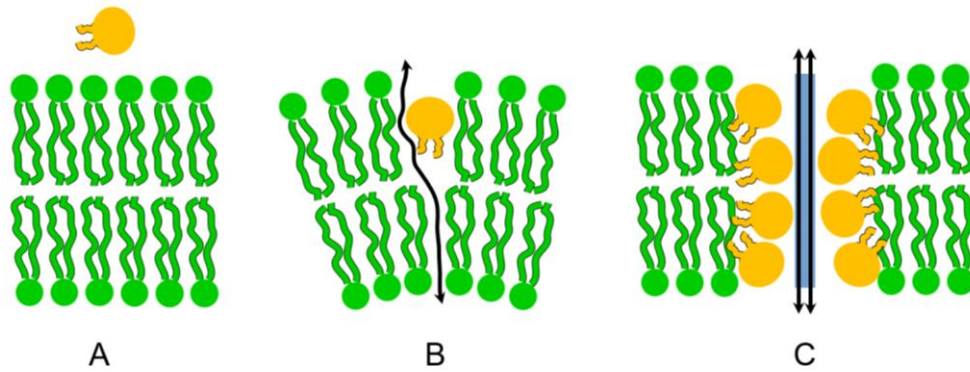
Figure 7.8 Representation of the interaction mechanisms between RLs (orange spheres) and GUVs (green lipids). A: RL-unbound GUV bilayer. B: a RL molecule bound to the outer leaflet of the GUV via first mechanism (RL-insertion). C: aggregated RL molecules on the surface of a pore via the second mechanism referred to as pore formation. The black line on Figure 7.8 panel B is indicative of a tortuous path through which the inner/outer solution exchange would occur due to possible RL-induced increase of the GUV permeability. And the black lines on panel C refer to the easy solution exchange through the pore, here represented by a cyan cylinder with radius r_p and height t_b.

7.4.1 Homogeneous GUVs

We assume that RL molecules interact with the *average lipid molecule* **E** (according to the definitions introduced in Appendix, Section 10.1) constituting the GUV with two equilibrium processes. The first process describes the embedding of free RLs in solution into the outer leaflet of the vesicle, with an increase of the GUV area and a possible increase of the GUV volume, an event that could occur when the inclusion of RLs increases the permeability of the lipid bilayer to the aqueous solution [Haines1994, Chabanon2018]. We refer to this first process as ***RL-insertion*** (Figure 7.8 B).

The second process is an aggregation among the RL molecules already present in the GUV vesicle. This aggregation is necessary for the formation of pores, which are stabilized by the disposal of aggregated RL molecules into the pores' internal surface [Haines1994]. In such a case, marked effects on both GUV area and volume are predictable. We call this second process ***pore formation*** (Figure 7.8 panel C). The two processes are treated as two consecutive and reversible reactions, according to the following kinetic scheme

Equation 7.14

$$m\mathrm{RL} + \mathbf{E} \underset{k_{1-}}{\overset{k_{1+}}{\rightleftharpoons}} \mathrm{RL}_m\mathbf{E}$$
$$n\mathrm{RL}_m\mathbf{E} \underset{k_{2-}}{\overset{k_{2+}}{\rightleftharpoons}} (\mathrm{RL}_m\mathbf{E})_n,$$
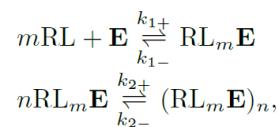
where m and n are the effective kinetic orders of the two processes. Direct and reverse kinetic constants of the first process are k_{1+} (in units of $s^{-1}M^{-m}$) and k_{1-} (in units of s^{-1}), whereas k_{2+} (in units of $s^{-1}M^{1-n}$) and k_{2-} (in units of s^{-1}) refer to the second process. As a result of the two consecutive processes, a fraction f_1 of RL will be dispersed into the GUV through RL-insertion and a fraction f_2 of RL will be involved in pore formation. These fractions can be defined as follows

$$f_1 = \frac{m[\mathrm{RL}_m\mathbf{E}]}{C_{\mathrm{RL}}}$$
$$f_2 = \frac{mn[(\mathrm{RL}_m\mathbf{E})_n]}{C_{\mathrm{RL}}}$$

where C_{RL} is the nominal concentration of RL (corresponding to the concentration of RL in glucose solution at $t=0$, see Appendix, Chapter 10). We also define the total fraction f of RL entered into the GUV, $f=f_1+f_2$. It is easy to express the concentration of RL not bound to the GUV and the concentration of lipid molecule not interacting with RL molecules as follows, $[\mathrm{RL}]=C_{\mathrm{RL}}(1-f)$, $[\mathbf{E}] = C -[1/(m)]C_{\mathrm{RL}}f$, where C is the nominal concentration of lipids. With these definitions, the scheme Equation 7.14 leads to the following system of differential equations,

$$\begin{cases} \frac{d}{dt}f_1 = F_1 - F_2 \\ \frac{d}{dt}f_2 = F_2 \end{cases}$$

where F_1 and F_2 are the following factors

$$F_1 = k_{1+}C_{\mathrm{RL}}^{m-1}(1 - f)^m(mC - C_{\mathrm{RL}}f) - k_{1-}f_1$$
$$F_2 = k_{2+}m^{1-n}nC_{\mathrm{RL}}^{n-1}f_1^n - k_{2-}f_2$$

The solution of the system 7.16 can be performed with numerical methods and allows to derive the two time-functions $f_1(t)$ and $f_2(t)$. These functions are exploited to model the increase, as a function of time, of both GUV area and volume, as seen by the microscope observations. The GUV area at $t=0$ is $A_0=N\,a/2$, where N is the number of lipid molecules that form the GUV lipid bilayer and a is the average area per lipid polar head (see Appendix, Section 10.1, Table 10.1). The area increase due to the first process (RL-insertion) depends on the $f_1(t)$ fraction, according to $A_1(t)=N\,a_{\mathrm{RL}}\,\zeta f_1(t)$, where a_{RL} is the average area of the RL polar head molecule, here considered to be constant, and ζ is the nominal

RL-to-lipid molar ratio.

Also the second process (pore formation) will contribute to the overall increase of the GUV area seen by the microscope observations. For the sake of simplicity, we assume that all pores have the same cylindrical shape, with average radius r_p and lateral area $2\pi r_p t_b$, t_b being the thickness of the bilayer. Each pore will contribute to increase the GUV area by πr_p^2 and will involve an average number of RL molecules corresponding to $n_{RL,p}=2\pi r_p t_b/a_{RL}$. By these assumptions, the GUV area increase due to the pore formation process is $A_2(t)=N\ \zeta f_2(t)\ \pi r_p^2/n_{RL,p}$. In summary, the overall GUV area is modeled by the following equation

$$
\begin{aligned}
A(t) &= A_0 + A_1(t) + A_2(t) \\
&= N\left[\frac{a}{2} + a_{\mathrm{RL}}\zeta\left(f_1(t) + \frac{r_p}{2t_b}f_2(t)\right)\right].
\end{aligned}
$$

The time evolution of the GUV volume depends, in general, on the volume flux $J=(1/A)dV/dt$ of the water solution across the membrane, which, in turn, depends on various factors, including osmotic pressure, membrane elasticity, curvature, permeability and presence of pores as well as on their time variation. However, our experiments do not contain the information necessary to determine all these parameters. Under these conditions, we propose the simple hypothesis that the rate of increase of the GUV volume caused by the first process (RL-insertion) is directly proportional to the rate of increase of the GUV area relative to the same process, $[(dV_1(t))/(dt)] \propto [(d\,A_1(t))/(dt)]$, hence

$$
V_1(t) = \lambda_1 N a_{\mathrm{RL}}\zeta f_1(t),
$$

where λ_1 is a constant with dimensions of a length. Likewise, we assume that the rate of GUV volume increase due to the second process (pore formation) is directly proportional to the corresponding rate of GUV area increase, $[(dV_2(t))/(dt)] \propto [(d\,A_2(t))/(dt)]$, so that

$$
V_2(t) = \lambda_2 N a_{\mathrm{RL}}\zeta\frac{r_p}{2t_b}f_2(t),
$$

where a second constant, λ_2, with dimensions of a length has been introduced. The GUV volume will be

Equation 7.21

$$
\begin{aligned}
V(t) &= V_0 + V_1(t) + V_2(t) \\
&= V_0 + N a_{\mathrm{RL}} \zeta \left[\lambda_1 f_1(t) + \lambda_2 \frac{r_p}{2 t_b} f_2(t) \right]
\end{aligned}
$$

The experimental values of A and V obtained by microscope observations as a function of the time after the mixing of GUV and RL solution can be simultaneously fitted with Eqs.18 and 21. As a result all the kinetic parameters that rule the processes shown in scheme 14 can be derived.

7.4.2 Two-phase-domain GUVs

In the case of GUVs formed by separated L_d and L_o phases, we can extend the previous kinetic model by considering the following four processes that involve RL molecules and both average disordered and average ordered lipid molecules ($\mathbf{E}_d$ and $\mathbf{E}_o$, respectively, see Sect. S2 in SI for details),

Equation 7.22

$$
\begin{aligned}
m_d \mathrm{RL} + \mathbf{E}_d &\underset{k_{d1-}}{\overset{k_{d1+}}{\rightleftharpoons}} \mathrm{RL}_{m_d} \mathbf{E}_d \\
n_d \mathrm{RL}_{m_d} \mathbf{E}_d &\underset{k_{d2-}}{\overset{k_{d2+}}{\rightleftharpoons}} (\mathrm{RL}_{m_d} \mathbf{E})_{n_d} \\
m_o \mathrm{RL} + \mathbf{E}_o &\underset{k_{o1-}}{\overset{k_{o1+}}{\rightleftharpoons}} \mathrm{RL}_{m_o} \mathbf{E}_o \\
n_o \mathrm{RL}_{m_o} \mathbf{E}_o &\underset{k_{o2-}}{\overset{k_{o2+}}{\rightleftharpoons}} (\mathrm{RL}_{m_o} \mathbf{E})_{n_o}
\end{aligned}
$$
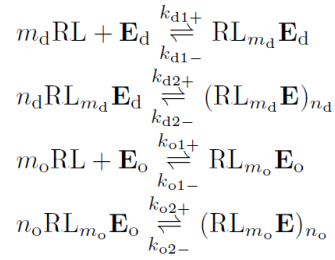
where m_α and n_α are the kinetic orders of RL-insertion (with direct and reverse constants $k_{\alpha 1+}$ and $k_{\alpha 1-}$) and pore formation (with direct and reverse constants $k_{\alpha 2+}$ and $k_{\alpha 2-}$), respectively, occurring in the α-phase (with $\alpha = d,o$). The concentrations of all species involved in the four processes must obey mass balance constraints, according to

Equation 7.23

$$
\begin{aligned}
C_d &= [\mathbf{E}_d] + [\mathrm{RL}_{m_d} \mathbf{E}_d] + n_d [(\mathrm{RL}_{m_d} \mathbf{E})_{n_d}] \\
C_o &= [\mathbf{E}_o] + [\mathrm{RL}_{m_o} \mathbf{E}_o] + n_o [(\mathrm{RL}_{m_o} \mathbf{E})_{n_o}] \\
C_{\mathrm{RL}} &= [\mathrm{RL}] + m_d [\mathrm{RL}_{m_d} \mathbf{E}_d] + m_d n_d [(\mathrm{RL}_{m_d} \mathbf{E})_{n_d}] \\
&\quad + m_o [\mathrm{RL}_{m_o} \mathbf{E}_o] + m_o n_o [(\mathrm{RL}_{m_o} \mathbf{E})_{n_o}].
\end{aligned}
$$

We hence introduce the fractions of RL involved in *RL-insertion* or *pore formation* over both phases,

Equation 7.24

$$f_{d,1} = \frac{m_d[\mathrm{RL}_{m_d}\mathbf{E}_d]}{C_{RL}}$$

$$f_{d,2} = \frac{m_d n_d[(\mathrm{RL}_{m_d}\mathbf{E})_{n_d}]}{C_{RL}}$$

$$f_{o,1} = \frac{m_o[\mathrm{RL}_{m_o}\mathbf{E}_o]}{C_{RL}}$$

$$f_{o,2} = \frac{m_o n_o[(\mathrm{RL}_{m_o}\mathbf{E})_{n_o}]}{C_{RL}}$$

To note, the total fractions of RL bound either to L_d or L_o phases are $f_d = f_{d,1} + f_{d,2}$ and $f_o = f_{o,1} + f_{o,2}$, respectively, whereas the fraction of RL bound to the whole GUV is $f = f_d + f_d$. We can also derive the concentrations of the free RL, lipid disordered and lipid ordered molecules, $[RL] = (1-f)C_{RL}$, $[\mathbf{E}_d] = C_d - [1/(m_d)] f_d C_{RL}$ and $[\mathbf{E}_o] = C_o - [1/(m_o)] f_o C_{RL}$. The system of four processes reported in the scheme Equation 7.22 gives rise to the following system of differential equations,

Equation 7.25

$$\begin{cases} \frac{d}{dt} f_{d,1} = F_1 - F_2 \\ \frac{d}{dt} f_{d,2} = F_2 \\ \frac{d}{dt} f_{o,1} = F_3 - F_4 \\ \frac{d}{dt} f_{o,2} = F_4 \end{cases}$$

where F_j $(j=1,4)$ are the following factors

Equation 7.26

$$F_1 = k_{d1+}(1-f)^{m_d} C_{RL}^{m_d-1}(m_d C_d - f_d C_{RL}) - k_{d1-} f_{d,1}$$

$$F_2 = -k_{d2-} f_{d,2} + k_{d2+} m_d^{1-n_d} n_d f_{d,1}^{n_d} C_{RL}^{n_d-1}$$

$$F_3 = k_{o1+}(1-f)^{m_o} C_{RL}^{m_o-1}(m_o C_o - f_o C_{RL}) - k_{o1-} f_{o,1}$$

$$F_4 = -k_{o2-} f_{o,2} + k_{o2+} m_o^{1-n_o} n_o f_{o,1}^{n_o} C_{RL}^{m_o-1}$$

The system can be solved by numerical methods, allowing the simultaneous determination of the four functions $f_{d,1}(t)$, $f_{d,2}(t)$, $f_{o,1}(t)$ and $f_{o,2}(t)$. Then, on the basis of the same mechanisms invoked for the determination of the time dependency of the GUV area and volume of homogeneous GUVs (see Eqs. 7.18 and 7.21), we can easily derive the area of the α-phase of the GUV,

as well as the volume of the α-phase of the GUV

Equation 7.27

$$
\begin{aligned}
A_\alpha(t) &= A_{\alpha,0} + A_{\alpha,1}(t) + A_{\alpha,2}(t) \\
&= N_\alpha \left[\frac{a_\alpha}{2} + a_{\mathrm{RL}}\zeta_\alpha \left(f_{\alpha,1}(t) + \frac{r_{p,\alpha}}{2t_{b,\alpha}} f_{\alpha,2}(t) \right) \right]
\end{aligned}
$$

Equation 7.28

$$
\begin{aligned}
V_\alpha(t) &= V_{\alpha,0} + V_{\alpha,1}(t) + V_{\alpha,2}(t) \\
&= V_{\alpha,0} + N_\alpha a_{\mathrm{RL}}\zeta_\alpha \left[\lambda_{\alpha,1} f_{\alpha,1}(t) + \lambda_{\alpha,2} \frac{r_{p,\alpha}}{2t_{b,\alpha}} f_{\alpha,2}(t) \right]
\end{aligned}
$$

where the parameters referring to the α-phase have the same meaning as the corresponding ones in Equations 7.18 and 7.21. It is worth noting that the kinetic model for two-phase-domain GUV allows to fit, by a unique calculation, four experimental curves, corresponding to the areas and the volumes of both Ld and Lo GUV phases.

7.5   Analytical method applied to the interaction of GUVs with mono and di-rhamnolipids

Optical microscopy experiments, in both phase contrast and fluorescence modes, were performed on GUVs formed by POPC and three ternary mixtures of DOPC:SM:CHOL (molar ratios 1:1:1, 3:5:2 and 5:3:2). To optimize the optical contrast and to highlight the Ld phases when the microscope is set in fluorescence mode, all experiments were done on samples with 0.2 M glucose solution and in the presence of 0.1 mol % of the fluorescence probe Rho-PE in the membranes, which preferentially interacts with Ld phases.

A first series of microscope observations was performed in the absence of RLs, for the sake of control. Figure 7.9 shows a representative fluorescence mode microscope snapshot for each of the four investigated GUV systems. It is evident that all the GUVs have a spherical shape, indicating the absence of any frustration process by the 0.2 M glucose solution or 0.1 mol % Rho-PE probe.

It is possible to see that both DOPC:SM:CHOL 1:1:1 and 3:5:2 GUVs (Figure 7.9, panels B and C) show Ld-Lo phase coexistence: the brilliant white micro-scale phases are in fact due to the presence of the fluorescence probe Rho-PE inserted in the Ld phase mainly formed by DOPC. Otherwise, DOPC:SM:CHOL 5:3:2 GUVs are homogeneous, that is, do not show Ld-Lo phase coexistence probably because they have mostly DOPC in their composition (Figure 7.9 panel D).
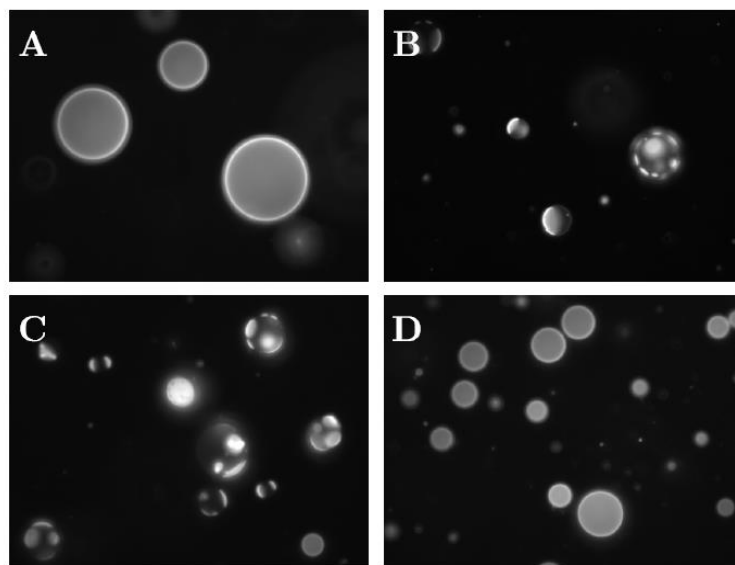
Figure 7.9 . Representative optical microscope images in fluorescence mode of GUVs formed by POPC (A) and DOPC:SM:CHOL in molar ratios 1:1:1 (B), 3:5:2 (C) and 5:3:2 (D) in the presence of 0.2 M glucose.

After doing the control observations, to make sure that the GUVs were well formed, I have carried out experiments with GUVs in the presence of either mono-RL or di-RL. Considering the CMCs determined at 0.2 M glucose, we have chosen, for both RLs, the same concentrations: 0.06, 0.12 and 0.25 mM. Notice that, for mono-RL, 0.06 mM is at CMC, whereas 0.12 mM and 0.25 mM are approximately twice and three times the CMC.

In the following Sections I will report the microscope data results obtained for each of the four GUV systems in the presence of the three concentrations of mono-RL and di-RL as a function of the time elapsed, after mixing GUVs and RLs solutions. In order to get a meaningful comparison between mono-RL and di-RL, I will discuss similarities and differences of the time-resolved effects on the GUVs provoked by either mono-RL or di-RL at the same concentrations.

7.5.1 POPC GUVs with mono and di-rhamnolipids

Microscope images in phase contrast and fluorescence mode of POPC GUVs in the presence of mono-RL and di-RL are reported in Figure 7.10, where panels A, B and C refer to mono-RL and panels D, E and F to di-RL. The bottom row of each panel contains the same snapshots of the top row superimposed with regular or distorted circles obtained by the best contour surrounding the GUVs with the ImageJ macro (see Section 7.3). The concentrations of both RLs are expressed in colors: red for 0.06 mM, green for 0.12 mM and blue 0.25 mM. Each panel shows snapshots of one carefully selected GUV taken at different times. The time is shown in the bottom left corner in seconds, elapsed after mixing GUVs with mono-RL or di-RL solutions, which is time 0 s. These snapshots are aligned

in the top row of each panel and, whenever possible, the first and the last snapshot are the ones taken in fluorescence mode.

It is worth recalling that for each sample almost 1200 snapshots have been recorded and only a few of them are shown in Figure 7.10. However, the shape analysis with the macros has been applied to approximately 120 snapshots for each series (Figures 10.1 to 10.24 on Appendix, Chapter 10).

As described in Section 7.3, for one-phase GUVs images, the shape analysis with the macro finds the best contour that encompasses the GUV and provides its average radius R as well as the area A and volume V of the solid of revolution corresponding to the contour (Eqs.7.9 and 7.10). Figure 7.11 reports, for each of the samples, the parameters R, A and V as a function of the time after mixing the solutions of GUVs and RLs where the label of the panels corresponds to the one used in Figure 7.10.

A detailed analysis of the time-behavior of A and V as a function of time have been analyzed with the kinetic model introduced in Section 7.4, by means of a unique fitting calculation based on Equation 7.21 and 7.22, respectively (solid black line on Figure 7.11) and all the fitting parameters are reported in Table 7.2. By evaluating changes in surface area, volume and permeability of GUVs, it is possible to separate the main roles of mono-RL and di-RL on plasma membrane models.
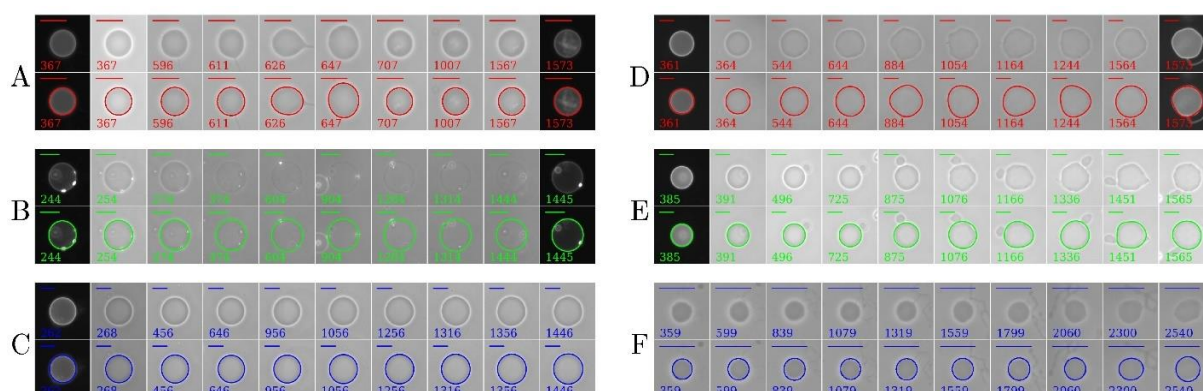
Figure 7.10 Representative POPC GUV fluorescence and phase contrast images dispersed in 0.06 mM (red), 0.12 mM (green) and 0.25 mM (blue)of either mono-RL (panel A, B and C) or di-RL (panel D, E and F). The time sequence, expressed in seconds in the bottom left corner of each image, refers to the elapsed time after mixing RLs with GUV solution, which is time 0 s. The images located above in each panel were superimposed with the best contour surrounding the GUVs determined with the ImageJ macro, which correspond to the images located below. The top left bars span 20 μm.
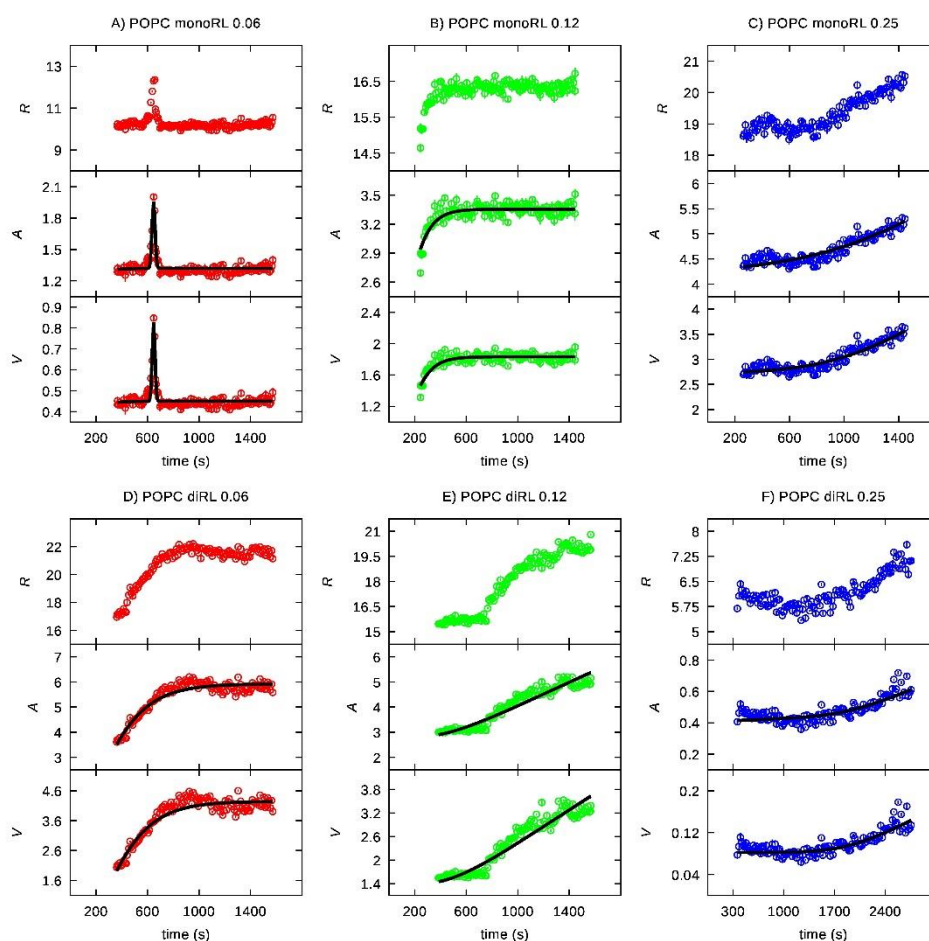
Figure 7.11 Time-dependence of the geometrical parameters of POPC GUVs in the presence of 0.06 mM, 0.12 mM and 0.25 mM (red, green and blue, respectively) mono-RL (panel A, B and C) and di-RL (panel D, E and F). The top plots correspond to GUVs average radius R (μm)

The results of the representative POPC GUV in the presence of 0.06 mM mono-RL are shown in panel A of Figure 7.10 and 7.11. Up to about 640 s, they remain almost constant, indicating negligible morphological changes. Afterward, a sharp increase of the GUV dimension is seen. Subsequently the GUV area returns to the original value preserving the original membrane surface area over time. This behavior indicates that mono-RL molecules are inserted in the membrane, producing an excess surface area and consequently the formation of small micro sized vesicles, called buds (Figure 7.10-A) that quickly burst in order to release the excess area, allowing the GUV to restore its original size [Come2021]. Notice that this rapid burst process has been simply described by two Gaussian functions, which have been added to both A and V (Figure 7.11-A). When exposed to the same concentration of di-RL (0.06 mM, panel D of both Figures 7.10 and 7.11), all parameters R, A and V of the selected GUV increased up to nearly 900 s. Subsequently, the GUV formed buds and shows shape fluctuations, maintaining the morphological changes until the end of experiment (Figure 7.10-D).

The POPC GUV exposed to 0.12 mM mono-RL (panel B on Figure 7.10 and 7.11) kept its initial shape and had a slight increase of its area at the beginning of the experiment, no membrane permeability was observed (visual loss of contrast). As it can be observed in Figure 7.10, panel B, there was the appearance of small dots over the membrane surface (dark dots in phase contrast mode and fluorescent dots in fluorescence mode). It was speculated that such dots must represent complex aggregates composed of lipids, mono-RL and Rho-PE fluorophore molecules with dimensions of a few microns. When mixed with 0.12 mM di-RL (Figure 7.10, panel E), the selected POPC GUV had a different behavior compared to the same concentration of mono-RL, showing fluctuation of shape, formation of buds and increase of size that was kept over time until the end of the observation (Figure 7.11, panel E).

In the experiments performed with 0.25 mM mono-RL, we observe a slight increase of R, A and V (Figure 7.11, panel C). On the contrary, when 0.25 mM of di-RL is added (panel F of Figure 7.10 and 7.11), the POPC GUV shows fluctuation of shape, formation of buds and increase of size, as it happens before with the addition of smaller concentrations of di-RL. Experiments with 0.25 mM di-RL indicates a more significant increase of R, A and V than the one seen in the presence of 0.25 mM of mono-RL. Besides, with 0.25 mM di-RL, the vesicles form buds and lose of visual contrast (Figure 7.10-F). This effect may indicate membrane permeabilization, leading to by glucose-sucrose exchange between inner and outer GUV compartments [Come2021].

It is possible to evaluate results obtained by fitting A and V time-trends with the kinetic model, which involves two RL:GUV mechanisms, free insertion and pore formation (Table 7.2). Regarding the parameter λ_{1d}, which measures the POPC GUV permeability via the free insertion mechanism ($f_1(t)$), from mono-RL to di-RL the values strongly changed from $\approx 3 \cdot 10^{-2}$ to $2 \cdot 10^{-5}$, indicating a very different effect provided by the two RLs species on the POPC membrane, confirming that di-RL interacts more strongly with these GUVs than mono-RL.

		mono-RL 0.06		mono-RL 0.12		mono-RL 0.25		di-RL 0.06		di-RL 0.12		di-RL 0.25	
		A		B		C		D		E		F	
1	N_d (10^9)	0.50	± 0.02	0.96	± 0.04	13.4	± 0.1	0.60	± 0.02	8.5	± 0.3	1.28	± 0.01
2	$V_{d(0)}$ ($10^4\ \mu m^3$)	0.021	± 0.007	0.017	± 0.003	2.72	± 0.03	0.021	± 0.004	1.38	± 0.03	0.0822	± 0.0008
3	λ_{1d} (μm)	0.035	± 0.005	0.032	± 0.003	0.030	± 0.003	0.00005	± 0.00002	0.00001	± 0.00002	0.00005	± 0.00002
4	λ_{2d} (μm)	0.010	± 0.001	0.010	± 0.001	0.0123	± 0.0007	0.0106	± 0.0002	0.0102	± 0.0003	0.0041	± 0.0001
5	r_{pd} (Å)	280	± 50	290	± 40	290	± 50	497	± 5	470	± 10	500	± 5
6	m_d	1.21	± 0.01	1.08	± 0.01	1.99	± 0.08	1.45	± 0.01	1.14	± 0.05	1.39	± 0.01
7	n_d	2.81	± 0.03	2.34	± 0.02	2.90	± 0.09	3.18	± 0.03	3.14	± 0.03	5.67	± 0.08
8	pk_{d1+} ($s^{-1}M^{-md}$)	-3.28	± 0.04	-2.31	± 0.03	-1.9	± 0.2	-3.92	± 0.04	0.20	± 0.03	0.24	± 0.04
9	pk_{d1-} (s^{-1})	6.9	± 0.1	6.76	± 0.07	12.5	± 0.2	11.3	± 0.2	7.6	± 0.2	12.0	± 0.1
10	pk_{d2+} ($s^{-1}M^{1-nd}$)	-12.1	± 0.2	-9.7	± 0.1	-25.0	± 0.6	-19.9	± 0.2	-28.9	± 0.6	-70.1	± 0.7
11	pk_{d2-} (s^{-1})	12.6	± 0.2	10.7	± 0.3	25.2	± 0.7	18.2	± 0.2	21.2	± 0.5	59.1	± 0.8
12	h_A ($10^3\ \mu m^2$)	0.64	± 0.03	–		–		–		–		–	
13	$t_{A,0}$ (s)	647	± 6	–		–		–		–		–	
14	σ_A (s)	12.2	± 0.6	–		–		–		–		–	
15	h_V ($10^4\ \mu m^3$)	0.38	± 0.02	–		–		–		–		–	
16	$t_{V,0}$ (s)	647	± 6	–		–		–		–		–	
17	σ_V (s)	11.1	± 0.5	–		–		–		–		–	

Table 7.2 Parameters obtained by the simultaneous best fit of the POPC GUV area and volume.

Looking at the values calculated for the interaction of mono-RL with POPC GUV (Table 7.2), the direct kinetic constant pk_{d1+} shows a variation from 0.06 mM ($\approx$ -3.28, with k_{1+} expressed in $s^{-1}\ M^{-1.2}$), to 0.25 mM ($\approx$ -1.90), which means that at 0.06 mM the mono-RL interacts more rapidly with membrane by the first mechanism (*RL-insertion*). Interestingly the concentration 0.06 mM is under the CMC, presuming a faster rate interaction mono-RL:GUV before the formation of micelles. The corresponding reverse kinetic constants, pk_{1-} (with k_{1-} expressed in s^{-1}) for both mono-RL and di-RL, show positive values, with an average of $\approx$ 9.5, indicating a much slower rate for this parameter.

Table 7.2 shows that also for the di-RL the insertion mechanism is higher at 0.06 mM than at 0.12 and 0.25 mM di-RL concentrations. At 0.06 mM the value of $pk_{d1+} \approx$ - 3.92 (expressed in $s^{-1}\ M^{-1.2}$) is much lower than that one at 0.12 mM ($pk_{d1+} \approx$ 0.20) and at 0.25 mM ($pk_{d1+} \approx$ 0.24), while the values of the inverse process, measured by pk_{d1-}, do not show marked differences. On the other hand, considering the pk_{d2+} results, we note that the values are lower at 0.12 and 0.25 mM di-RL ($\approx$ -28.9 and $\approx$ -70.1, respectively, with with k_{2+} expressed in $s^{-1}M^{1-nd}$) compared to the one at 0.06 mM ($\approx$ -19.9), indicating that the speed of pore formation, once di-RL has penetrated the membrane, is higher at the highest

concentrations of di-RL.

The overall effect of these parameters can be better understood by evaluating the time dependency of the fraction lipids bound to the POPC GUVs, which, according to the two foreseen mechanisms of *RL-insertion* and *pore formation*, is the sum of $f_1(t)$ and $f_2(t)$. Plots of $f(t)$, $f_1(t)$ and $f_2(t)$, obtained by the fitting parameters shown in Table 7.3, reported in Figure 7.14 as solid, dashed and dotted lines, respectively. Also the calculation of the volume fractions of the solution that has entered into the POPC GUVs through the two mechanisms, $V_1(t)/V(t)$ and $V_2(t)/V(t)$ are reported in the bottom panels of Figure 7.12 as dashed and dotted lines, respectively, and their sum as a solid line ($V(t)$).

In general, the fractions of molecules interacting with the POPC GUVs are quite small, in the orders 10^{-2} and 10^{-5} for both mono-RL and di-RL , suggesting that most of RL molecules remain in solution (panels A1 to F1 in Figure 7.12).
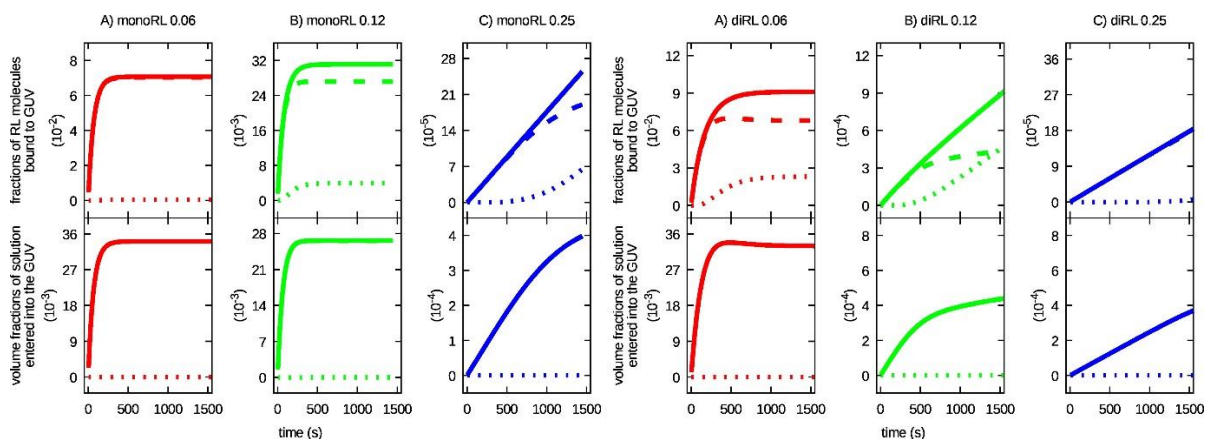
Figure 7.12 Fractions of mono-RL (top panels A to C on the left) and di-RL (top panels A to C on the right) molecules bound to GUVs and volume fractions of solution entering into GUVs for mono-RL (bottom panels A to C on the left) and di-RL (bottom panels A to C on the right), as a function of time. The colours are related to the concentrations: 0.06 mM, red; 0.12 mM, green; 0.25 mM, blue. The line type is related to the different RL-GUV interaction mechanism: dashed, fraction due to RL-insertion, $f_1(t)$ (top panels) or $V_1(t)/V(t)$ (bottom panels); dotted, fraction due to pore formation, $f_2(t)$ (top panels) or $V_2(t)/V(t)$ (bottom panels); solid, sum of the effects of both mechanisms, $f(t)$ (top panels) or $(V_1(t)+V_2(t))/V(t)$ (bottom panels).

For GUVs in the presence of mono-RL in 0.06 to 0.12 mM concentrations, the fractions of molecules interacting with POPC membranes are basically by RL-insertion mechanism (Figure 7.12 panels A and B on the left). In Figure 7.12 panel C on the left is possible to see that first the interaction GUV started with mono-RL-insertion and after 1000 seconds there was also a small part of molecules bonding to the GUV by pore formation.

Regarding di-RL, in the experiments performed with 0.06 mM (Figure 7.12 panel A on the right) di-RL-insertion is the first mechanism of interaction with POPC GUVs and, after 500 seconds, a smaller part of the molecules bounded to the membrane by pore formation. When exposed to 0.12 mM of di-

RL the first mechanism was di-RL-insertion but then the pore formation had an important growth until the end of the experiment (1500 seconds), panel B on the right of Figure 7.12. For 0.25 mM the interaction between di-RL and POPC GUVs happened basically by di-RL-insertion (panel C on the right of Figure 7.12).

7.5.2 DOPC:SM:CHOL (1:1:1) GUVs with mono and di-rhamnolipids

Microscope images in phase contrast and fluorescence mode of DOPC:SM:CHOL 1:1:1 GUVs are reported in Figure 7.13 in the presence of mono-RL, panels A to C, and di-RL, panels D to F. The concentrations of both RLs are expressed in colors: red for 0.06 mM, green for 0.12 mM and blue 0.25 mM.

Figure 7.14 reports the parameters R, A and V for each sample as a function of the time, after mixing the solutions of GUVs and RLs. For two-phase-domain GUVs, observed with di-RL (panels D to F on Figure 7.14), it was obtained the values for the average radii of Ld and Lo phases (R_d and R_o, respectively), the distance between the centers of the two phases (r_{do}) and the related values of phase areas (A_α, with α = d,o, Equation 7.12) and volumes (V_α, Equation 7.13). Fitting curves of the time-behavior of A and V are shown in black solid curves in Figure 8.14 and corresponding fitting parameters are listed in Table 7.3.
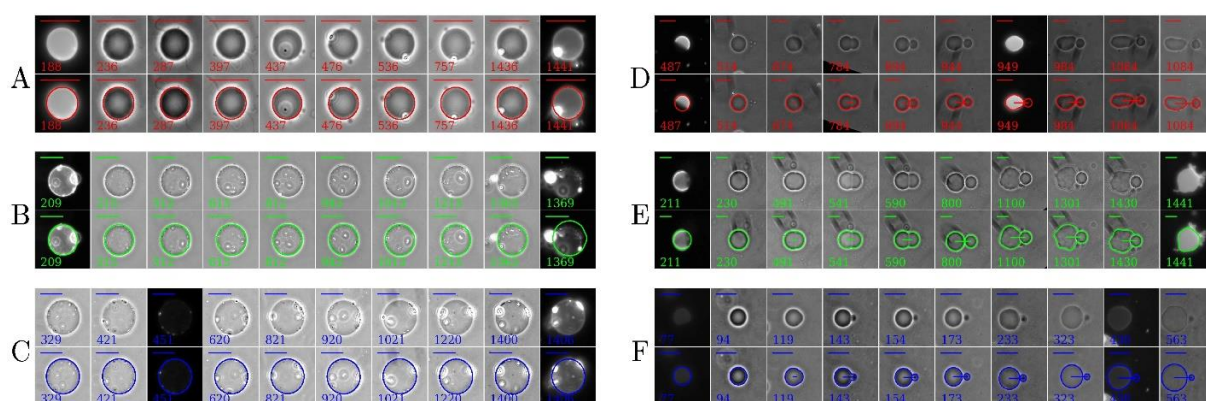
Figure 7.13 Representative DOPC:SM:CHOL (1:1:1) GUV fluorescence and phase contrast images dispersed in 0.06 mM (red), 0.12 mM (green) and 0.25 mM (blue) mono-RL (panel A, B and C, respectively) or di-RL (panel D, E and F, respectively). See caption of Figure 7.10 for other details.

The incubation of mono-RL with DOPC:SM:CHOL (1:1:1) GUVs, which have Lo-Ld phase coexistence membrane, immediately promoted lipid mixing, identified by a homogeneous Rh-PE distribution (Figure 7.13 panel A to C). Otherwise di-RL conducted to Lo outward budding over time (Figure 7.13 panel D to F). Interestingly, this latter effect was previously reported by incubating the commercial mono and di-RL mixture with the same model plasma membrane [Come2021]. However,

here we further observe that di-RL can also promote a change in Ld phase permeability to sugar molecules depending on biosurfactant concentration (Figure 8.13, panels B and C).
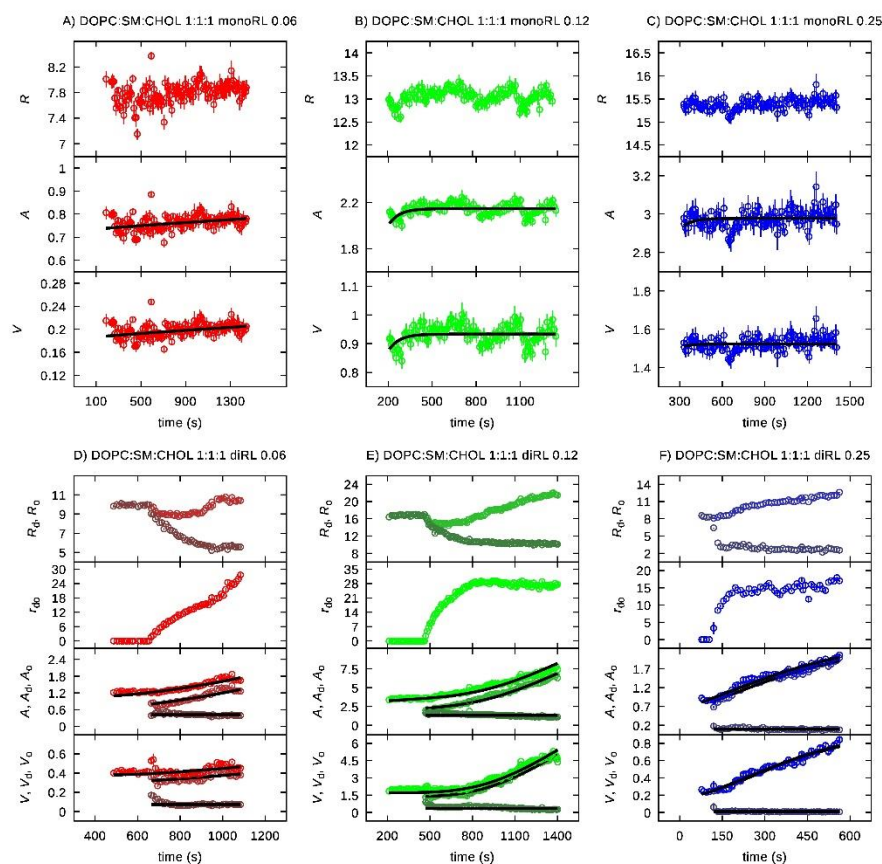
Figure 7.14 Time-dependence of the geometrical parameters of DOPC:SM:CHOL (1:1:1) GUVs in the presence of 0.06 mM, 0.12 mM and 0.25 mM (red, green and blue, respectively) of mono-RL (panel A to C) and di-RL (panel D to F). Panels A to C: see caption of Figure 7.11

The analysis of the time-behavior of areas and volumes of DOPC:SM:CHOL 1:1:1 GUVs in the presence of mono-RL has been performed by applying the kinetic model (Section 7.4.1, Eqs. 7.18 and 7.21). Fitting curves are shown as black solid lines in Figure 7.14 with fitting parameters displayed in Table 7.3. Table 7.3 also shows the parameters GUV volume and area in the presence of di-RL, that regard the interpretation with the kinetic model in the two-phase-domain version (see. Section 7.4.2) giving the possibility of interpretation of the parameters for Lo and Ld phase.

	Mono-RL 0.06		Mono-RL 0.12		Mono-RL 0.25		Di-RL 0.06		Di-RL 0.12		Di-RL 0.25	
	A		B		C		D		E		F	
1 N_d (10^9)	2.29	±0.07	0.236	±0.002	0.44	±0.02	1.69	±0.02	5.32	±0.05	1.73	±0.02
2 $V_{d(0)}$ ($10^4\ \mu m^3$)	0.115	±0.001	0.09	±0.02	0.650	±0.007	0.301	±0.003	1.34	±0.01	0.165	±0.002
3 λ_{1d} (μm)	0.033	±0.002	0.033	±0.002	0.032	±0.002	0.0011	±0.0005	0.0002	±0.0003	0.0021	±0.0008
4 λ_{2d} (μm)	0.0047	±0.0003	0.0045	±0.0001	0.00337	±0.00003	0.0015	±0.0001	0.0098	±0.0001	0.0069	±0.0001
5 r_{pd} (Å)	437	±10	452	±5	472	±9	498	±5	499	±5	492	±5
6 m_d	1.02	±0.01	1.01	±0.01	1.02	±0.01	1.00	±0.01	1.00	±0.01	1.00	±0.01
7 n_d	3.14	±0.03	1.01	±0.01	1.05	±0.01	3.15	±0.03	4.23	±0.04	1.27	±0.01
8 pk_{d1+} ($s^{-1}M^{-md}$)	−1.59	±0.06	−2.15	±0.02	−2.05	±0.04	0.010	±0.002	0.046	±0.002	−0.313	±0.004
9 pk_{d1-} (s^{-1})	3.22	±0.03	3.20	±0.03	3.44	±0.03	10.0	±0.1	10.0	±0.1	5.98	±0.06
10 pk_{d2+} ($s^{-1}M^{1-nd}$)	−21.0	±0.2	3.03	±0.05	3.85	±0.04	−27.7	±0.3	−42.3	±0.4	2.18	±0.02
11 pk_{d2-} (s^{-1})	27.8	±0.7	4.45	±0.04	4.79	±0.05	31.4	±0.3	41.6	±0.4	6.13	±0.06
18 N_o (10^9)	−		−		−		2.24	±0.02	7.39	±0.07	0.518	±0.006
19 $V_{o(0)}$ ($10^4\ \mu m^3$)	−		−		−		0.058	±0.001	0.362	±0.004	0.0113	±0.0001
20 λ_{1o} (μm)	−		−		−		0.0207	±0.0003	0.017	±0.002	0.021	±0.001
21 λ_{2o} (μm)	−		−		−		0.15	±0.03	0.03	±0.03	0.15	±0.03
22 r_{po} (Å)	−		−		−		370	±50	390	±40	380	±40
23 m_o	−		−		−		1.00	±0.01	1.81	±0.09	2.6	±0.1
24 n_o	−		−		−		7	±2	7	±2	7	±2
25 pk_{o1+} ($s^{-1}M^{-mo}$)	−		−		−		0.17	±0.02	0.34	±0.04	0.59	±0.07
26 pk_{o1-} (s^{-1})	−		−		−		4.47	±0.04	4.4	±0.4	4.7	±0.6
27 pk_{o2+} ($s^{-1}M^{1-no}$)	−		−		−		70	±10	130	±20	190	±30
28 pk_{o2-} (s^{-1})	−		−		−		58	±9	100	±20	170	±20

Table 7.3 Parameters obtained by the simultaneous best fit of the DOPC:SM:CHOL 1:1:1 GUV areas and volumes in the presence of mono-RL and di-RL shown as solid black lines in Figure 7.14.

Concerning the interaction of mono-RL with ternary 1:1:1 GUVs, the biosurfactant at 0.06 mM (at CMC) not just favored lipid mixing, but leads to filaments formation at first 400 s, followed by a significant protrusion over the membrane surface and the appearance of small buds (see snapshot of 437 s Figure 7.13, panel A) that are kept over time. This must be due to the mono-RL insertion in the outer membrane leaflet affecting the spontaneous membrane curvature. Interestingly, the area excess released through filaments/buds/membrane protrusion practically preserved the area/volume of the original GUV, as shown by the measured values of radius R, area A and volume V (Eqs. 7.2, 7.9 and 7.10 on Section 7.4, respectively) displayed on Figure 7.13. For 0.12 mM and 0.25 mM of mono-RL concentrations, the effects on ternary 1:1:1 GUVs are rather similar (Figure 7.13 panels B and C): the GUVs spherical shape and dimension are preserved over incubation time, no membrane permeability increase is observed, with the appearance of small dots over the membrane surface, as it happened with POPC GUVs in the presence of 0.12 mM mono-RL.

For DOPC:SM:CHOL 1:1:1 GUVs in the presence of di-RL (panels D to F on Figure 7.13), it was possible to see similarity with the results described by Ref. [Come2021] in experiments performed with a commercial mono-RL/di-RL mixture, that is the Lo phase outwardly budding, which appears dark in fluorescence mode. During the experiment time, the Ld phase showed shape and size fluctuation and loss of phase contrast, whereas the Lo phase remained with its initial circular shape. In the experiment performed with 0.06 mM di-RL (Figure 7.14, panel A), the protrusion of Lo phase starts after 600 s in contact with di-RL, with 0.12 mM after 400 s (Figure 7.14, panel B) and at 0.25 mM (Figure 7.14, panel C) the protrusion occurs before 200 s, suggesting that the concentration of di-RL has an impact on Lo phase protrusion.

Also in the presence of 0.12 and 0.25 mM di-RL the ternary DOPC:SM:CHOL 1:1:1 GUV had a significant loss of contrast, with the Ld phase becoming almost transparent by the end of the experiment (Figure 7.13, panel C).

The plots of area and volume for 0.06 and 0.12 mM di-RL (panels A and B on Figure 7.14) show that, after the protrusion of the Lo phase, both A_d (Ld area) and A (total area) increased, whereas A_o (the area of the Lo phase) has a slight decrease, suggesting that the main contribution to the increase of A derives from A_d and thus revealing that the most important effect of di-RL on the plasma membrane is its insertion in the Ld phase, as previously observed for the mixture [Come2021].

Panel B on Figure 7.14 shows that up to 800 s the volume of GUV in the presence of 0.12 mM di-RL is constant, the area of the Ld phase slightly increases and the one of the Lo phase does not change. This result indicates that di-RL gets into the membrane only via the Ld phase, without significantly increasing its permeability to the solution. After 800 s, the GUV volume increases, due to the increase of membrane permeability that determines an exchange between inner and outer solution, with a concomitant decrease of the optical contrast, as seen in Figure 7.13, panel B. Panel C of Figure 7.14 (0.25 mM di-RL) shows that both volume and area of Ld phase increase, indicating that up to the beginning of the experiment the GUV permeability increases allowing the inner/outer membrane solution exchange. The results from the microscope observations (Figure 7.13) globally show that di-RL has a greater impact on ternary 1:1:1 GUVs than mono-RL, especially in the Ld phase.

Results exposed on Table 7.3 show that, in the presence of mono-RL, the values of pk_{1+} calculated for 0.06, 0.12 and 0.25 mM are similar, with values ranging from ≈ -2.15 to ≈ -1.59 (k_{1+} is expressed in $s^{-1}M^{-1.2}$). However, after attacking in the membrane, mono-RL are more likely to make pores in experiments performed with 0.06 mM, because the value of pk_{2+} for this case (≈ -21.0, with k_{2+} expressed in $s^{-1}M^{1-nd}$) is much smaller than the ones at 0.12 mM and 0.25 mM (≈ 3.03 and ≈ 3.85, respectively).

More in detail, at 0.12 and 0.25 mM mono-RL concentration, well above the CMC, the fraction of molecules forming the pores is negligible: the very large majority of molecules interacting with the membrane are freely bound to the GUV surface, more likely with the outer leaflet. At both 0.12 and 0.25 mM the *RL-insertion* process reaches an equilibrium condition after around 400 s from the solutions' mixing (Figure 7.14).

Table 7.3 also shows a great difference between the two biosurfactants, mono-RL and di-RL, concerning the parameter λ_{1d}. For mono-RL, the values of λ_{1d} is ≈ 0.033, whereas for di-RL it varies from ≈ 0.0001 to ≈ 0.0021, suggesting that mono-RL has a lower impact in varying water permeability across the membrane.

Considering the parameters of GUV volume and area in the presence of di-RL in Table 7.3, that regard the interpretation of the kinetic model in the two-phase-domain version, the kinetic order m_d of the RL-insertion process occurring in the Ld phase is ≈ 1, at any di-RL concentration, similar to the values observed for mono-RL. On the other hand, the related direct kinetic constant shows that the fastest rate of di-RL:GUV interaction occurs at 0.25 mM, with the smallest value of $pk_{1+} \approx -0.313$ (k_{1+} expressed in $s^{-1}M^{-1}$), in respect to the values for 0.06 and 0.12 mM concentrations (≈ 0.010 and ≈ 0.046, respectively). However, at 0.06 mM and 0.12 mM di-RL, the smaller values of pk_{2+} indicate that the *pore formation* mechanism is faster for the smaller concentrations, ≈ -27.7 and ≈ -42.3 respectively (the unit of k_{d2+} is $s^{-1}M^{1-nd}$), confirming a strong concentration dependency of the pore formation mechanism.

These concentration effects can be rationalized considering that, since all the investigated conditions are above the CMC for di-RL in 0.2 M glucose solution (0.028 ± 0.005 mM), the micellar shapes formed by di-RL can change as a function of concentration (for example becoming more elongated), therefore the mechanism of the diRL-insertion into the membrane, which would mainly involve di-RL extracted from the micelles, may depend on the concentration of di-RL.

The corresponding reverse kinetic constants, pk_{1-} (with k_{1-} expressed in s^{-1}) for both mono-RL and di-RL, show positive values, with an average of ≈ 5.1, indicating a much slower rate for this parameter.

About the interaction of di-RL with the DOPC:SM:CHOL 1:1:1 Lo domain, the model parameters are shown in the second half of Table 7.3. The kinetic order of the di-RL-insertion process, m_o, slightly increase from ≈ 1 to ≈ 2.6 by increasing di-RL concentration, and smooth variations are also found for the related direct kinetic constant pk_{o1+}, despite the unit of $k_{o\ 1+}$ ($s^{-1}M^{-mo}$) depends on m_o. Conversely, the reverse kinetic constants $pk_{o1-} \approx 4.5$ are quite independent of di-RL concentration. The values of r_{po}, λ_{2o} and λ_{1o} for the Lo phase of the GUVs in the presence of di-RL do not deserve any comments,

being the rates of free insertion and pore formation so low that any water penetration effect is hampered.

By using the derived set of fitting parameters describing the interaction of di-RL with DOPC:SM:CHOL 1:1:1 GUVs, we have subsequently calculated, in function of time, the fractions of di-RL molecules involved in the two Ld and Lo phases and in the two foreseen processes, *RL-insertion* and *pore formation*, $f_1(t)$ and $f_2(t)$, respectively) as well as the volume fraction of the solution that has entered into the GUV via the two mechanisms ($f(t)$). Results are shown in Figure 7.14. In general, the fraction of di-RL bound to the GUV are in the order of 10^{-4} to 10^{-3}, in line with the values detected for mono-RL or for the commercial mixture of mono-RL/di-RL [Come2021].

Also the calculation of the volume fractions of the solution that has entered into the GUV through the two mechanisms, $V_1(t)/V(t)$ and $V_2(t)/V(t)$ are reported in the bottom panels of Figure 7.14 as dashed and dotted lines, respectively, and their sum as a solid line. We observe that the overall volume fraction is low, in the order of 10^{-3}, increases with the mono-RL concentration, and it is only due to the RL-insertion process, suggesting that mono-RL has a negligible effect in modifying DOPC:SM:CHOL 1:1:1 membrane permeability to sugar molecules.
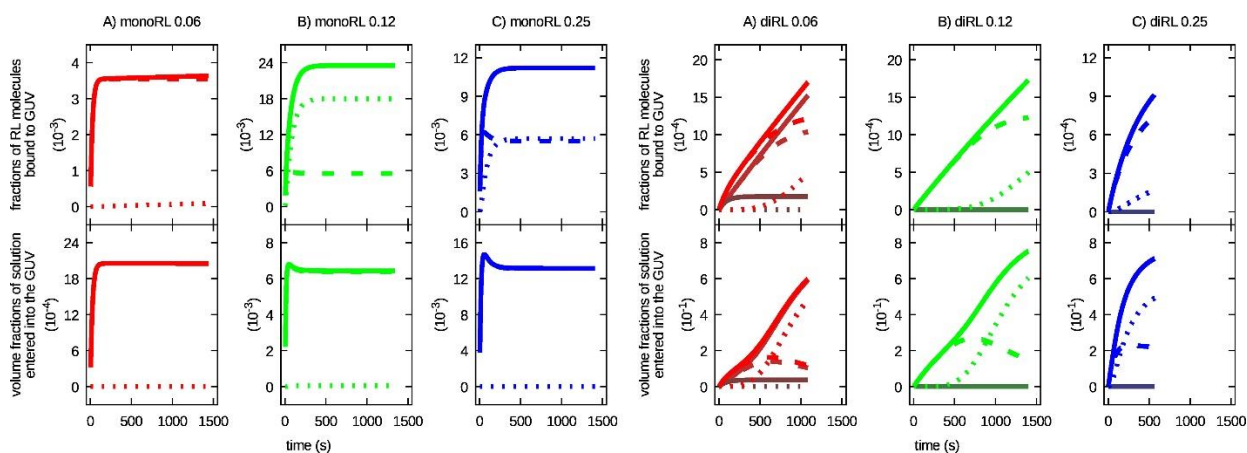
Figure 7.15 Fractions of mono-RL (top panels A to C on the left) and di-RL (top panels A to C on the right) molecules bound to GUVs and volume fractions of solution entering into GUVs for mono-RL (bottom panels A to C on the left) and di-RL (bottom panels A to C on the right), as a function of time. The colours are related to the concentrations: red for 0.06 mM, green for 0.12 mM and blue for 0.25 mM. See caption of Figure 7.10 for other details. Panels A to C on the left: see caption of Figure 7.12 for other details. Panels A to C on the right: intermediate-shade-dashed lines: $f_{d,1}(t)$; intermediate-shade-dotted lines: $f_{d,2}(t)$; intermediate-shade-solid lines: $f_d(t)=f_{d,1}(t)+f_{d,2}(t)$; dark-shade-dashed lines: $f_{o,1}(t)$; dark-shade-dotted lines: $f_{o,2}(t)$; dark-shade-solid lines: $f_o(t)=f_{o,1}(t)+f_{d,2}(t)$; brilliant-dashed lines: $f_1(t)=f_{d,1}(t)+f_{o,1}(t)$; brilliant-dotted lines: $f_2(t)=f_{d,2}(t)+f_{o,2}(t)$; brilliant-solid lines: $f(t)=f_1(t)+f_2(t)$. Bottom panels: intermediate-shade-dashed lines: $V_{d,1}(t)/V(t)$; intermediate-shade-dotted lines: $V_{d,2}(t)/V(t)$; intermediate-shade-solid lines: $(V_{d,1}(t)+V_{d,2}(t))/V(t)$; dark-shade-dashed lines: $V_{o,1}(t)/V(t)$; dark-shade-dotted lines: $V_{o,2}(t)/V(t)$; dark-shade-solid lines: $(V_{o,1}(t)+V_{o,2}(t))/V(t)$; brilliant-dashed lines: $(V_{d,1}(t)+V_{o,1}(t))/V(t)$; brilliant-dotted lines: $(V_{d,2}(t)+V_{o,2}(t))/V(t)$; brilliant-solid lines: $(V_{d,1}(t)+V_{o,1}(t)+V_{d,2}(t)+V_{o,2}(t))/V(t)$.

When in contact with 0.06 mM of mono-RL (panel A on the left on Figure 7.15), the only way this

biosurfactant bounds to the ternary 1:1:1 GUVs is by the first mechanism (RL insertion), because the dashed line is superimposed by continuous line. Although when the concentration of mono-RL is increased to 0.12 mM, the second mechanism (pore formation) is seen (panel B on the left of Figure 7.15). For the concentration 0.25 mM of mono-RL both mechanisms happened simultaneously (panel C on the left of Figure 7.15).

It is possible to see that at 0.06 mM di-RL (panel D on the left of Figure 7.15) most of the di-RL molecules are bound via the first mechanism (di-RL-insertion) occurring over the Ld phase (intermediate-shade-dashed line), with a fraction that at the longest times seems to reach a steady value of $\approx 10^{-3}$. Also, after ≈ 400 s from the beginning of the experiment, the fraction due to pore formation in the Ld phase surface starts to grow, without reaching a steady value, at least within the duration of the measurements. The contribution to the total fraction (brilliant-solid line) due to di-RL molecules interacting with the Lo phase is only caused by diRL-insertion mechanism (dark-shade-dashed line superimposed with the dark-shade-solid lines) accounting for $\approx 2 \, 10^{-4}$, being the one due to pore formation totally negligible (dark-shade-dotted lines).

Still about the interaction with 0.06 mM of di-RL, looking at the volume fractions of the solution entering into the GUV (Figure 7.15, panel A on the right), we see that, as expected, the Ld phase is mostly involved (intermediate-shade lines very close to the brilliant-solid lines). After ≈ 500 s from the beginning of the experiment, the contribution due to pore formation (intermediate-shade-dotted line) in Ld is ≈ 0.2, similar to the one due to di-RL-insertion and the possible concomitant increase of membrane permeability (intermediate-shade-dashed line), and then becomes much higher, ≈ 0.6. Hence, despite the fraction of di-RL forming pores in Ld ($f_{d,2}(t)$) is lower than the one just embedded in Ld ($f_{d,1}(t)$), mostly of the solution entering in the GUV passes through the pores and not from the possible increase of the membrane permeability due to the RL-insertion mechanism. Results at the highest concentrations of di-RL are easier to understand, since no contribution due to the Lo phase (dark-shade lines all ≈ 0) has been observed.

At 0.12 mM di-RL the fraction of molecules bound to the GUV via the diRL-insertion mechanism (Fig 10 top panel B, intermediate-shade-dashed line superimposed with the intermediate-shade-solid line) continuously grows and reaches a maximum of $\approx 10^{-3}$, very similar to the corresponding value at 0.06 mM di-RL, after ≈ 500 s from the beginning of the experiment. Also the volume of the solution entering into the GUV due to this mechanism (Figure 7.15, panel B on the right, intermediate-shade-dashed line superimposed with the brilliant-shade-dashed line) reaches a maximum of ≈ 0.2, as for the 0.06 mM di-RL case. Moreover, from 500 s onward, the fraction of di-RL forming pores at the Ld surface (Figure 7.15 panel B on the right, intermediate-shade-dotted line superimposed with the brilliant-shade-dotted line) grows up apparently without reaching a steady value and the volume

fraction of the solution entering through these pores (Figure 7.15, panel B on the right, intermediate-shade-dotted line superimposed with the brilliant-shade-dotted line) also grows to more than ≈ 0.6.

At 0.25 mM di-RL the whole process occurs at shorter times: the maximum volume fraction solution entering into the GUV by the di-RL-insertion mechanism (Figure 7.15, panel C on the right, intermediate-shade-dashed line superimposed with the brilliant-shade-dashed line) is again ≈ 0.2 and it is reached after ≈ 200 s from the beginning of the experiment.

7.5.3 DOPC:SM:CHOL (3:5:2) GUVs with mono and di-rhamnolipids

Microscope images in phase contrast and fluorescence mode of DOPC:SM:CHOL 3:5:2 GUVs are reported in Figure 7.16 in the presence of mono-RL, panels A to C, and di-RL, panels D to F. The concentrations of both RLs are expressed in colors: red for 0.06 mM, green for 0.12 mM and blue 0.25 mM. The plots on Figure 7.17, panels A to C for mono-RL and D to F for di-RL, report the obtained values for the average radii of Ld and Lo phases (R_d and R_o, respectively), the distance between the centers of the two phases (r_{do}) and the related values of phase areas (A_α, with $\alpha = d,o$, Equation 7.12) and volumes (V_α, Equation 7.13). Fitting curves of the time-behavior of A and V are shown in black solid curves in Figure 7.17 and corresponding fitting parameters are listed in Table 7.4.

The images from Figure 7.16 shows that the ternary DOPC:SM:CHOL 3:5:2 GUVs maintained the Ld-Lo phase coexistence in experiments performed with both mono-RL or di-RL, contrasting with ternary DOPC:SM:CHOL 1:1:1 GUVs, shown on Figure 7.12, in which only GUVs in contact with di-RL maintained both Ld and Lo phases while mono-RL promoted lipid mixing with the ternary GUV becoming homogeneous.
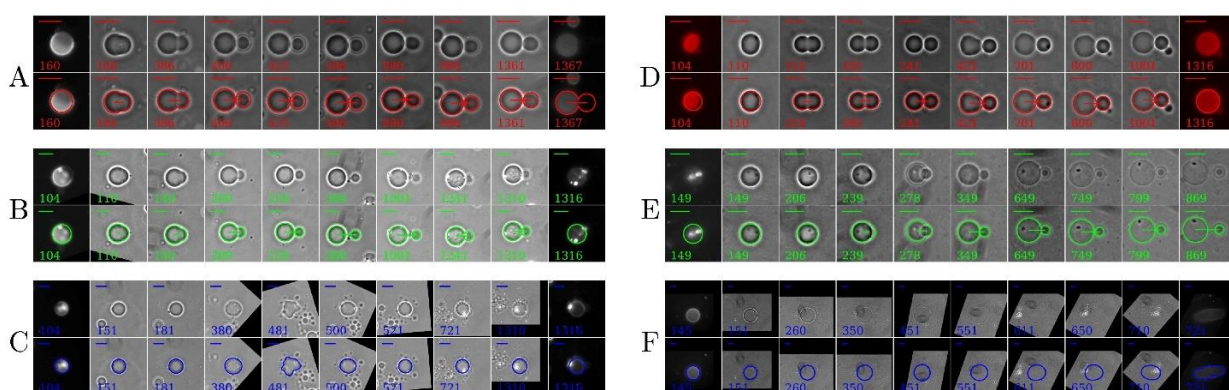

Figure 7.16 Representative DOPC:SM:CHOL (3:5:2) GUV fluorescence and phase contrast images dispersed in 0.06 mM (green), 0.12 mM (blue) and 0.25 mM (blue) mono-RL (panel A, B and C respectively) and di-RL (panel D, E and F). See caption of Figure 7.10 for other details.
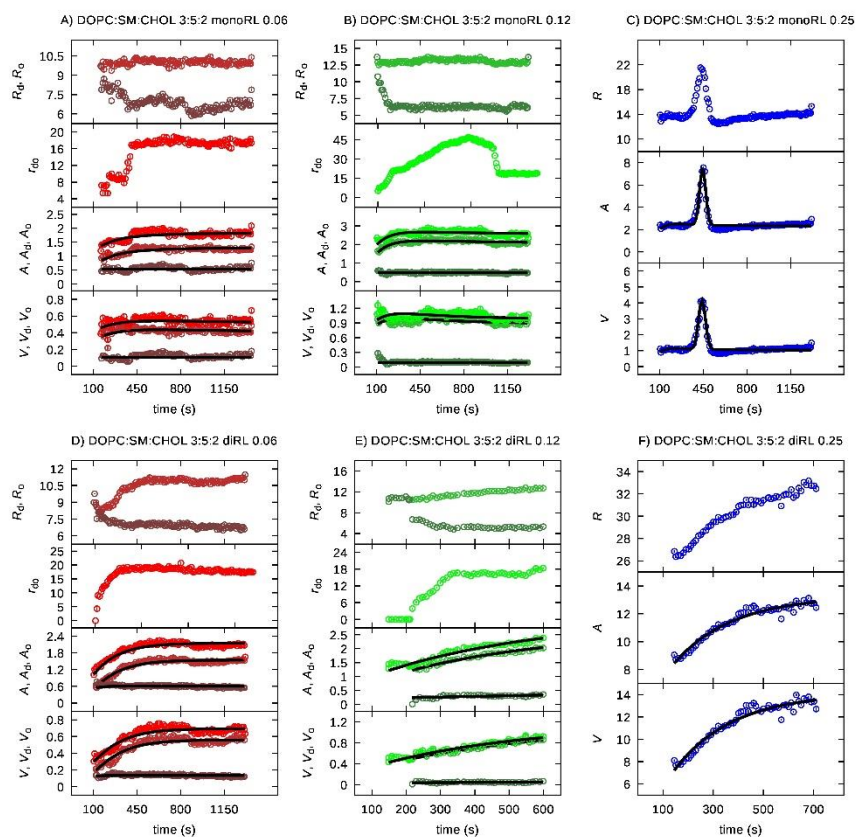
Figure 7.17 Time-dependence of the geometrical parameters of DOPC:SM:CHOL 3:5:2 GUVs in the presence of mono-RL (panel A, B and C) and di-RL (panel D, E and F) in function of time. See the caption of Figure 7.14 for the meaning of the different panels and for the line colors

Concerning the interaction of mono-RL with ternary 3:5:2 GUVs, the biosurfactant at 0.06 mM (at CMC) promoted the Lo phase (that looks dark in fluorescence mode) moving outward budding at the beginning of the experiment, before 200 s, followed by the appearance of small buds until 400 s in the Ld phase, with Lo phase maintaining size and shape (Figure 7.16, panel A). This must be due to the mono-RL insertion in the outer membrane leaflet of Ld phase affecting the spontaneous membrane curvature. The area excess released through filaments/buds/membrane protrusion practically preserved the area/volume of the original GUV, as shown by the measured values of radius R, area A and V displayed on Figure 7.17. In the experiments performed with 0.12 mM of mono-RL (panel B on Figure 7.16 and 7.17), the Lo phase moves outwarding of the GUV, maintaining the size and shape, while the Ld phase developed bright spots, that were already seen in POPC and ternary 1:1:1 GUVs in contact with mono-RL.

Looking at the results for the experiments taken with 0.06 mM and 0.12 mM, also the Lo phase was outwardly budding maintaining its circular shape, while Ld phase showed shape and size fluctuations (Figure 7.16 panel D and F), like it happened with ternary 1:1:1 GUVs experiments. The images also

show a significant loss of contrast, especially with 0.12 mM di-RL when the Ld phase became almost transparent by the end of the experiment (Figure 7.16 panel E).

The Ld-Lo coexistence phase was not well defined when ternary 3:5:2 GUVs are in contact with mono-RL and di-RL at 0.25 mM concentration. In particular, GUVs in contact with 0.25 mM mono-RL show form and size fluctuation until 500 s and bright spots (panels C in Figure 7.16), whereas, in contact with 0.25 mM di-RL, the response is very different, since GUV loses contrast and become almost transparent by the end of the experiment (panels F in Figure 7.16).

As described before for the experiments with 1:1:1 ternary GUVs, the plots of area and volume for DOPC:SM:CHOL 3:5:2 GUVs shows that after the protrusion of Lo the main contribution to the increase of total area A derives from A_d. Panel B on Figure 7.17 (0.12 mM monoRL) shows that the plot of A and A_d are growing curves while the volume V and V_d are straight lines, indicating that the size increasing of the GUV is due to the interaction of mono-RL in the membranes and not because the introduction of water inside the vesicle. In the plot for 0.06 mM di-RL (Figure 7.16, panel D), the volume of Ld phase is constant until 300 s, although the area increases from the beginning of the experiment, which shows that until 300 s di-RL molecules are introduced to the membrane, afterwards also water molecules start to get inside the GUV. Concerning the GUV in contact with 0.12 mM di-RL, until 300 s area and volume of both Ld and Lo phases are constant, subsequently they start to increase (Figure 7.16, panel E).

The analysis of the time-behavior of areas and volumes of DOPC:SM:CHOL 3:5:2 GUVs in the presence of mono-RL and di-RL has been performed by applying the kinetic model (Sections 7.4.1 and 7.4.2). Fitting curves are shown as black solid lines in Figure 7.17 with fitting parameters displayed in Table 7.4.

		Mono-RL 0.06	Mono-RL 0.12	Mono-RL 0.25	Di-RL 0.06	Di-RL 0.12	Di-RL 0.25
		A	B	C	D	E	F
1	N_d (10^9)	1.05 ± 0.01	1.56 ± 0.02	1.29 ± 0.01	0.30 ± 0.08	1.2 ± 0.2	8.58 ± 0.09
2	$V_{d(0)}$ (10^4 μm³)	0.229 ± 0.005	0.609 ± 0.008	0.144 ± 0.003	0.01 ± 0.04	0.25 ± 0.03	0.35 ± 0.03
3	λ_{1d} (μm)	0.025 ± 0.001	0.025 ± 0.001	0.0458 ± 0.0005	0.03 ± 0.02	0.00 ± 0.06	0.074 ± 0.001
4	λ_{2d} (μm)	0.000453 ± 0.000003	0.000457 ± 0.000003	0.001 ± 0.001	0.0046 ± 0.0001	0.004 ± 0.001	0.0160 ± 0.0002
5	r_{pd} (Å)	14.6 ± 0.4	14.6 ± 0.4	5.00 ± 0.05	480 ± 60	400 ± 40	39.6 ± 0.4
6	m_d	1.12 ± 0.01	1.12 ± 0.01	1.05 ± 0.01	2.97 ± 0.03	1.11 ± 0.01	2.47 ± 0.02
7	n_d	3.03 ± 0.03	3.02 ± 0.03	4.53 ± 0.05	1.26 ± 0.05	1.00 ± 0.01	3.21 ± 0.03
8	pk_{d1+} (s⁻¹M⁻^{md})	-1.96 ± 0.02	-1.95 ± 0.02	-1.80 ± 0.02	-10.0 ± 0.2	-0.83 ± 0.02	-6.50 ± 0.07
9	pk_{d1-} (s⁻¹)	6.45 ± 0.06	6.40 ± 0.06	10.5 ± 0.1	7 ± 1	1.1 ± 0.2	3.46 ± 0.03
10	pk_{d2+} (s⁻¹M^{1-nd})	-22.1 ± 0.2	-22.0 ± 0.2	-36.5 ± 0.4	4.88 ± 0.09	0.5 ± 0.1	-27.4 ± 0.3
11	pk_{d2-} (s⁻¹)	23.4 ± 0.4	23.2 ± 0.4	26.3 ± 0.3	5.8 ± 0.2	5.94 ± 0.06	17.4 ± 0.2
12	h_A (10^3 μm²)	–	–	5.0 ± 0.1	–	–	–
13	$t_{A,0}$ (s)	–	–	444 ± 4	–	–	–
14	σ_A (s)	–	–	25.2 ± 0.8	–	–	–
15	h_V (10^4 μm³)	–	–	3.08 ± 0.08	–	–	–
16	$t_{V,0}$ (s)	–	–	439 ± 4	–	–	–
17	σ_V (s)	–	–	28.3 ± 0.8	–	–	–
18	N_o (10^9)	2.57 ± 0.03	2.18 ± 0.02	–	0.48 ± 0.02	1.08 ± 0.09	–
19	$V_{o(0)}$ (10^4 μm³)	0.088 ± 0.002	0.055 ± 0.001	–	0.12 ± 0.04	0.026 ± 0.003	–
20	λ_{1o} (μm)	0.008 ± 0.000	0.008 ± 0.000	–	0.003 ± 0.008	0.150 ± 0.045	–
21	λ_{2o} (μm)	0.0116 ± 0.0001	0.0116 ± 0.0001	–	0.002 ± 0.002	0.0020 ± 0.0003	–
22	r_{po} (Å)	282 ± 3	281 ± 3	–	400 ± 200	500 ± 20	–
23	m_o	1.13 ± 0.01	1.13 ± 0.01	–	1.01 ± 0.01	1.00 ± 0.01	–
24	n_o	1.01 ± 0.01	1.00 ± 0.01	–	10 ± 1	1.13 ± 0.04	–
25	pk_{o1+} (s⁻¹M⁻^{mo})	-0.97 ± 0.01	-0.97 ± 0.01	–	-1.91 ± 0.07	1.1 ± 0.1	–
26	pk_{o1-} (s⁻¹)	0.113 ± 0.001	0.113 ± 0.001	–	5.65 ± 0.06	5.6 ± 0.5	–
27	pk_{o2+} (s⁻¹M^{1-no})	-1.15 ± 0.01	-1.14 ± 0.01	–	-98 ± 5	0.12 ± 0.03	–
28	pk_{o2-} (s⁻¹)	0.113 ± 0.001	0.112 ± 0.001	–	30 ± 10	7.6 ± 0.4	–

Table 7.4 Parameters obtained by the simultaneous best fit of the DOPC:SM:CHOL 3:5:2 GUV areas and volumes shown as solid black lines in Figure 7.16.

The results reported in Table 7.4 for the experiments performed with mono-RL show that, for the Ld phase the values of pk_{1+} are almost the same for the three concentrations studied, varying from ≈ -1.96 to ≈ -1.80 (with k_{1+} expressed in s⁻¹M⁻¹). On the other hand, the value of pk_{2+} is smaller for 0.25 mM concentration (≈ -36.5 with k_{d2+} expressed in s⁻¹M^{1-nd}), showing that the water pore formation was faster when the ternary 3:5:2 GUV was in contact with the highest concentration of mono-RL. Considering the Lo phase in the presence of mono-RL, values of pk_{1+} and pk_{2+} are higher than the ones of Ld phase, as it happens with experiments performed with ternary 1:1:1 GUVs, suggesting an overall

faster interaction of mono-RL with the Ld phase than with the Lo phase.

Regarding the Ld phase for experiments performed with di-RL, the fastest rate of RL-GUV interaction occurs at 0.06 mM, with the smallest value of pk_{1+} (≈ -10.0 in in $s^{-1}M^{-1}$), then 0.25 mM (≈ -6.50) and 0.12 mM (≈ -0.83). However, at 0.25 mM of di-RL, the smaller values of pk_{2+} (≈ -27.4) indicates that pore formation is faster at this concentration. The results on Table 7.4 also confirms a more relevant RL:GUV interaction with the Ld phase, being the values of pk_{1+} calculated for the Lo phase higher than the ones for the Ld phase.

Considering Ld phase, Table 7.4 shows that pore radii (r_{pd}) of 3:5:2 GUVs are bigger with di-RL (from ≈ 39.6 to ≈ 400) than with mono-RL (from ≈ 5.00 to ≈ 14.6). The parameters λ_{2d} have the same order of magnitude for the three concentrations of mono-RL and 0.06 mM of di-RL, and are much higher for 0.12 and 0.25 mM concentration of di-RL. On the other hand, the parameters λ_{1d} for mono-RL and di-RL are very similar, with the same order of magnitude. We also notice that, for DOPC:SM:CHOL 3:5:2 GUVs, values of r_{po}, λ_{2o} and λ_{1o} for the Lo phase in the presence of mono-RL and di-RL do not deserve any comments, because the rates of free insertion and pore formation are very low.

Plots of $f_1(t)$ and $f_2(t)$, *RL-insertion* and *pore formation*, and $f(t)$, the sum of both, are reported in Figure 7.14 in a function of time as dashed, dotted and solid lines, respectively, for mono-RL (panels A1 to C1) and di-RL (panels D1 to F1). Also the calculation of the volume fractions of the solution that has entered into the DOPC:SM:CHOL 3:5:2 GUVs through the two mechanisms, $V_1(t)/V(t)$ and $V_2(t)/V(t)$, are reported as dashed and dotted lines, respectively, and their sum as a solid line ($V(t)$) in panels A2 to C2 for mono-RL and D2 to F2 for di-RL.
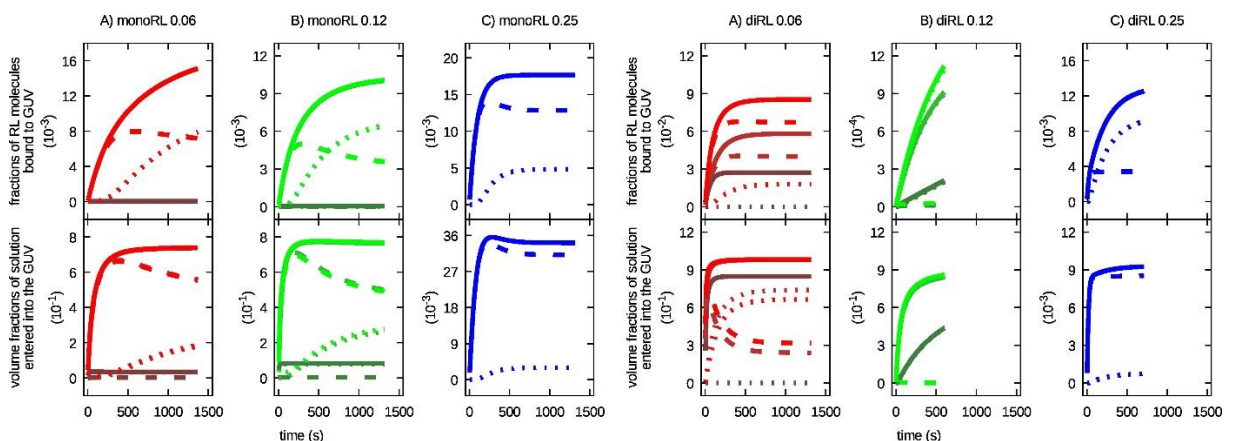

Figure 7.18 Fractions of mono-RL (panels A to C on the left) and di-RL (panels A to C on the right) molecules bound to GUVs and volume fractions of solution entering into GUVs (bottom panels) as a function of time. The color is related to the concentrations: 0.06 mM, red; 0.12 mM, green; 0.25 mM, blue. The line type is related to the different RL:GUV interaction mechanism. See the caption of Figure 7.15 for more details.

As it happened in previous results, most of mono-RL and di-RL molecules remain in solution, because the fractions of molecules interacting with DOPC:SM:CHOL 3:5:2 GUVs varies in the orders 10^{-2} to 10^{-4} for both mono-RL and di-RL (Figure 7.18).

As it happened in previous results, most of mono-RL and di-RL molecules remain in solution, because the fractions of molecules interacting with DOPC:SM:CHOL 3:5:2 GUVs varies in the orders 10^{-2} to 10^{-4} for both mono-RL and di-RL (panels A to B Figure 7.18).

It is possible to see that at 0.06 mM (Figure 7.18 - panel A on the left) the molecules of mono-RL bound to the 3:5:2 GUVs via the first mechanism (RL-insertion) on the Ld phase (intermediate-shade-dashed line), then after about 250 s the contribution of the pore formation (intermediate-shade-dotted line) to the total fraction (brilliant-solid line) starts to grow and around 1200 s started to be the most important mechanism of interaction mono-RL-GUV. The same behavior was seen in the interaction 3:5:2 GUV and 0.12 mM mono-RL, although for this concentration, the contribution of pore formation mechanism for the total RL:GUV bounding became bigger than RL insertion in a shorter time, after 500 seconds. Still about 0.06 and 0.12 mM of mono-RL, there is no contribution to the total fraction (brilliant-solid line) due to mono-RL molecules interacting with the Lo phase because all the dark-shade lines remained ≈ 0 fractions. Regarding volume of solution that enters in the membrane for 0.06 and 0.12 mM of mono-RL (panels A and B on the right on Figure 7.18), both mechanisms collaborate to the total amount that passes through the membrane in Ld phase, although mostly of the solution entering in the GUV passes because of the increase of membrane permeability due to the RL-insertion mechanism. The interaction of 0.25 mM mono-RL with 3:5:2 GUVs happens mostly by the first mechanism (RL-insertion), on panel C1 on the left of Figure 7.17 is possible to see that the $f_1(t) \approx 15$ and $f_2(t) \approx 5$.

Regarding the results for di-RL, when in concentration 0.06 mM (Figure 7.18), in the Ld phase both process happens with the di-RL-insertion being the most important mechanism ($f_{d1}(t) \approx 6$ and $f_{d2}(t) \approx 2$), with the whole process stabilized after ≈ 100 seconds of experiment (bright red continuous line). For the ternary 3:5:2 GUVs, the plots for 0.06 mM shows that there is interaction with the membrane also in Lo phase, because the dashed and continuous dark red line are stable at ≈ 3. When in contact with 0.12 mM of di-RL (panel B on the right of Figure 7.18) the most important mechanism of interaction with Ld phase was by pore formation, because we see the dotted lines superimposed by the continuous line. The interaction kept growing until the end of the experiment. Also the pore formation is more important when ternary 3:5:2 are in contact with 0.25 mM di-RL, because the dashed line stabilized in $f_1(t) \approx 4$ and dotted line continued to grow following th continuous line $f_1(t)$.

7.5.4 DOPC:SM:CHOL (5:3:2) GUVs with mono and di-rhamnolipids

Figure 7.19 shows microscope images in phase contrast and fluorescence mode of DOPC:SM:CHOL 5:3:2 GUVs in the presence of mono-RL, panels A to C and di-RL, panels D to F. As it was said before, these ternary GUVs do not show Ld-Lo phase separation.

The plots on Figure 7.20 reports the obtained values for the average radius *R* as well as the area *A* and volume *V*. Fitting curves of the time-behavior of *A* and *V* are shown in black solid curves in Figure 7.19 and corresponding fitting parameters are listed in Table 7.5.
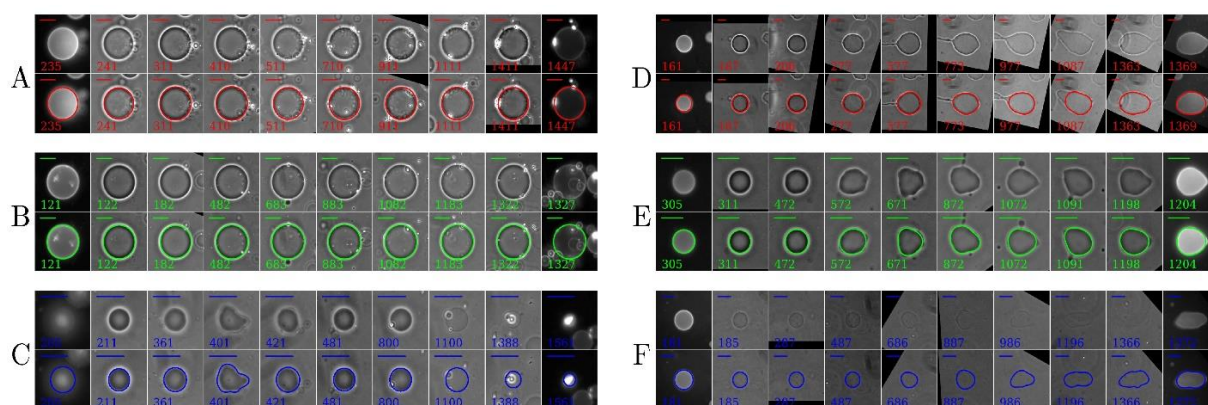

Figure 7.19 Representative DOPC:SM:CHOL (5:3:2) GUV fluorescence and phase contrast images dispersed in 0.06 mM (red), 0.12 mM (green) and 0.25 mM (blue) of mono-RL (panels A, B and C, respectively) and di-RL (panels D, E and F, respectively). See caption of Figure 7.10 for other details.
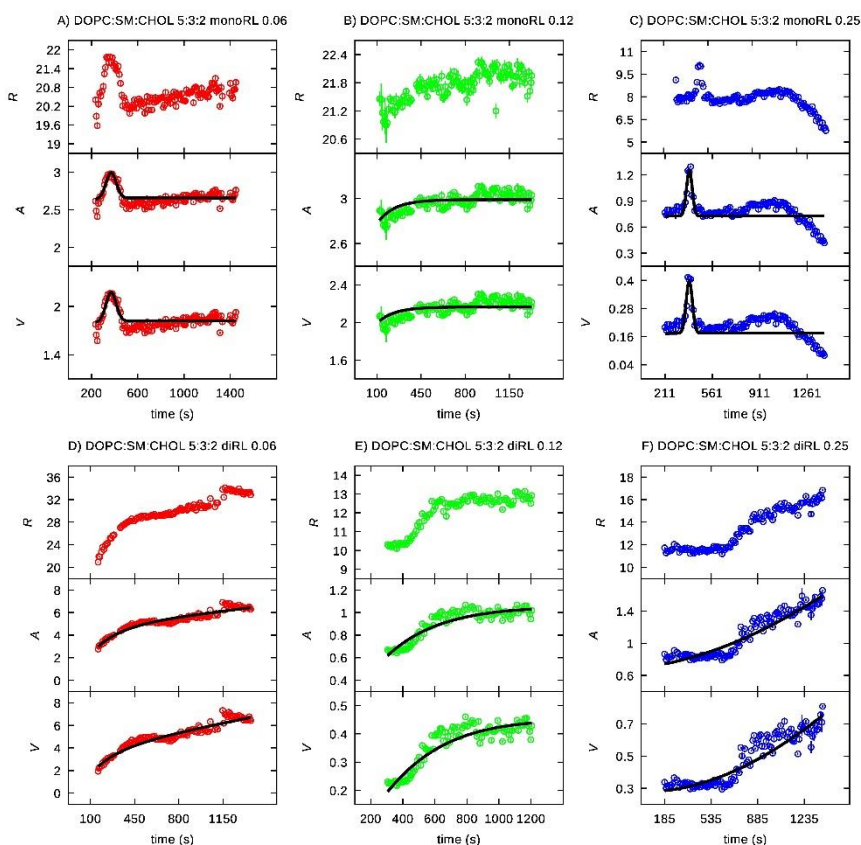
Figure 7.20 . Time-dependence of the geometrical parameters of DOPC:SM:CHOL (5:3:2) GUVs in the presence of 0.06 mM, 0.12 mM and 0.25 mM (red, green and blue circles respectively) of mono-RL (panel A, B and C) and di-RL (panel D, E and F). See the caption of Figure 7.11 for more details

In experiments performed with mono-RL, the response of ternary 5:3:2 GUVs with 0.06 mM was the appearance of bright spots on the surface already at the beginning of the experiment and, after 300 s in contact with mono-RL, the vesicle formed buds (Figure 7.19, panel A). A sharp increase of the GUV dimension is seen (Figure 7.20, panel A), then the GUV area returned to the original value, with a slight increase of its size up to the end of the experiment. The only change on ternary 5:3:2 GUVs in contact with 0.12 mM of mono-RL is the appearance of bright spots after about 180 s and a slight increase of its area (Figures 7.19 and 7.20, panel B), as it was seen in the POPC and ternary 1:1:1 GUVs in contact with mono-RL. When the concentration of mono-RL was increased to 0.25 mM, besides the appearance of bright spots, after 800 s of contact, we observe shape fluctuation, loss of visual contrast and size decrease (Figure 7.19 panel C).

The response of ternary 5:3:2 GUVs to the exposure with 0.06 mM and 0.12 mM di-RL was similar, characterized by size increase, shape fluctuation and buds formation with slight loss of contrast (Figure 7.19, panel D and E). In presence of 0.25 mM di-RL, these GUVs show a strong loss of contrast and fluctuation of size and shape, becoming almost transparent by the end of the experiment

(Figure 7.19, panel F). More in detail, Figure 7.19, panel D-F, shows that at the most concentrate condition (0.25 mM di-RL) the interaction with the vesicle occurs only after 500 s, when both area and volume started to increase, whereas, at 0.06 mM and 0.12 mM, an increase of area and volume was seen already at the beginning of the experiment.

		Mono-RL 0.06	Mono-RL 0.12	Mono-RL 0.25	Di-RL 0.06	Di-RL 0.12	Di-RL 0.25
		A	B	C	D	E	F
1	N_d (10^9)	9.7 ± 0.1	10.0 ± 0.1	2.32 ± 0.02	2.13 ± 0.02	0.197 ± 0.003	2.73 ± 0.03
2	$V_{d(0)}$ $(10^4 \ \mu m^3)$	1.66 ± 0.02	1.81 ± 0.02	0.0647 ± 0.0009	0.011 ± 0.003	0.012 ± 0.003	0.277 ± 0.003
3	λ_{1d} (μm)	0.081 ± 0.001	0.081 ± 0.001	0.0803 ± 0.0008	0.09 ± 0.00	0.00 ± 0.00	0.000 ± 0.000
4	λ_{2d} (μm)	0.0180 ± 0.0002	0.0180 ± 0.0002	0.0180 ± 0.0002	0.0177 ± 0.0003	0.012 ± 0.001	0.0076 ± 0.0002
5	r_{pd} $(Å)$	6.35 ± 0.06	6.36 ± 0.06	6.35 ± 0.06	280 ± 10	487 ± 7	489 ± 5
6	m_d	1.06 ± 0.01	1.08 ± 0.01	1.01 ± 0.01	1.70 ± 0.02	2.56 ± 0.03	1.76 ± 0.02
7	n_d	5.63 ± 0.06	5.63 ± 0.06	5.63 ± 0.06	1.18 ± 0.01	1.00 ± 0.01	1.13 ± 0.01
8	pk_{d1+} $(s^{-1}M^{-md})$	-0.395 ± 0.004	-0.405 ± 0.004	-0.378 ± 0.004	-4.65 ± 0.05	-7.39 ± 0.07	-1.66 ± 0.02
9	pk_{d1-} (s^{-1})	4.74 ± 0.05	4.95 ± 0.05	4.03 ± 0.04	6.30 ± 0.06	6.75 ± 0.07	17.5 ± 0.7
10	pk_{d2+} $(s^{-1}M^{1-nd})$	-49.9 ± 0.5	-50.9 ± 0.5	-47.6 ± 0.5	7.51 ± 0.08	7.78 ± 0.08	5.62 ± 0.09
11	pk_{d2-} (s^{-1})	21.6 ± 0.2	22.0 ± 0.2	20.7 ± 0.2	20.0 ± 0.8	5.13 ± 0.05	16.8 ± 0.4
12	h_A $(10^3 \ \mu m^2)$	0.34 ± 0.03	–	0.53 ± 0.07	–	–	–
13	$t_{A,0}$ (s)	370 ± 4	–	391 ± 4	–	–	–
14	σ_A (s)	44 ± 4	–	21 ± 3	–	–	–
15	h_V $(10^4 \ \mu m^3)$	0.36 ± 0.03	–	0.23 ± 0.03	–	–	–
16	$t_{V,0}$ (s)	370 ± 4	–	390 ± 4	–	–	–
17	σ_V (s)	44 ± 4	–	22 ± 3	–	–	–

Table 7.5 Parameters obtained by the simultaneous best fit of the DOPC:SM:CHOL 5:3:2 GUV areas and volumes shown as solid black lines in Figure 7.19.

Table 7.5 shows that, in the experiments performed with mono-RL, the values of pk_{1+} are very similar, meaning that the tendency for mono-RL to attack to ternary 5:3:2 GUVs are equivalent with different concentrations, 0.06, 0.12 or 0.25 mM. On the other hand, in the presence of di-RL, both mechanisms, RL-insertion and pore formation, were faster at 0.06 mM concentration, because the values pk_{1+} ($\approx$ -4.64) and pk_{2+} (≈ 7.52) were smaller than the ones at 0.12 mM and at 0.25 mM concentration. It is important to notice the difference between the values of pk_{1+} calculated for mono-RL, from ≈ -0.405 to ≈ -0.395, and di-RL, from ≈ -4.64 to ≈ -1.66, which means di-RL are more likely of attaching to the membrane than mono-RL.
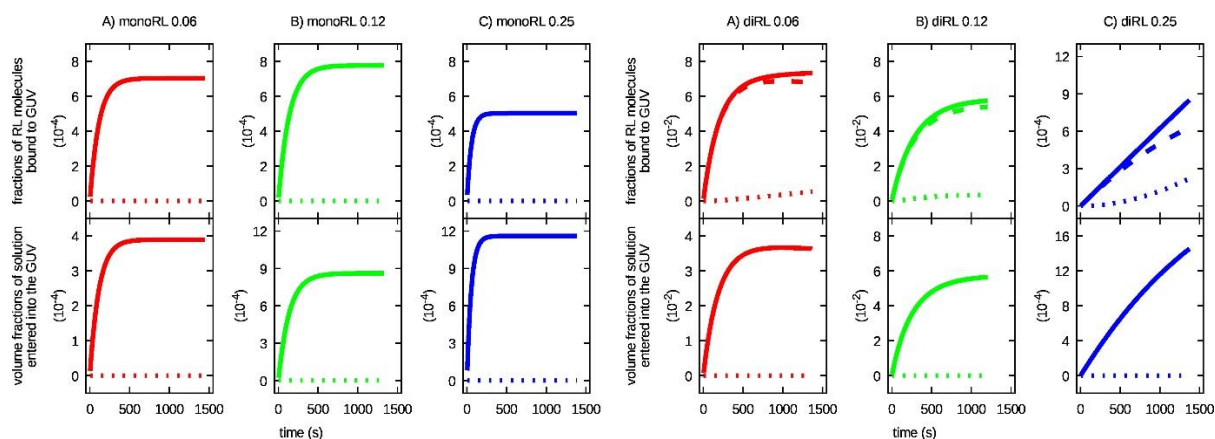
Figure 7.21 Fractions of mono-RL and di-RL molecules bound to GUVs (top panels) and volume fractions of solution entering into GUVs (bottom panels) as a function of time. The color is related to the concentrations: 0.06 mM, red; 0.12 mM, green; 0.25 mM, blue. The line type is related to the different RL:GUV interaction mechanism. See the caption of Figure 7.14 for more details

The plots for ternary 5:3:2 GUVs shows a similar behavior when in contact with 0.06 and 0.12 mM (panels A and B on the left of Figure 7.21) with no pore formation and the lines stabilized at $f(t)$ and $f_1(t) \approx 6$. Also for 0.25 mM the only interaction mono-RL-GUV was by RL insertion, although for this concentration $f(t)$ and $f_1(t)$ stabilized at ≈ 4.

Regarding the interaction 5:3:2 GUVs and di-RL the plots for the experiments with 0.06 and 0.12 mM shows that the most important interaction with the membrane was by insertion and stabilized after 500 seconds, with the dashed lines being almost superimposed by the continuous lines (panel A to C on the right on Figure 7.21). Regarding the interaction with 0.25 mM of di-RL, the lines continued growing until the end of the experiment, with the RL insertion being the most important mechanism. Although the panel F2 shows that the solution enters in the membrane only by the first mechanism with the dashed line being superimposed by the continuous line while the dotted line remained $f_2(t) \approx 0$.

8 Conclusion

During this PhD work, I studied the biophysical properties of the two major types of molecules that compose rhamnolipids: mono and di-rhamnolipids. Rhamnolipids are biosurfactants produced by bacteria *P. aeruginosas*, which have different applications because of their significant tensioactive and emulsifying properties. It is important to investigate the physicochemical properties of mono-RL and di-RL separately to understand their contribution to the characteristics of this important biosurfactant. To this aim, I used techniques such as X-ray diffraction and SAXS. Also phase-contrast and fluorescence mode optical microscopy experiments were performed with GUVs exposed to mono-RL and di-RL, with the aim to investigate the interaction of these biosurfactants with plasma membrane at molecular level and, consequently, to understand their impact in local microbiota of environments as sea water, soils and underground water.

The first step for the realization of this PhD study was the separation of mono-RL and di-RL from the commercial rhamnolipids mixture using a silica gel column chromatography. The purification of both was confirmed by electrospray mass spectroscopy. The samples with purified mono-RL showed mostly molecules with molecular weight of 502 Da, that can be attributed to Rha-C_{10}-$C_{10:1}$, and mostly of molecules of the di-RL samples corresponded to molecular weight of 648 Da, that characterizes the Rha-Rha-C_{10}-$C_{10:1}$. The characterization of mono-RL and di-RL started with the determination of their CMC in water and 0.2 M glucose solution, because this is the solution where GUVs are dispersed to be observed in the microscope. Results indicate that the CMC in 0.2 M glucose solution for mono-RL is 0.062±0.005 mM and for di-RL is 0.028±0.005 mM.

XRD experiments at hydration content up to 45 w/w% have shown that di-RL is much more ordered than mono-RL and forms, at least up to 20 w/w% of water, lamellar phases. The bilayer thicknesses derived for the two molecules were $d_{HH} = 25.8 \pm 0.1$ Å for mono-RL and $d_{HH} = 27.5 \pm 0.1$ Å for di-RL.

SAXS experiments obtained for RL solutions up to 110 mM and, for di-RL, also in the presence of 100 mM NaCl have shown, for the first time, a different micellar behaviour of the two molecules. Di-RLs have a spherocylinder shape, with a length in the order of 300 Å and an aggregation number of approximatively 70. In pure water at pH 7.5 spherocylinders are well separated, due to a low contribution of attractive forces, whereas at 100 mM NaCl long range attractive interactions are more marked. The polar heads of di-RL in the spherocylinder geometry are highly hydrated, contains almost all the sodium counterions, and show an area per hydrated molecule in the order of 800 $Å^2$. However, the area at the polar / apolar interface

of di-RL in this geometry is much lower, in the order of 170 Å^2. Regarding mono-RL, which are much less soluble and, at pH 7.5, do precipitate in the presence of NaCl, our SAXS analysis has shown that they form bicelles, with a radius of the internal flat bilayers in the order of 20 Å. Their interactions are weak, due to the presence of a large amount of sodium counterion among the water that hydrates the polar heads. The overall thickness of the flat domain of the bicelles, including the widely hydrated polar head is in the order of 35 Å, larger than the one obtained by XRD, for samples much more concentrated.

A novel minimal kinetic model of GUV-RL interaction was developed by our study group that was able to fit, in a synergistic way, both the area and the volume variations that were measured from the GUV images as a function of time after the contact between GUV and mono-RL or di-RL. Important parameters that our model is able to calculate are the fractions of RL molecules in contact with the GUVs compared to all the RL molecules present in the samples. The RL-GUV interaction is depicted by two mechanisms: the first concerns single molecules inserted in the outer leaflet of the membrane (*RL-insertion*) and the second concerns molecules that, once bound to the membrane, self-assemble leading to the formation of pores (*pore formation*). This quantitative analysis was applied to GUVs, which are simple model membrane systems of cell-size that mimic biological membranes, interacting with either mono-RL or di-RL.

With the images from the microscope observations in absence of mono-RL and di-RL it is possible to see that both ternary DOPC:SM:CHOL 1:1:1 and 3:5:2 GUVs have Ld-Lo phase coexistence. Otherwise, DOPC:SM:CHOL 5:3:2 GUVs are homogeneous, that is, do not show Ld-Lo phase coexistence, probably because they have mostly DOPC in their composition. The fluorescence probe Rho-PE inserts in the membrane in the Ld phase, mainly formed by DOPC, making it visible with the fluorescence mode optical microscopy.

When POPC GUVs were in contact with mono-RL the only changes on GUVs were the formation of buds, bright spots and a little increase of the size. Although when mixed with di-RL the POPC GUVs showed fluctuation of size and shape, with formation of buds. About the parameters calculated with the kinetic model, the one that measures GUV permeability in terms of solution entering the GUV, via the insertion mechanism, showed difference from mono-RL to di-RL, with the last one promoting increase of the membrane permeability, indicating that di-RL interacts more strongly with these GUVs than mono-RL. The interaction of mono-RL with POPC GUVs by the RL-insertion was faster with 0.06 mM than the higher concentrations. Interestingly the concentration 0.06 mM is under the CMC, presuming a faster rate interaction mono-RL:GUV before the formation of micelles. Also for di-RL the insertion mechanism is higher at the lowest concentration. Although, considering the results for

pore formation, the velocity, once di-RL has penetrated the membrane, is higher at the 0.25 mM.

The ternary 1:1:1 GUVs in contact with mono-RL did not maintain both Ld and Lo phase and the GUVs maintained their circular shape and size during the experiments. In contact with di-RL, differently from the mono-RL experiments, the ternary GUVs show Ld-Lo phase coexistence. The di-RL-GUV interaction occured basically in the Ld domain, since, after the protrusion lost shape and contrast, while Lo remaining practically intact. All the experiments with di-RL have been performed at concentrations above the CMC in 0.2 M glucose (0.028 ±0.005 mM), but even in this conditions, it was possible to observe that the di-RL-GUV interaction increases as the concentration of di-RL grows, both for diRL-insertion and pore formation processes. The concentration effects can be understood considering that the micellar shapes formed by di-RL can change depending on the concentration. It is important to point that the mechanism of pore formation happens faster as the concentrations of di-RL grows, with the whole process going much faster at 0.25 mM di-RL than to 0.06 mM. To note, as it happened with POPC GUVs, it was possible to see a more marked interaction effect of di-RL with DOPC:SM:CHOL 1:1:1 GUV system, when compared with mono-RL.

The DOPC:SM:CHOL 3:5:2 GUVs had a different response comparing with ternary 1:1:1 GUVs in the presence of mono-RL, because maintained the Ld-Lo phase coexistence. The mono-RL promoted the Lo phase outward budding maintaining the size and shape, while the Ld phase developed bright spots. In contact with di-RL, the Ld domain had fluctuation of shape and size with loss of visual contrast, while Lo remains practically intact. The parameters calculated for mono-RL show that, for the Ld phase the velocity of the interaction by the RL-insertion are almost the same for the three concentrations. On the other hand, the value of pore formation showed that this mechanism happened faster when the ternary 3:5:2 GUVs were in contact with 0.25 mM of mono-RL. For the 3:5:2 GUVs interacting with di-RL, the fastest rate of RL-GUV interaction occurs at 0.06 mM. However, as it happened with mono-RL, the pore formation is faster at 0.25 mM concentration.

When ternary 5:3:2 GUVs were in contact with mono-RL, the only changes seen for 0.06 and 0.12 mM concentration was the formation of bright spots. In the presence of 0.25 mM also shape and size fluctuation was seen. In the presence of di-RL these GUVs showed size increase, shape fluctuation and buds formation with loss of contrast. The parameters calculated for this type of GUV shows that, in the experiments performed with mono-RL the different concentrations did not influence in the RL-insertion mechanism. Although, in the presence of di-RL, both mechanisms (RL-insertion and pore formation) happens faster at 0.06 mM concentration. Also the values confirm that di-RL are more likely of attaching to the membrane than mono-RL.

To conclude, the overall picture that emerges can be summarized as follows. The ternary GUVs had

different response in the presence of mono-RL, because while in 3:5:2 GUVs both Lo-Ld phase coexistence is maintained, when in contact with 1:1:1 GUVs they promote lipid mixture. The experiments showed a more marked interaction effect of di-RL in the four types of GUVs than mono-RL. Also, in cases where the lipid bilayer presents phases coexistence, the interaction with di-RL affects significantly the Ld phase. Even if with the results we were able to see that the fraction of mono-RL and di-RL involved in GUV interaction is much lower than the amount that remains in solution, then, once inside the membrane, the fraction of RLs involved in the pore formation is always lower than that dispersed in the GUV membrane. The importance of this work was the introduction of a new methodology to derive from observations with the phase-contrast microscope a kinetic model of interaction between surfactants and model membranes constituted by lipid domains. The method allowed to give a quantitative confirmation of the most relevant interaction of di-RL with GUVs than mono-RL.

We are confident that the data collected in this PhD thesis regarding the ability of mono-RL and di-RL to aggregate and interact with membranes can be useful for the development of advanced biotechnological applications.

9 Bibliography

Abdel-Mawgoud, A. M., Lépine, F., & Déziel, E. (2010). Rhamnolipids: diversity of structures, microbial origins and roles. *Applied microbiology and biotechnology*, 86(5), 1323-1336.

Aislabie, J., Saul, D. J., & Foght, J. M. (2006). Bioremediation of hydrocarbon-contaminated polar soils. *Extremophiles*, *10*(3), 171-179.

Akbari, S., Abdurahman, N. H., Yunus, R. M., Fayaz, F., & Alara, O. R. (2018). Biosurfactants - a new frontier for social and environmental safety: a mini review. *Biotechnology Research and Innovation*, *2*(1), 81-90.

Ampelli, C., Centi, G., Passalacqua, R., & Perathoner, S. (2016). Electrolyte-less design of PEC cells for solar fuels: prospects and open issues in the development of cells and related catalytic electrodes. *Catalysis Today*, *259*, 246-258.

Andrei A. Bunaciu, Elena gabriela Udrištioiu & Hassan Y. Aboul-Enein (2015) X-Ray Diffraction: Instrumentation and Applications, *Critical Reviews in Analytical Chemistry*, 45:4, 289-299

Antoniou, E., Fodelianakis, S., Korkakaki, E., & Kalogerakis, N. (2015). Biosurfactant production from marine hydrocarbon-degrading consortia and pure bacterial strains using crude oil as carbon source. *Frontiers in microbiology*, *6*, 274.

Aranda, F. J., Espuny, M. J., Marqués, A., Teruel, J. A., Manresa, Á., & Ortiz, A. (2007). Thermodynamics of the interaction of a dirhamnolipid biosurfactant secreted by Pseudomonas aeruginosa with phospholipid membranes. *Langmuir*, *23*(5), 2700-2705.

Arino, S., Marchal, R., & Vandecasteele, J. P. (1996). Identification and production of a rhamnolipidic biosurfactant by a Pseudomonas species. *Applied Microbiology and Biotechnology*, *45*(1), 162-168.

Baeurle, S. A., & Kroener, J. (2004). Modeling Effective Interactions of Micellar Aggregates of Ionic Surfactants with the Gauss-Core Potential. *Journal of Mathematical Chemistry*, 36(4), 409–421.

Barathi, S., & Vasudevan, N. (2001). Utilization of petroleum hydrocarbons by Pseudomonas fluorescens isolated from a petroleum-contaminated soil. *Environment international*, *26*(5-6), 413-416.

Bento, F. M., Camargo, F. A. D. O., Okeke, B., & Frankenberger-Júnior, W. T. (2003). Bioremediation of soil contaminated by diesel oil. *Brazilian journal of Microbiology*, *34*, 65-68.

Becher, P. (1965). Physical properties of emulsions. *Emulsions: Theory and Practice. 2nd Ed. Reinhold Publishing Corporation, New York.*

Becker, W. M., Kleinsmith, L. J., Hardin, J., & Bertoni, G. P. (2009). The world of the cell. *Person.*

Britannica, The Editors of Encyclopaedia. "Surfactant". *Encyclopedia Britannica*, Invalid Date, https://www.britannica.com/science/surfactant. Accessed 7 September 2021.

Bhatia, T., Husen, P., Brewer, J., Bagatolli, L. A., Hansen, P. L., Ipsen, J. H., & Mouritsen, O. G. (2015). Preparing giant unilamellar vesicles (GUVs) of complex lipid mixtures on demand: Mixing small unilamellar vesicles of compositionally heterogeneous mixtures. *Biochimica et Biophysica Acta (BBA)-Biomembranes*, *1848*(12), 3175-3180.

Boisselier, E., Demers, E., Cantin, L., & Salesse, C. (2017). How to gather useful and valuable information from protein binding measurements using Langmuir lipid monolayers. *Advances in Colloid and Interface Science*, 243, 60-76.

Chabanon, M., & Rangamani, P. (2018). Solubilization kinetics determines the pulsatory dynamics of lipid vesicles exposed to surfactant. *Biochimica et Biophysica Acta (BBA)-Biomembranes*, 1860(10), 2032-2041.

Chen, M. L., Penfold, J., Thomas, R. K., Smyth, T. J. P., Perfumo, A., Marchant, R., ... & Grillo, I. (2010). Solution self-assembly and adsorption at the air− water interface of the monorhamnose and dirhamnose rhamnolipids and their mixtures. *Langmuir*, 26(23), 18281-18292.

Chen, S., Maksimchuk, A. Umstadter, D. Experimental observation of relativistic nonlinear Thomson scattering. *Nature* 396, 653–655 (1998).

Davidson, M. W., & Abramowitz, M. (2002). Optical microscopy. *Encyclopedia of imaging science and technology*, *2*(1106-1141), 120.

Desai, J. D., & Banat, I. M. (1997). Microbial production of surfactants and their commercial potential. *Microbiology and Molecular biology reviews*, *61*(1), 47-64.

Eby, G.N. (2004), Principles of Environmental Geochemistry. *Brooks/Cole-Thomson Learning*, 212-214.

Edwards, K. R., Lepo, J. E., & Lewis, M. A. (2003). Toxicity comparison of biosurfactants and synthetic surfactants used in oil spill remediation to two estuarine species. *Marine Pollution Bulletin*, *46*(10), 1309-1316.

Etkin, D. S., & Welch, J. (1997). Oil Spill Intelligence Report International Oil Spill Database: Trends In Oil Spill Volumes And Frequency1. In *International Oil Spill Conference* (Vol. 1997, No. 1, pp. 949-951). American Petroleum Institute.

Feigenson, G. W. (2007). Phase boundaries and biological membranes. *Annu. Rev. Biophys. Biomol. Struct.*, *36*, 63-77.

Frankenberger Jr, W. T. (1992). Hydrocarbon contaminated soils and groundwater. v. 2. *Chelsea: Lewis Publishers*, 237-293

Frolov, V. A., Shnyrova, A. V., & Zimmerberg, J. (2011). Lipid polymorphisms and membrane shape. *Cold Spring Harbor perspectives in biology*, *3*(11), a004747.

Griebler, C., & Avramov, M. (2015). Groundwater ecosystem services: A review. Freshwater Science, 34, 355–367.

Gudiña, E. J., Rodrigues, A. I., Alves, E., Domingues, M. R., Teixeira, J. A., & Rodrigues, L. R. (2015). Bioconversion of agro-industrial by-products in rhamnolipids toward applications in enhanced oil recovery and bioremediation. *Bioresource technology*, *177*, 87-93.

Guinier, A., Fournet, G., & Yudowitch, K. L. (1955). Small-angle scattering of X-rays.

Haines, T. H. (1994). Water transport across biological membranes. *FEBS letters*, *346*(1), 115-122.

Hishida, M., Seto, H., & Yoshikawa, K. (2005). Smooth/rough layering in liquid-crystalline/gel state of dry phospholipid film, in relation to its ability to generate giant vesicles. *Chemical physics letters*, 411(1-3), 267-272.

Ho, C. S., Lam, C. W. K., Chan, M. H. M., Cheung, R. C. K., Law, L. K., Lit, L. C. W., ... & Tai, H. (2003). Electrospray ionisation mass spectrometry: principles and clinical applications. *The Clinical Biochemist Reviews*, *24*(1), 3.

Hommel, R. K. (1994). Formation and function of biosurfactants for degradation of water-insoluble substrates. In *Biochemistry of microbial degradation* (pp. 63-87). Springer, Dordrecht.

Hošková, M., Ježdík, R., Schreiberová, O., Chudoba, J., Šír, M., Čejková, A., Masák J., Jirků V., Řezanka, T. (2015). Structural and physiochemical characterization of rhamnolipids produced by Acinetobacter calcoaceticus, Enterobacter asburiae and Pseudomonas aeruginosa in single strain and mixed cultures. *Journal of biotechnology*, *193*, 45-51.

Howe, J., Bauer, J., Andrä, J., Schromm, A. B., Ernst, M., Rössle, M., ... & Brandenburg, K. (2006). Biophysical characterization of synthetic rhamnolipids. *The FEBS journal*, *273*(22), 5101-5112.

Hung, H. C., & Shreve, G. S. (2001). Effect of the hydrocarbon phase on interfacial and thermodynamic properties of two anionic glycolipid biosurfactants in hydrocarbon/water systems. *The Journal of Physical Chemistry B*, *105*(50), 12596-12600.

Jarvis, F. G., & Johnson, M. J. (1949). A glyco-lipide produced by Pseudomonas aeruginosa. *Journal of the American Chemical Society*, *71*(12), 4124-4126.

Karlapudi, A. P., Venkateswarulu, T. C., Tammineedi, J., Kanumuri, L., Ravuru, B. K., ramu Dirisala, V., & Kodali, V. P. (2018). Role of biosurfactants in bioremediation of oil pollution-a review. *Petroleum*, *4*(3), 241-249.

Kostorz, G. (1991). Small-angle scattering studies of phase separation and defects in inorganic materials. Journal of Applied Crystallography, 24(5), 444-456.

Lang, S., Wagner, F. (1987). Structure and properties of biosurfactants. *Kosaric, N., Cairns, W.L., Gray, N.C.C. (Eds.), Biosurfactants and Biotechnology*, 21–45.

Lasic, D. (1993). Liposomes. *American Scientist*, *80*(1), 20-31.

Lebrón-Paler, A., Pemberton, J. E., Becker, B. A., Otto, W. H., Larive, C. K., & Maier, R. M. (2006). Determination of the acid dissociation constant of the biosurfactant monorhamnolipid in aqueous solution by potentiometric and spectroscopic methods. *Analytical chemistry*, *78*(22), 7649-7658.

Lingwood, D., & Simons, K. (2010). Lipid rafts as a membrane-organizing principle. *science*, *327*(5961), 46-50.

Liu, Z., Zeng, Z., Zeng, G., Li, J., Zhong, H., Yuan, X., ... & Xie, G. (2012). Influence of rhamnolipids and Triton X-100 on adsorption of phenol by Penicillium simplicissimum. *Bioresource technology*, *110*, 468-473.

Liu Y., Zhong H., Liu Z., Jiang Y., Tan F., Zeng G., He Y. (2014). Purification and characterization of the biosurfactant rhamnolipid. *Chinese journal of chromatography*, *32*(3), 248-255.

Lytvynenko, L.M. & Prosvirnin, Sergey & Schuenemann, K.. (2005). Wave Diffraction by Periodic Multilayered Structures. *Radio Phys. Radio Astron.,* 10.

Manley, S., & Gordon, V. D. (2008). Making giant unilamellar vesicles via hydration of a lipid film. *Current protocols in cell biology*, *40*(1), 24-3.

Malik, Z.A.; Ahmed, S. Degradation of petroleum hydrocarbons by oil field isolated bacterial consortium. Afr. J. Biotechnol. 2012, 11, 650–658.

Margesin, R., & Schinner, F. (1999). Biological decontamination of oil spills in cold environments. *Journal of Chemical Technology & Biotechnology*, *74*(5), 381-389.

Martiradonna, L. A photograph of crystal order. *Nature* 511, 7 (2014).

Mateo, M. P., Nicolas, G., Piñon, V., Ramil, A., & Yañez, A. (2005). Laser cleaning: an alternative method for removing oil-spill fuel residues. *Applied surface science*, *247*(1-4), 333-339.

Mitra S. and Roy P. BTEX: a serious groundwater contaminant. Res. J. Environ. Sci., 5 (2011), pp. 394-398.

Mueller, J. G., Cerniglia, C. E., & Pritchard, P. H. (1996). Bioremediation of environments contaminated by polycyclic aromatic hydrocarbons. *Biotechnology Research Series*, *6*, 125-194.

Mukherjee, P. K. (2019). Bioassay-Guided Isolation and Evaluation of Herbal Drugs. *Quality Control and Evaluation of Herbal Drugs. Elsevier*, 515-537.

Mulligan, C. N. (2005). Environmental applications for biosurfactants. *Environmental pollution*, *133*(2), 183-198.

Mulligan, C.N., Gibbs, B.F. (1993). Factors influencing the economics of biosurfactants. *Kosaric, N. (Ed.), Biosurfactants, Production, Properties, Applications*, 329–371.

Nam, K., Chung, N., Alexander, M., 1998. Relationship between organic matter content of soil and the sequestration of phenanthrene. *Environmental Science and Technology 32*, 785-788.

Nakama Y. (2017) Chapter 15 - Surfactants, Editor(s): Kazutami Sakamoto, Robert Y. Lochhead, Howard I. Maibach, Yuji Yamashita, *Cosmetic Science and Technology*, 231-244.

Okoh, A. I.; Trejo-Hernandez, M. R. (2006). Remediation of petroleum hydrocarbon polluted systems: exploiting the bioremediation strategies. *African Journal of Biotechnology*, v. 5, n. 25,.

Ornitz, B., Champ, M. (2002). Oil spills first principles: prevention and best response, Elsevier.

Pao-Wen G.L., Tsung C.C., Chih-Hung C., Ming-Zhi W., Han-Wei H. (2013) Effects of soil organic matter and bacterial community shift on bioremediation of diesel-contaminated soil, *International Biodeterioration & Biodegradation,* 85, 661-670.

Pauw, B. R. (2013). Everything SAXS: small-angle scattering pattern collection and correction. *Journal of Physics: Condensed Matter*, *25*(38), 383201.

Pedersen, J. S. (1997). Analysis of small-angle scattering data from colloids and polymer solutions: modeling and least-squares fitting. *Advances in colloid and interface science*, 70, 171-210.

Peker, S., Helvacı, Ş., & Özdemir, G. (2003). Interface− Subphase Interactions of Rhamnolipids in Aqueous Rhamnose Solutions. *Langmuir*, *19*(14), 5838-5845.

Perinelli, D. R., Cespi, M., Lorusso, N., Palmieri, G. F., Bonacucina, G., & Blasi, P. (2020). Surfactant self-assembling and critical micelle concentration: one approach fits all?. *Langmuir*, *36*(21), 5745-5753.

Perinelli, D. R., Vllasaliu, D., Bonacucina, G., Come, B., Pucciarelli, S., Ricciutelli, Casettari, L. (2017). Rhamnolipids as epithelial permeability enhancers for macromolecular therapeutics. *European Journal of Pharmaceutics and Biopharmaceutics*, *119*, 419-425.

Raei, E., Nikoo, M. R., & Pourshahabi, S. (2017). A multi-objective simulation-optimization model for in situ bioremediation of groundwater contamination: application of bargaining theory. *Journal of Hydrology*, *551*, 407-422.

Rangel-Yagui, C., Pessoa-Jr, A., & Blankschtein, D. (2004). Two-phase aqueous micellar systems: an alternative method for protein purification. *Brazilian Journal of Chemical Engineering*, *21*, 531-544

Reeves, J. P., & Dowben, R. M. (1969). Formation and properties of thin-walled phospholipid vesicles. *Journal of cellular physiology*, *73*(1), 49-60.

Rikalović, M. G., Vrvić, M. M., & Karadžić, I. M. (2015). Rhamnolipid biosurfactant from Pseudomonas aeruginosa: from discovery to application in contemporary technology. *Journal of the Serbian Chemical Society*, *80*(3), 279-304.

Rosen M.J.; Kunjappu, J.T. Surfactants and interfacial phenomena. John Wiley & Sons, 2012.

Ryland, A. L. (1958). X-ray diffraction. Volume 35:2. Presented as part of the Symposium on An Analysis Group inan Industrial Research Organization before the Divisions of Chemical Education and Analytical Chemistry at the 130th Meeting of the American Chemical Society.

Sánchez M, Aranda FJ, Espuny MJ, Marqués A, Teruel JA, Manresa Á, Ortiz A (2007) Aggregation behaviour of a dirhamnolipid biosurfactant secreted by Pseudomonas aeruginosa in aqueous media. J Colloid Interf Sci 307:246–253

Schneider, C. A., Rasband, W. S., & Eliceiri, K. W. (2012). NIH Image to ImageJ: 25 years of image analysis. *Nature methods*, *9*(7), 671-675.

Schindler, H. (1980). Introduction to Biological Membranes - A good chance missed, Mahendra Kumar Jain, Roger Curtis Wagner (Eds.), John Wiley and Sons, New York and Basel (1980), p. xiii+ 382, 0 471 03471 1.

Seklemova, E.; Pavlova, A.; Kovacheva, K. Biostimulation-based bioremediation of diesel fuel: Field demonstration. Biodegrad., 12:311-316, 2001.

Shao B., Liu Z., Zhong H., Zeng G., Liu G., Yu M., Zhao C. (2017). Effects of rhamnolipids on microorganism characteristics and applications in composting: a review. *Microbiological research*, *200*, 33-44.

Shastri, L., & Sumant, O. (2018). Surfactants market by type (cationic, anionic, nonionic, amphoteric, and others) and application (household detergent, personal care, industrial & institutional cleaner, oilfield chemical, agricultural chemical, food processing, paint & coating, adhesive. *Global Opportunity Analysis and Industry Forecast*, *2025*, 1-311.

Sherma, J., & Fried, B. (Eds.). (2003). *Handbook of thin-layer chromatography*. CRC press.

Shull, C. G., & Roess, L. C. (1947). X-Ray Scattering at Small Angles by Finely-Divided Solids. I. General Approximate Theory and Applications. *Journal of Applied Physics*, *18*(3), 295-307.

Silva, E.J.; Rocha e Silva, N.M.P.; Rufino, R.D.; Luna, J.M.; Silva, R.O.; Sarubbo, L.A. Characterization of a biosurfactant produced by Pseudomonas cepacia CCT6659 in the presence of industrial wastes and its application in the biodegradation of hydrophobic compounds in soil. *Colloids Surf. B Biointerfaces* 2014, 117, 36–41.

Silva, R. D. C. F., Almeida, D. G., Rufino, R. D., Luna, J. M., Santos, V. A., & Sarubbo, L. A. (2014). Applications of biosurfactants in the petroleum industry and the remediation of oil spills. *International journal of molecular sciences*, *15*(7), 12523-12542.

Spinozzi, F., & Amaral, L. Q. (2016). Pore model in the melting regime of a lyotropic biomembrane with an anionic phospholipid. *Langmuir*, *32*(50), 13556-13565.

Spinozzi, F., Paccamiccio, L., Mariani, P., & Amaral, L. Q. (2010). Melting regime of the anionic phospholipid DMPG: new lamellar phase and porous bilayer model. *Langmuir*, *26*(9), 6484-6493.

Srivastava, N., Singh, A., Kumari, P., Nishad, J. H., Gautam, V. S., Yadav, M., ... & Kharwar, R. N. (2021). Advances in extraction technologies: isolation and purification of bioactive compounds from biological materials. In *Natural Bioactive Compounds* (pp. 409-433). Academic Press.

Swaminathan, J., & Ehrhardt, C. (2011). Liposomes for pulmonary drug delivery. In *Controlled pulmonary drug delivery* (pp. 313-334). Springer, New York, NY.

Tahara, Y., & Fujiyoshi, Y. (1994). A new method to measure bilayer thickness: cryo-electron microscopy of frozen hydrated liposomes and image simulation. *Micron*, *25*(2), 141-149.

Tcholakova, S., Denkov, N. D., & Lips, A. (2008). Comparison of solid particles, globular proteins and surfactants as emulsifiers. *Physical Chemistry Chemical Physics*, *10*(12), 1608-1627.

Testa, S. M., & Winegardner, D. L. (1991). Aquifer restoration and soil remediation alternatives. Restoration of Petroleum contaminated Aquifers, Lewis Publishers Inc. MI, USA, 153-190.

Thavasi, R., Jayalakshmi, S., & Banat, I. M. (2011). Effect of biosurfactant and fertilizer on biodegradation of crude oil by marine isolates of Bacillus megaterium, Corynebacterium kutscheri and Pseudomonas aeruginosa. *Bioresource technology*, *102*(2), 772-778.

Touchstone, J. C. (1992). *Practice of thin layer chromatography*. John Wiley & Sons.

Tsumoto, K., Matsuo, H., Tomita, M., & Yoshimura, T. (2009). Efficient formation of giant liposomes through the gentle hydration of phosphatidylcholine films doped with sugar. *Colloids and Surfaces B: Biointerfaces*, *68*(1), 98-105.

Veatch, S. L., & Keller, S. L. (2005). Seeing spots: complex phase behavior in simple membranes. *Biochimica et Biophysica Acta (BBA)-Molecular Cell Research*, *1746*(3), 172-185

Vidali, M. "Bioremediation. An overview: " *Pure and Applied Chemistry*, vol. 73, no. 7, 2001, pp. 1163-1172.

Vilcáez, J., Li, L., & Hubbard, S. S. (2013). A new model for the biodegradation kinetics of oil droplets: application to the Deepwater Horizon oil spill in the Gulf of Mexico. *Geochemical transactions*, *14*(1), 1-14.

Walde P., Cosentino K., Enge, H., Stano P. (2010). Giant vesicles: preparations and applications. *ChemBioChem*, *11*(7), 848-865.

Watanabe, K. (2001). Microorganisms relevant to bioremediation. *Current opinion in biotechnology*, *12*(3), 237-241.

Williams, T. & Kelley, C. (2011). Gnuplot 4.5: an interactive plotting program. URL http://gnuplot.info.

Yoon, J. H., & Shoemaker, C. A. (1999). Comparison of optimization methods for ground-water bioremediation. Journal of Water Resources Planning and Management, 125(1), 54-63.

Zhang YM, Miller RM (1994) Effect of a Pseudomonas rhamnolipid biosurfactant on cell hydrophobicity and biodegradation of octadecane. Appl Environ Microbiol 60:2101–2106.

Zhong, H., Zeng, G.M., Liu, J.X. *et al.* Adsorption of monorhamnolipid and dirhamnolipid on two *Pseudomonas aeruginosa* strains and the effect on cell surface hydrophobicity. *Appl Microbiol Biotechnol* 79, 671–677 (2008).

10 Appendix

10.1 Determination of the molecular parameters of the GUV:RL systems

We consider a GUV formed by mixing n lipid molecules ($\mathbf{L}_i$, with $i=1,n$), according to mixing mole ratios x_i. In our case $\mathbf{L}_i$ can be POPC, DOPC, SM or CHOL. Hence the average molecule constituting the GUV will be represented by the formula $(1/\sum_i x_i)\,\mathbf{L}_{1,x_1}\mathbf{L}_{2,x_2}\dots\mathbf{L}_{n,x_n}$, hereafter shortly indicated by $\mathbf{E}$. If the GUV shows L_d–L_o phase separation, we can distinguish, among the n molecules, n_d molecules that form the L_d phase and n_o molecules that form the L_o phase. In particular, the average molecule constituting the L_d phase of the GUV will be represented by the formula $(1/\sum_{i\in L_d} x_i)\,\mathbf{L}_{i_1,x_{i_1}}\mathbf{L}_{i_2,x_{i_2}}\dots\mathbf{L}_{i_{n_d},x_{i_{n_d}}}$, being $i_1,i_2,\dots$ the indexes of the n_d molecules that form the L_d phase. We indicate this formula by $\mathbf{E}_d$ Likewise, the average molecule constituting the L_o phase of the GUV has the formula $(1/\sum_{i\in L_o} x_i)\,\mathbf{L}_{i_1,x_{i_1}}\mathbf{L}_{i_2,x_{i_2}}\dots\mathbf{L}_{i_{n_o},x_{i_{n_o}}}$, being $i_1,i_2,\dots$ the indexes of the n_o molecules that form the L_o phase. We call in short this formula $\mathbf{E}_o$. Let M_i and a_i the molecular weight and the area per polar head of the i-molecule. On this basis, we can calculate the average molecular weight and the average area per polar head by referring to the effective molecule $\mathbf{E}$ forming the whole GUV (a and M, respectively) as well as to both the molecules $\mathbf{E}_d$ forming the GUV L_d phase (a_d and M_d, respectively) and the molecules $\mathbf{E}_o$ forming the GUV L_o phase (a_o and M_o, respectively),

Equation 10.1

$$M = \frac{\sum_i M_i x_i}{\sum_i x_i} \qquad a = \frac{\sum_i a_i x_i}{\sum_i x_i}$$
$$M_{\mathrm{d}} = \frac{\sum_{i \in \mathrm{L_d}} M_i x_i}{\sum_{i \in \mathrm{L_d}} x_i} \qquad a_{\mathrm{d}} = \frac{\sum_{i \in \mathrm{L_d}} a_i x_i}{\sum_{i \in \mathrm{L_d}} x_i}$$
$$M_{\mathrm{o}} = \frac{\sum_{i \in \mathrm{L_o}} M_i x_i}{\sum_{i \in \mathrm{L_o}} x_i} \qquad a_{\mathrm{o}} = \frac{\sum_{i \in \mathrm{L_o}} a_i x_i}{\sum_{i \in \mathrm{L_o}} x_i}$$

The molar concentration of the lipid mixture with formula $\mathbf{E}$ forming the whole GUV is $C=c/M$, where c is the total w/v lipid concentration. Hence the molar concentrations of the lipids with formulas $\mathbf{E_d}$ and $\mathbf{E_o}$ that form the $\mathrm{L_d}$ and the $\mathrm{L_o}$ phases, respectively, are

Equation 10.2

$$C_{\mathrm{d}} = C \frac{\sum_{i \in \mathrm{L_d}} x_i}{\sum_i x_i} \qquad C_{\mathrm{o}} = C \frac{\sum_{i \in \mathrm{L_o}} x_i}{\sum_i x_i}$$

with the straightforwad condition $C=C_{\mathrm{d}}+C_{\mathrm{o}}$. If C_{RL} is the molar concentration of RL (monoRL or diRL, depending on the sample), we can also calculate the nominal ratio ζ between the RL molecules in the sample and the lipid molecules $\mathbf{E}$ forming the GUV as well as the nominal ratios of the RL molecules in the sample referred to the lipid molecules $\mathbf{E_d}$ and $\mathbf{E_d}$, respectively,

Equation 10.3

$$\zeta = \frac{C_{\mathrm{RL}}}{C} \qquad \zeta_{\mathrm{d}} = \frac{C_{\mathrm{RL}}}{C_{\mathrm{d}}} \qquad \zeta_{\mathrm{o}} = \frac{C_{\mathrm{RL}}}{C_{\mathrm{o}}}$$

Notice that the condition $\zeta^{-1}=\zeta_{\mathrm{d}}^{-1}+\zeta_{\mathrm{o}}^{-1}$ holds.

GUV system	Letters	C_{RL}	C	C_{d}	C_{o}	a	a_{d}	a_{o}	ζ	ζ_{d}	ζ_{o}
		mM	μM	μM	μM	Å^2	Å^2	Å^2			
POPC	A,D	0.06	3.76	3.76	–	63.5	63.5	–	15.9	15.9	–
POPC	B,E	0.12	3.76	3.76	–	63.5	63.5	–	31.9	31.9	–
POPC	C,F	0.25	3.76	3.76	–	63.5	63.5	–	66.4	66.4	–
DOPC:SM:CHOL 1:1:1	A,D	0.06	4.56	1.52	3.04	45.3	64.0	36.0	13.2	39.5	19.7
DOPC:SM:CHOL 1:1:1	B,E	0.12	4.56	1.52	3.04	45.3	64.0	36.0	26.3	78.9	39.5
DOPC:SM:CHOL 1:1:1	C,F	0.25	4.56	1.52	3.04	45.3	64.0	36.0	54.8	164.4	82.2
DOPC:SM:CHOL 3:5:2	A,D	0.06	4.22	1.27	2.95	47.1	64.0	39.9	14.2	47.4	20.3
DOPC:SM:CHOL 3:5:2	B,E	0.12	4.22	1.27	2.95	47.1	64.0	39.9	28.4	94.8	40.6
DOPC:SM:CHOL 3:5:2	C,F	0.25	4.22	1.27	2.95	47.1	64.0	39.9	59.2	197.5	84.6

		CRL	a	ad	ao	C	Cd	Co	ζ	ζd	ζo
DOPC:SM:CHOL 5:3:2	A,D	0.06	4.25	2.13	2.13	50.9	64.0	37.8	14.1	28.2	28.2
DOPC:SM:CHOL 5:3:2	B,E	0.12	4.25	2.13	2.13	50.9	64.0	37.8	28.2	56.4	56.4
DOPC:SM:CHOL 5:3:2	C,F	0.25	4.25	2.13	2.13	50.9	64.0	37.8	58.8	117.6	117.6

Table 10.1 Molar concentrations, areas per polar heads and nominal RL-to-lipid ratios of all the investigated GUV-RL systems. Letters refer to figures and tables of the main text. CRL is the molar concentration of either monoRL or diRL. C is the molar concentration of **E**, the average lipid molecule forming the GUV. Cd and Co are the molar concentrations of **E**d and **E**o, the average lipids molecules that, in the case of phase-separation, form the disordered and the ordered phase of the GUV, respectively. a, ad and ao are the areas per polar head of **E**, **E**d and **E**o, respectively. ζ, ζd and ζo are the RL-to-**E**, RL-to-**E**d and RL-to-**E**o nominal molar ratios, respectively.

In Table 10.1 molar concentrations, areas per polar heads and nominal RL-to-lipid ratios of all the investigated GUV-RL systems are listed.

10.2 Collection of all microscope GUV images analyzed with asymmetric contour method

After the GUVs were mixed with a solution of either mono-RL or di-RL, about 1200 snapshots were recorded for each microscope observation. Then, to analyze the images with the novel kinetic model, 120 snapshots were chosen from each experiment, selecting the images with a 10 seconds interval. The selected images can be seen in Figures 10.1 to 10.24. The line around the GUVs correspond to the shape analysis with the macros and the color correspond to the concentrations: red for 0.06 mM, green for 0.12 mM and blue for 0.25 mM.
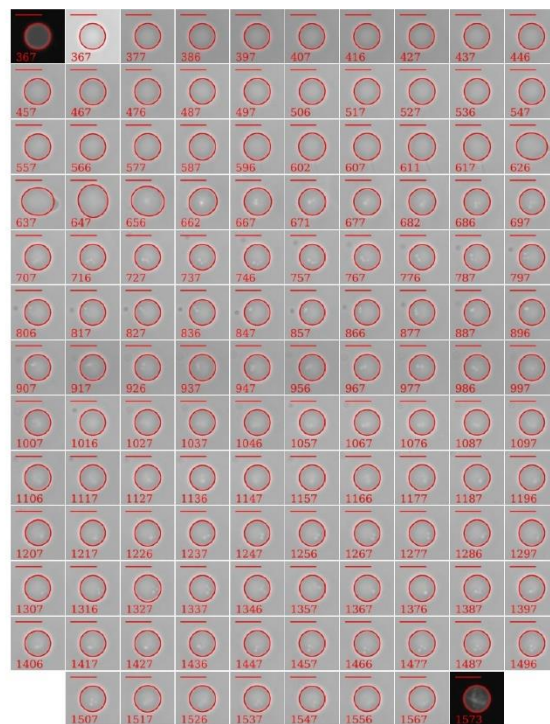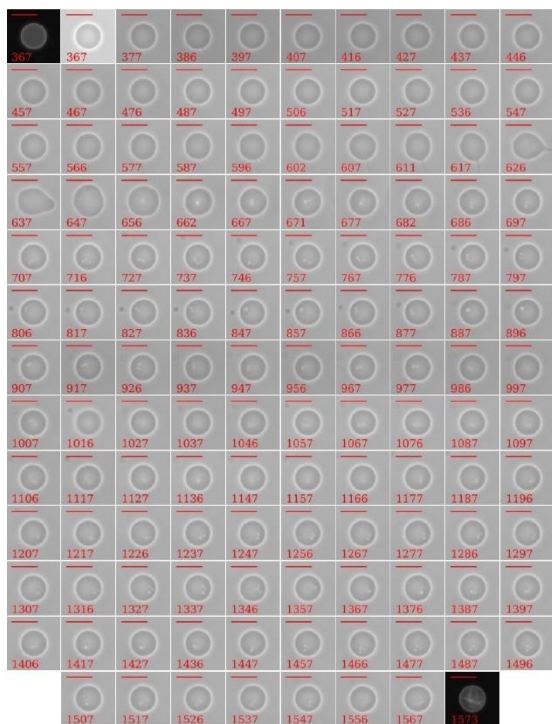
Figure 10.1 Microscope POPC GUV images (left) and best fit contours (right) in the presence of 0.06 mM mono-RL.
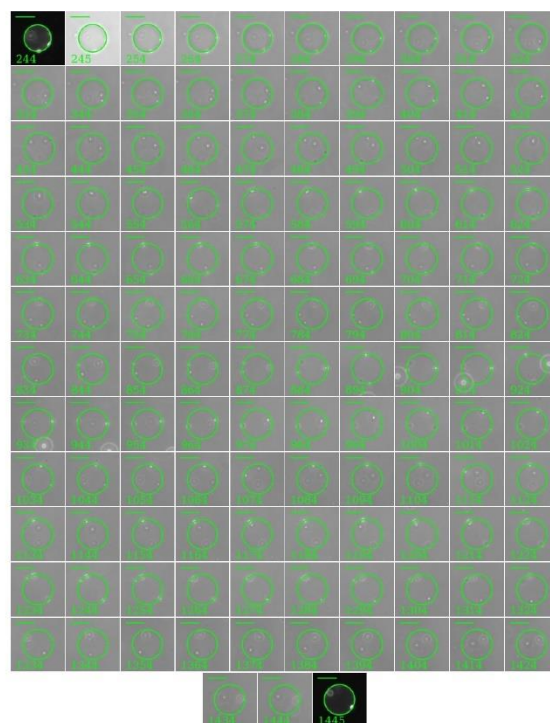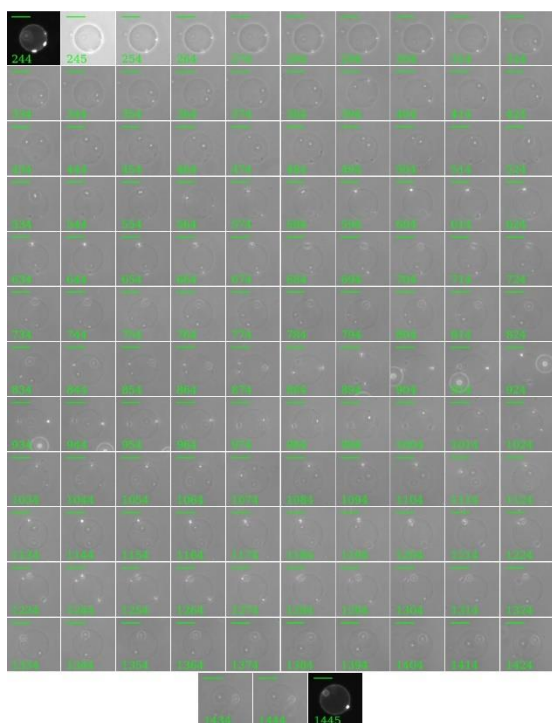
Figure 10.2 Microscope POPC GUV images (left) and best fit contours (right) in the presence of 0.12 mM mono-RL.
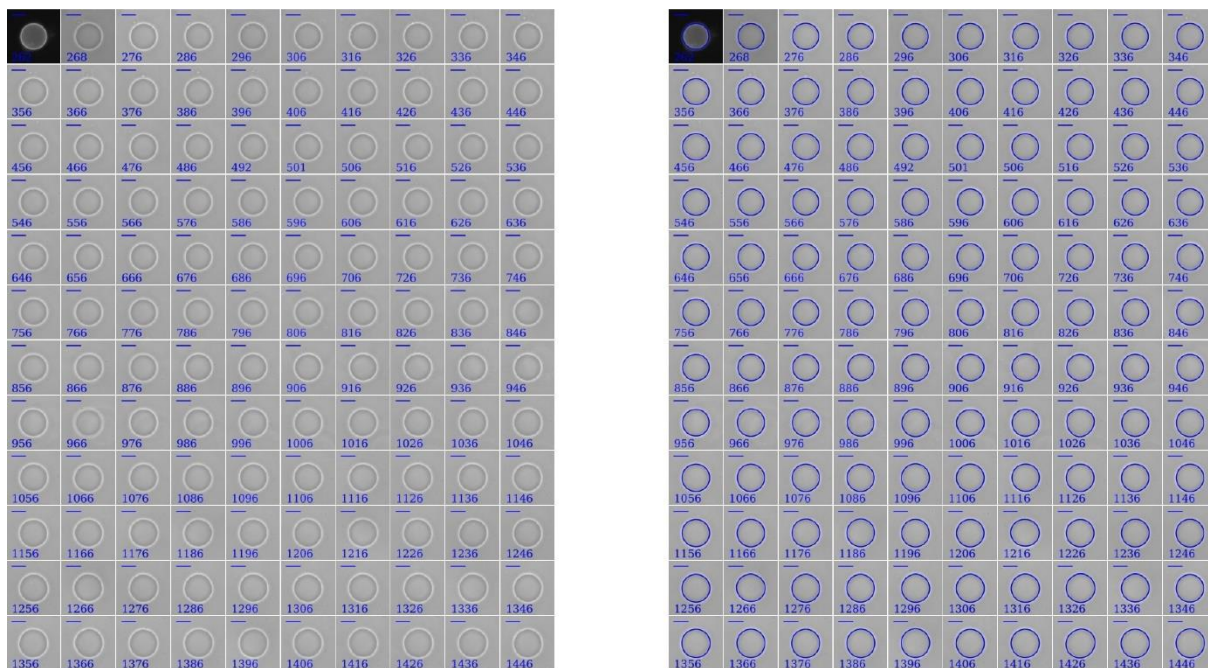
Figure 10.3 Microscope POPC GUV images (left) and best fit contours (right) in the presence of 0.25 mM mono-RL.
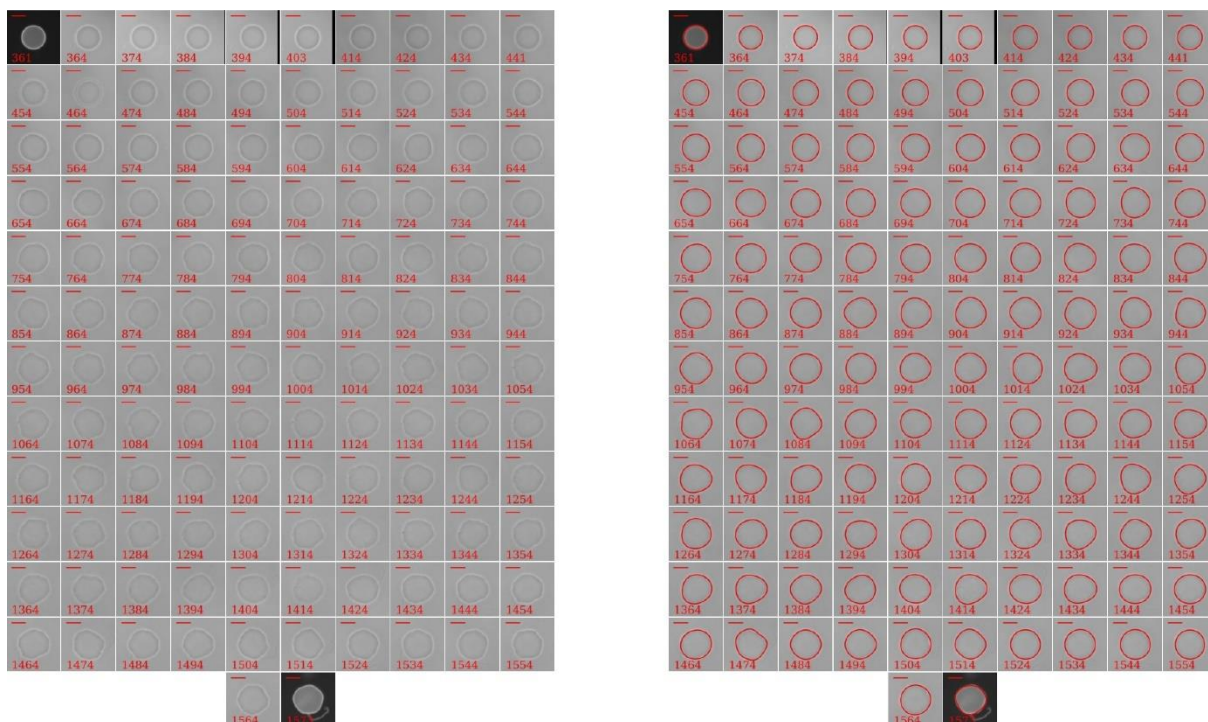
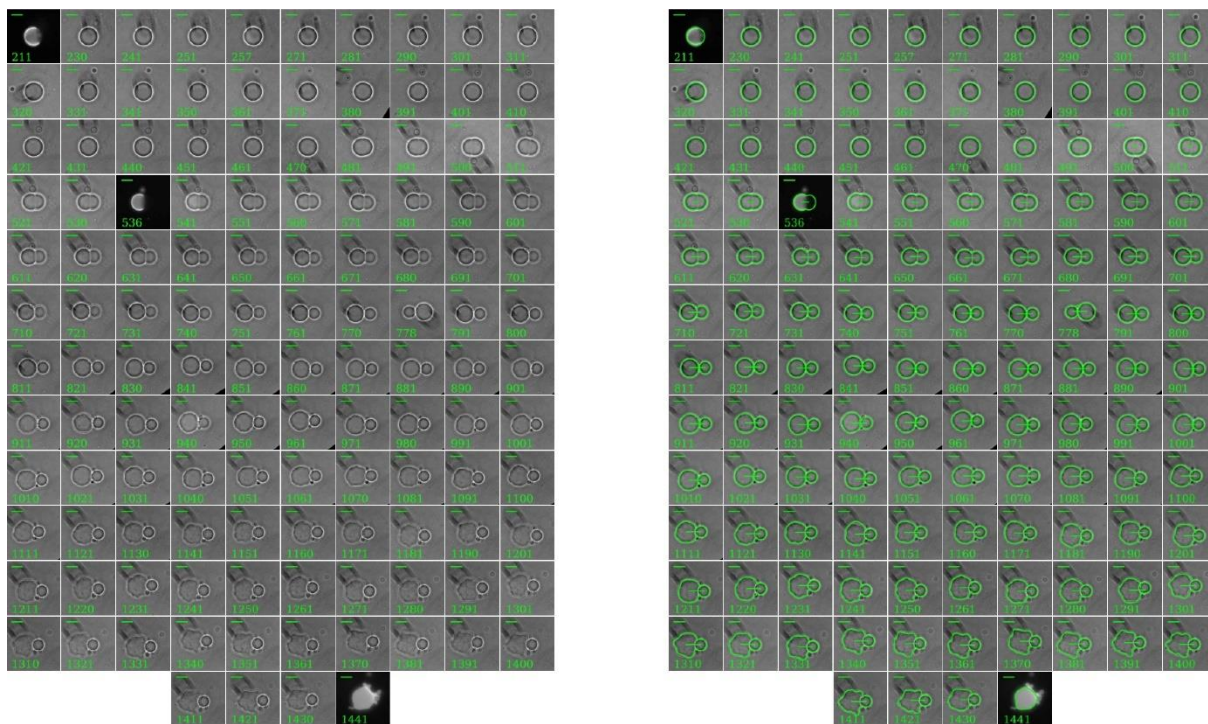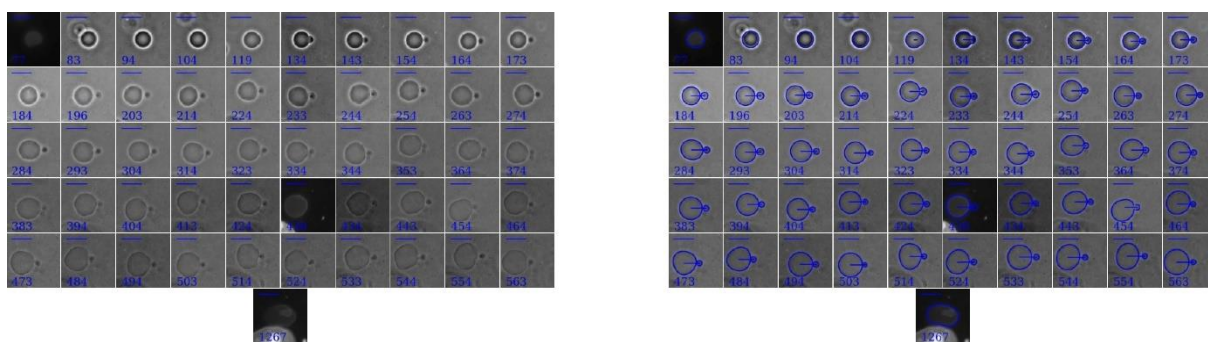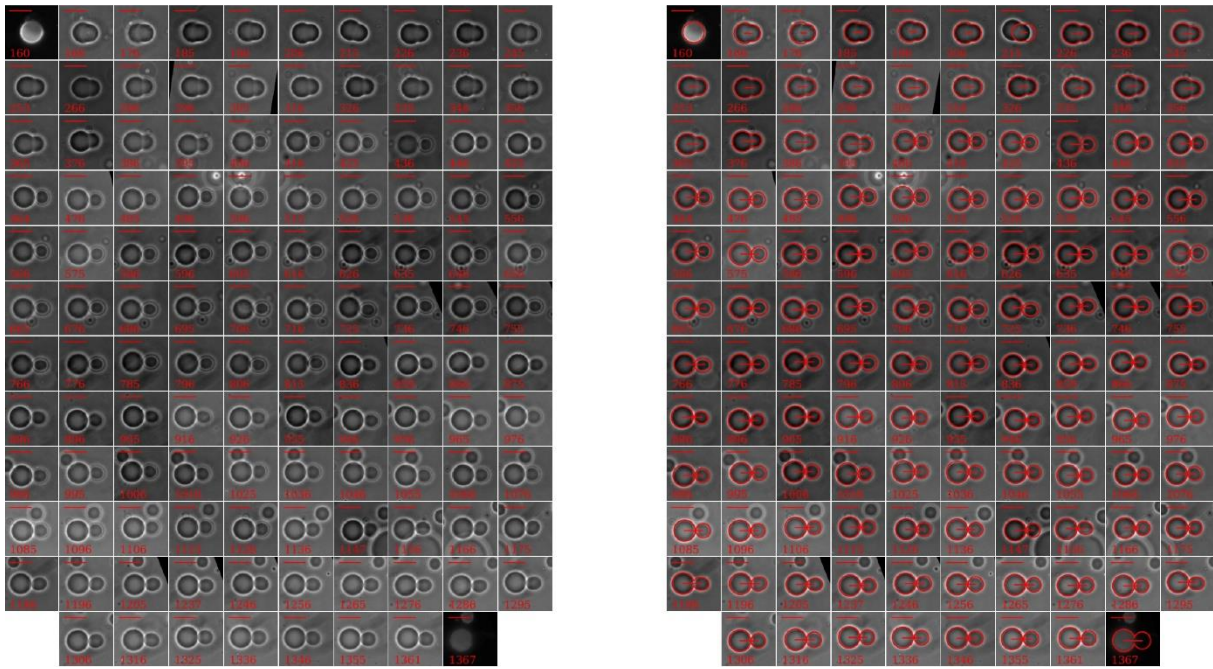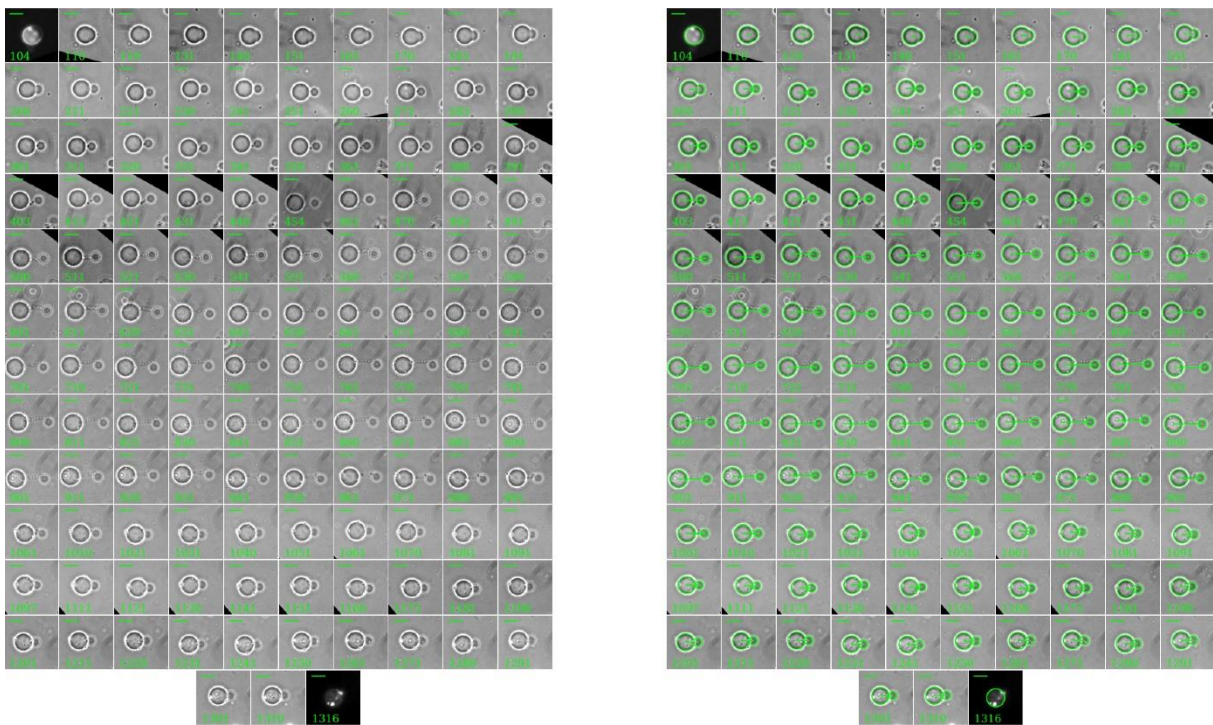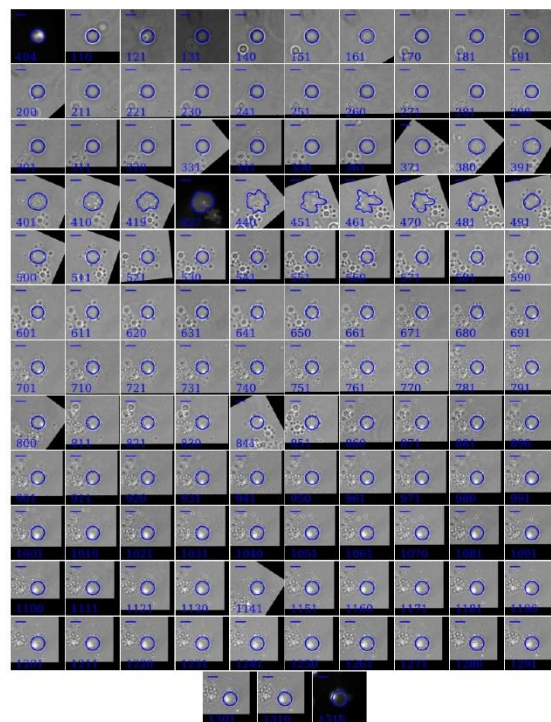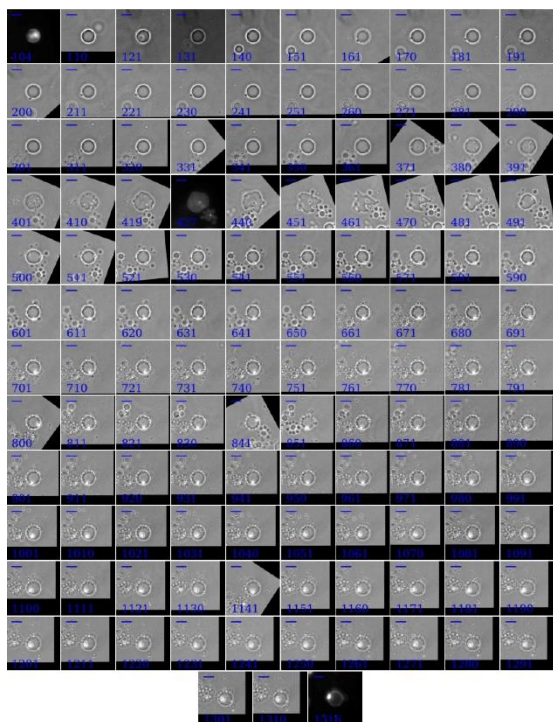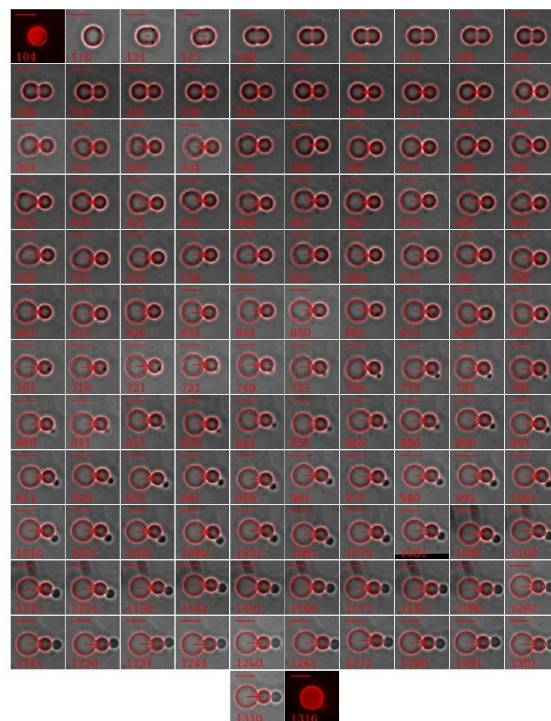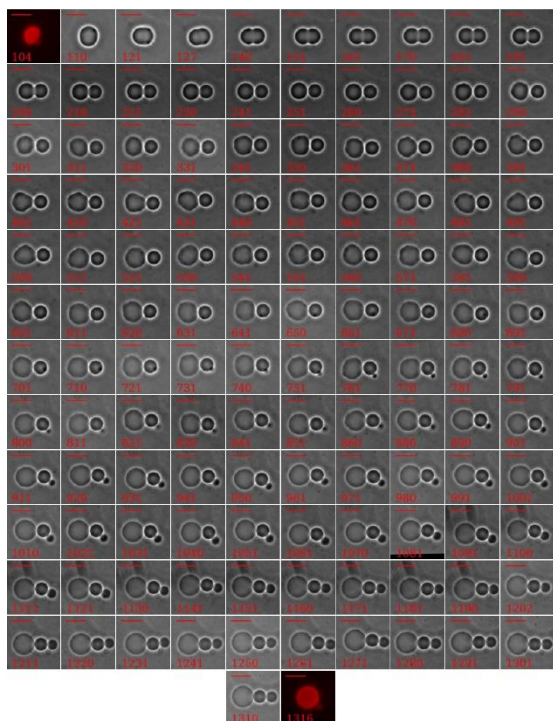Figure 10.4 Microscope POPC GUV images (left) and best fit contours (right) in the presence of 0.06 mM di-RL.
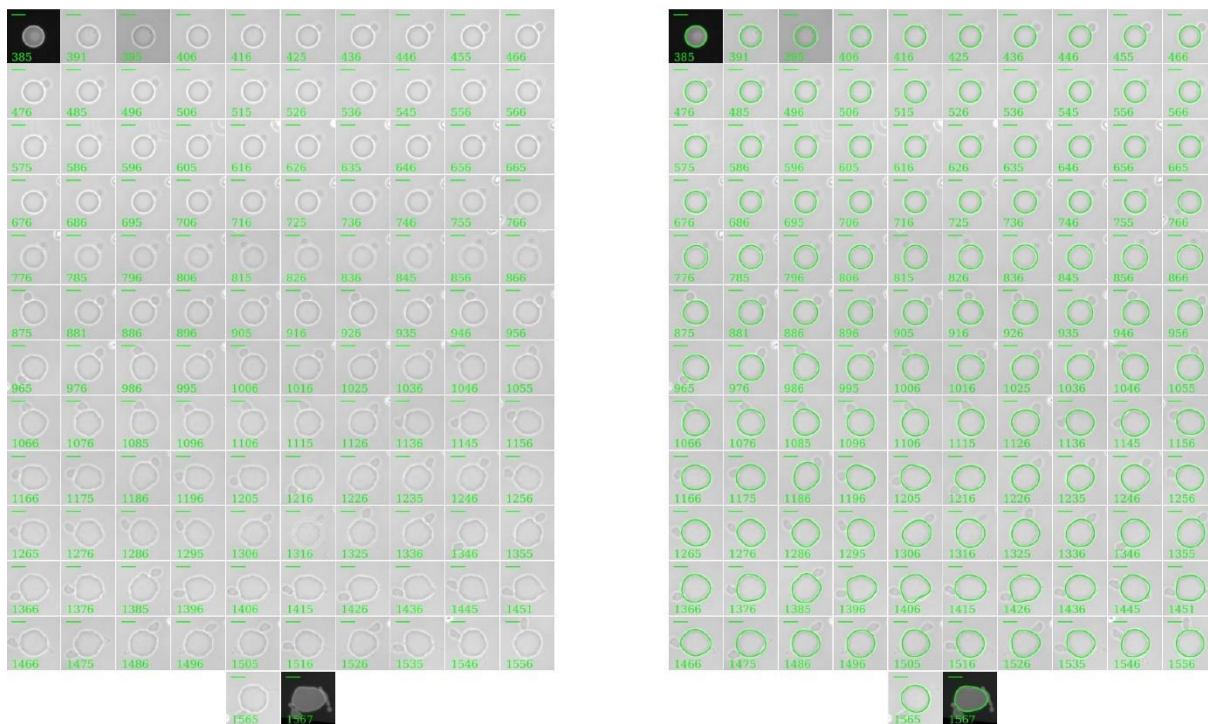
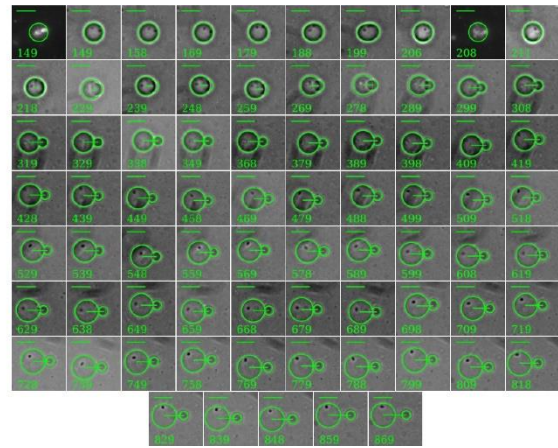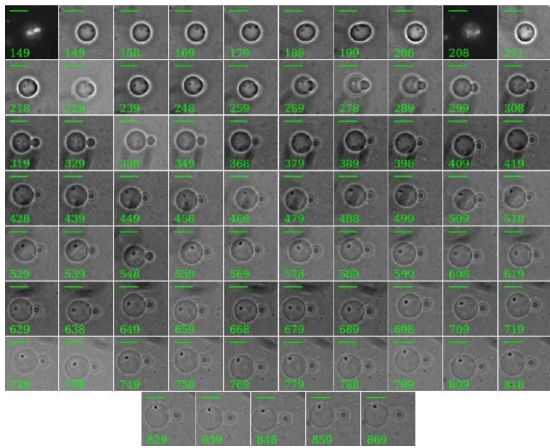Figure 10.5 Microscope POPC GUV images (left) and best fit contours (right) in the presence of 0.12 mM di-RL.
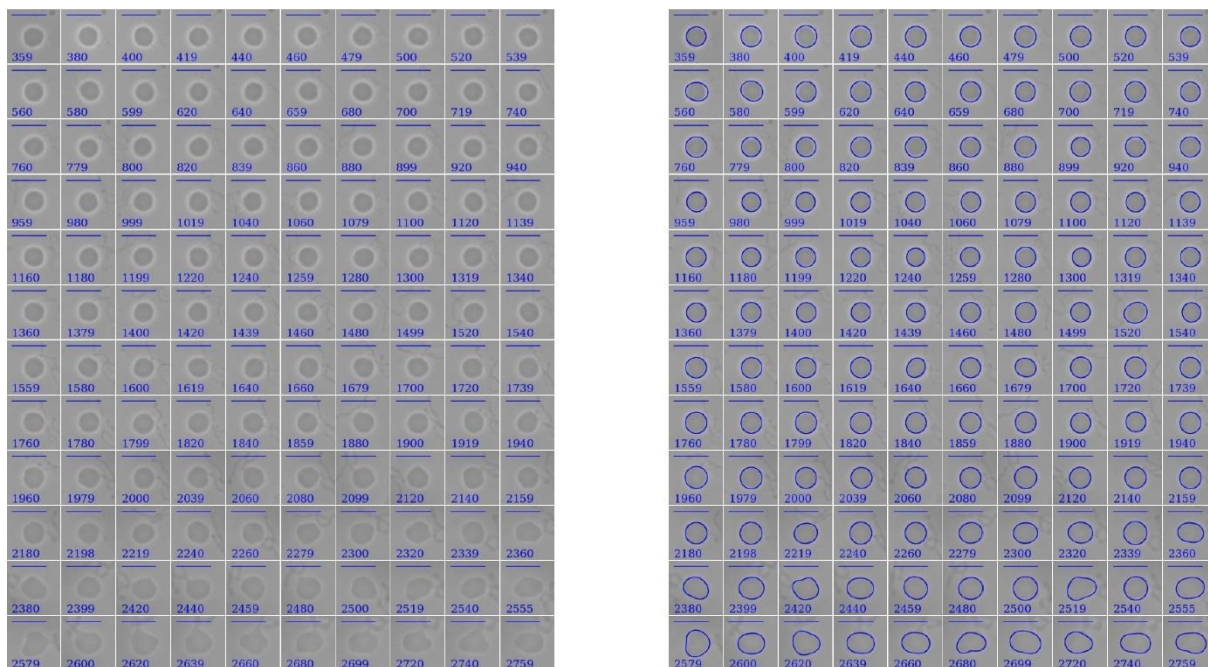
Figure 10.6 Microscope POPC GUV images (left) and best fit contours (right) in the presence of 0.25 mM di-RL.
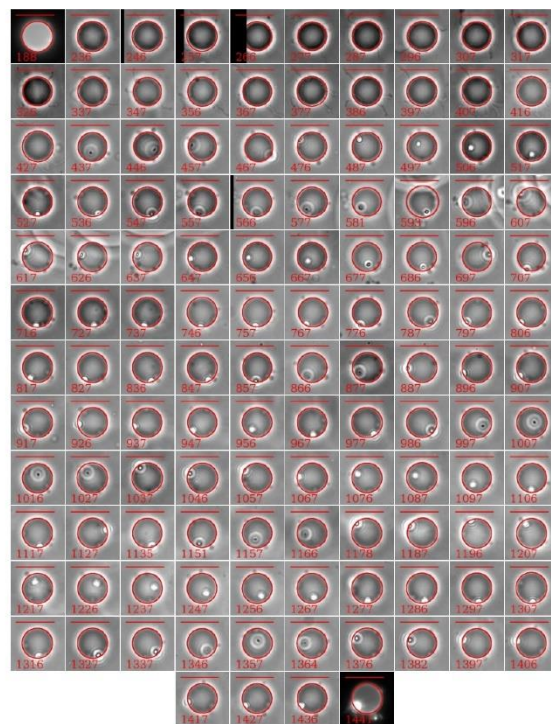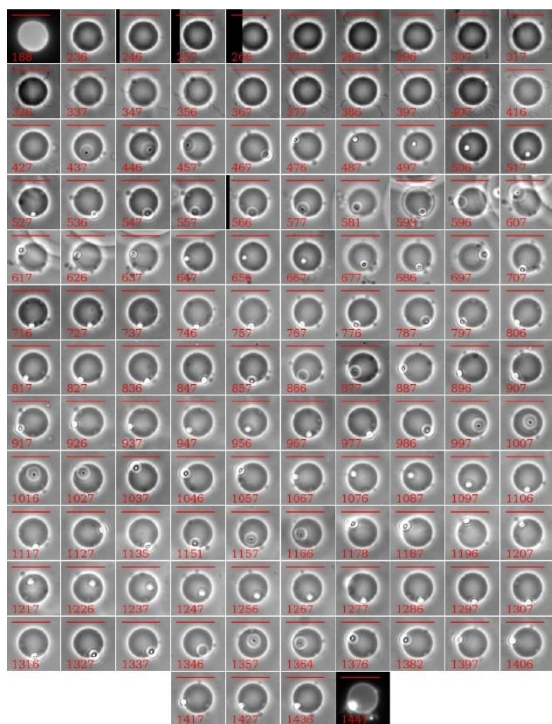
Figure 10.7 Microscope POPC GUV images (left) and best fit contours (right) in the presence of 0.25 mM di-RL.
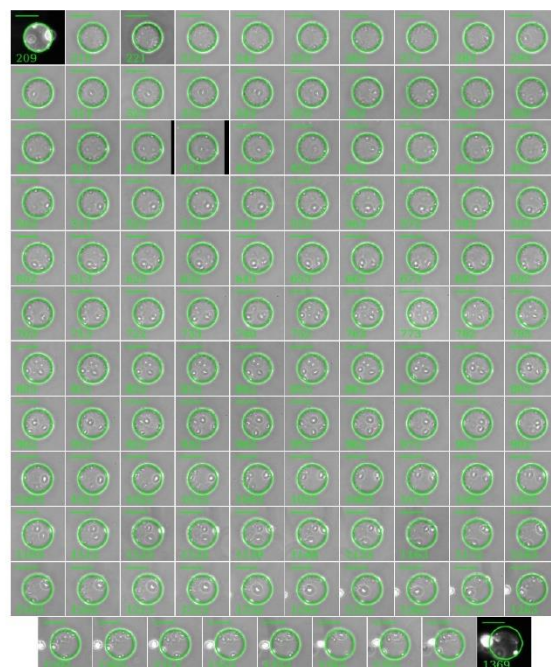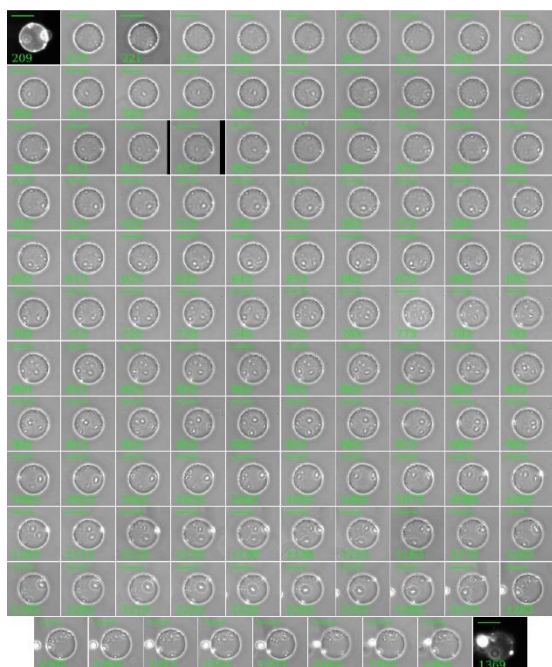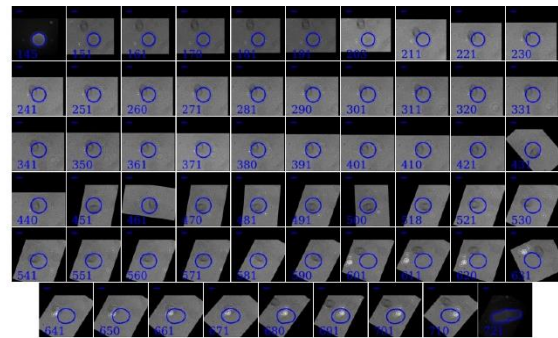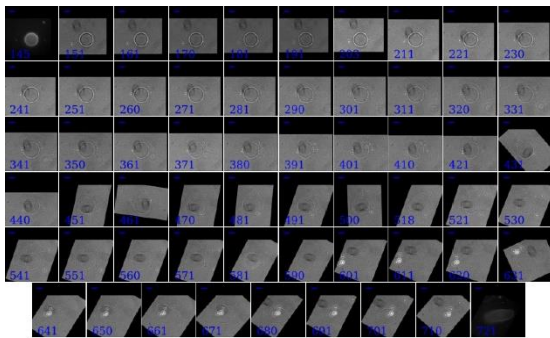

Figure 10.8 Microscope DOPC:SM:CHOL 1:1:1 GUV images (left) and best fit contours (right) in the presence of 0.12 mM mono-RL.
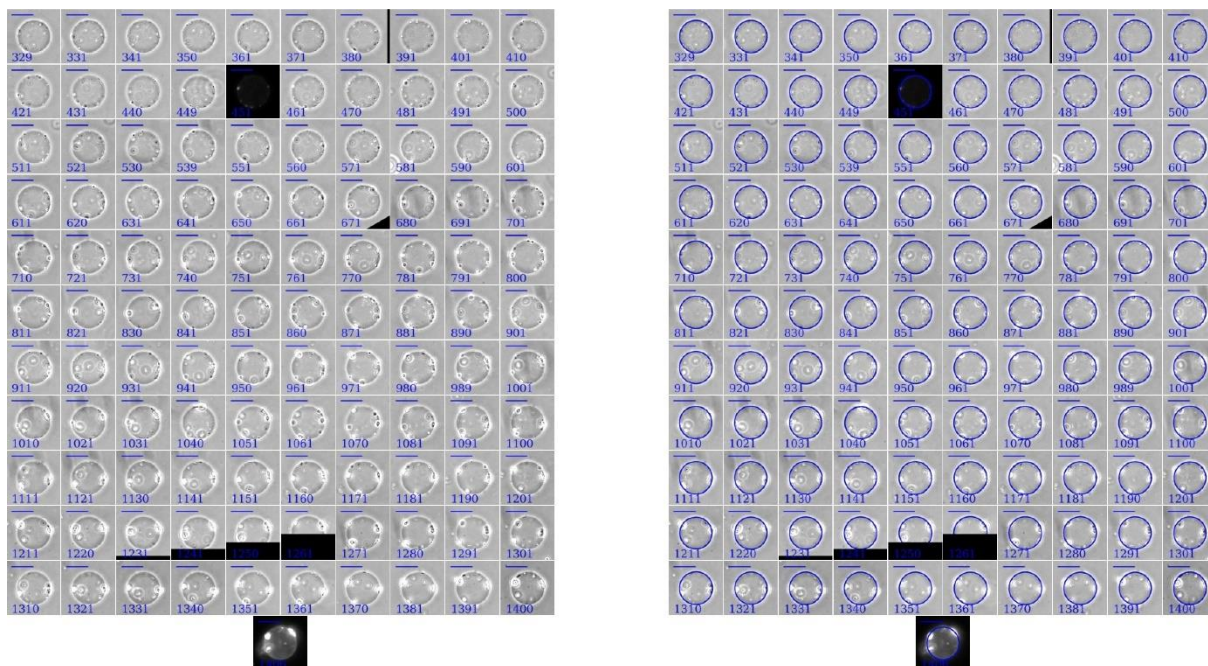
Figure 10.9 Microscope DOPC:SM:CHOL 1:1:1 GUV images (left) and best fit contours (right) in the presence of 0.25 mM mono-RL.
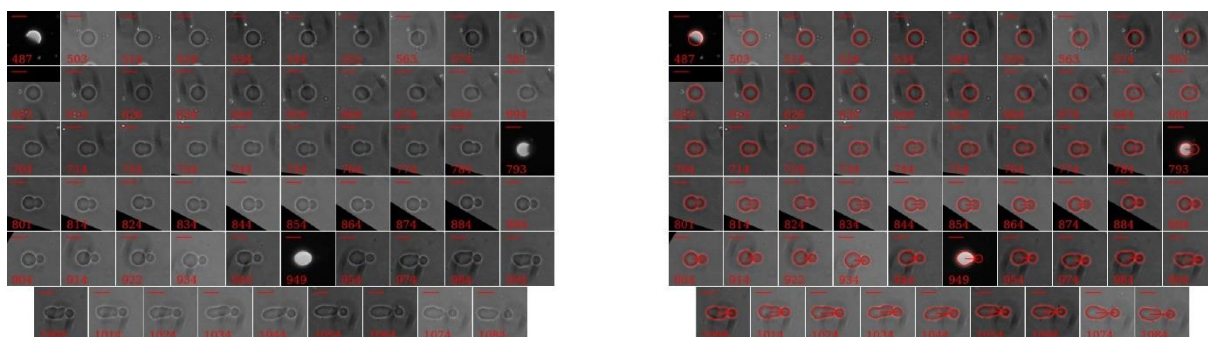
Figure 10.10 Microscope DOPC:SM:CHOL 1:1:1 GUV images (left) and best fit contours (right) in the presence of 0.06 mM di-RL.

Figure 10.11 Microscope DOPC:SM:CHOL 1:1:1 GUV images (left) and best fit contours (right) in the presence of 0.12 mM di-RL.

Figure 10.12 Microscope DOPC:SM:CHOL 1:1:1 GUV images (left) and best fit contours (right) in the presence of 0.25 mM di-RL.
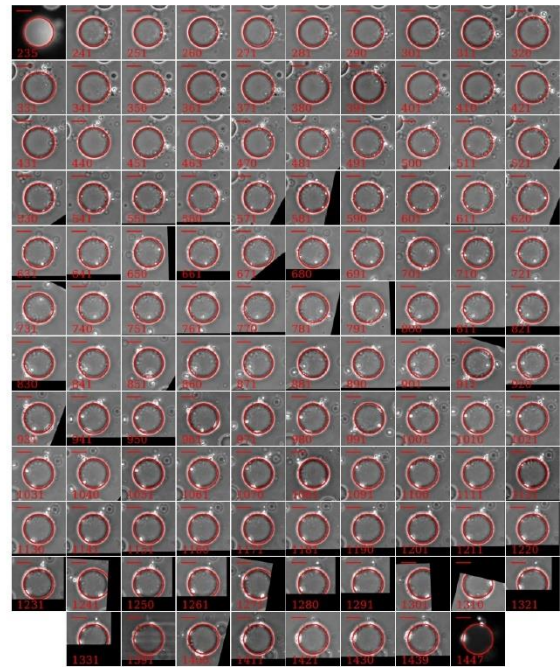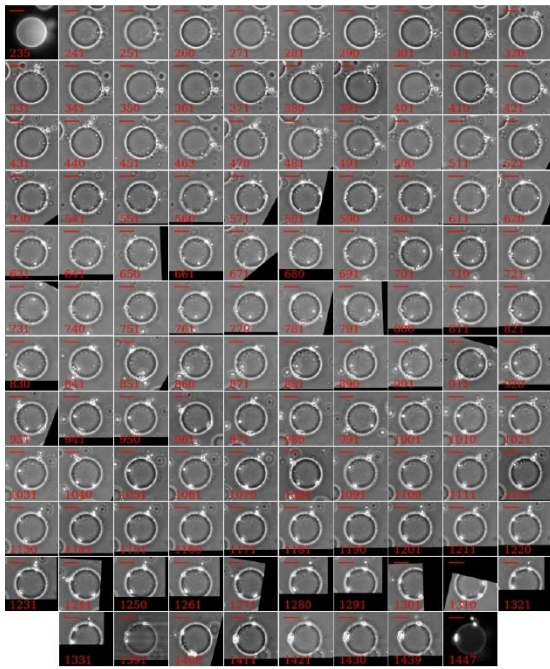
Figure 10.13 Microscope DOPC:SM:CHOL 3:5:2 GUV images (left) and best fit contours (right) in the presence of 0.06 mM mono-RL.
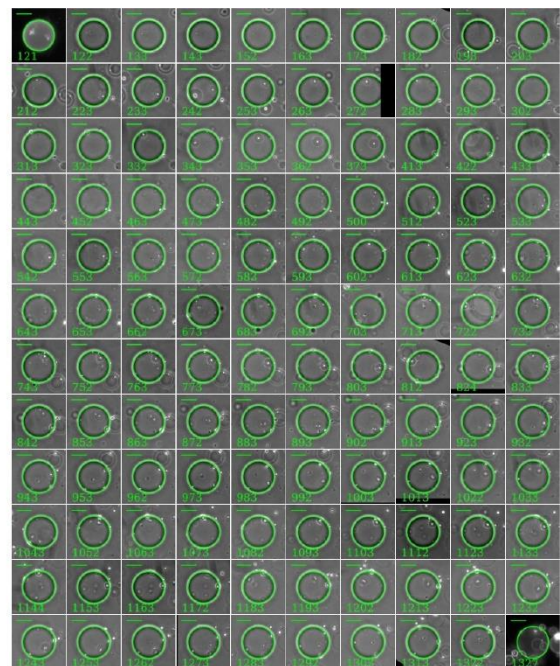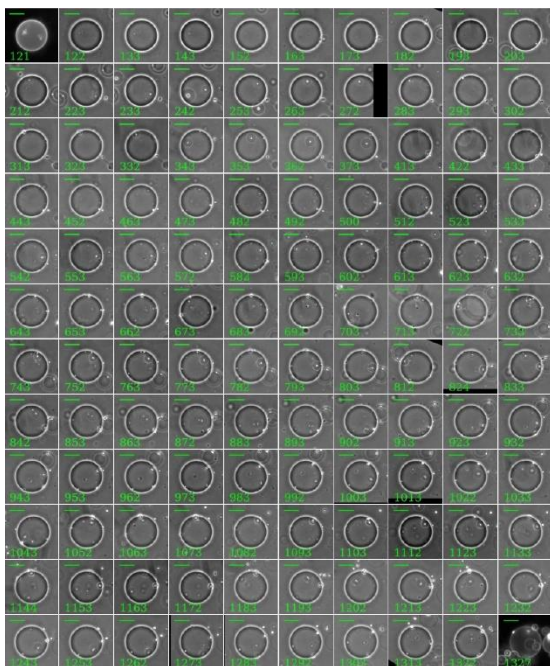

Figure 10.14 Microscope DOPC:SM:CHOL 3:5:2 GUV images (left) and best fit contours (right) in the presence of 0.12 mM mono-RL.
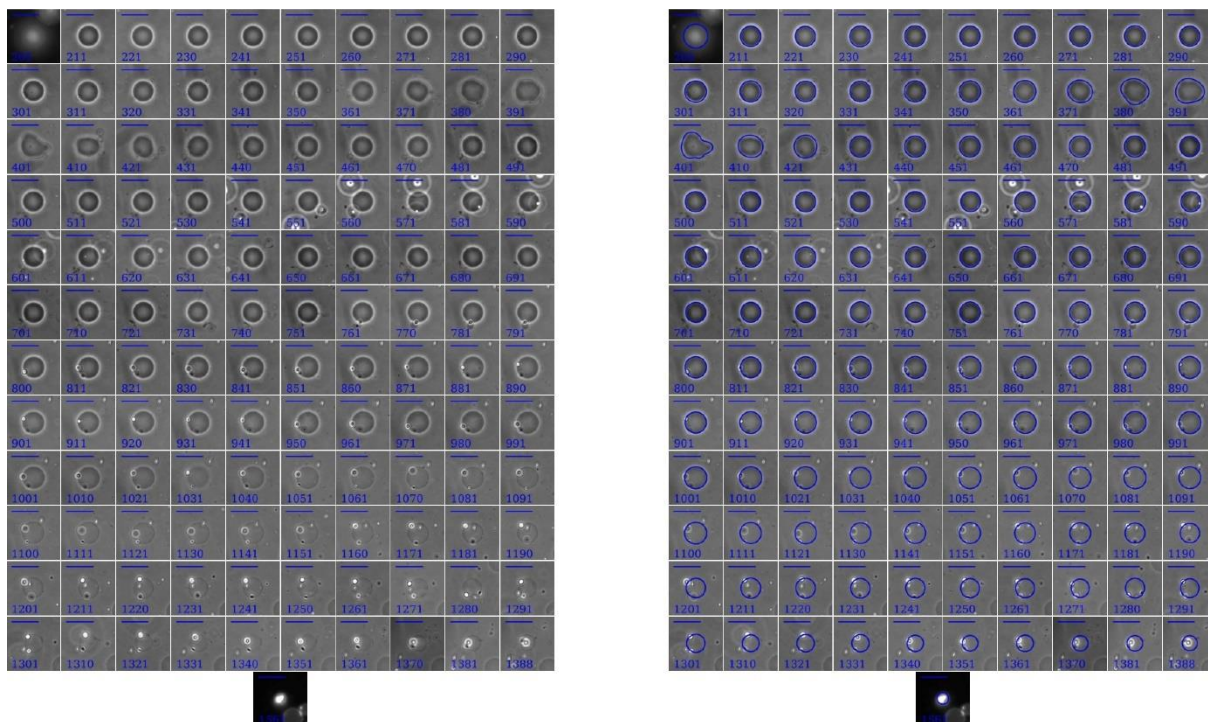
Figure 10.15 Microscope DOPC:SM:CHOL 3:5:2 GUV images (left) and best fit contours (right) in the presence of 0.25 mM mono-RL.

Figure 10.16 Microscope DOPC:SM:CHOL 3:5:2 GUV images (left) and best fit contours (right) in the presence of 0.06 mM di-RL.

Figure 10.17 Microscope DOPC:SM:CHOL 3:5:2 GUV images (left) and best fit contours (right) in the presence of 0.12 mM di-RL.

Figure 10.18 Microscope DOPC:SM:CHOL 3:5:2 GUV images (left) and best fit contours (right) in the presence of 0.25 mM di-RL.

Figure 10.19 Microscope DOPC:SM:CHOL 5:3:2 GUV images (left) and best fit contours (right) in the presence of 0.06 mM mono-RL.

Figure 10.20 Microscope DOPC:SM:CHOL 5:3:2 GUV images (left) and best fit contours (right) in the presence of 0.12 mM mono-RL.

Figure 10.21 Microscope DOPC:SM:CHOL 5:3:2 GUV images (left) and best fit contours (right) in the presence of 0.25 mM mono-RL.
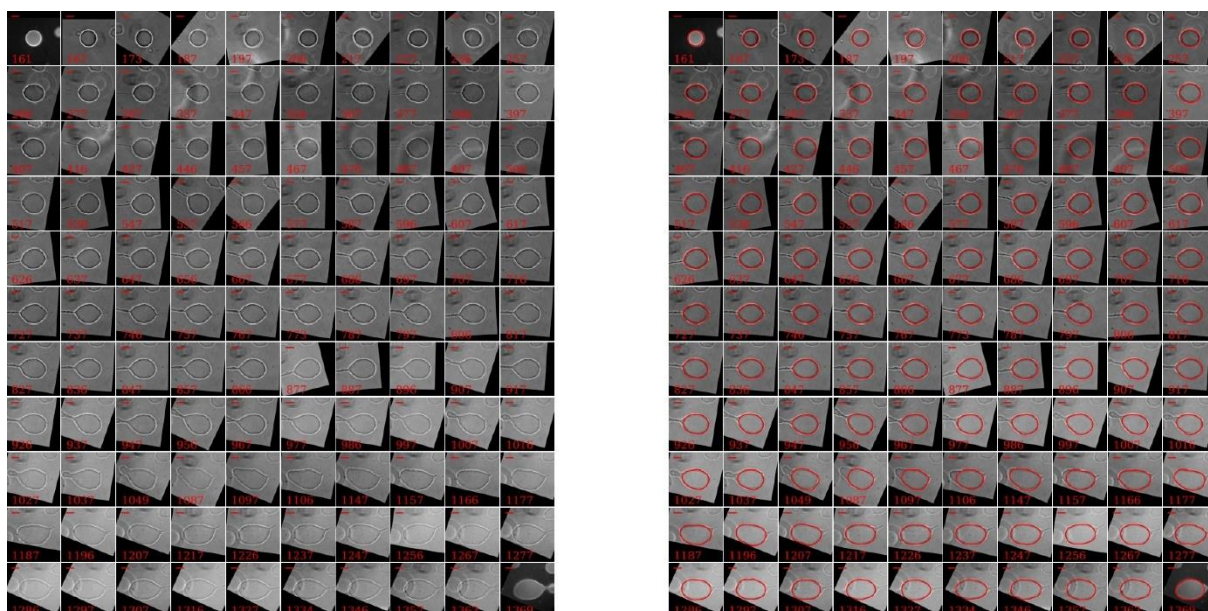

Figure 10.22 Microscope DOPC:SM:CHOL 5:3:2 GUV images (left) and best fit contours (right) in the presence of 0.06 mM di-RL.
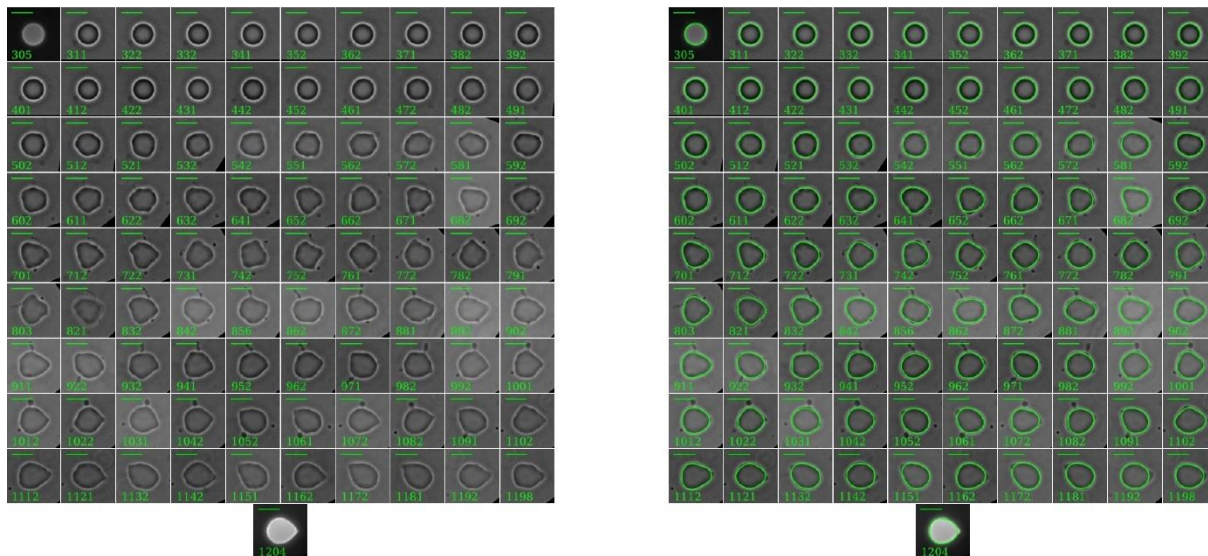
Figure 10.23 Microscope DOPC:SM:CHOL 5:3:2 GUV images (left) and best fit contours (right) in the presence of 0.12 mM di-RL.
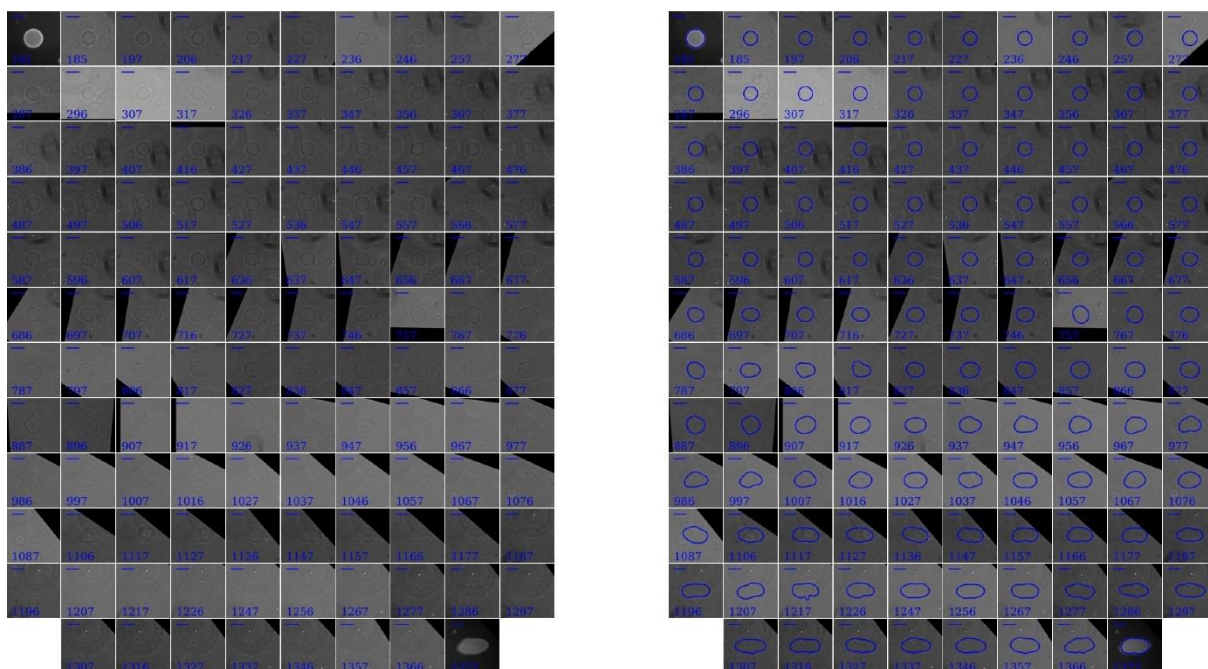

Figure 10.24 Microscope DOPC:SM:CHOL 5:3:2 GUV images (left) and best fit contours (right) in the presence of 0.25 mM di-RL.